Measurement of Associated Z^0-Boson and b-Jet Production in Proton-Proton Collisions with the CMS Experiment

Dissertation
zur Erlangung des Doktorgrades
des Department Physik
der Universität Hamburg

vorgelegt von

Johannes Hauk

aus Buchen

Hamburg
2012

Gutachter der Dissertation: Priv.-Doz. Dr. Achim Geiser
Prof. Dr. Peter Schleper

Gutachter der Disputation: Priv.-Doz. Dr. Achim Geiser
Prof. Dr. Joachim Mnich

Datum der Disputation: 30. Mai 2012

Vorsitzender des Prüfungsausschusses: Dr. Michael Martins
Vorsitzender des Promotionsausschusses: Prof. Dr. Peter Hauschildt

Leiterin des Departments Physik: Prof. Dr. Daniela Pfannkuche
Dekan der MIN-Fakultät: Prof. Dr. Heinrich Graener

Abstract

In this thesis, data of proton-proton collisions at a centre-of-mass energy of $\sqrt{s} = 7\,\text{TeV}$, delivered by LHC and recorded with the CMS experiment in 2010 and 2011, is used to perform one technical and two physics analyses. The technical one develops and uses a method to estimate the precision of the knowledge of the true geometry of the CMS inner tracking system in 2011 data. It is used to quantify the remaining deviation between assumed and true geometry, and this is employed in the reconstruction of trajectories of charged particles, and thus optimises the performance of CMS.

The first physics analysis calculates the ratio of cross sections of top-pair production ($\mathrm{t\bar{t}}$) and inclusive Z^0-boson production (i.e. Z^0/γ^* restricted to masses around the Z^0 peak) in their muonic decay modes – leading to two spatially isolated high-momentum muons – on the full 2010 dataset spanning $35.9\,\text{pb}^{-1}$. The advantage over absolute cross-section measurements is that common experimental or theoretical uncertainties cancel, like it is definitely the case for the measured luminosity. Furthermore, the $\mathrm{t\bar{t}}$ cross section can be normalised using the ratio and the theoretical Z^0 cross section, instead of the luminosity measurement. The processes are separated by the invariant dimuon mass, which shows a peak around the Z^0 mass for the Z^0 events, and a smooth wide curve for $\mathrm{t\bar{t}}$ events. The final combination of the $\mathrm{t\bar{t}}$ cross section measurements normalised to luminosity, respectively to the Z^0 as standard candle, results in improved precision.

The second physics analysis is the cross-section measurement of associated Z^0-boson and b-jet production (bZ^0) in $2.2\,\text{fb}^{-1}$ of 2011 data, again in the decay channel $\mathrm{Z}^0 \to \mu^+\mu^-$, but now requiring in addition the presence of at least one b-tagged jet. This process is very similar to $\mathrm{t\bar{t}}$, since both contain two muons and two b jets in the final state. Since their cross sections are also similar, both processes are the main backgrounds for each other—however they can be separated by their difference in missing transverse energy $\not{E}_\mathrm{T}$, arising in $\mathrm{t\bar{t}}$ from the undetected neutrinos, while there is no natural $\not{E}_\mathrm{T}$ in general in bZ^0. The focus lies on the estimation of the $\mathrm{t\bar{t}}$ background, measuring this contribution in the dimuon invariant mass sideband region above the Z^0 peak where it dominates, and extrapolating it into the signal region around the Z^0 peak. The inclusive cross section $\sigma_{\text{inc}}^{\mathrm{bZ}^0}$, defined for $60\,\text{GeV} < M_{\mathrm{Z}^0} < 120\,\text{GeV}$, $\mathrm{Z}^0 \to \mu^+\mu^-$, and at least one b jet on hadron-level in the kinematic range $p_\mathrm{T}^\mathrm{b} > 25\,\text{GeV}$, $|\eta^\mathrm{b}| < 2.1$ and $\Delta R(\text{jet,muons}) > 0.5$ yields $\sigma_{\text{inc}}^{\mathrm{bZ}^0} = 5.97 \pm 0.10\,(\text{stat.})^{+0.78}_{-0.93}\,(\text{syst.})\,\text{pb}$. The result is slightly above the prediction—this can be an indication that potential associated Higgs-boson and b-jet production cross sections might also be above the prediction.

Zusammenfassung

In dieser Dissertation werden Daten von Proton-Proton-Kollisionen des LHC aus den Jahren 2010 und 2011 bei einer Schwerpunktsenergie von $\sqrt{s} = 7\,\mathrm{TeV}$, aufgezeichnet mit dem CMS-Experiment, für eine technische und zwei Physikanalysen verwendet. Die technische entwickelt und verwendet eine Methode zur Bestimmung der Genauigkeit der Kenntnis der wahren CMS-Spurdetektorgeometrie in Daten aus 2011. Dies wird genutzt, um die Abweichung von angenommener und wahrer Geometrie zu quantifizieren, was wiederum in der Spurrekonstruktion geladener Teilchen verwendet wird und somit die Güte von CMS optimiert.

Die erste Physikanalyse berechnet unter Verwendung des kompletten 2010er Datensatzes, $35.9\,\mathrm{pb}^{-1}$ entsprechend, das Wirkungsquerschnittsverhältnis von Top-Paar- ($\mathrm{t\bar{t}}$) und Z^0-Boson-Produktion (d.h. Z^0/γ^* beschränkt auf Massen um den Z^0-Peak) in ihren myonischen Zerfallsmodi, welche in zwei räumlich isolierten hochenergetischen Myonen resultieren. Dies hat gegenüber absoluten Wirkungsquerschnittsmessungen den Vorteil, dass sich gemeinsame experimentelle oder theoretische Unsicherheiten kürzen, was definitiv auf die Luminosität zutrifft. Des Weiteren kann der $\mathrm{t\bar{t}}$-Wirkungsquerschnitt anstelle der Luminositätsmessung unter Verwendung des Verhältnisses und des theoretischen Z^0-Wirkungsquerschnittes normiert werden. Die Prozesse werden anhand der invarianten Dimyonmasse separiert, welche für Z^0-Ereignisse einen Peak um die Z^0-Masse und eine weite glatte Verteilung für $\mathrm{t\bar{t}}$-Ereignisse aufweist. Die Kombination der $\mathrm{t\bar{t}}$-Wirkungsquerschnittsmessungen, normiert zur Luminosität beziehungsweise zu Z^0 als Standardkerze, führt zu höherer Präzision.

Die zweite Physikanalyse ist die Wirkungsquerschnittsmessung von assoziierter Z^0-Boson- und b-Jet-Produktion (bZ^0) in $2.2\,\mathrm{fb}^{-1}$ der 2011er Daten, wiederum im Zerfallskanal $\mathrm{Z}^0 \to \mu^+\mu^-$, allerdings unter zusätzlicher Forderung mindestens eines Jets, welcher als von einem b-Quark stammend identifiziert ist. Dieser Prozess ist $\mathrm{t\bar{t}}$ sehr ähnlich, da beide je zwei Myonen und zwei b-Jets im Endzustand aufweisen. Da auch ihre Wirkungsquerschnitte ähnlich sind, sind sie Hauptuntergründe füreinander; jedoch können sie mittels ihres Unterschiedes in fehlender Transversalenergie $\not{E}_\mathrm{T}$, in $\mathrm{t\bar{t}}$ bedingt durch die nicht messbaren Neutrinos, während in bZ^0 allgemein keine natürliche $\not{E}_\mathrm{T}$ auftritt, getrennt werden. Das Hauptaugenmerk liegt auf der $\mathrm{t\bar{t}}$-Untergrundbestimmung: der Beitrag wird im Seitenband der Dimyonmasse oberhalb des Z^0-Peaks, wo er dominiert, gemessen und in die den Z^0-Peak einschließende Signalregion extrapoliert. Der inklusive Wirkungsquerschnitt $\sigma_\mathrm{inc}^{\mathrm{bZ}^0}$, definiert für $60\,\mathrm{GeV} < M_{\mathrm{Z}^0} < 120\,\mathrm{GeV}$, $\mathrm{Z}^0 \to \mu^+\mu^-$, und mindestens einen b-Jet auf Hadron-Ebene im kinematischen Bereich $p_\mathrm{T}^\mathrm{b} > 25\,\mathrm{GeV}$, $|\eta^\mathrm{b}| < 2.1$ und $\Delta R(\text{jet,muons}) > 0.5$, beträgt $\sigma_\mathrm{inc}^{\mathrm{bZ}^0} = 5.97 \pm 0.10\,(\text{stat.})^{+0.78}_{-0.93}\,(\text{syst.})\,\mathrm{pb}$. Das Ergebnis ist leicht oberhalb der Vorhersage; dies kann ein Indiz dafür sein, dass potentielle Wirkungsquerschnitte assoziierter Higgs-Boson- und b-Jet-Produktion ebenfalls über der Vorhersage liegen könnten.

Contents

1 Introduction **1**

2 Theory **5**

2.1 The Standard Model of Particle Physics . . . 5
  2.1.1 Elementary Particles . . . 6
  2.1.2 Interactions . . . 7
  2.1.3 Electroweak Unification and Higgs Mechanism . . . 11
  2.1.4 Theories beyond the Standard Model . . . 12
2.2 Proton-Proton Collisions . . . 13
  2.2.1 Structure of the Proton . . . 15
  2.2.2 Factorisation Theorem . . . 15
  2.2.3 Partonic Cross Section . . . 16
  2.2.4 Parton Distribution Functions . . . 16
  2.2.5 Underlying Event, Pileup and Non-Collision Background 18
2.3 Relevant Processes . . . 18
  2.3.1 Top-Pair Production and Decay . . . 18
  2.3.2 Z^0-Boson Production and Decay . . . 21
  2.3.3 Z^0-Boson Production in Association with Beauty Quarks 24
2.4 Particle Interactions with Matter . . . 28

3 The CMS Experiment at the LHC **31**

3.1 The LHC Accelerator . . . 31
3.2 The CMS Experiment . . . 32
  3.2.1 Detector Components and Particle Identification . . . 33
  3.2.2 Trigger and Data Acquisition . . . 39
  3.2.3 Data Quality Certification . . . 40
3.3 The CMS Tracker . . . 41
  3.3.1 Design . . . 41

3.3.2 Operation Mode of Silicon Modules 44
3.3.3 Track Reconstruction 46
3.3.4 Track Refit 49
3.4 Event Simulation 50
3.4.1 Monte Carlo Method 50
3.4.2 Event Generators 51
3.4.3 Detector Simulation with GEANT4 53
3.5 Event Reconstruction and Object Identification 53
3.5.1 Primary Vertex Identification 54
3.5.2 Muon Reconstruction 54
3.5.3 Muon Identification and Isolation 55
3.5.4 Jet Reconstruction 57
3.5.5 Jet Identification 60
3.5.6 Heavy Flavour Tagging 61
3.5.7 Missing Transverse Energy 62
3.6 Luminosity Measurement 62

4 Estimation of the Tracker Alignment Precision 65
4.1 Influence of Misalignment on the Event Reconstruction 66
4.1.1 Alignment and Calibration Database 66
4.1.2 Hit Residuals and χ^2-Value of Track Fit 68
4.1.3 Influence of Misalignment and Alignment Precision on the Tracker Performance 69
4.2 Tracker Alignment 71
4.2.1 Track-Based Alignment 73
4.3 Implementation of the Alignment Precision 76
4.4 Basic Principle of Estimation of Alignment Precision 77
4.4.1 Normalised Hit Residual Distributions 77
4.4.2 Implementation of the Estimation Method 81
4.4.3 Estimation of Nominal Residual Width from Simulation 83
4.5 Systematic Influences 84
4.6 Detector Granularity for Estimate of Alignment Precision 85
4.7 Results 88
4.7.1 Geometry of Prompt Reconstruction 89
4.7.2 Comparison to Geometry of Reprocessing 94
4.7.3 Systematic Studies introducing Misalignments 99
4.8 Conclusions 101

5 Cross-Section Ratio of Top-Pair and Z^0-Boson Production 105
5.1 Data and Simulated Samples 106
5.2 Event Selection 108
5.2.1 $t\bar{t}$ Selection 108
5.2.2 Z^0 Selection 111
5.3 Background Estimation 113
5.4 Results 114
5.4.1 Definition of Cross Sections 115
5.4.2 Estimates for Total Efficiency 116
5.4.3 Systematic Uncertainties 119
5.4.4 Cross Sections and Cross-Section Ratios 124
5.5 Conclusions 127

6 Measurement of Associated Z^0-Boson and b-Jet Production 129
6.1 Data and Simulated Samples 130
6.2 Event Selection 131
6.2.1 Selection Efficiencies and Simulation Scale Factors 132
6.2.2 Selection Steps and Event Yields 134
6.3 Definition of Cross Section and Generalities of Measurement . . 137
6.3.1 General Thoughts 137
6.3.2 Definition of Cross Section 140
6.3.3 Generalities of Cross-Section Measurement 141
6.4 Purity of b Jets 142
6.5 Estimation of the $t\bar{t}$ Background 143
6.5.1 Description of the Method 144
6.5.2 Ingredients and Corresponding Uncertainties 146
6.5.3 $t\bar{t}$ Contamination Results and Discussion 152
6.5.4 Systematic Influence of Pileup 157
6.6 Final Background Estimate 161
6.6.1 Appraisal of All Backgrounds 161
6.6.2 Background Calculation and Discussion 164
6.7 Selection Efficiencies and Correction Factors 164
6.8 Measurement of Cross Section 167
6.8.1 Cross-Section Calculation and Systematic Uncertainties . 168
6.8.2 Results 170
6.9 Conclusions 171

7 Summary 173

A Appendix for Chapter 4 179

A.1 Tracker Alignment 179

A.1.1 Important Sets of Alignment Parameters 179

A.2 Implementation of the Alignment Precision 182

A.2.1 Alignment Precision Record 182

A.2.2 Implementation in the Track Reconstruction 183

A.2.3 Coordinate Systems 185

A.3 Basic Principle of Estimation of Alignment Precision 189

A.3.1 Unbiased Track Prediction 189

A.4 Cluster Parameter Estimators 190

A.4.1 Pixel CPE 190

A.4.2 Strip CPE 190

A.5 Systematic Influences 193

A.5.1 Misalignment 193

A.5.2 Miscalibration 193

A.5.3 Coordinate System 194

A.5.4 Detector Effects 194

A.5.5 Biases from Track Reconstruction 195

A.5.6 Implementation of Local Method 195

A.5.7 Incorrect Modelling of Data 196

A.6 Modelling of Data and Event Selection 198

A.7 Track and Hit Selection 201

A.7.1 Track Selection 201

A.7.2 Hit Selection 209

A.8 Results 216

A.8.1 Additional Figures for Prompt Geometry 216

B Appendix for Chapter 6 227

B.1 Updated Result of Correction Factor $\rho_{R_{\mathrm{t\bar{t}}}}$ 227

B.2 $\mathrm{t\bar{t}}$ Background in $\mathrm{bZ^0}$, $\mathrm{Z^0} \rightarrow \mathrm{ee}$ 228

List of Tables 233

List of Figures 237

Bibliography 241

Chapter 1

Introduction

One thought-provoking issue that mankind fascinates is the origin of the world we live in and all the matter that forms ourselves and everything we observe. Abstract reasoning of many philosophers led to many conceptions, and the idea of matter consisting of different elements and of atomism – fundamental building blocks of matter – can be traced back to the ancient Greeks. A long time later, after the concepts of atoms and of particles such as electrons and alpha particles were established by scientific research in physics and chemistry, Rutherford's scattering experiment discovering the atomic nucleus founded a vital technique to analyse the composition of matter in sub-atomic dimensions. Research on the experimental side – mainly via scattering experiments – and on the theoretical side, extended the picture and the new discipline particle physics was born. The knowledge obtained throughout the last hundred years is described nowadays by the Standard Model of particle physics, which reduces all matter and its behaviour to a set of fundamental particles—matter constituents which interact by exchange of force mediating particles. All but the so-called Higgs boson are meanwhile established. However, there are indications that this theory is an approximation in the energy range investigated, by reason of divergencies when extrapolating to higher energies—several theoretical approaches, e.g. introducing additional heavy particles or extra space dimensions, try to describe physics beyond the Standard Model. Since November 2009 the Large Hadron Collider (LHC) [1] at the European Organization for Nuclear Research CERN (see Figure 1.1) accelerates protons and provides proton-proton collisions, embracing an extensive physics programme. This establishes a new era of particle physics, providing measurements at a previously unknown energy scale.

In this thesis, collisions provided by LHC at a centre-of-mass energy of $\sqrt{s} = 7\,\mathrm{TeV}$ and recorded with the Compact Muon Solenoid Experiment (CMS) [2] are analysed; three different studies, a technical and two physics analyses, are presented. CMS is a multi-purpose detector with the typical arrangement of different detector systems. The inner tracking system (called tracker) is the biggest all-silicon tracker ever built. It is the entity of interest in the technical analysis presented in this work. The tracker is intended to reconstruct trajectories of charged particles traversing the tracker volume (referred to as tracks) based on a set of local coordinate measurements of penetrated silicon modules (named hits). In order to reach the precision required by physics analyses, the positions and orientations of the modules need to be known better than their spacial resolution is. Despite the high mounting precision, a more precise determination of the module parameters is necessary. These corrections of the nominal geometric positions are called alignment, and it is based mainly on sophisticated stochastic approaches using millions of reconstructed tracks. The remaining deviations of estimated and real module parameters are called misalignment.

The misalignment can be quantified with an uncertainty taken into account in the track reconstruction—it is called the alignment precision. This is important for both, high efficiency in track finding, and most correct parameterisation of tracks. Many CMS physics analyses use tracker information, suffering from potential incorrect error estimates; and especially the identification of hadronic jets initiated by beauty quarks (b-tagging) needs precise track estimates. The technical analysis presented in this thesis describes a method developed for estimating the alignment precision with a stochastic approach using millions of reconstructed tracks, and the results. On one hand, improvements of alignment can be confirmed when comparing results for different geometries. On the other hand, a set of alignment precision parameters can be produced and used in the track reconstruction for optimal performance.

Proton-proton collisions are complicated processes due to the inner proton structure formed by quarks and gluons—the collisions lead to many particles in the measured final state. Especially muons can be well tracked down and measured precisely in such a crowded environment. All analyses presented use events with muons stemming mainly from decays of the electroweak gauge bosons $\mathrm{W}^{\pm}$ and Z^0, which are produced either directly or originate from top quark decays in top-pair production. Profound understanding of the protons defining the initial state of the process is essential for the interpretation of the measurement and to calculate and simulate processes of interest. Deep insight into the proton structure is obtained especially by the experiments at the HERA accelerator at DESY, allowing a description of proton scattering processes via the deconvolution of perturbatively predictable parts and precisely measured empiric parts.

The processes studied in the physics analyses of this work are the following Standard Model processes incorporating the two heaviest fundamental particles discovered so far, the top quark and the Z^0 boson: the inclusive production of Z^0 bosons, but also a specific sub-case of this process, the production of Z^0 bosons in association with b quarks (bZ^0), and top-pair production ($\mathrm{t\bar{t}}$). The latter two processes require high energies, thus only at TeVatron measurements could be performed before the LHC era. In 2010 LHC offered the first observation of the top quark and bZ^0 in Europe, while a cross-section measurement of inclusive Z^0 production was possible already with good precision and not limited by statistical power. The production rates of these processes at LHC exceed those at TeVatron by far, allowing precision measurements of several quantities. An important intention of the early LHC measurements is to probe the Standard Model at the TeV scale and to search for hints of new physics in these well understood processes, but also their usage in detector calibration and as benchmark for other processes. The process bZ^0 might also help optimising the proton description by constraining the beauty-quark content of the proton. In this thesis, the muonic decay channels are evaluated; the topology of the processes become similar and they are main backgrounds for each other.

Instead of providing absolute cross sections, the measurement of cross-section ratios can result in higher precision due to cancellations of experimental and possibly also theoretical uncertainties. The 2010 data is used to provide the $\mathrm{t\bar{t}}$-to-Z^0 ratio of cross sections in dimuonic final states, testing the Standard Model predictions. The well measured and precisely calculated inclusive Z^0 production is also used as an alternative to the direct luminosity measurement for normalisation of the $\mathrm{t\bar{t}}$ cross section, i.e. Z^0 is used as a standard candle.

The main topic described in this thesis is the measurement of the bZ^0 cross section in the 2011 data. It is of special relevance as benchmark process – but also as important background – for specific production and decay channels of potential Higgs-boson measurements, in the Standard Model as well as in some supersymmetric models. Different theoretical calculation schemes result in big deviations of the central values of the cross section of associated Higgs-boson and b-jet production (bH), but within the huge uncertainties. Due to the similarity of bZ^0 and bH, the bZ^0 cross-section measurement in comparison to theory predictions might indicate the behaviour of the bH cross section to be measured, with respect to a calculated one.

The thesis is structured as follows. Chapter 2 summarises the theoretical background needed for this work, Chapter 3 describes the experiment and explains all relevant points of the event reconstruction. The technical analysis concerning the estimation of the alignment precision is detailed in Chapter 4. In Chapter 5 the measurement of the cross-section ratio of top-pair and inclusive Z^0 production is shown. Chapter 6 presents the analysis of the bZ^0 process and the measurement of its cross section. Finally, a summary and conclusions are noted down in Chapter 7.

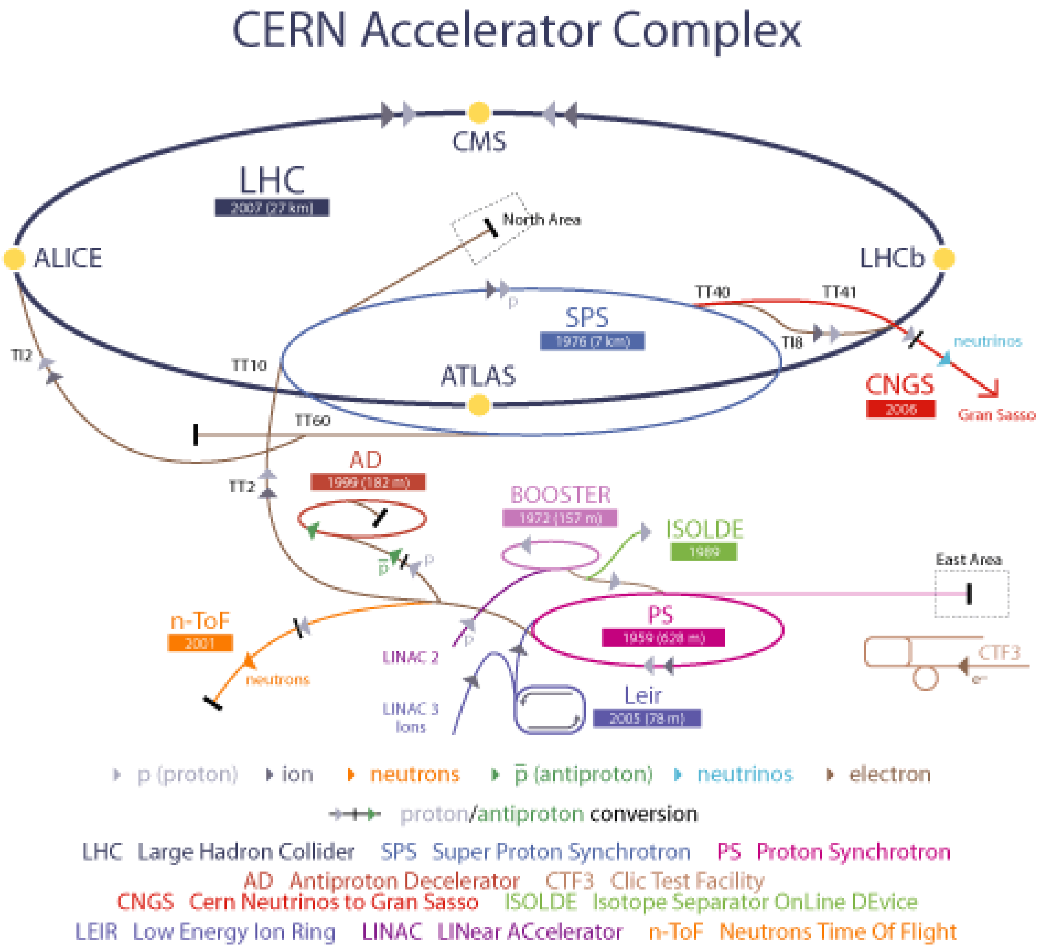

Figure 1.1: The CERN accelerator complex [3]. LHC is the last ring (dark grey line) in a chain of particle accelerators. The smaller accelerators are used as pre-accelerators, and as final accelerators for several smaller experiments.

Chapter 2

Theory

In this chapter, the relevant theoretical background for this work is explained. The current understanding of high-energy physics is based on the Standard Model, which explains all matter and interactions based on elementary particles. All measurements in this thesis are based on proton-proton collisions, which require a sophisticated description of this initial state, in order to understand the effects influencing the measurement. The relevant processes for the physics analyses in Chapter 5 and Chapter 6 are production and decay of two specific fundamental particles, the top quark and the Z^0 boson. Finally, a short overview of particle interactions with detector material is given as background for the technical analysis in Chapter 4 and for the description of the CMS experiment in Chapter 3.

2.1 The Standard Model of Particle Physics

The Standard Model of particle physics (SM) summarises our present understanding of matter and possible interactions, obtained in the last decades by experimental and theoretical research. In this model, all visible matter that can be observed in the universe is composed of 12 elementary particles, which are fermions; their interactions are based on the exchange of force mediating particles, which are bosons. The three included forces are given by the electromagnetic, the weak and the strong interaction. Gravity as the fourth known interaction is not described in this model, its strength is many orders of magnitude smaller than the other forces.

The Standard Model is defined as a relativistic quantum field theory. The interactions are the result of local gauge invariance of the wave functions of the fermions. Extensive descriptions of the Standard Model can be found e.g. in [4], the most important details as needed for this thesis are outlined in this chapter.

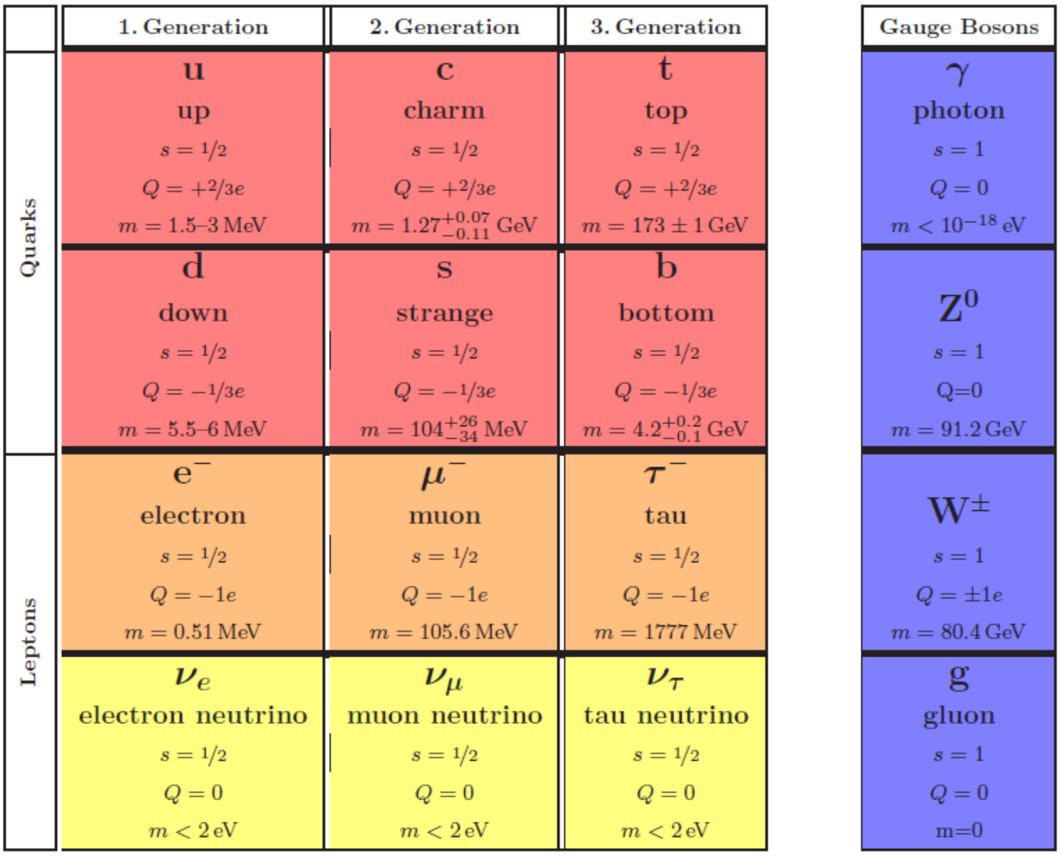

	1. Generation	2. Generation	3. Generation	Gauge Bosons
Quarks	u up $s = 1/2$ $Q = +2/3e$ $m = 1.5\text{–}3\,\text{MeV}$	c charm $s = 1/2$ $Q = +2/3e$ $m = 1.27^{+0.07}_{-0.11}\,\text{GeV}$	t top $s = 1/2$ $Q = +2/3e$ $m = 173 \pm 1\,\text{GeV}$	γ photon $s = 1$ $Q = 0$ $m < 10^{-18}\,\text{eV}$
	d down $s = 1/2$ $Q = -1/3e$ $m = 5.5\text{–}6\,\text{MeV}$	s strange $s = 1/2$ $Q = -1/3e$ $m = 104^{+26}_{-34}\,\text{MeV}$	b bottom $s = 1/2$ $Q = -1/3e$ $m = 4.2^{+0.2}_{-0.1}\,\text{GeV}$	Z^0 $s = 1$ Q=0 $m = 91.2\,\text{GeV}$
Leptons	e^- electron $s = 1/2$ $Q = -1e$ $m = 0.51\,\text{MeV}$	μ^- muon $s = 1/2$ $Q = -1e$ $m = 105.6\,\text{MeV}$	τ^- tau $s = 1/2$ $Q = -1e$ $m = 1777\,\text{MeV}$	$W^\pm$ $s = 1$ $Q = \pm 1e$ $m = 80.4\,\text{GeV}$
	ν_e electron neutrino $s = 1/2$ $Q = 0$ $m < 2\,\text{eV}$	ν_μ muon neutrino $s = 1/2$ $Q = 0$ $m < 2\,\text{eV}$	ν_τ tau neutrino $s = 1/2$ $Q = 0$ $m < 2\,\text{eV}$	g gluon $s = 1$ $Q = 0$ m=0

Figure 2.1: Elementary particles of the Standard Model, listed with spin quantum number, electric charge and mass in the $\overline{\text{MS}}$ scheme (taken from [5], based on numbers from [6]). Shown are all discovered particles, the Higgs boson is not shown.

2.1.1 Elementary Particles

All known and discovered particles contained in the Standard Model are shown in Figure 2.1, and are sorted by their characteristics. The fermions which are the matter particles, are separated from the force mediating gauge bosons. The fermions are grouped by their possible interactions: the quarks underlie all three forces (electromagnetic, weak and strong interaction), while the leptons cannot interact strongly. Furthermore, there is a separation of the charged leptons, which can interact electromagnetically and weakly, while the neutral leptons – called neutrinos – are liable to the weak force only. The quarks are classified by the sign of their electric charge into positively charged up-type and negatively charged down-type quarks.

The fermions are arranged in three generations. Each generation spans four fermions, which have almost the same properties as the corresponding particles in the other generations; only their masses differ and increase in general from generation to generation. The masses vary over several orders of magnitude. The top quark has a special role, since its mass is by far the biggest mass of all known elementary particles, comparable to masses of heavy atoms. For each of the 12 fermions, there exists an antiparticle with identical properties, but opposite charge.

The gauge bosons correspond to the different possible interactions, which are described by the exchange of these bosons between the matter particles. The gluon corresponds to the strong interaction. The photon carries the electromagnetic force. The weak processes are based on three gauge bosons called Z^0, W^+ and W^-.

One additional boson of the Standard Model has not been observed to this day, it is called the Higgs boson. The existence of such a particle is based on strong theoretical arguments as will be discussed in Chapter 2.1.3.

2.1.2 Interactions

The fermions and their interactions are mathematically described in relativistic quantum field theory by terms in the Lagrangian density of the fields. The postulated invariance under certain continuous gauge transformations – represented by Lie groups – conditions the form of the interaction terms. The force mediating particles are linked to the generators of the specific gauge group. Following the Noether theorem for classical mechanics or the Ward–Takahashi identities, which is the analogon in quantum field theory, each invariance leads to a conserved physical quantity that can be identified as a specific charge of the interacting particle.

Electromagnetic Interaction

Particles carrying electric charge interact by the exchange of virtual photons—these are the quanta of the electromagnetic field. It is described by the theory of quantum electrodynamics (QED), which is one of the best understood and most exactly verified theories in physics (see e.g. [8] or [9]). The electromagnetic field is described as a field, which couples to a charged Dirac particle, in a way which is found by demanding gauge invariance of the Lagrangian term with respect to an arbitrary time and space dependent unitary transformation from the symmetry group $\mathrm{U}(1)_{\mathrm{em}}$. The coupling constant of the electromagnetic interaction, given as

$$\alpha = \frac{e^2}{4\pi} \ll 1\,, \tag{2.1}$$

is small and hence it can be used as an expansion parameter in perturbation theory. The different orders of perturbation theory can be visualised as Feynman diagrams. The enumeration begins with leading order (LO), followed by next-to-leading order (NLO), then next-to-next-to-leading order (NNLO) and so on. Exemplary diagrams are presented in Figure 2.2. Due to the low mass of the photon, which is in fact assumed to be completely massless, the range of the force is unlimited.

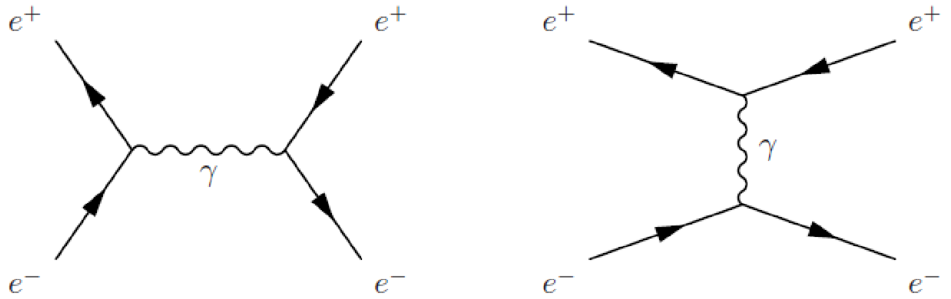

(a) s-channel (b) t-channel

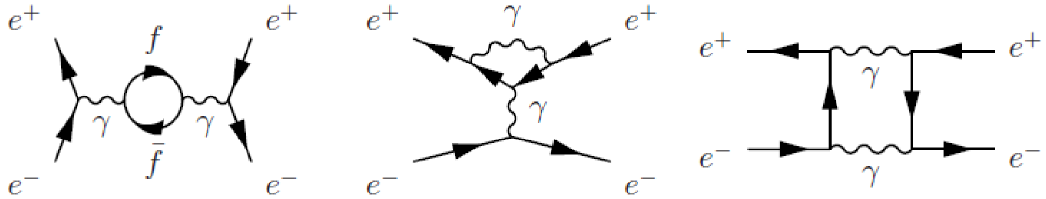

(c) s-channel with virtual $f\bar{f}$-loop (d) t-channel with vertex correction (e) box graph

Figure 2.2: Exemplary Feynman diagrams for Bhabha scattering [7] (electron-positron scattering). The figure is taken from [5], and shows the two leading order (LO) graphs with two vertices in (a) and (b), as well as three examples of next-to-next-to-leading order (NNLO) graphs with four vertices in (c), (d) and (e). NLO is given by the interference term of LO and NNLO (virtual), and Feynman graphs as for LO with additional photon radiation (real).

Strong Interaction

The description of the strong interaction is given by the theory of quantum chromodynamics (QCD), based on the gauge group $\mathrm{SU}(3)_{\mathrm{C}}$. The group theory leads to the fact, that the corresponding charge – called colour – has three different eigenstates named red, green and blue. Given the structure of the group it can be deduced, that there exists an octet of eight gluons, carrying a colour and an anticolour, and a singlet which is invariant under colour transformation. However, a singlet gluon is not observed in nature. If there was a singlet gluon, the group would be U(3) and not SU(3). Since the gluons themselves carry colour charges, they can directly interact with each other—this is a consequence of the non-Abelian character of the group.

The strength of the strong interaction is quantified by the strong coupling constant α_{s}. It depends on the momentum transfer Q^2 of an interaction, and accordingly on the distance of two interacting quarks. At large distances of the order 10^{-15} m, corresponding to low values of Q^2, α_{s} becomes very large. Consequently, quarks are always bound into hadrons and cannot be observed as free particles. This phenomenon is called confinement of the quarks—when two quarks are more and more separated in distance, the gluon field energy increases drastically, and at a certain distance the creation of a quark-antiquark pair is energetically favoured. Depending on the situation, this can lead to a whole production chain of several hadrons. The sequential pair-production effect is called hadronisation, and is especially important in high-energy collisions where outgoing quarks and gluons can occur. The confinement constrains the colour fields to string-like objects called flux-tubes. Thus, the range of the force is effectively limited to 10^{-15} m – which is roughly the size of atomic nuclei – although the gluons are massless.

The possible bound states of quarks – the hadrons – need to form a colour singlet. These can be either mesons (quark-antiquark pair), or baryons (three quarks respectively three antiquarks). Other combinations which are theoretically possible like pentaquarks (four quarks and one antiquark) have not been firmly discovered, although indications have been seen in some experiments like [10]. Of special importance in this thesis are protons, since they define the initial state of the scattering experiment. Protons are a bound state of three valence quarks uud, accompanied by gluons and fluctuating sea quarks, which show up pair-wise. All these particles are embraced by the denotation partons.

On the contrary, at small distances of interacting quarks (high values of Q^2) α_{s} becomes small. This effect is called asymptotic freedom of the quarks, and the behaviour allows the calculation of interactions at high energy scales with perturbative QCD. The characteristic scale of QCD is given by $\Lambda_{\mathrm{QCD}} = O(200\text{–}300\,\mathrm{MeV})$, where the coupling reaches the order of unity (formally, it becomes infinite) and consequently perturbation theory cannot be applied. The exact value of Λ_{QCD} depends on its definition, i.e. on the order used to define α_{s} and thus on the renormalisation scheme and on the number of considered flavours. More details are given in the following sections.

Weak Interaction

Historically, the first description of the weak force is based on the interaction of four fermions with the Fermi coupling constant G_F. The β-decay of atomic nuclei was described as a direct decay of the neutron into a proton, an electron and an antineutrino. The four-fermion vertex is still a good approximation for lepton-lepton scattering at low momentum transfer, but renormalisability made it necessary to instead describe the weak interaction by an exchange of Z^0 or $\mathrm{W}^\pm$. The β-decay is a weak interaction with electrically charged currents, but also reactions with neutral current have been observed in nuclei-neutrino reactions e.g. with the Gargamelle experiment [11]. The gauge bosons themselves have been first observed at the experiments UA1 and UA2 ([12], [13] and [14]), and have meanwhile been measured with very high precision using the accelerators LEP, SLC and TeVatron [15][16]. Due to the large mass of the weak gauge bosons, the range of weak interactions is strongly restricted—it is much weaker than the other two forces at low energy scales, but at short distances the magnitude gets similar to the electromagnetic one.

The weak eigenstates of the quarks differ from their mass eigenstates. As a consequence, the quark flavours can be transformed, and also the generation can change; up-type quarks convert into down-type quarks and vice versa via flavour-changing charged currents, based on the coupling to $\mathrm{W}^\pm$. Flavour-changing neutral currents by Z^0-exchange are not observed. The transition probability between different quark flavours is described by the Cabibbo–Kobayashi–Maskawa matrix (CKM-matrix, see [17]), which transforms down-type mass eigenstates into weak eigenstates,

$$\begin{pmatrix} u' \\ s' \\ b' \end{pmatrix} = \begin{pmatrix} V_{ud} & V_{us} & V_{ub} \\ V_{cd} & V_{cs} & V_{cb} \\ V_{td} & V_{ts} & V_{tb} \end{pmatrix} \times \begin{pmatrix} u \\ s \\ b \end{pmatrix} . \tag{2.2}$$

Unitarity of the CKM-matrix is assumed in the Standard Model. Transitions within the same generation are preferred, especially $|V_{tb}|$ is very close to 1. The weak interaction couples only to left-handed (eigenstate of chirality) fermions, and to right-handed antifermions. Thus, it violates parity P [18] and also charge conjugation C. The combined operation CP is almost conserved, but small violations could be also measured [19][20]. This requires that also time inversion T is violated, since CPT needs to be conserved in each field theory.

A similar mixing has been observed in the lepton sector for neutrinos, their mass eigenstates are not identical to the flavour eigenstates. This causes neutrino oscillations among the different generations and is evidence for finite neutrino masses—the masses itself are not yet known, but their differences are. The mixing is described by the Maki–Nakagawa–Sakata matrix (MNS-matrix), see [21] and [22]. In the original Standard Model the neutrinos are massless, but neutrino masses can be introduced as a simple extension.

2.1.3 Electroweak Unification and Higgs Mechanism

Formulating the weak interaction as a gauge theory requires the Lagrangian to be invariant with respect to transformations of the SU(2) symmetry group. Three gauge fields W_μ^1, W_μ^2 and W_μ^3 are introduced, which couple to fermions with the coupling constant g. Since the fields of $\mathrm{W}^\pm$ couple only to left-handed fermions, they can be identified as linear combinations of the first two fields,

$$\mathrm{W}^\pm = \frac{1}{\sqrt{2}}\left(\mathrm{W}_\mu^1 \mp i\mathrm{W}_\mu^2\right) . \tag{2.3}$$

Formally the left-handed and right-handed particles can be distinguished by an additional quantum number, the weak isospin I. Left-handed particles are ordered in doublets with $I_3 = -\frac{1}{2}$ for a charged lepton or a down-type quark and $I_3 = +\frac{1}{2}$ for the neutrino or up-type quark of the same generation. Right-handed particles are singlets with $I_3 = 0$.

An additional U(1) symmetry gives a fourth field B_μ with coupling constant g'. Since both fields W_μ^3 and B_μ couple to the neutrinos, they cannot be identified as the electromagnetic field. Instead, the orthogonal linear combinations A_μ and Z_μ are introduced—A_μ represents the electromagnetic field, Z_μ is responsible for the neutrino coupling:

$$\mathrm{Z}_\mu = \frac{1}{\sqrt{g^2+g'^2}}(g\mathrm{W}_\mu^3 - g'\mathrm{B}_\mu) = \mathrm{W}_\mu^3 \cos\vartheta_\mathrm{W} - B_\mu \sin\vartheta_\mathrm{W} , \tag{2.4}$$

$$\mathrm{A}_\mu = \frac{1}{\sqrt{g^2+g'^2}}(g'\mathrm{W}_\mu^3 + g\mathrm{B}_\mu) = \mathrm{W}_\mu^3 \sin\vartheta_\mathrm{W} + \mathrm{B}_\mu \cos\vartheta_\mathrm{W} , \tag{2.5}$$

with the weak mixing angle ϑ_W, which is a free parameter of the Standard Model and needs to be determined experimentally [23][24]. The elementary electric charge follows

$$e = g \cdot \sin\vartheta_\mathrm{W} = g' \cdot \cos\vartheta_\mathrm{W} . \tag{2.6}$$

The weak isospin and the electric charge Q are linked to the weak hypercharge Y via the Gell-Mann–Nishijima relation

$$Y = 2(Q - I_3) . \tag{2.7}$$

The electroweak theory is expressed as the gauge symmetry $\mathrm{SU(2)_L} \otimes \mathrm{U(1)_Y}$ of the weak isospin and the weak hypercharge. The model is also called the Glashow–Salam–Weinberg model [25].

The drawback of this model is, that originally all gauge bosons need to be massless in order to conserve gauge symmetry, which is in contradiction to the observations. As solution, an additional spin 0 quantum field is postulated and all particles are assumed to be massless; the field couples to the particles, they obtain their mass dynamically through this coupling. This is called the Higgs mechanism [26]. In order to make the mechanism work, a non-vanishing vacuum expectation value of the Higgs field is necessary, and this leads to the fact that the symmetry $\mathrm{SU}(2)_\mathrm{L} \otimes \mathrm{U}(1)_\mathrm{Y}$ must be broken.

The corresponding scalar particle is the Higgs boson. The masses of the other bosons arise in agreement with the observations. The masses of the fermions and the Higgs boson itself however cannot be deduced from this formalism, and are free parameters of the Standard Model. But the mass of the Higgs boson is connected to those of the other particles via radiative corrections, so there are hints resulting from precision measurements of other particles. The search for the Higgs boson is an important goal at LHC.

Another argument for the existence of the Higgs boson arises from divergencies in theoretical cross sections. The non-Abelian electroweak group structure results in a self-coupling of the gauge bosons. For some processes with longitudinally polarised bosons, the scattering amplitude can exceed the unitarity limit at tree level. The divergency vanishes assuming additional Feynman graphs containing the Higgs boson with a mass lower than $O(1\,\mathrm{TeV})$ [27].

2.1.4 Theories beyond the Standard Model

The Standard Model describes most observations in high energy physics very precisely, but there are observations and theoretical aspects in different domains of physics which seem to be in conflict. Gravity is not included in the model, and the theory of general relativity is incompatible with field theory. Furthermore, gravitational measurements show that the visible matter contributes only a small fraction of the energy density of the universe—an ansatz to solve the problem is the postulation of additional dark matter and dark energy [28]. The CP violation of the Standard Model is not sufficient to explain the asymmetry between matter and antimatter in the observable universe.

Another problem is the hierarchy problem between the electroweak unification scale and the grand unification scale – the scale where the electroweak and the strong force are assumed to become equal in strength – which is orders of magnitude larger. The Planck scale, which is the scale where quantum effects of gravity become important, is even larger. The Higgs mass should be much larger than the masses of the other Standard Model particles, as the radiative corrections are of the same order of magnitude at these very large scales. A Higgs mass of the order of the top quark mass can only be explained by a fine-tuning mechanism in which the quantum corrections cancel each other.

Many theoretical models have been developed throughout the last decades in order to solve several of these problems, but also many of them have been disproved by new measurements. There are theories like Technicolour or Topcolour which try to explain electroweak symmetry breaking without a Higgs boson—instead new particles and interactions should occur at energy scales above the measured ones [29]. Also the Standard Model does not exclude further generations of matter particles, but the precise measurement of the Z^0 resonance peak requires them, and in particular the associated neutrino, to have masses bigger than at least half the Z^0 mass. Other models are based on extra space dimensions and include gravity. In most of these models, these dimensions are curled up and of finite size. It is distinguished between models where only gravity can propagate in these extra dimensions with sizes of $O(10\,\mu\mathrm{m})$ [30][31], and models with very small universal extra dimensions, like Kaluza–Klein models [32]. Another ansatz is based on a symmetry between fermions and bosons, called supersymmetry. Each fermion (boson) gets assigned a boson (fermion) superpartner with exactly the same quantum number except of the spin. Since no such particle has been observed so far, supersymmetry must be broken; i.e. the masses of the superpartners must be much higher than the corresponding Standard Model partner. LHC provides the exploration of physics at a new energy scale, thus there are many direct searches for predictions of these theories, but also model independent searches for exotic effects are part of the physics programme.

The Standard Model analysis described in Chapter 6 can have significant impact especially on specific supersymmetric Higgs analyses. Supersymmetric models require more than one Higgs boson. In the Minimal Supersymmetric Standard Model (MSSM), five Higgs bosons exist [33]. Two of them carry electric charge ($H^{\pm}$), three are neutral (h^0, H^0 and A^0). The h^0 and H^0 are CP-even eigenstates, like the Standard Model Higgs boson, while the A^0 is CP-odd. The mass of h^0 is expected to be relatively small and hence is similar to the Standard Model one. More complex supersymmetric models can require even more Higgs bosons.

2.2 Proton-Proton Collisions

While the underlying theory of particle interactions can be elegantly formulated using the Lagrangian formalism, the deduced verifiable predictions are usually formulated as the cross sections and branching ratios of the analysed scattering process. Two types of subprocesses are distinguished at high-energy hadron colliders: the hard scattering, where rates and properties can be predicted with good precision using perturbation theory, an the soft scattering, where properties are dominated by non-perturbative QCD effects and which are described by phenomenological models [34]. Although the processes of interest in this thesis are hard processes, they are often accompanied by additional soft processes and a good understanding of those is crucial.

Proton-proton collisions are complicated processes (see Figure 2.3) due to the internal hadronic structure of the proton [36]. The distribution of quarks and gluons within the proton has to be considered alongside the hard process. The factorisation theorem separates the perturbative QCD calculations, used for the short-distance process-dependent cross section including initial (ISR) and final state radiation (FSR), and the empirical part for determining the long-distance functions which include hadronisation, parton distribution functions (also called parton density functions) and models of multiple partonic interactions (MPI).

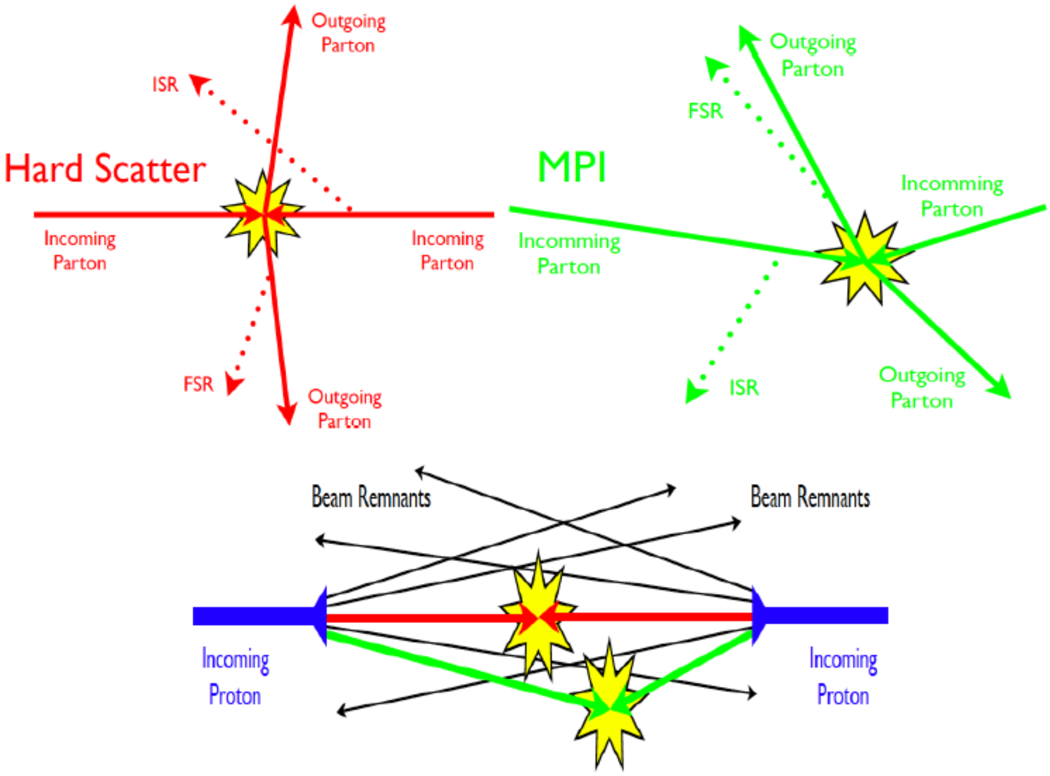

Figure 2.3: Components of a proton-proton collision [35]. The final state is a superposition of several contributions: products of the partonic hard scattering with the highest transverse momentum including initial (ISR) and final state radiation (FSR), hadrons produced in additional multiple partonic interactions (MPI), and beam remnants resulting from the hadronisation of the partonic constituents that did not participate in hard scatterings.

2.2.1 Structure of the Proton

The three valence quarks of the proton determine the quantum numbers and dominate its low-energy behaviour. The sea quarks are virtual quark-antiquark pairs which form upon the splitting of a gluon and become relevant at high energies. Conversely, the annihilation of sea quarks forms gluons, or additional gluons are radiated, resulting in a constant flux between sea quarks and gluons. The distribution of the partons within the proton is given by parton density functions (PDFs), which take the form $f_{a|\mathrm{p}}(x, Q^2)$. They give the probability to find a parton a with the momentum fraction x at the momentum scale Q^2 inside the proton p. The PDFs are assumed to give a universal description of the specific hadron, independent of the regarded scattering process.

2.2.2 Factorisation Theorem

The factorisation theorem as formulated by Drell and Yan [37] characterises the hard interaction between two protons. It postulates, that the cross section for a particular process σ_{AB} can be reformulated as a convolution of the partonic cross section $\hat{\sigma}_{ab\to\mathrm{X}}$ of the interacting partons with the PDF of the proton $f_{a|\mathrm{A}}(x, \mu_{\mathrm{F}})$. The theorem is valid for the asymptotic scaling limit, i.e. the squared centre of mass energy s going to infinity while the ratio $\hat{s}/s$ remains fixed. Here, $\hat{s} = x_a x_b s$ is the squared centre of mass energy of the interacting partons, carrying the momentum fraction x_a and x_b of the respective proton.

As long as $\alpha_{\mathrm{s}} < 1$, the perturbative series converges—the gluon radiation is well described if the renormalisation scale is comparable to the momentum scale of the radiation. Singularities from collinear gluon emission result in the perturbative calculation breaking down. The singularities of gluons with low transverse momentum are removed with the factorisation by introducing an arbitrary scale μ_{F}, the factorisation scale, which creates an artificial limit between the part of the calculation using matrix elements and the part using PDFs. This is similar to the renormalisation scale μ_{R}, which removes the divergencies in loop corrections, and absorbs them into the coupling constant α_{s}. To calculate a cross section in a certain order of α_{s}, the partonic cross section and the PDFs are needed in this respective order. The scale-invariant factorisation theorem reads

$$\sigma_{\mathrm{AB}} = \int dx_a dx_b f_{a|\mathrm{A}}(x_a, \mu_{\mathrm{F}}^2) f_{b|\mathrm{B}}(x_b, \mu_{\mathrm{F}}^2) \left\{\hat{\sigma}_{\mathrm{LO}}(\mu_{\mathrm{F}}, \mu_{\mathrm{R}}) + \alpha_{\mathrm{s}}(\mu_{\mathrm{R}}^2)\hat{\sigma}_{\mathrm{NLO}}(\mu_{\mathrm{F}}, \mu_{\mathrm{R}}) + \dots\right\}_{ab\to\mathrm{X}} . \tag{2.8}$$

In any finite order of the partonic cross-section expansion, the predicted cross section depends on the renormalisation scale μ_{R} and the factorisation scale μ_{F}. The scales are usually set to the same order of magnitude as the momentum scale of the hard interaction.

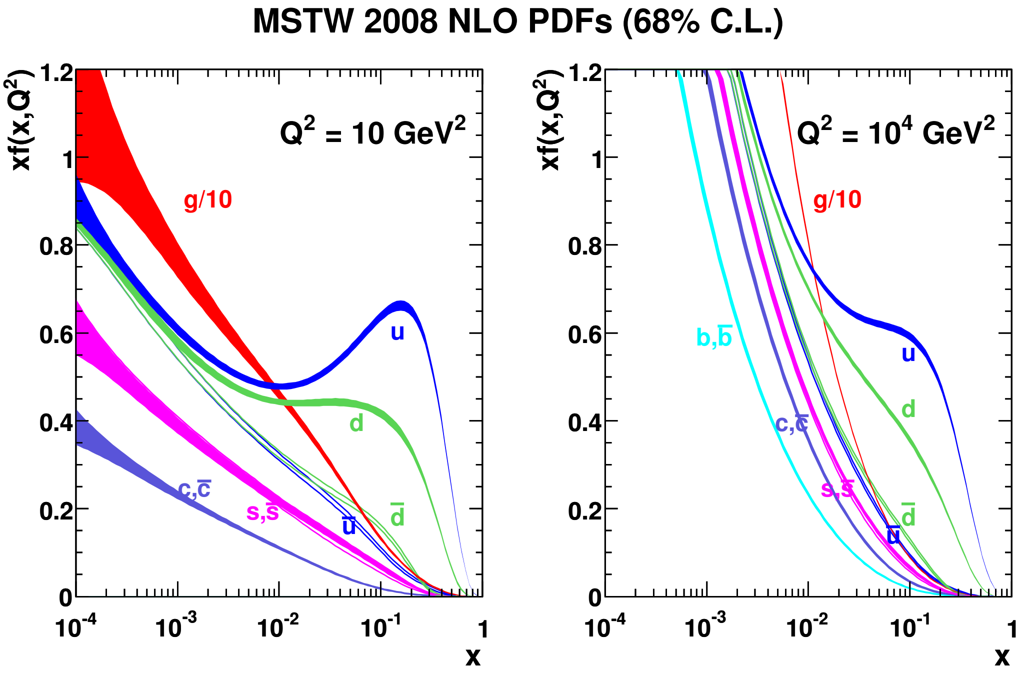

Figure 2.4: MSTW NLO PDFs at $Q^2 = 10\,\mathrm{GeV}^2$ and $Q^2 = 10^4\,\mathrm{GeV}^2$ [38]. The density at high values of the momentum fraction x is dominated by the valence quarks. Going to smaller x-values, the sea quarks become more important, and especially the gluon distribution (scaled down by a factor 10) shows a significant rise and becomes dominant.

2.2.3 Partonic Cross Section

A matrix element describes the complex amplitude of an interaction. The partonic cross section $\hat{\sigma}$ for a given process is calculated by integrating the squared matrix element over the available phase space, which has to be done numerically in most cases. LO calculations give a good estimate of the expected cross section. In the case of strong scale dependencies of the LO approximation – or when probing high-precision measurements – NLO calculations become necessary. NLO corrections contain all Feynman diagrams with an extra factor of α_s, comprising virtual corrections and ISR and FSR. The corrections are of special importance in case of shape differences for the distribution of a specific quantity, like the rapidity of produced Z^0 bosons and their decay products as used in Chapter 5. The strength of the NLO calculation with respect to the LO one is quantified by the K-factor, which is the ratio between the LO and NLO cross section in a given kinematic range.

2.2.4 Parton Distribution Functions

Given that PDFs also contain non-perturbative information of the proton structure, they cannot be derived in perturbative QCD. Instead, a starting distribution of a certain PDF is extracted from data through a global fit independent of the experimental setup. Given a parameterised starting distribution, the scale dependence – or the Q^2-evolution – is treated with perturbative QCD as described by the DGLAP equations [39][40][41][42],

$$\frac{\partial f_{a|\mathrm{p}}(x, Q^2)}{\partial \lg Q^2} = \frac{\alpha_\mathrm{s}}{2\pi} \int_x^1 \frac{dz}{z} \left\{ P_{aa'}(z, \alpha_\mathrm{s}) f_{a'|\mathrm{p}}(\frac{x}{z}, Q^2) \right\} , \tag{2.9}$$

where the splitting function $P_{aa'}(z, \alpha_\mathrm{s})$ gives the probability that the parton a evolves into another parton a', carrying the momentum fraction z, by emitting a gluon or quark. Known as the Altarelli–Parisi splitting functions, they describe the amplitudes of the processes that generate additional partons. They can be calculated as perturbative expansions in α_s:

$$P_{aa'}(z, \alpha_\mathrm{s}) = P_{aa'}^{\mathrm{LO}}(x) + \frac{\alpha_\mathrm{s}}{2\pi} P_{aa'}^{\mathrm{NLO}}(z) + \left(\frac{\alpha_\mathrm{s}}{2\pi}\right)^2 P_{aa'}^{\mathrm{NNLO}}(z) + \ldots . \tag{2.10}$$

The PDFs are fitted to data gained from different experimental setups like deep-inelastic scattering at HERA [43], fixed target experiments [44], or neutrino-nucleon scattering [45], but also other collider data e.g. from TeVatron are used as input. For the usage within CMS, PDF sets of various groups are available, such as CTEQ [46], MSTW [47] and HERAPDF [43]. An example is visualised in Figure 2.4.

There are two different basic calculation schemes to calculate cross sections based on PDFs. One is the fixed-flavour scheme, where the considered quark flavours are kept fixed, independent of the energy scale. This means that the number of flavours is given by the definition of the respective fixed-flavour scheme; three-flavour (u,d,s) and four-flavour (u,d,s,c) schemes exist. The possible processes in the matrix element are identical for each energy scale. The other is the variable-flavour scheme. The number of considered quark flavours is given by a step function depending on the energy scale, the heavy flavours are taken into account in the PDFs if the scale of the hard process is big enough. This means that the number of flavours is given by the energy of the initial state as defined by the collision process and the energy scale of the process of interest which is calculated in the matrix element.

Of special importance in Chapter 6 is the PDF of the b quark, since it has a big impact on corresponding theoretical calculations. It was hardly experimentally accessible and experimental measurements of processes sensitive to it – like the process measured in Chapter 6 – are thus not yet included in PDF fits. It is calculated from theory in all variable flavour PDF sets. Fixed flavour sets do not contain it by definition. Due to sum rules, the absolute uncertainty is similar to the other parton PDFs, but since it is the smallest contribution the relative uncertainty is rather big.

2.2.5 Underlying Event, Pileup and Non-Collision Background

As explained in Figure 2.3, the hard interaction of interest in a proton-proton collision is accompanied by several other activities. The hard interaction depends only on the state of the interacting partons, the source of the partons is irrelevant. Everything except the hard interaction of the two colliding particles defines the underlying event (UE), which is specific to the initial state [48].

Since the colliding proton bunches at LHC contain up to $1.15 \cdot 10^{11}$ protons, it is quite possible that more than one proton pair collides, which leads to additional energy flow close to the interaction of interest. Also contributions from previous bunches can occur. This effect is called pileup.

Beyond UE and pileup, there are further contributions which do not stem from proton-proton collisions and can influence a measurement. On one hand there are muons originating from cosmic showers. On the other hand there are interactions of protons with the remaining gas in the beampipe or the beampipe itself; these can also occur far outside the experiment, leading to so-called beam halo contributions. All the mentioned effects need to be considered in a measurement.

2.3 Relevant Processes

In Chapter 5, a measurement of the ratio of the inclusive production cross-sections of the heaviest fundamental particles known so far is presented. These are the top quark and the Z^0 boson. Also their possible decays are of relevance, since they are identified by specific final states of the interaction, based on muons and electrons. Chapter 6 presents also a measurement of the Z^0, but in a more exclusive production mode—they are required to be produced in association with beauty quarks, which can also be identified in the final state of the interaction. These processes are explained in the following, and the relevance of the measurements is outlined. They are all Standard Model processes which have been observed already at previous experiments. However, one important reason for all of these measurements is probing the Standard Model at the new energy scale defined by LHC. This means also, that these are tests of theoretical calculation schemes like higher order calculations in perturbative QCD. An overview of important production cross sections is given in Figure 2.5.

2.3.1 Top-Pair Production and Decay

Due to the very high mass of the top quark, it was experimentally accessible only at the TeVatron collider before the LHC era, where it was also discovered in 1994 [49][50]. However, the production rate was not sufficient for precision measurements of several quantities. Thus, one important task of LHC analyses is to perform precision measurements and also completely new measurements of

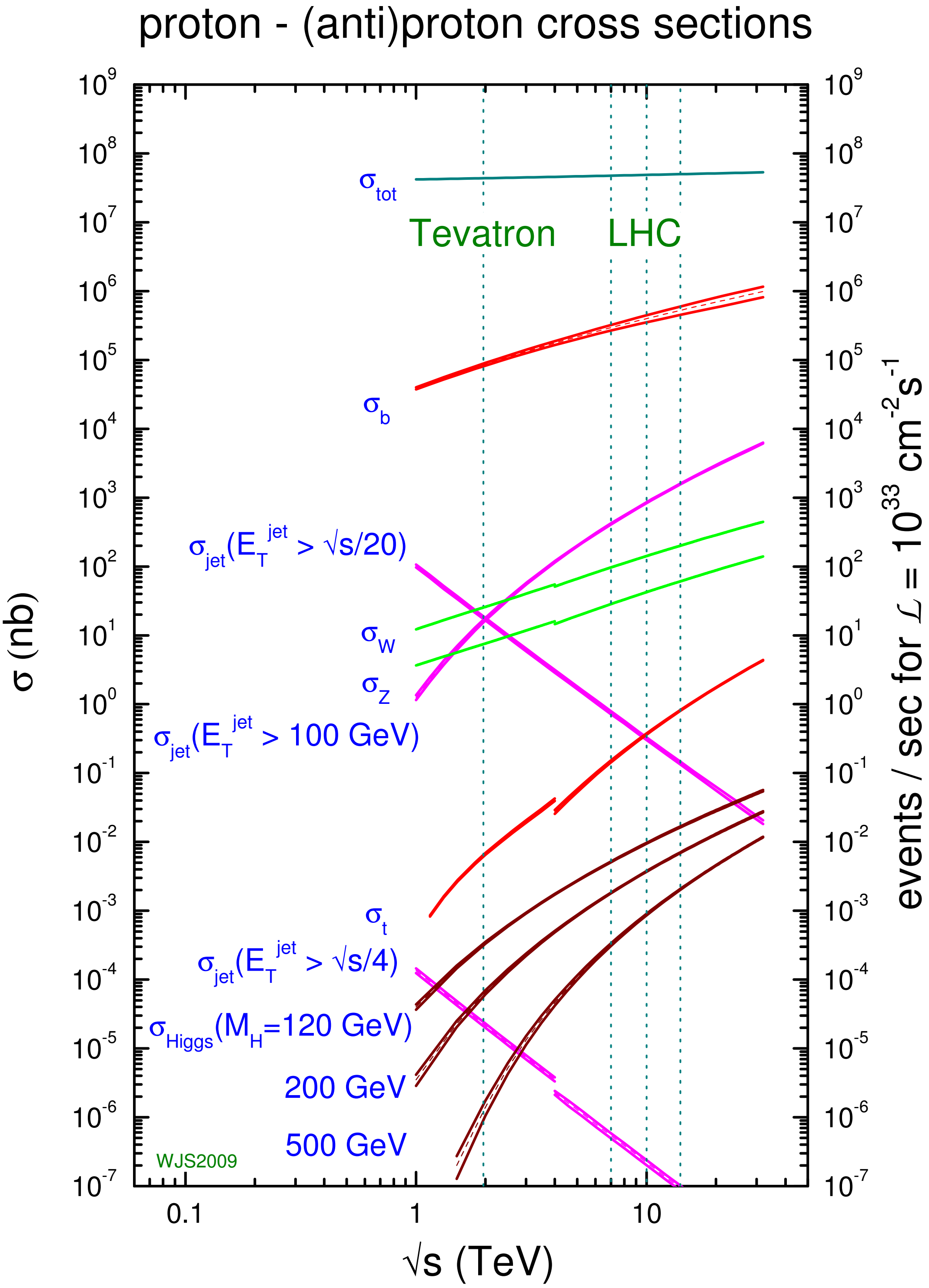

Figure 2.5: MSTW Standard Model production cross sections at TeVatron and LHC in NLO [38].

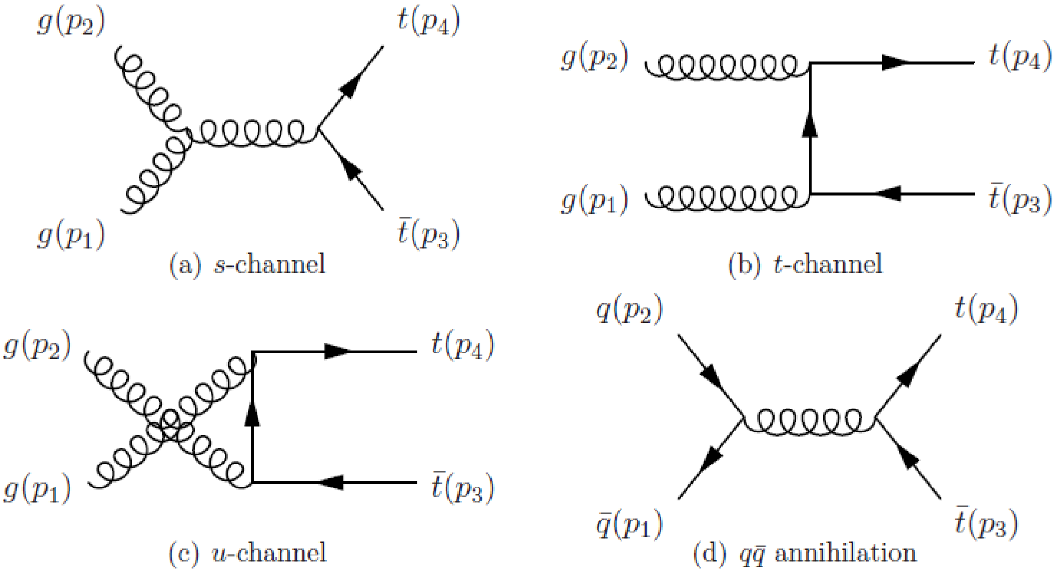

Figure 2.6: LO Feynman graphs of $t\bar{t}$ production [5]. There are three different channels of gluon-gluon fusion (a)–(c), and the quark-antiquark annihilation (d). At centre-of-mass energies as delivered by LHC the gluon-gluon fusion is dominant and contributes about 90 %.

top quark properties. An overview of the results from TeVatron, the objectives of LHC measurements, and their impact on other physics – like constraints of the Higgs boson mass and searches of physics beyond the Standard Model – can be found in [5]. Another important point why a precise understanding of the process is relevant is that it contributes a direct irreducible background to several measurements—which is here of special importance in Chapter 6, where it is the main background.

Single-top production, based on the weak interaction, is meanwhile well established. In hadron collisions however, predominantly top-pairs $t\bar{t}$ are produced, since the quark flavour is conserved in the strong interaction—and this is the process of interest in this work. The main production mechanisms are visualised in Figure 2.6. A precise (approximate NNLO) calculation of the inclusive production cross section in proton-proton collisions with $\sqrt{s} = 7\,\text{TeV}$ results in $165 \pm 10\,\text{pb}$ [51].

The only possible decay of the top quark in the Standard Model is into a W boson and a down-type quark. The branching fractions for different quark flavours are given by the CKM-matrix. Assuming its unitarity, and in accordance with all direct measurements, $|V_{\text{tb}}|^2$ is very close to one. Given the expected precision of the measurement in this work, it allows the assumption that all top quarks decay into beauty quarks. Due to the high top mass, the top decay is the only known decay where the W boson is on-shell. The lifetime of the top quark of the order $10^{-25}\,\text{s}$ is very short, and is about one order of magnitude shorter than the hadronisation time scale. Thus, on one hand no hadrons containing top quarks exist, but on the other hand the strong

Table 2.1: Branching ratios BR of $t\bar{t}$ decays for dileptonic (ll), semileptonic(l+hadrons) and all hadronic decays. Also shown are the sub-channels for decays with leptons involved. The BRs are calculated from the W branching ratios as stated in [6].

Decay	BR [%]	Sub-Decay	BR [%]
ll	10.50 ± 0.12	ee	1.16 ± 0.02
		$\mu\mu$	1.12 ± 0.02
		$\tau\tau$	1.27 ± 0.03
		eμ	2.27 ± 0.04
		eτ	2.42 ± 0.05
		$\mu\tau$	2.38 ± 0.05
l+hadrons	43.80 ± 0.40	e+hadrons	14.53 ± 0.19
		μ+hadrons	14.29 ± 0.21
		τ+hadrons	15.21 ± 0.28
all hadronic	45.70 ± 0.26		

interaction can influence the final state due to connections between initial or intermediate state and the final state [52].

The decay modes of $t\bar{t}$ are classified solely by the decay of the two W bosons. Possible W decays are into: charged lepton (e, μ, τ) and corresponding neutrino; two quarks (ud', cs'). In LO, all channels have the same probability, whereas the hadronic modes need to be counted thrice because of three possible colour states. It is distinguished between decays where both W bosons decay leptonically (dileptonic), one leptonic and one hadronic decay (semileptonic), and all hadronic decays. In this thesis, only the dileptonic decays are relevant which have a combined branching ratio BR $\approx 1/9$, and each sub-channel has BR $\approx 1/81$. The exact fractions are given in Table 2.1.

Besides the relevance of top-pair measurements for physics, these events can be used also for calibration. The dileptonic decay with final eμ state can be selected very cleanly, while the jets in the event are mainly b jets. This allows the estimation of the efficiency of tagging b jets (see Chapter 3.5.6) from data, which could be used in other analyses e.g. in a measurement as presented in Chapter 6.

2.3.2 Z^0-Boson Production and Decay

As can be explained with the electroweak unification, each process with photon exchange can also take place with Z^0 exchange instead, as long as the participating particles have the relevant chirality. Conversely, each process with Z^0 exchange can take place with photon exchange, if the participating particles are charged. The processes of interest in this thesis are based on charged particles both, in the initial and in the final state. Thus, the gauge boson exchange is an interference between the Z^0 and virtual photons γ^*. However,

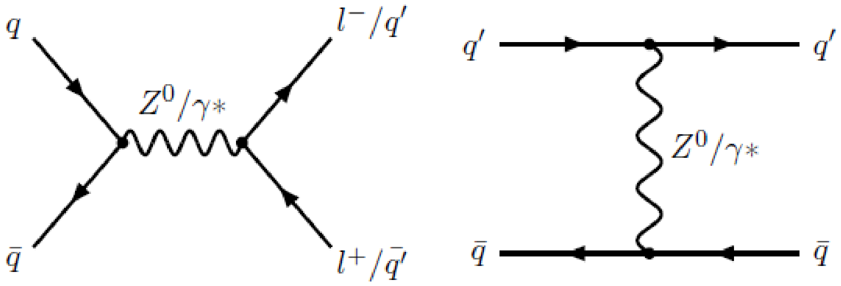

(a) Drell-Yan LO (b) t-channel LO

Figure 2.7: LO Feynman graphs of Z^0/γ^* exchange [53].

the analysed processes are restricted to an invariant boson mass around the Z^0 peak, and in the peak the photon term and the interference term are only a small contribution to the total cross section—but their influence increases at the tails of the peak. In Figure 2.7 the Z^0/γ^* exchange in LO is shown. The relevant process in this work is the s-channel exchange, and only the leptonic decay of the Z^0/γ^*– which is called Drell–Yan process – is considered. More precisely, the decay into a muon-pair is measured. Throughout this thesis, this interfering process in the s-channel is referred to as Z^0 production.

The Z^0 is produced by the annihilation of a quark-antiquark pair of same flavour, or at higher orders it can be radiated by a quark excited by a gluon. At LHC, the LO contribution to the production is about 65 %, while the remaining 35 % originate from higher order corrections. The production rate at LHC is high—for a precise comparison with data, LO and NLO predictions are insufficient and more accurate predictions of at least NNLO are needed and used in Chapter 5. The Z^0 peak can be described by a Breit-Wigner function. The shape of the Z^0/γ^* interference effect is well confirmed by measurements, see Figure 2.8.

The lifetime of the Z^0 is about 10^{-25} s. Possible decays are into all fermion-antifermion pairs, except of the top quark due to its high mass. The branching ratios are listed in Table 2.2. The electroweak theory leads to the fact, that the coupling depends also on the electric charge. The decay into neutrinos is more probable than into charged leptons. The decay probability into quarks of specific colour is in between, for up-type quarks it is lower than for down-type quarks, but the colour factor $n_C = 3$ – reflecting the three possible colour states – makes hadronic decays most probable. The branching ratio does not depend on the lepton flavour, which is known as lepton universality. However at hadron colliders, only muonic or electronic decays allow a precise identification and invariant mass measurement of the Z^0. In this thesis, only the decay into muons is considered.

The decomposition of the quark flavours involved in Z^0 production is visualised in Figure 2.9. At the TeVatron, the contributions from u and d quarks is completely dominating the production. Besides the lower energy, the possibility to create a Z^0 directly from the valence quarks raises these contributions.

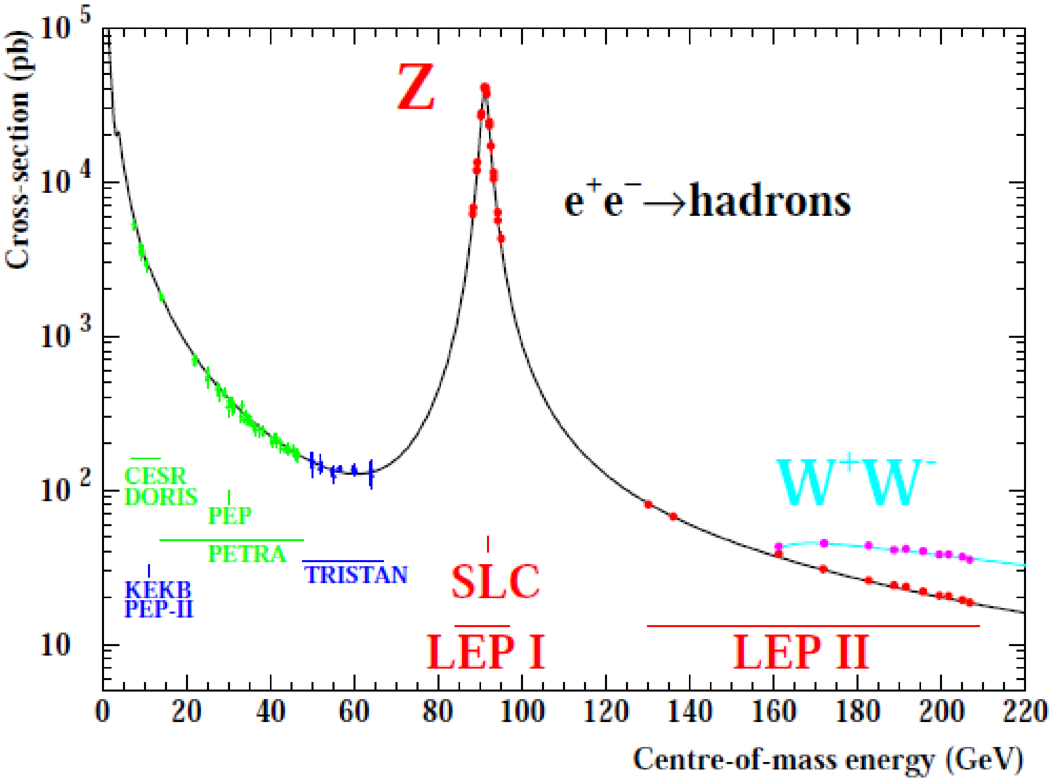

Figure 2.8: Hadronic cross section of Z^0/γ^* as a function of centre-of-mass energy [15]. The solid line is the SM prediction, the points are experimental measurements. Also indicated are the energy ranges of various e^+e^- accelerators.

Table 2.2: Branching ratios BR of Z^0 decays on the Z^0 peak as stated in [6].

Decay	BR [%]
ee	3.363 ± 0.004
$\mu\mu$	3.366 ± 0.007
$\tau\tau$	3.367 ± 0.008
neutrinos	20.00 ± 0.06
hadronic	69.91 ± 0.06

At LHC, these two flavours are still dominant; and their relative PDF uncertainties are rather small. In addition, significant contributions from s, c and b quarks arise, and their PDFs show increasing relative uncertainties—thus, they dominate the theoretical uncertainty based on PDFs. The contribution from b quarks to the Z^0 production is already of the order of few percent at $\sqrt{s} = 7\,\text{TeV}$, as it is used in this work.

Measurements of inclusive Z^0 production have been an important early measurement at new colliders ever since their discovery. They have well-predicted cross sections and are produced copiously. For all initial state setups there are specific decays with very clean detector signatures and they provide first electroweak precision measurements, making them benchmark physics processes. For these reasons, Z^0 production can serve as standard candle and can be used for estimating the collider luminosity, or as reference process in cross-section ratios like in Chapter 5. The measurement is also important e.g. for the estimation of the weak mixing angle – which can be estimated from the mass ratio of Z^0 and $W^\pm$ – or constraining the PDFs using the rapidity distribution [55]. Also new physics could appear through radiative corrections. Furthermore, due to its high production rate compared to other processes of interest, it is an important background to other analyses.

At LHC, the leptonic decays can be used for various calibration tasks using tag-and-probe methods, due to the sharp constraint from the well known shape of the Z^0 peak and the possibility of a very clean signal selection. These are e.g. efficiency estimates of lepton triggers, lepton reconstruction, identification and spacial isolation. Also it is one of few major processes to calibrate the lepton energy measurements. In addition, it is used in the tracker alignment (see Chapter 4.2.1).

Another important process is the Z^0 production in association with hadronic jets. It is dominated by additional gluon radiation, forming gluon jets through hadronisation. This is a main background to analyses with leptons and jets in the final state, like dileptonic top-pair decays as explained in Chapter 2.3.1. Furthermore it is used to tune the simulation, and for calibration of jet energy measurements where the transverse momentum balance between Z^0 and jets can be exploited.

2.3.3 Z^0-Boson Production in Association with Beauty Quarks

As mentioned in Chapter 2.3.2, the Z^0 production in association with jets is an important measurement at LHC. In this section, a specific sub-process is considered, the production of a Z^0 boson in association with beauty quarks. In order to define the process as a measurable process, a kinematic selection on the b quark – or more precisely on the resulting jet – is essential, which separates the process from the inclusive Z^0 production. This process with kinematic b-jet selection is meant throughout this thesis whenever Z^0 production in association with b quarks or b jets is mentioned, and it is referred to as bZ^0—thus it is a

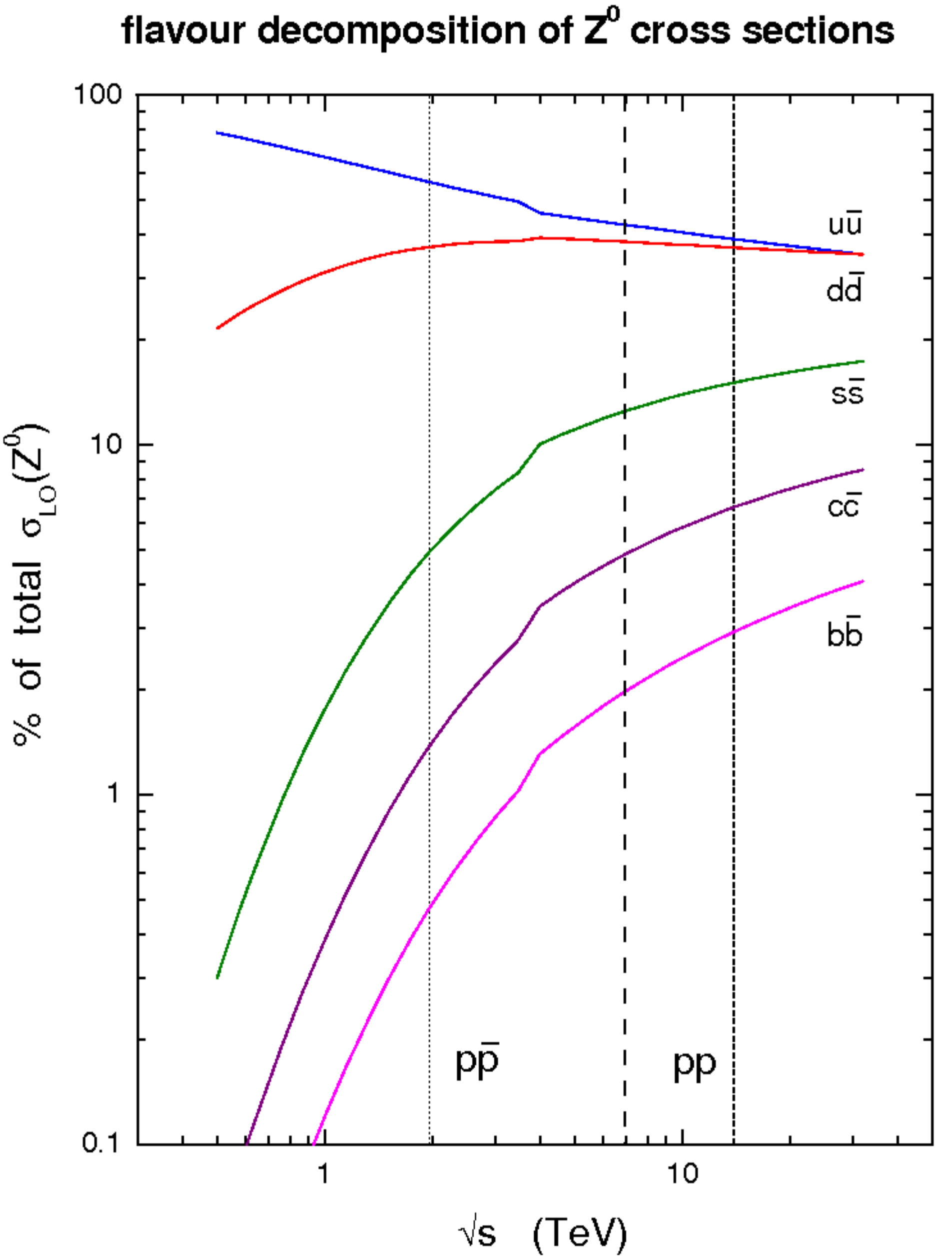

Figure 2.9: Initial state flavour decomposition of inclusive Z^0 cross sections in LO as a function of the centre-of-mass energy [54], corresponding to the Feynman graphs shown in Figure 2.7. The left vertical line indicates the TeVatron at $\sqrt{s} = 1.96\,\mathrm{TeV}$, the other two lines signify LHC at $\sqrt{s} = 7\,\mathrm{TeV}$ and $\sqrt{s} = 14\,\mathrm{TeV}$.

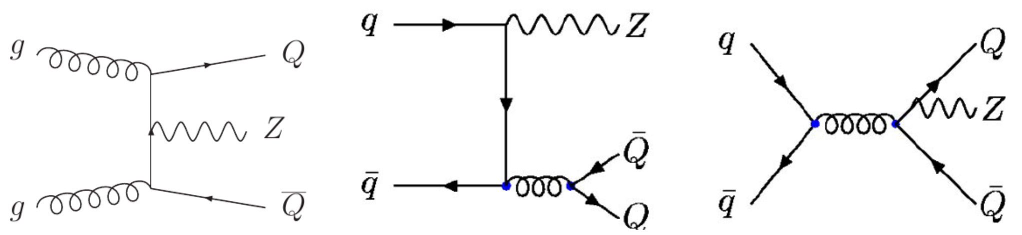

Figure 2.10: LO Feynman graphs for bZ^0 production in 4-flavour scheme [56]. The b quark is labelled Q, while q can be any of the lighter quarks. The gluon-gluon process (left) is dominant at LHC. For quark-antiquark processes, ISR (middle) has the bigger contribution than FSR (right).

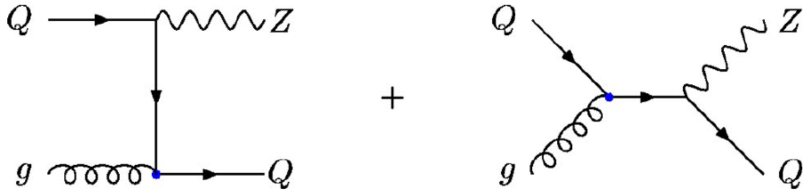

Figure 2.11: LO Feynman graphs for bZ^0 production in 5-flavour scheme [56]. The b quark is labelled Q.

sub-process of the associated jet production. An observation requires to find an additional b jet in the measured phase space, the experimental separation of these b jets from other jets is explained in Chapter 3.5.6. As shown in Figure 2.9 in LO approximation for inclusive Z^0 production, the fraction of Z^0 events originating from b quarks is of the order of few percent. The process bZ^0 is not contained in this figure since it is present only in higher orders of the inclusive production, but in fact it is of similar size; the LO for the exclusive process of production in association with b quarks is explained in the following.

There exist two different ansatzes for theoretical calculations of bZ^0. One is the 4-flavour scheme, a fixed-flavour scheme as illustrated in Figure 2.10 for LO. PDFs are used for u, d, s and c quarks, as well as for gluons. By definition there are no b quarks in the PDFs, they only arise from gluon splitting in the hard process. NLO calculations with massive b quarks exist [57]. The other one is the variable-flavour scheme with LO processes as shown in Figure 2.11. On the Z^0 scale the variable-flavour scheme has five flavours, so it is also called 5-flavour scheme. It allows the b quark to directly participate in the hard scattering by integrating the gluon splitting to b quarks into the PDFs, i.e. the PDF for b quarks is defined. NLO calculations have been performed using massless b quarks [58][59][60]. At LO these are partly different processes, but at NLO they become more similar. To all orders in perturbation theory, the result of both schemes can be made exactly identical, if also mass effects are fully accounted for. Still, at any finite order the results will differ, depending on the ordering of the perturbative expansion. Furthermore, the results differ due to the poorly constrained b quark PDF, but within the corresponding large uncertainties. In the calculation of associated Higgs-boson and b-jet production the differences but also the uncertainties become even larger, the two different calculation schemes lead to deviations of about 30 % between the central values [61].

Measurements of the described process could be performed only at the TeVatron before the LHC era [62][63]. In Chapter 6 a measurement of this process is presented; the Z^0 is identified by its muonic decay. This measurement is of relevance for several reasons. It is an important benchmark process, since it is a test of the presented schemes of QCD calculations—and a precision measurement with more data might help to constrain the b quark PDF, whose uncertainty is nowadays completely given by theoretical uncertainties. As explained in Chapter 2.3.2 the contribution to the calculations of the inclusive Z^0 cross section is a dominant contribution, and can thus improve luminosity estimates using Z^0 events. Furthermore it is especially important for measurements of associated Higgs-boson and b-jet production. This process might have a measurable cross section for the Standard Model Higgs boson. And especially the neutral Higgs bosons in supersymmetric models like the MSSM might have an enhanced cross section, since their coupling to down-type quarks is strongly enhanced in some models.

Moreover, bZ^0 is a significant background to several analyses, which requires a good understanding of the process. One example are top-pair analyses in dileptonic final states as explained in Chapter 2.3.1, since the topology is very similar. The same is valid for several Higgs analyses both, in the Standard Model (H) and in supersymmetric models ($\Phi = \mathrm{h,H,A}$). Examples are:

- $H \to Z^0 Z^0 \to llbb$ for heavy Higgs,
- $H \to Z^0 Z^0 \to llll$ since ≈ 10 % of b quarks decay semileptonically,
- $Z^0 H \to Z^0 bb$ for light Higgs,

and since the Z^0 in bZ^0 production has also other decay modes, which are similar to the Higgs decay modes, all Higgs production processes associated with b-jets, and decay modes like

- $\Phi \to \tau\tau$,
- $\Phi \to \mu\mu$,
- $\Phi \to bb$.

In general the process is also a relevant background for all searches of new physics in channels with leptons and b jets in the final state.

Finally, the process can also be used in order to calibrate the jet energy measurement specifically for b jets based on the transverse momentum balance of Z^0 and b jets—in analogy to inclusive jet calibrations with Z^0 production associated with inclusive jets.

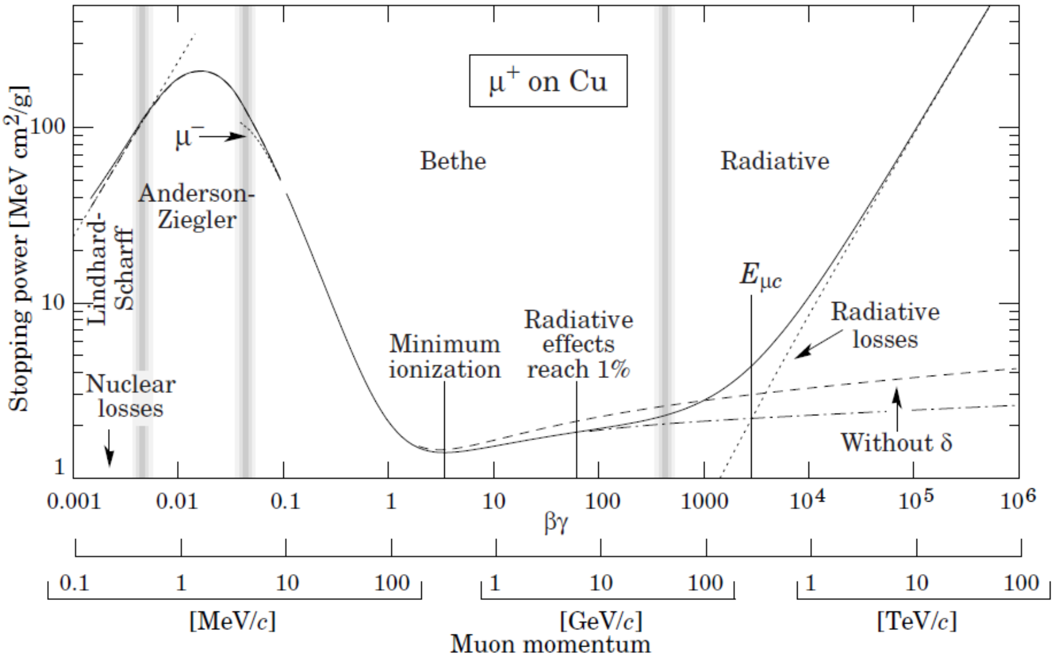

Figure 2.12: Stopping power for positively charged muons in copper [64].

2.4 Particle Interactions with Matter

In order to measure the fundamental quantities of the particles described in Chapter 2.1.1, the particles, or in case of short lifetimes their decay products, are forced to interact with matter – the active detector material – such that the energy or the momentum and possibly their point of origin and flight direction can be quantified. Depending on the particle's characteristics, different types of reactions take place with varying strength [64]. For tracking devices, the goal is to keep the interactions as small as possible, but big enough to obtain a measurable signal. In calorimeters however it is aimed for complete energy loss of the specific particles in order to measure their energy, while keeping the interaction with other particles as small as possible. Obviously, interactions with inactive detector material should be kept at a minimum. The technical analysis described in Chapter 4 aims for the measurement of the achieved alignment precision of the tracker—thus it is important to keep the interaction with all detector material throughout the tracker under control and as small as possible. Many different reactions with the detector material are possible, depending also on the kinematics of the specific particle. Figure 2.12 shows the dependence of the energy loss for muons on their momentum.

Each charged particle reacts with the atoms of the material. A wide kinematic range can be described by the Bethe–Bloch equation, where the main energy loss is based on ionisation and atomic excitation, which are inelastic scatterings. Within this range there is the point of minimum ionisation, and above is a plateau where the energy loss stays small. At higher energies, radiative effects begin to be important. At lower energies various corrections must be made, and also the sign of the charge starts to play a role. Given the typical kinematic regime of particles at LHC, the particles show the following behaviour. Muons are mainly in the region with small energy loss, thus they are called minimum ionising particles. Electrons however predominantly lose energy by bremsstrahlung in the electric field of the nuclei, photons by pair production—these effects lead to electromagnetic showers in material. For hadrons the additional effects of elastic and inelastic collisions with the atomic nuclei due to the strong interaction show up, which lead to hadronic showers in dense material. All charged particles also contribute to elastic Rutherford scattering, also called Coulomb scattering. Although it does not contribute significantly to the overall energy loss, this scattering causes a deflection of the particle trajectory.

A particle traversing a medium is deflected by many small angle scatters, this effect is called multiple scattering. The main source of multiple scattering is the Coulomb scattering from nuclei, but for hadrons also the strong interaction contributes, thus leading to bigger scattering angles in general. The overall deflection angle can be described approximately by a Gaussian core, but there are also non-Gaussian tails. For muons the multiple scattering is smaller than for other particles due to the above mentioned reasons. And it is smaller when going to higher energies, which is a purely kinematic effect. Summarising, muons above a certain momentum threshold are used in Chapter 4 since they provide track measurements which are maximally unbiased by detector effects.

Chapter 3

The CMS Experiment at the LHC

This chapter constitutes a summary of the experimental setup used for the analyses in this thesis, beginning with a description of the particle accelerator and the CMS experiment. The tracker of CMS, and the track reconstruction, is explained in more detail, since it is the component under study in the technical analysis described in Chapter 4. Furthermore, the simulation of events to allow modelling of and comparison to data is described. The full event reconstruction as needed for this thesis is explained. All performed measurements are based on events identified by muons originating from decays of electroweak gauge bosons, either directly produced or arising from top pair decays; the physics analysis in Chapter 5 requires in addition the measurement of hadronic jets, and in Chapter 6 jets identified as stemming from b quarks are in use. The chapter closes with a description of the luminosity measurement.

3.1 The LHC Accelerator

The Large Hadron Collider (LHC) is a synchrotron accelerator for the exploration of physics at the TeV scale. This storage ring is placed at CERN near Geneva, built in the former tunnel of the Large Electron-Positron Collider (LEP) with a circumference of 26.7 km. Counter-rotating proton bunches collide with a maximal centre of mass energy of $\sqrt{s} = 14\,\mathrm{TeV}$ at luminosities of up to $10^{34}\,\mathrm{cm}^{-2}\mathrm{s}^{-1}$. At this luminosity about 20 collisions per bunch crossing are expected. Time intervals between bunch collisions can be lowered to 25 ns, corresponding to 2808 proton bunches containing $1.15 \cdot 10^{11}$ protons each. Superconducting dipole magnets provide a magnetic field of up to 8 T to keep the bunches in their orbit. In contrast to former superconducting accelerators LHC uses superfluid helium II, which requires extremely low temperatures below 2 K.

LHC is designed to cover a wide range of physics topics, like search for the Higgs boson, supersymmetric particles, extra dimensions and the investigation

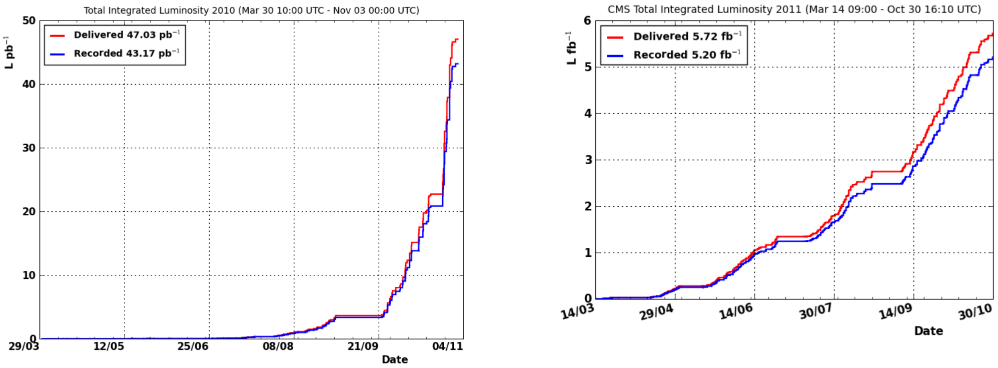

Figure 3.1: Integrated luminosity for data taking periods 2010 (left) [70] and 2011 (right) [71]. Shown is the luminosity as delivered by LHC (upper line), and as recorded by CMS (lower line).

of top quark properties. LHC can also provide lead-nuclei collisions, which allows e.g. to study the quark-gluon plasma.

The beams collide in four interaction points, where the main experiments are placed. The multipurpose experiments A Toroidal LHC Apparatus (ATLAS) [65] and CMS address a wide range of physics topics including those mentioned above. The experiments at the other two interaction points, A Large Ion Collider Experiment (ALICE) [66] and LHC beauty (LHCb) [67], are built for specific measurements. LHCb is designed to study heavy flavour physics in c- and b-meson decays, in particular CP violation and rare decays. ALICE focuses on lead-lead collisions to gain insight into the origin of confinement and the mechanism of mass generation. Two further experiments for forward physics are placed close to ATLAS and CMS, namely LHC forward (LHCf) [68] and Total Elastic and Diffractive Cross Section Measurement (TOTEM) [69].

In November 2009 the LHC became operational, and provided collisions at $\sqrt{s} = 0.9\,\text{TeV}$ and $\sqrt{s} = 2.36\,\text{TeV}$. Since March 2010 the energy is increased to $\sqrt{s} = 7\,\text{TeV}$. The maximum instantaneous luminosity is gradually increased over several orders of magnitude throughout the data taking periods. Figure 3.1 shows the integrated luminosity as delivered by LHC and as recorded by CMS.

3.2 The CMS Experiment

CMS encloses the solid angle around the nominal interaction point almost hermetically. The basic design relies on arranging the individual detectors around the beam pipe in a preferably symmetric approach. As for most multipurpose detectors CMS is composed of a tracking system close to the beam pipe, followed by the calorimeters, enclosed by a muon system. Each system has a central region in shape of cylindrical shells (barrel), and a backward

Table 3.1: Design parameters of CMS.

Entire detector	weight	12500 t
	length	21.60 m
	radius	7.30 m
Solenoid	field strength	3.8 T
	length	12.90 m
	inner radius	2.95 m
Strip tracker	length	5.80 m
	inner radius	0.20 m
	outer radius	1.16 m
Pixel Tracker	inner radius	0.04 m
	outer radius	0.15 m

and forward region arranged in bilateral symmetry, based on a disc shape (endcaps). A superconducting magnet coil is placed immediately outside of the calorimeters. The resulting solenoid field is nearly homogeneous inside at a strength of 3.8 T, and outside it is mainly bent into the iron return yoke, which embeds the different stations of the muon system, at about 2 T. Figure 3.2 illustrates the experiment, Table 3.1 gives some important characteristics. All details, like almost all numbers and figures of this chapter, if not referenced otherwise, can be found in [2].

The convention of the global $(x|y|z)$ coordinate system of CMS is such, that the origin lies in the centre of the detector, thus in the nominal interaction point. The Cartesian coordinates are defined as a right-handed system as follows: the z-axis points along the beam pipe in the anti-clockwise direction of LHC; the y-axis is oriented vertically upwards; the x-axis points horizontally to the midpoint of LHC. Accordingly the cylindrical $(r|\phi|z)$ and the spherical $(r'|\phi|\theta)$ coordinate system is given, following the commonly used convention as detailed in Figure 3.3. The pseudorapidity η equals the rapidity of massless particles and is defined as

$$\eta = -\ln\left[\tan\left(\frac{\theta}{2}\right)\right] . \tag{3.1}$$

A period where LHC provides beams is called LHC fill. If the beams are stable, data can be taken. An uninterrupted data-taking period of CMS, keeping constant detector conditions, is called a run. Each run is subdivided in so-called lumi sections with a time duration of 90 seconds.

3.2.1 Detector Components and Particle Identification

The different detector components will be discussed briefly and their role in particle identification is explained. The final identification of stable particles and of instable particles via their decay chains is a complex combination of the results of all different detectors.

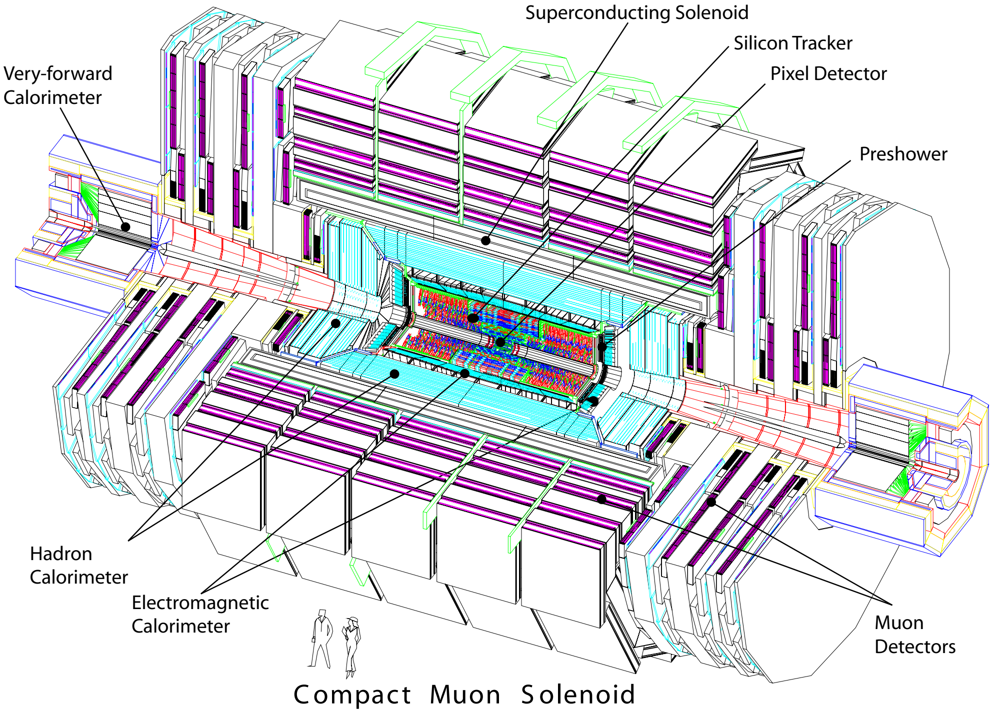

Figure 3.2: Longitudinal section of the CMS experiment. The people in the foreground illustrate the proportions.

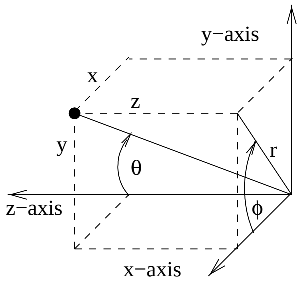

Figure 3.3: Cartesian, cylindrical and spherical coordinate systems of CMS. All are right-handed. The radius r is the distance to the z-axis, the azimuthal angle ϕ starts from the x-axis in direction of the y-axis, the polar angle θ is the angle relative to the z-axis.

Tracker

Since the tracker is the component under study in the technical analysis presented in Chapter 4, it is explained in more detail in Chapter 3.3. The tracker detects charged particles, and measures their curvature due to the bending in the magnetic field. More specifically it is used to reconstruct their point of origin, the flight direction at this vertex, the sign of the charge and the momentum. The reconstruction of primary and secondary vertices is based on the reconstructed trajectories, and the primary vertices are the basis of the reconstruction of the beamspot. The beamspot describes the area where the corresponding proton bunches overlap, thus the collisions occur. Studies about the tracking efficiency, the performance of tracking and primary vertex reconstruction, the determination of the beamspot and the estimation of momentum scale and resolution can be found in [72], [73] and [74].

The tracker can be used partly for particle identification. Particles from prompt decays can be separated from in-flight decays of particles traversing the tracker volume. The behaviour when penetrating the detector material, e.g. multiple scattering and energy loss, can help to identify particles. Hadronic jets can be separated from single particles, and in combination with secondary vertices heavy flavour decays can be identified (b-tagging). The tracker covers the area $|\eta| \leq 2.5$ with silicon modules, but particles at $|\eta| > 2.4$ cross only few modules for reconstruction.

Electromagnetic Calorimeter

The electromagnetic calorimeter (ECAL) consists of 75848 PbWO_4 crystals, which cover the region $|\eta| \leq 3$. They are oriented towards the collision point, but with a tilt of 3° to optimise for the readout of the shower shape. The dimensions of the crystals are chosen as $\Delta\eta \times \Delta\phi = 0.0174 \times 0.0174$. Figure 3.4 gives a graphical overview of the components. The barrel (EB) extends to $|\eta| \leq 1.479$, where the endcaps (EE) take over up to $|\eta| \leq 3$. The material is chosen such, that electrons and photons initiate electromagnetic showers in the field of the atoms (bremsstrahlung, photoeffect, Compton effect, pair production), whilst hadrons pass the crystals with mainly small energy loss. In front of EE the preshower detectors (ES) are mounted, measuring the space $1.653 \leq |\eta| \leq 2.6$. These are sampling calorimeters, equipped with silicon strip sensors. They improve the position resolution of electromagnetic particles and help to identify neutral pions.

The depth of the material corresponds to a radiation length of $25.8\,\mathrm{X}_0$. Thus, electrons and photons can be identified and their energy can be measured by their scintillation light with photo diodes. The resolution of the electromagnetic calorimeter is given by

$$\left(\frac{\sigma}{E}\right)^2 = \left(\frac{2.8\%}{\sqrt{E}}\right)^2 + \left(\frac{0.12}{E}\right)^2 + (0.30\%)^2 \tag{3.2}$$

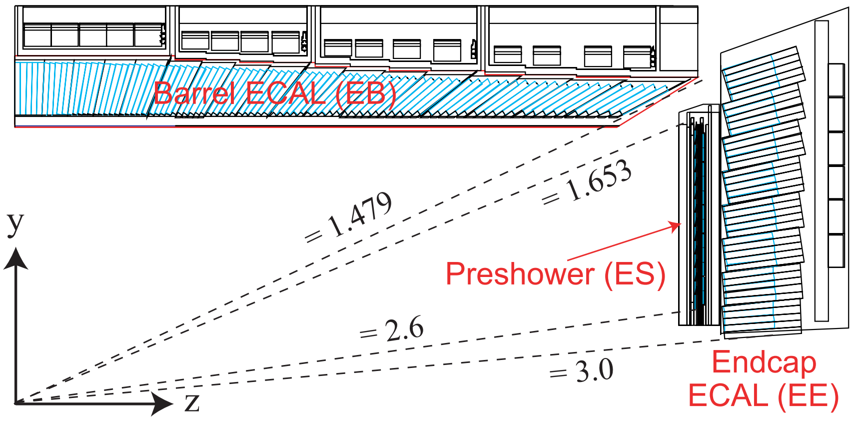

Figure 3.4: Longitudinal section of a quarter of the electromagnetic calorimeter components (ECAL). Shown is the barrel (EB), the endcap (EE), and the preshower detector (ES). Taken from [75].

with the energy given in GeV [75]. The first term is stochastic, the second due to noise, and the third is a constant arising from leakage of energy, non-uniformity of the light collection and calibration errors.

Hadronic Calorimeter

The hadronic calorimeter system (HCAL) spans the barrel (HB), the endcaps (HE), the outer calorimeter (HO) and the forward calorimeters (HF), as shown in Figure 3.5. The design is mainly based on the decision to place it within the solenoid. HB and HE consist of alternating brass absorbers and layers of scintillator material, covering the solid angle to $|\eta| \leq 1.3$ and $|\eta| \leq 3.0$ respectively. The layers are arranged in towers with individual readout of size $\Delta\eta \times \Delta\phi = 0.087 \times 0.087$ in HB matching 5×5 crystals of ECAL, and $\Delta\eta \times \Delta\phi = 0.17 \times 0.17$ in HE. The HO scintillators complete the measurement in the region with a smaller material budget around the solenoid. The HF is a radiation hard component based on iron absorbers and quartz fibres as active material, extending the range to $|\eta| \leq 5.2$.

The hadronic interaction length is above $10\,\lambda_\mathrm{I}$ in all regions, except of a small gap between HB and HE. Elastic and inelastic collisions of particles with atomic nuclei lead to hadronic showers. Energy deposits from hadrons are measured in the scintillator layers. Besides the identification of hadrons and jets, the large angular coverage is needed to search for imbalances in the transverse energy. It allows the indirect detection of neutrinos and potential other particles which do not interact with the detector. The energy resolution of the HCAL is

$$\left(\frac{\sigma}{E}\right)^2 = \left(\frac{100\%}{\sqrt{E}}\right)^2 + (5\%)^2 \tag{3.3}$$

for energies given in GeV [76].

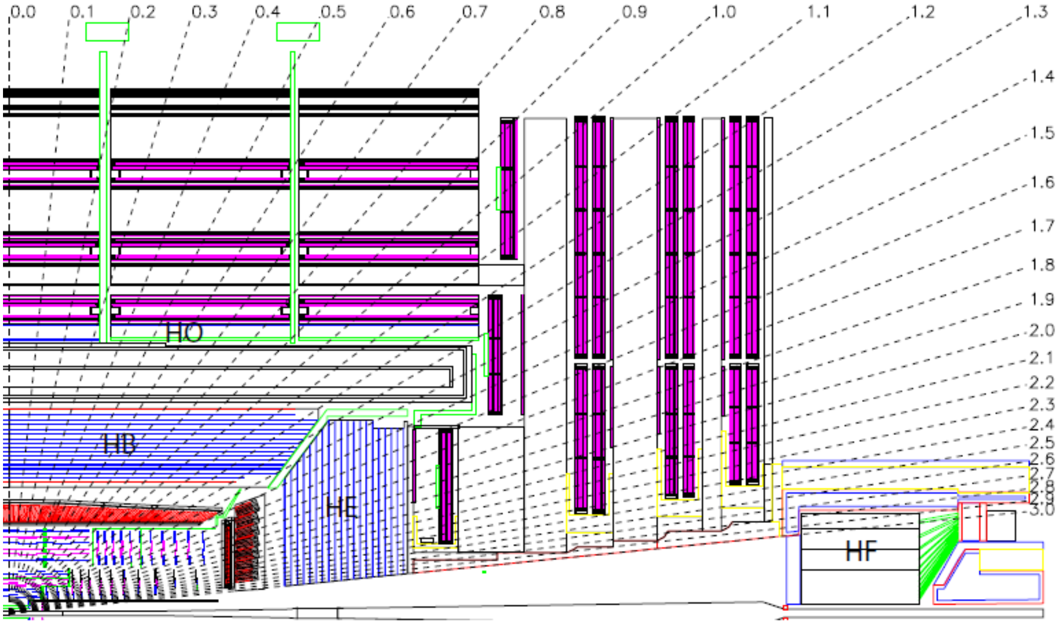

Figure 3.5: Longitudinal section of a quarter of the hadronic calorimeter components (HCAL). Shown is the barrel (HB), the endcap (HE), the outer calorimeter (HO) and the forward calorimeter (HF).

Muon System

The muon system measures the minimum-ionising muons. It is assembled from muon chambers ("stations"), alternating with iron plates which build the return yoke of the magnetic field, displayed in Figure 3.6. Two types of gaseous tracking chambers are used, these are drift tubes (DT) in the barrel region $|\eta| \leq 1.2$, and in the forward region $|\eta| \leq 2.4$ cathode strip chambers (CSC) are installed. The layout with layers, composed of these stations, guarantees that almost always four layers can be hit. Each station reconstruct trajectory segments, which are then combined. In both regions also resistive plate chambers (RPC) are placed within $|\eta| \leq 1.6$, which are used for triggering, timing and as a coarse additional position measurement.

The muon system is used for muon identification and to improve the resolution of their transverse momentum above 100 GeV via the bending in the magnetic field. Ultimate precision is reached in combination with the tracking system, as demonstrated in Figure 3.7. The momentum resolution of muons with $p_\mathrm{T} = 100\,\mathrm{GeV}$ is approximately 1–2%. Muons are important signatures for interesting physics processes, especially since they can be triggered very well.

Forward Calorimeters

In addition to the detector components discussed above, there are two more detectors in the very forward region, the Centauro And Strange Object Research

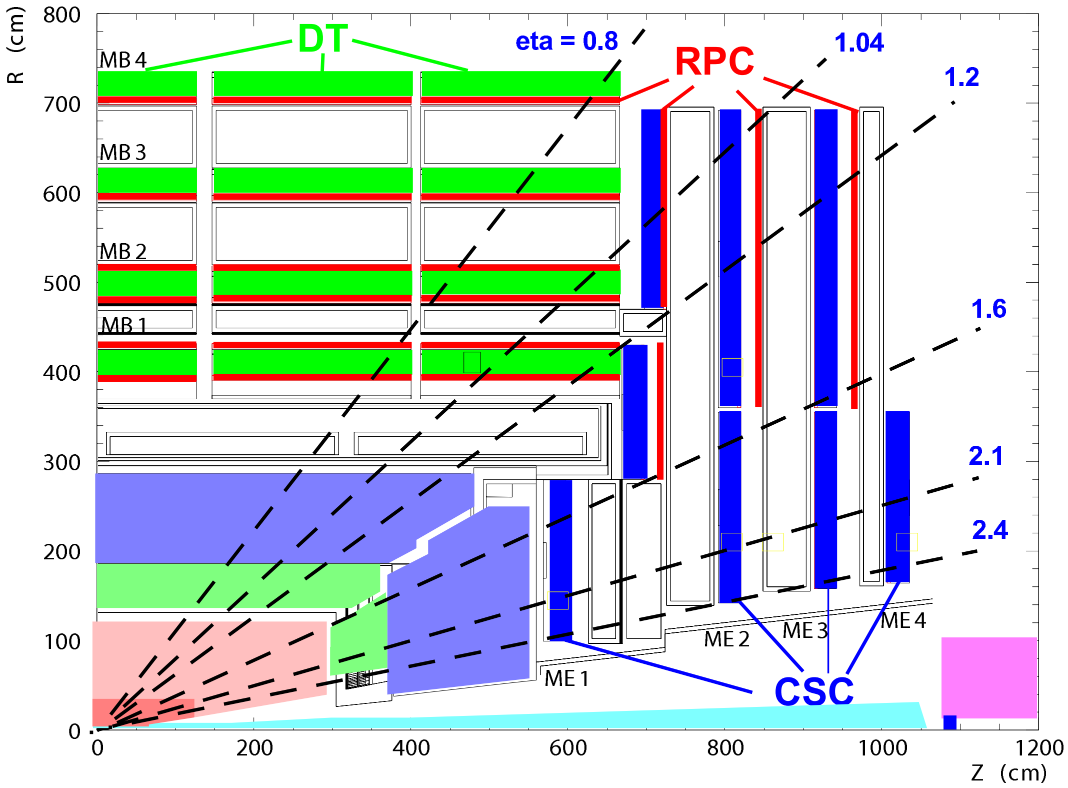

Figure 3.6: Longitudinal section of a quarter of the muon system. Shown are the drift tubes (DT), the cathode strip chambers (CSC) and the resistive plate chambers (RPC).

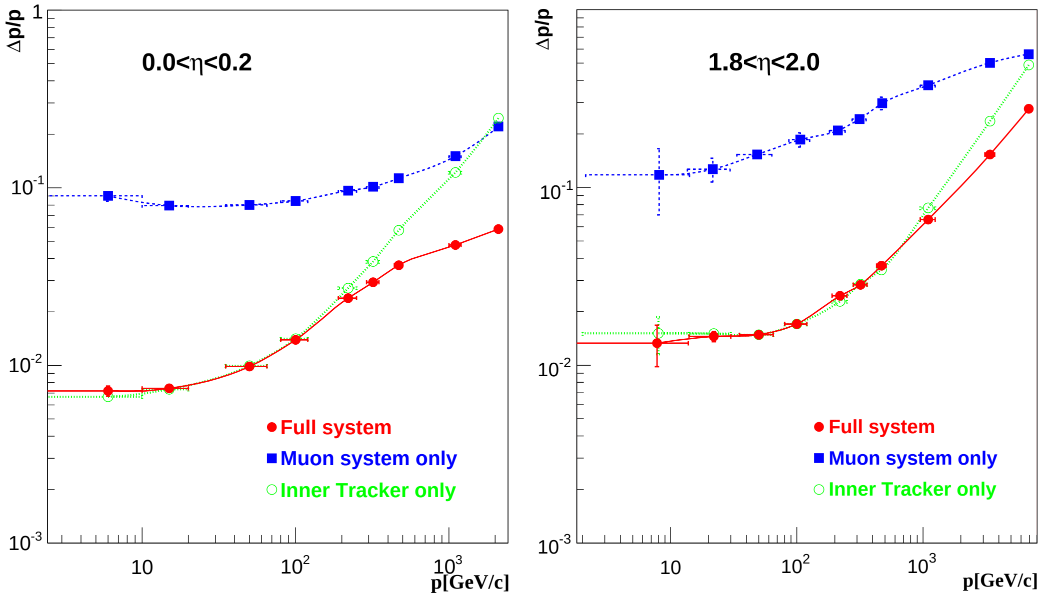

Figure 3.7: Momentum resolution of muons using the tracker only (green), of standalone muons from the muon system only (blue), and of a global muon fit combining both (red). Two different pseudorapidity regions are shown [76].

(CASTOR) and a set of two zero degree calorimeters (ZDC). CASTOR is installed surrounding the beam pipe on one side of CMS, at a distance around 15 m from the nominal interaction point. It covers the region $5.2 < |\eta| < 6.6$. ZDC is mounted between the two beampipes about ±140 m away from the collision point, measuring neutral particles within $|\eta| \geq 8.3$.

3.2.2 Trigger and Data Acquisition

Due to the high collision rate of up to 40 MHz, including several interactions per event resulting in an event size of about 1 MByte, the recording of all data is technically not achievable. A strict preselection of events needs to be done during the data taking (online). The trigger system achieves to reduce the rate of interesting events with a two-step approach. The preselection of events is defined in configurable trigger menus. The level-1 trigger (L1T) filters events to a rate of about 10–100 kHz, then the high-level trigger (HLT) takes over and selects about 100 Hz for storage. This requires an adjustment of the trigger menus to the instantaneous luminosity to optimise for the maximum possible output. Therefore later trigger menus require either tighter selections or triggers are prescaled, which means that they are not accepted always but reduced to a fraction, given by the prescale factor.

L1T is based on customisable hardware with flexible logic. The decision whether to keep or discard an event has to take place within $3.2\,\mu$s; for this time the event is stored in pipeline memories. A minimised event reconstruction is applied, coarsely segmented data from calorimeters and the muon system are used. The architecture can be seen in Figure 3.8. It is divided into local, regional and global components. The energy deposits in the calorimeters are used to reconstruct measurement objects like electron, photon or jet candidates. Global quantities like the missing transverse energy are also estimated. Track segments are reconstructed locally in DT and CSC. These are combined to tracks separate in DT and CSC. The RPC also constructs muon candidates. The information is then fed into the global muon trigger, including calorimeter information about signatures of minimum-ionising particles and isolation. Finally all information is gathered and based on the active trigger menu the event is kept or discarded.

HLT is based on software employing a computer farm. It uses the events which are accepted by L1T as input. A fast version of the event reconstruction is applied, using information from all detector components. The event selections are given in trigger paths. A trigger path defines which physics objects need to be found to accept an event. The full bandwidth is shared amongst different physics groups by sets of trigger paths. The physics objects reconstructed in HLT needs to be seeded from reconstructed objects of the L1T. The finally accepted events are stored and a full event reconstruction is done.

This work is completely based on muon triggers. Muon candidates from L1T (L1) are the seeds for the HLT reconstruction, which is divided into two steps. First, standalone muons (L2) are reconstructed in the muon system only.

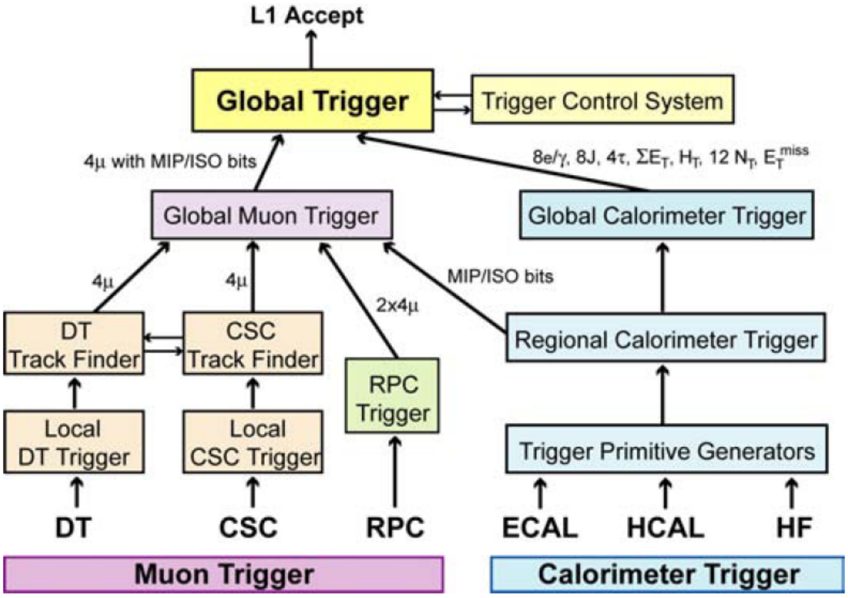

Figure 3.8: Architecture of level-1 trigger (L1T). The different trigger lines based on information from calorimeters and the muon system are shown.

Their isolation with respect to the calorimeter is checked. Selections on these L2 muons can be made in the trigger path. Second, those L2 muons which are not rejected are used as input for global muon reconstruction (L3) using also tracker tracks. Their tracker isolation is checked. The selection criteria for L3 muons in the trigger path cause the final trigger decision. Typically the trigger paths have increasing thresholds on the transverse momentum p_T for L1, L2 and L3 muons.

In Chapter 5 single muon triggers with certain p_T thresholds are used. At least one selected L3 muon needs to be found. In Chapter 6 double muon triggers are applied. At least two selected L3 muons above certain p_T thresholds are required, while the threshold can differ for both. In Chapter 4 a single muon trigger with $p_T > 17\,\text{GeV}$ and additional requirement on the isolation is applied. At least one isolated selected L3 muon is required.

3.2.3 Data Quality Certification

Important information about the usefulness of the data for analyses comes from the data quality monitoring (DQM). The data taken is qualified and certified on different stages. DQM runs online with a parallel data stream to control the status of the detector components and monitor distributions for different physics objects to allow fast feedback. It is also applied offline during the full event reconstruction to spot suspicious behaviour. For each full offline reconstruction of the data, the quality is certified centrally. The granularity of this certification corresponds to the lumi sections.

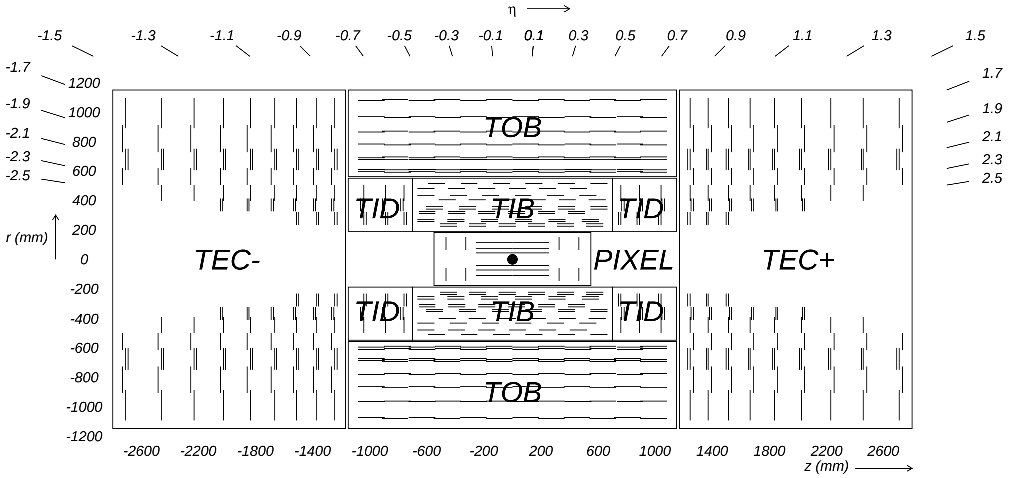

Figure 3.9: Schematic longitudinal section of the CMS tracker. Single lines represent single modules (single-sided modules), double lines relate to combined $r\phi$- and stereo-modules (double-sided modules).

In all analyses of this work, only data is used, which is centrally certified as good for physics analyses. This requires, that LHC provides stable beams, and that all detector components of CMS including the magnet work properly during the respective lumi section.

3.3 The CMS Tracker

Since the tracker is used intensively for several parts of this thesis, it is described in more detail than the other detector components.

3.3.1 Design

The tracker has a length of 5.8 m and a diameter of 2.5 m and contains 16588 silicon modules as the only active material. It is of high granularity to keep the occupancy low at high luminosities, and to have good resolution on particle quantities. It is composed of the pixel detector close to the beampipe, built from 1440 silicon pixel modules, surrounded by the strip detector with 15148 silicon strip modules. The silicon sensors are n-doped wafers, on which p-doped pixels (pixel detector) or strips (strip detector) are applied. The whole tracker is subdivided into six mechanically independent structures, called subdetectors (see Figure 3.9). All modules are assembled into hermetic layers, in the central region subdetectors with fixed radius r, in the forward region subdetectors with constant z. Relevant parameters of the modules are given in Table 3.2.

The pixel detector consists of the subdetectors pixel barrel (BPIX) and the pixel forward (FPIX). BPIX embeds three layers at radii 4.4 cm, 7.3 cm and

Table 3.2: Characteristics of silicon modules, sorted by subdetector. TIB and TOB are separated and enumerated for different layers, TID and TEC for different rings. Given are the number of modules, their thickness, the pitch of the pixels or strips respectively, and the number of readout channels.

Subdetector	Modules	Thickness [μm]	Pitch [μm]	Channels
BPIX	768	285	100×150	varying
FPIX	672	285	100×150	varying
TIB 1–2	1 536	320	80	768
TIB 3–4	1 188	320	120	512
TOB 1–4	3 528	500	183	512
TOB 5–6	1 680	500	122	768
TID 1	288	320	97	768
TID 2	288	320	128	768
TID 3	240	320	143	512
TEC 1	288	320	97	768
TEC 2	576	320	128	768
TEC 3	640	320	143	512
TEC 4	1 008	320	126	512
TEC 5	1 440	500	143	768
TEC 6	1 008	500	184	512
TEC 7	1 440	500	158	512
Overall	**16 588**			$\approx 66 \times 10^6$ pixels $\approx 9.3 \times 10^6$ strips

10.2 cm. FPIX encloses two layers on each side at $|z| = 34.5\,\text{cm}$ and 46.5 cm. Each part is assembled in two half-barrels separated by the x-z-plane, so that it can be mounted while the beampipe is closed. The modules are rectangular, the number of pixels depends on their size, which is optimised for the mounting position. The pixel pitches are fixed values of $100 \times 150\,\mu\text{m}^2$. Thus, the number of readout channels in pixel modules depend on their size. The resolution is about $15\,\mu$m in the global $r\phi$-direction and $20\,\mu$m in the other measurement direction.

The strip detector is composed of four subdetectors; these are the tracker inner barrel (TIB) and the tracker outer barrel (TOB) in the central region, the forward region is covered by the tracker inner discs (TID) and the tracker endcaps (TEC). TIB and TOB are separated into half-barrels separated by the x-y-plane. The modules of TIB are assembled in layerwise mounting structures. TOB modules are mounted on rods, six per rod, and inserted into the stiff skeleton of the half barrels. TIB is made of four layers, TOB of six. Within the layers of TID and TEC, the modules are arranged in rings. TID has three layers per side, each holds three rings, the modules are mounted on the rings. Nine layers per side are mounted in the TEC, each having up to seven rings. But the rings do not correspond to a mechanical structure in TEC. Instead there is a petal-like structure with ϕ-symmetry, 16 petals are integrated per layer.

Each layer consists of two sublayers with an offset. The sublayers are arranged such, that particles coming from the nominal collision point cross a module of the layer. The overlaps between the modules lead to cases where more than one module per layer is penetrated in the active measurement area. Most of the strip modules are placed as single modules in the sublayers, called single-sided modules. The strips are oriented parallel to the z-direction in TIB and TOB, and radial in r-direction in TID and TEC. Thus, the only sensitivity of the measurements is in ϕ-direction. At several places, two modules are arranged together, called double-sided modules; they are mounted very close to each other or in TIB even glued together. One is oriented as the single modules described above ($r\phi$-module). The other one is parallel, except of a small tilt around the module's normal, leading to a stereo angle of 100 mrad (stereo-module). In TIB and TOB the two inner layers are equipped with stereo modules, in TID and TEC stereo modules are located at the inner two rings and the fifth ring of TEC.

The modules in TIB and TOB are rectangular with parallel strips. The modules in TID and TEC are wedge-shaped, the strips are radial with a virtual intersection point in the distance of the beam line. In TOB and in the TEC rings 5–7 modules with two silicon sensors are used. The sensors are positioned such, that the strips of both add to long strips. A small gap between both is spanned by wires, connecting the two corresponding strips. The 15148 strip modules hold 24244 sensors. The dimensions of the modules can be seen in Figure 3.10. The strip modules are based on 512 or 768 readout channels, which means strips. Their distance of 80–184 μm leads to a spacial resolution in the

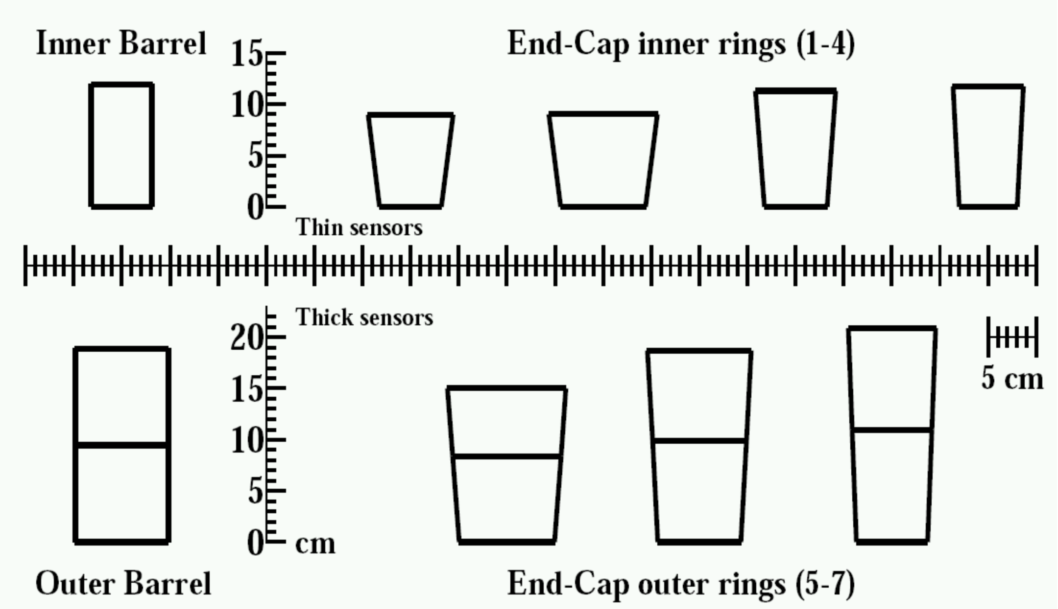

Figure 3.10: Shapes of silicon strip modules in TIB, TOB, TID and TEC. The TID modules are identical to the TEC modules in the inner three rings.

sensitive coordinate of about 23–53 μm for the single strips. The double-sided modules provide also sensitivity in the other coordinate, but less accurately. Corresponding to the stereo angle, the resolution is about a factor 10 worse.

The intrinsic resolution of the sensors is mainly based on the pitch of the strips respectively pixels. The strip pitch grows mainly with the distance to the beam line, contrary to the pixel pitches which stay constant. The position uncertainties are 15–53 μm when exactly one channel shows a signal. In this case possible positions are discrete values assigned to the channel's centre. This can be improved when taking into account the signal measured in neighbouring channels. Charge depositions on adjacent channels from one single traversing particle are read out together. They are called a cluster. Weighting of the different amounts of induced charge allows almost continuous position measurements in the sensitive directions. This leads to even smaller uncertainties. The highest precision in a measurement direction is reached for two-channel and three-channel clusters.

3.3.2 Operation Mode of Silicon Modules

The silicon sensors are composed of an n-type doped wafer, onto which the p-type doped pixels or strips are applied. The resulting depletion layer gets amplified through appliance of a voltage; it is a reverse-biasing diode. When a particle penetrates the depleted region, charge carriers are freed by ionisation. The electric field leads to a drift to the surface. A small, but measurable current pulse results in the readout channels of the pixels or strips.

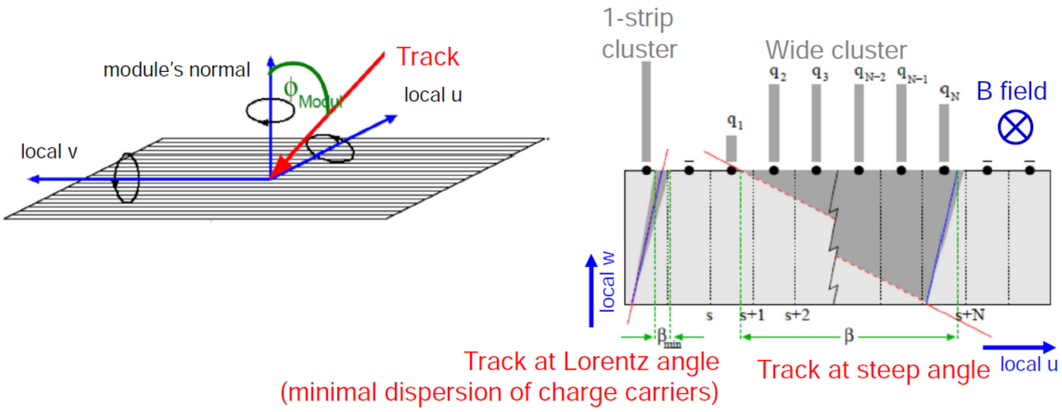

Figure 3.11: Drift of charge carriers in silicon sensors. Shown is a barrel strip module, with a local $(u|v|w)$ coordinate system as defined in Chapter 4.1.1. Left: 3-dimensional view on the module. A particle has a certain incident angle on the module with respect to the normal. Right: 2-dimensional transversal section. The black dots mark the strips, the grey bars above them the induced signal on this channel. Due to the Lorentz angle, the drift direction is shifted, indicated by the blue line. Two cases are shown. The dip angle of the left track equals the Lorentz angle, the charge dispersion is minimal, and stems only from the dispersion effects due to the drift. The right track is very steep, leading to signals on many strips. The clusters need to be corrected for the Lorentz angle and for the natural dispersion.

Due to the high particle flux and the amount of hadronic interactions, the tracker needs to be as radiation resistant as possible. Modules were irradiated and checked in physical performance tests, see e.g. [77]; lower operating temperatures show better results. Temperatures at about −10 ℃ are chosen to improve radiation hardness. In addition, the power supply of the modules causes heat, which has to be absorbed. The cooling is done with a specific pipeline system for cooling liquid connected to all modules. Radiation damages are compensated with variation of the voltage.

The strong magnetic field overlays the electric field within the sensors, and induces Lorentz forces on the charge carriers drifting to the readout channels. This effect occurs especially in the barrel modules where both directions are orthogonal, while in the forward modules both fields are mainly parallel. The drift direction is changed by a certain angle called Lorentz angle, which influences the charge division of the different channels, as illustrated in Figure 3.11. A correction in the reconstruction is necessary. The calibration of the Lorentz angle is explained e.g. in [78].

Two different signal readout schemes can be applied during data taking. One is the peak mode, which reads the full signal shape. This mode is used sometimes in cosmic data taking. However it is too slow for collisions at high bunch-crossing rates. Thus the second mode is used, which is called deconvolution mode. In principle only the turn-on curve is measured at three points and then the signal shape is extrapolated. The drawback of the method is, that not all charge carriers reach the channels in time, the effective active depletion area gets thinner. Also this effect needs to be corrected, since the cluster shape is manipulated. The calibration is based on so-called backplane corrections.

The analogue signal in the strip modules is read out by custom integrated circuits called APV. Each APV spans 128 neighbouring strips. In the pixel modules read-out chips (ROC) are used, each covering 52×80 neighbouring pixels. The channels show a significant increase of the noise when going to the edges of the modules. This effect needs to be taken into account in the reconstruction. The signals are transmitted via optical fibres for further processing.

3.3.3 Track Reconstruction

The track reconstruction in the CMS tracker is a complex challenge, because of the high charged particle multiplicity of about 1000 per event as expected at the design luminosity of LHC. The reconstruction is based on two consecutive steps, the local and the global reconstruction. The local reconstruction uses the digitised detector readout of the raw signal to find and quantify possible hits, which are passings of a particle through the silicon sensors. The global reconstruction searches for possible combinations of these hits to aggregate tracks from these possible hits—which are then input for the physics analyses. The track reconstruction requires in addition event-independent information; the local reconstruction depends on the calibration, the global reconstruction needs all information which is gathered in the starting point of the global reconstruction, as defined later in this chapter.

Local Reconstruction

The electric signals of the readout electronics, called raw data, are at first digitised and stored. The noise becomes already suppressed in this step, and the excess of the signal strength is transformed into a charge equivalent. The local reconstruction is defined in two subsequent steps, the clustering and the hit conversion. The procedure is separated between pixel and strip detector.

Clusters are built in the clustering, taking the calibration of the readout electronics into account. Neighbouring channels fulfilling a certain threshold scheme are grouped. The scheme requires specific signal-to-noise ratios for the individual channels and for the whole cluster.

The clusters are translated into possible hit measurements in the hit conversion. This is done with a cluster parameter estimator (CPE) algorithm. The hits get assigned a position and a corresponding uncertainty in the local coordinate frame of the silicon module. The resulting hit coordinates and uncertainties, as well as the charge and the profile of the clusters, form the endpoint of the local reconstruction.

Table 3.3: Iterative tracking steps [81]. Given are the seeding layers and track requirements for different steps (min. p_T, max. d_0, max. d_z, min. number of hits). The * indicates the impact parameter with respect to a pixel vertex. The definitions correspond to the ones as used for this work, changes are possible.

Step	Seeding layers	p_T [GeV]	d_0 [cm]	d_z [cm]	# hits
0	pixel triplets	0.8	0.2	3.0σ	3
1	pixel pairs	0.6	0.05	0.2*	3
2	pixel triplets	0.075	0.2	3.3σ	3
3	triplets: pixel, TIB 1+2, TID/TEC ring 1+2	0.25–0.35	2.0	10.0	3
4	pairs: TIB 1+2, TID/TEC ring 1+2	0.5	2.0	12.0	6
5	pairs: TOB 1+2, TEC ring 5	0.6	6.0	30.0	6

Global Reconstruction

The starting point of the global reconstruction spans besides the results of the local reconstruction important information about the modules. On one hand these are the geometrical arrangement of the modules, and their intrinsic shape. The alignment parameters give the positions and orientations of the modules in the global tracker frame, and deformations of the module shape with respect to plain modules. On the other hand, quality records about the status of the individual modules are taken into account. Channels or even whole modules which cannot give signals or which cause noise are deselected. These records contain information about the status of the module itself, and of the readout electronics and the cabling.

The global reconstruction is based on three successive steps, the seed finding, the pattern recognition and the final fit. The layer-wise mechanical construction and readout is important, in general tracks are composed of hits from neighbouring layers. The default tracking algorithm, used in reconstruction and described here, is the combinatorial track finder (CTF). A detailed description, together with performance studies can be found in [79]. It is a Kalman filter [80]. The Kalman filter is used for both track finding and fitting. The tracking sequence is an iterative approach, CTF is run multiple times. Hits used in previous iterations are not considered anymore, and CTF is run again with progressively looser requirements; the main difference is in the seed finding. Table 3.3 lists the requirements for the different iterations.

The seed finding searches for starting points, which are called seeds, consisting of a first hit combination with coarse estimates of the track parameters. Seeds are generated from hit triplets, or hit pairs and the beam line. Mainly neighbouring layers are used for seed finding, especially the inner layers. The

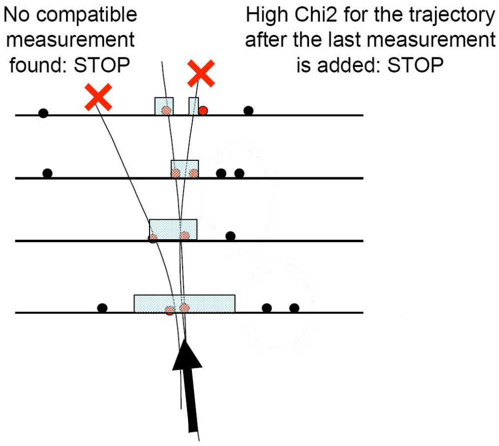

Figure 3.12: Kalman filter based track pattern recognition [79].

starting parameters of the trajectory are gained from a helix fit through the three points. There are different seeding layers requested at the different iteration steps.

In the pattern recognition track candidates are built, starting from the seeds of the seed finding. For every seed a propagation to the next (sub-)layer is probed. The size of the propagation window depends on the uncertainty of the track parameters. If a hit is found inside the window, it is added to the candidate and the track parameters are updated. If more than one hit is compatible, one candidate is built for each. In addition, one candidate is always added without a hit in the specific layer; this is necessary, since sometimes real hits cannot be reconstructed. At most one, and sometimes no layer without hit, are allowed in the different iteration steps. For each new candidate the propagation to the next layer is probed until the last layer is reached. Based on the χ^2 of the fit and the number of hits at each layer, only the five best candidates are kept for further propagation. The procedure is illustrated in Figure 3.12.

For the remaining candidates of the pattern recognition, the final fit is performed. The Kalman filter used is a so-called dynamic Least Squares Method. The trajectory in a homogeneous magnetic field can be assumed to be a helix, defined by five parameters. Due to the crossed material, this assumption is not completely correct. But effects like multiple scattering and energy loss are taken into account. On each crossed sensor however, the assumption of a helix is good enough. The trajectory state vector $\vec{T}$ on a module's surface is defined as

$$\vec{T} = \left(\frac{q}{p}, \frac{p_x}{p_z}, \frac{p_y}{p_z}, x, y \right) . \tag{3.4}$$

The components are: the inverse signed momentum, as well as incident angle and interception point in two orthogonal directions in a local module-wise coordinate system. The Kalman filter passes through all hits of the candidates and estimates the track parameters iteratively. The first hit of a candidate is

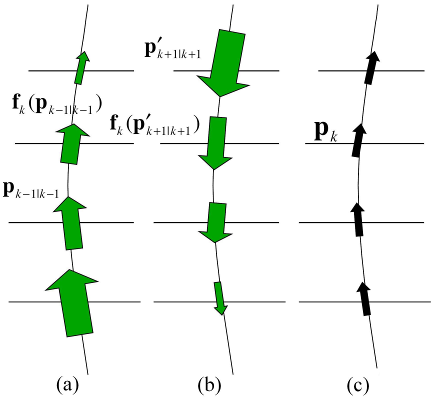

Figure 3.13: Track fitting [79]. The arrow size illustrates the precision of the track parameters on a given module for (a) forward fitting, (b) backward fitting and (c) trajectory smoothing.

the starting point, $\vec{T}$ is initialised with an estimate from the pattern recognition, and the uncertainties are set to high values. Then, three steps are carried out sequently for all hits of the track:

1. State vector and covariance matrix are propagated to the next module's surface to get a track prediction on it.
2. The obtained state gets combined to a new state, including the information of the hit on this module.
3. The χ^2 value of the fit is increased, reflecting the compatibility of the track prediction and the hit.

The drawback of this method is, that the final precision is obtained only for the last hit. Thus, a second fit is applied in the opposite direction and order. The two obtained states are combined with a Kalman smoother to the final estimate. The track parameters and corresponding uncertainties are determined. A schematic view is drawn in Figure 3.13. During the global reconstruction the hit parameters are estimated again with a more sophisticated CPE using information from the track, mainly the incident angle on the sensor's surface.

Finally, a cleaning of the track collection is applied to reduce ambiguities, and quality flags are assigned. The cleaning is based on the fact, that only the best track should be kept when tracks share the majority of hits.

3.3.4 Track Refit

The software contains the possibility to repeat the final fit only. This is referred to as refit. Since the input which is needed for the refit is stored independently of the applied alignment geometry and some calibrations, these conditions can be changed for the refit, and their influence can be studied. On the calibration side, important parameters of the reconstruction like the magnetic field or the Lorentz angle can be adjusted. On the alignment side, all alignment parameters and corresponding errors can be changed. Also the refit itself is configurable, and e.g. another CPE can be used.

The refit fits each track which is stored as the outcome from the global reconstruction. The clusters corresponding to the hits of the track and the original track parameters define the starting point. Only tracks which were found in the global reconstruction can be refit. But even if the conditions are identical to the ones used in the reconstruction, the refit does not converge in few cases. This can be due to linearisation effects. Sometimes the tracks get shorter, since the refit converges only for a part of the track. In addition, there is an outlier rejection for hits far off from the track prediction. This leads to the fact, that the number and the length of the tracks from the refit alters with different conditions, especially from the alignment side. In order to correct for material effects, the mass of the muon is assigned to the particles by default, but this is configurable. Most charged particles in the final state are pions, but since the analysis in Chapter 4 using the refit is based on muons, the default mass choice is optimal.

3.4 Event Simulation

Computer based event simulation plays a key role in many aspects of high energy physics. It allows to understand and predict the processes occurring in particle collisions and to model the distributions of the emerging decay particles, as well as their measurement with the detector. Simulation is used both, for calibration tasks and for predictions of physics signals and their backgrounds. Such a theoretical prediction is crucial to tune physics analyses during the active phase of the experiments, but also in the planning and construction stages of future experiments. The most important points for this thesis are outlined, more detailed explanations can be found e.g. in [35].

3.4.1 Monte Carlo Method

In particle physics, certain problems cannot be solved analytically, like the modelling of the complex final states at LHC with high particle multiplicities and the correction for detector effects of the measurement. The well-established solution is the Monte Carlo method. This method is a stochastic technique, i.e. numerical computation of results through repeated random sampling. It is particularly useful when analytical calculations are unfeasible and the regarded system has many coupled degrees of freedom, thus high-dimensional cases.

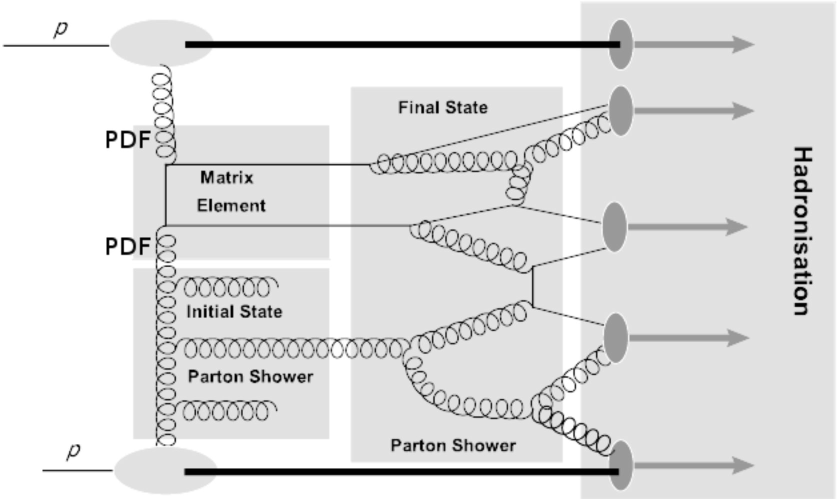

Figure 3.14: Basic steps common to most event generators (taken from [35], slightly modified).

3.4.2 Event Generators

Based on the factorisation theorem (see Chapter 2.2.2), the generation of a collision event is subdivided into several steps, as illustrated in Figure 3.14. The first step is to calculate the matrix element of the hard process at a fixed order of α_s, with the momenta of the ingoing partons being randomly chosen based on the input PDFs. Given the probabilistic nature of physics at this scale, the final state depends on the possible interactions which are fed into the generator. The outgoing partons are randomly distributed in the available phase space.

Following the calculation of the hard process, higher order QCD effects are added using parton shower models. Partons can emit gluons in ISR and FSR. The collinear part of the evolution of the partons during showering is based on the DGLAP evolution, see Equation 2.9, while the transverse component is again randomly distributed.

The next step is the hadronisation of the partons. Different models are in use. The models are exclusively phenomenological and need to be tuned to data, since the effect occurs at scales around Λ_QCD where perturbation theory breaks. At this stage the modelling of MPI and the full underlying event are also taken into account, as they depend heavily on the description of hadronisation.

Finally, the decay of unstable particles to stable particles is simulated. The output obtained is called hadron-level or generator-level, and is a possible level for cross-section definitions. This level is often used in detector calibration based on simulation, e.g. in the jet energy measurement, but also the other way around for generator tuning and better modelling of data, e.g. to match the jet multiplicity [82]. The output obtained before hadronisation is called parton-level, it is another possible level for cross-section definitions.

Event generators used in this work are listed in the following. As will be explained, the parton showering and hadronisation of all samples in use is done with PYTHIA, based on the Z2 tune for the underlying event [83][84], and also MPI are included.

Pythia

PYTHIA [85] is a multi-purpose event generator, which is commonly used in high energy physics, because of its easy handling and its relatively large predictive power. It contains all generation steps as described above, it can simulate all relevant collision initial states, and it is capable to simulate all Standard Model processes as well as processes in theories beyond the Standard Model. The hard scattering is calculated in LO approximation. The higher order corrections are approximated with parton showers. The hadronisation process is based on a string model. Whenever PYTHIA is mentioned in this thesis, the version PYTHIA6 is meant, since it is used for the simulated samples in use.

MadGraph

MADGRAPH [86] calculates matrix elements on tree level to arbitrary order. Unlike PYTHIA, the radiation of hard gluons in ISR and FSR is also calculated on matrix element level, i.e. the matrix elements for the hard process plus 0, 1, 2, … jets are calculated separately. A threshold needs to be set in order to avoid divergent soft gluon radiation. The different sub-processes are then combined, so the process is simulated with the LO cross section and the radiation of hard, well separated jets simulated on matrix element level. The method leads to a precise description of the event topology, but the cross section is strongly scale dependent. Thus, the cross section is normalised with the NLO prediction of MCFM [87][88]. In order to avoid double counting with the parton showering, phase space thresholds are used, which separate jets generated on matrix element level from jets of the parton showering. This matching is done for all samples used in this thesis with k_{T}-MLM [89] at a threshold of $k_{\mathrm{T}} = 20\,\mathrm{GeV}$. Parton showering and hadronisation are not implemented within MADGRAPH, it has to be interfaced to another generator, which is in this thesis always PYTHIA. Since the hard jet multiplicity is better modelled than in PYTHIA, samples with the hard processes calculated by MADGRAPH are used where jets are involved in the analyses—if such samples were available.

Tauola

TAUOLA [90] is a dedicated package for the simulation of τ decays, and has been applied to all simulated event samples used in this thesis. It takes spin information and QED corrections into account.

Powheg

POWHEG (POsitive Weight Hardest Emission Generator) [91][92][93] is optimised for heavy quark production in hadronic collisions. The hard process is evaluated at NLO, parton showering and hadronisation need to be done via the interface which is part of POWHEG. The interfacing is done such, that both the leading logarithmic accuracy of the shower and the NLO accuracy of the cross section are maintained in the output. In this thesis, again PYTHIA is used for parton showering and hadronisation. One specific sample of $Z^0 \to \mu\mu$ events is used in Chapter 5 since NLO precision is relevant there.

3.4.3 Detector Simulation with GEANT4

The event generators model the physics of the basic interactions only, i.e. the production of particles in collisions and close-by subsequent decays. Further decays or interactions with the material while traversing the detector volume are simulated with GEANT4 (GEometry ANd Tracking) [94][95] – which is also Monte Carlo based – and interfaced to the CMS software. All relevant interactions with matter consisting of different materials are included. Also the full CMS detector geometry including support structures and active material with signal readout, noise and crosstalk is simulated, and the magnetic field effects on the detector response are considered. The detector response is built in the digitisation step of the simulated signals. Finally, a full emulation of the trigger is added. The output has the same format as real collision events. The detector simulation transforms the generator-level to detector-level and makes simulation directly comparable to data measurements. Like for the event generators there are tuning parameters to minimise deviations between data and simulation.

3.5 Event Reconstruction and Object Identification

The physics analyses involve reconstructed physics objects, like electrons, photons, muons and jets. These objects define the final state of the interaction process. To obtain the objects, the information from the individual detectors as explained in Chapter 3.2.1 is combined. For instance, electrons and photons give similar signals in the ECAL, but can be separated by testing the association with charged tracks in the tracker. The analyses in this work are based on primary vertices, muons, jets, jets initiated by b quarks, and missing transverse energy; those are explained in detail. Also the final identification criteria for the objects, as chosen for the analyses, are discussed.

3.5.1 Primary Vertex Identification

Primary vertices are built from tracks with compatible impact parameters. The primary vertices which are used in the presented analyses have to follow these identification criteria: A primary vertex needs to be reconstructed from at least 5 tracks, and needs to be in the luminous region defined by maximal transversal distances of 2 cm and longitudinal distances of 24 cm from the origin. The selection is common in several CMS analyses. In all analyses of this work each data event is required to contain at least one good identified vertex. This criterion ensures a real collision.

3.5.2 Muon Reconstruction

Muons with small curvature – which means enough energy to not be trapped curling in the magnetic field – can pass the whole CMS detector. This is due to the behaviour of charged particles traversing matter in general, with the modifications arising from the possible interactions of the specific particle, as it is described in [64]. In general each particle has an energy where the ionisation of the material, and thus the energy loss of the particle, is minimal. The energy loss in this energetic regime can be approximated by the Bethe-Bloch formula [96]; in the relevant regime for most analyses at CMS, muons are close the the minimum ionisation region, while the other detected particle types are not. Thus, tracks of muons can be reconstructed both in the tracker and in the muon system. Signals in the muon system are used for muon identification. In addition muons are expected to depose only a small amount of their energy in the calorimeters, which is called minimum ionising particle (MIP) signature and can also be used for muon identification and isolation tests.

Muons are reconstructed at CMS by different algorithms based on the tracker tracks and signals in the muon system. An overview is given in Figure 3.15, performance studies can be found in [97]. The two relevant algorithms for the presented studies reconstruct the “global muons” and the “tracker muons”. Both are based on the local muon reconstruction in the muon system only, which provides track segments per station in CSC and DT, and hits per module of the RPC.

Tracker muons are built using an inside-out approach, starting with the tracks in the tracker. Tracks above $p_\mathrm{T} > 0.5\,\mathrm{GeV}$ and $\mathrm{p} > 2.5\,\mathrm{GeV}$ are extrapolated to the muon system and their compatibility with segments from the local muon reconstruction is checked. If a track can be matched geometrically to at least one segment in CSC or DT, it is considered to be a tracker muon. The only information used for the fit of the muon parameters is the tracker track.

Global muons are reconstructed outside-in. First, “stand-alone muons” are reconstructed. These are muon tracks based on the measurements in the muon system only. At least two compatible segments or hits are required, and

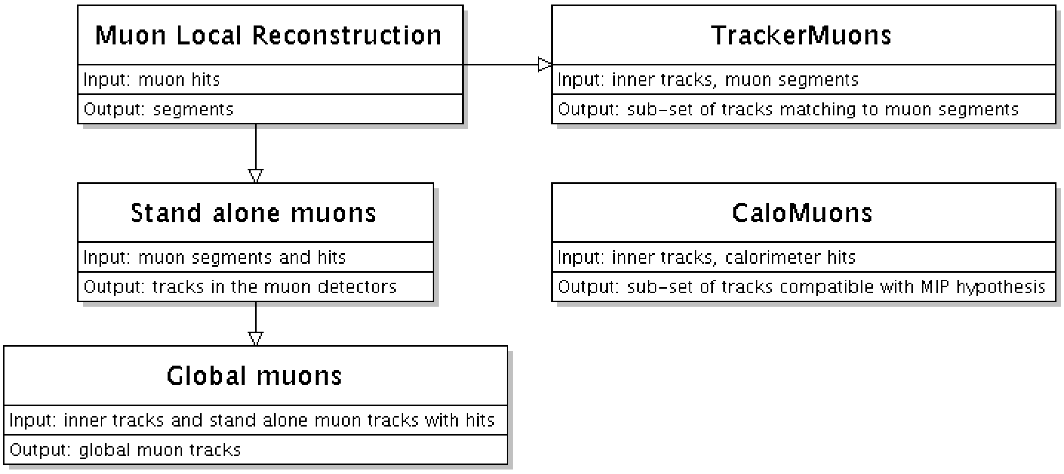

Figure 3.15: CMS muon reconstruction algorithms [98]. Shown are the reconstruction chains for tracker muons and global muons as explained in the text, and in addition “calo muons”. The latter are similar to the tracker muons, but use the MIP signature instead of the information from the muon system. In addition to the default settings for the algorithms, there are specific modifications of them used for reconstruction of HLT muons, high-p_T muons, cosmic muons and beam-halo muons, ending in one of the shown types.

at least one has to be a segment, allowing a track parameterisation. Second, the best matching track for every stand-alone muon is searched—at most one global muon per stand-alone muon can be reconstructed, the choice is based on the χ^2 of the fit. In about 1% of stand-alone muons originating from collisions, no compatible tracker track is found and no global muon is built. All measurements of both tracker and muon system are used for the fit of the muon parameters.

3.5.3 Muon Identification and Isolation

Identification

In the relevant energy regime above several GeV, the global muons are the best identified ones of all reconstructed muons, and provide the muon parameters with the best accuracy. They are the basis in this work, and their parameters are used in the analyses. However, additional identification criteria are applied on the reconstructed muons in order to reduce the muon fake rate while keeping the selection efficiency high. Furthermore only prompt muons originating from the hard interaction should be selected. These criteria are commonly used in a wide range of CMS analyses (see e.g. [99]). They are explained in the following.

- Muons have to be reconstructed both, as a tracker muon and as a global muon.

This requirement suppresses wrong matchings of a tracker track to the standalone muon in the global muon reconstruction, and linking of noise in the muon system to tracks in the tracker muon reconstruction. In addition, it is effective against muons from decay-in-flight processes, and punch-through hadrons where the hadronic shower leaks into the muon system.

- At least eleven hits in the tracker, summing pixel and strip hits.

This reduces the combinatorics to avoid wrong matchings, and ensures an accurate p_T measurement.

- At least one hit in the muon system is used for the global track fit.

This is an additional protection against punch-through hadrons and ensures a good muon parameter estimate.

- The χ^2 of the global fit, normalised to the number of degrees of freedom f, is $\chi^2/f < 10$.

This ensures a good quality of the global fit which is used for the muon parameter estimate, and reduces mismatchings of tracker tracks and standalone muons.

- The distance of closest approach with respect to the beam line in the x-y-plane is $|d_0| < 200\,\mu\mathrm{m}$.

Most cosmic muons are rejected by this requirement. Also many decay-in-flight muons are rejected. A remaining contribution from decays of b or c hadrons cannot be excluded.

The muons which pass the selection above are the muons as they are used in Chapter 5 with the 2010 data. The analyses in Chapters 4 and 6 with the 2011 data have additional identification criteria which are listed in the following.

- At least one hit in the pixel detector.

Decay-in-flight muons are further suppressed. The precision of the estimated muon trajectory close to the interaction region is enhanced.

- A muon consists of at least two segments from different muon stations in different layers.

The rate of punch-through hadrons is further reduced, as well as wrong track matchings. In addition, this requirement is consistent with the requirement in the muon trigger, where it is needed for a meaningful p_T prediction.

Isolation

All presented analyses are based on isolated muons—muons which are produced in the hard interaction and which are not accompanied by other particles. Muons which occur mainly from multi-jet events can be suppressed by requiring the spatial isolation from other particles. The isolation is defined inside a cone in the η-ϕ-space around the muon with the size $\Delta R = \sqrt{(\Delta\eta)^2 + (\Delta\phi)^2} < 0.3$. The isolation can be based on the tracker or on the calorimeters or both. The isolation in the tracker I_{trk} is given by the sum of the transverse momenta of all tracks within the cone, excluding the track from the muon. The isolation I_{ECAL} in ECAL and I_{HCAL} in HCAL is defined as the amount of the deposited transverse energy within the cone, while the energy within a smaller veto cone around the muon trajectory is excluded. The veto cone size is $\Delta R = 0.08$ in ECAL and $\Delta R = 0.1$ in HCAL.

In this work, a combined isolation using tracker and calorimeter isolation is in use. It is defined relative to the muon transverse momentum $p_{\mathrm{T}}(\mu)$. The combined relative isolation I_{comb} is required to be within

$$I_{\mathrm{comb}} = \frac{I_{\mathrm{trk}} + I_{\mathrm{ECAL}} + I_{\mathrm{HCAL}}}{p_{\mathrm{T}}(\mu)} < 0.15 \tag{3.5}$$

for the muons fulfilling the identification criteria described above. These isolated muons are used in all analyses.

3.5.4 Jet Reconstruction

Jet reconstruction provides information about the hard scattering process of the proton collision. Radiated quarks or gluons are measured as jets since their hadronisation in general causes the creation of many hadrons. Due to momentum conservation, the hadrons are collimated around the direction of the original parton. These bundles are reconstructed as a single physics object reducing the complexity of the final state—a jet.

The parameters of the original parton are reflected by the jet parameters, which are a composite measurement of the associated particles. Information from different subsystems can be used and combined in different ways, as defined in different jet types. Jet algorithms define the number and the size of the jets by regional grouping of the regarded information from the detector systems. The algorithms are defined independently of the information sources given by the jet types. The most important parameters to be measured are the jet direction and its energy. Systematic deviations between measured jet parameters and real parton parameters are balanced with phase-space dependent jet energy corrections.

Jet Algorithms

A jet algorithm defines jets as physical observables which can be measured. Important aspects of the design of algorithms are detailed in [100]. A main challenge is to provide infrared and collinear safety. The former means stability of the result in case of additional radiation of soft partons; the latter means insensitivity concerning splitting of the parton into collinear ones. The speed of an algorithm is an important criterion for the applicability, especially at trigger level. Several jet algorithms are in use at CMS.

Two main categories of jet algorithms can be distinguished. One category is the cone algorithms [101], a top-down approach maximising the energy flow within a cone of a given radius R in the η-ϕ space. On trigger level the "iterative cone" algorithm is applied due to its speed and predictable runtime [102]. The other category is the clustering algorithms [103] [104], sequential recombination algorithms with a bottom-up approach, combining adjacent objects to new objects and subsequently repeating this procedure. Two objects i and j are combined if a specific distance d_{ij} fulfils $d_{ij} < d_i$; with a characteristic threshold d_i. When the criterion cannot be fulfilled anymore, the final object is defined as a jet.

In this work the relevant distances are given as

$$\begin{aligned} d_{ij} &= \min\left(k_{\mathrm{T}_i}^{2p}, k_{\mathrm{T}_j}^{2p}\right) \frac{\Delta R_{ij}^2}{R^2}\,, \\ d_i &= k_{\mathrm{T}_i}^{2p}\,. \end{aligned} \tag{3.6}$$

Here, k_{T} is the transverse momentum, $\Delta R_{ij}^2 = (y_i - y_j)^2 + (\phi_i - \phi_j)^2$ is the angular distance of the objects with given ϕ and rapidity y; different configurations of the parameters R and p define specific algorithms. While the jet-radius parameter R gives a weight to d_{ij}, p sets the power to the momentum scale. The case with $p = 1$ is called k_{T} algorithm, $p = 0$ is the Cambridge-Aachen algorithm. The $p = -1$ case is named anti-k_{T} algorithm, and is the default choice for most analyses. Among several advantages [105], the shape of the anti-k_{T} jets is in general closer to a conic form than the other two variants.

Jet Types

The jet algorithms which specify the jet definitions can be run on different input objects, which are specified by the jet type. In simulated events it can be directly applied onto the generated particles of the final state, composing "generator jets". The true information can be used directly, it is independent of the detector. Depending on the analysis task, neutrinos are sometimes excluded since they cannot be measured directly; e.g. this is relevant to compare between measured quantities starting from reconstructed objects and the true quantities starting from the generated objects.

There are four jet types at CMS for the usage with reconstructed objects, performance studies can be found in [106]. "Calo jets" use the energy deposits in the calorimeters solely. Their energy resolution is not sufficient for many analysis purposes, in particular in the HCAL. It can be improved by taking

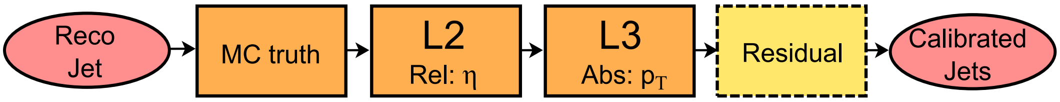

Figure 3.16: Jet energy correction scheme [5].

advantage of the excellent momentum resolution of the tracker, since the majority of the particles is charged. This is done for the "jet-plus-track (JPT) jets", tracks are matched to the calo jets and used to correct the energy measurement. A third approach are the "track jets", assembling tracks only. Their energy resolution is similar to the one of the calo jets, limiting the usability in physics analyses. The last approach is based on the concept of particle flow (PF) [107] and produces "PF jets". It is explained in more detail, since all jets in this thesis are PF jets.

PF uses information from all detector systems. The basic idea is to reconstruct all stable particles individually—the essential building blocks are tracker tracks, calorimeter clusters and muons. This leads to a list of reconstructed objects, the PF candidates. They span electrons, muons, photons, charged and neutral hadrons. From those, combined candidates are built, which are taus, jets and missing E_T, and also more complex objects are possible. Each candidate gets assigned the measured four-momentum and particle-specific properties. For the PF jets, a given jet algorithm is run on the collection of PF candidates to aggregate them into single jet objects.

Jet Energy Correction

The interesting parameters are the real parameters of the original parton. They are reflected by the measured jet parameters. Due to the jet definition and detector effects, systematic deviations between both can occur. They are balanced by a phase-space dependent calibration of the jet energy scale (JES), called jet energy correction (JEC). Details about JEC and the transverse momentum resolution of the jets can be found in [108] and [109].

JEC is divided into subsequent steps, the scheme is visible in Figure 3.16. Input are the uncorrected reconstructed jets ("reco jets"), the corrected jets ("calibrated jets") are the output. The first three steps are based on simulation, and correct for the deviation of the measured response and the true energy of the original parton. In the first step (MC truth correction), generator jets are matched to reco jets in simulated events. The measured energy is compared to the true value; their ratio as a function of p_T and η is the basis for the calibration. A global correction factor is applied to achieve the correct answer on average. In addition, the detector response depends on the kinematics of the original parton—this leads to the phase-space dependent corrections of the second and third step. The second step (L2 correction) ensures a flat response in η. The p_T-balance of the two jets in dijet events, resulting from the momentum conservation, is used. It is a relative correction, jets in the forward region are adjusted to have the same response as jets in the central region. The third step (L3 correction) is an absolute correction which scales the response with respect to p_{T}. It is calibrated on Z^0+jet and γ+jet events. Again, the p_{T}-balance is the basic ingredient. Either the balance of the gauge boson and the jet are used, or the full p_{T}-balance can be taken, since no real missing transverse momentum is expected in these events.

The first three steps of JEC are adequate for simulated events, since the corrections are gained from simulated samples. For data events however, additional corrections are applied in a fourth step (residual corrections), to account for differences on the detector responses in simulation and reality. These corrections are applied on data events only. They are p_{T}- and η-dependent and follow the approach of the L2 and L3 corrections. The residual correction is defined by the difference of these corrections on simulated and data events. For small values of $|\eta|$ the correction is small, but increases with bigger values [110]. The combination of simulation-based and additional data-based corrections leads to smaller systematic uncertainties as a purely data-based approach could provide. In general there is the possibility to apply additional correction steps, e.g. regarding the electromagnetic fraction or the flavour of the original parton, but mainly they are not applied in recent analyses.

3.5.5 Jet Identification

In this work only anti-k_{T} jets with a distance parameter of $R = 0.5$ are in use. The type is restricted to PF jets. The measured jet energy is corrected with the scheme described above. In the particle flow approach each physics object is used in the jet reconstruction; this leads to the fact that PF jets can be composed of individual objects, and e.g. even an isolated muon is reconstructed as a jet containing one charged particle. In addition, noise in the calorimeters can fake jets. Supplemental identification criteria are necessary to select only real hadronic jets; however they are kept at low thresholds to maintain high selection efficiencies. These criteria are common in many CMS analyses (see e.g. [111]). All jets have to fulfil the following requirements.

- Neutral hadronic fraction below 99%.
- Neutral electromagnetic fraction below 99%.
- At least two constituents.

For jets within $|\eta| < 2.4$, the range of the tracking systems, three additional criteria are applied:

- Charged hadronic fraction above 0%.
- Charged electromagnetic fraction below 99%.
- At least one charged constituent.

The jets passing the selection are used in the described analyses.

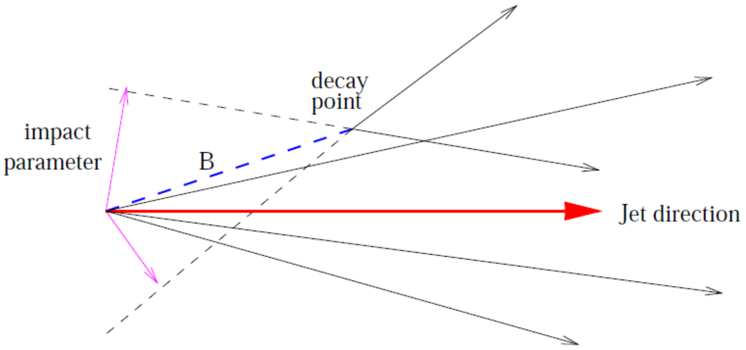

Figure 3.17: Topology of jets originating from b quarks [112]. The jet contains a B meson which decays at a secondary vertex with a spacial offset from the primary vertex due to its long lifetime.

3.5.6 Heavy Flavour Tagging

Jets which are initialised by heavy flavour quarks (c or b) can be distinguished from jets originating from gluons or light quarks (u, d, or s). This is due to the long lifetime of the D and B mesons formed during fragmentation, which allows a spatial distance measurement corresponding to the decay length. The effect is more pronounced for B mesons with a lifetime $\tau_{\mathrm{B}} \approx 1.6\,\mathrm{ps}$, which permits especially the tagging of b quarks. The corresponding decay length is $c\tau_{\mathrm{B}} \approx 500\,\mu\mathrm{m}$, and 5 charged particles result from the decay on average. The topology of b jets is shown in Figure 3.17. The tracker provides good impact parameter resolution and is used for b-tagging (see e.g. [112]). Besides the lifetime signatures, also the high masses of B mesons and a relatively high fraction of semileptonic decays can be used. These two signatures rely also on other detector components because of the mass measurement and the lepton identification respectively. Several algorithms are in use at CMS [113]. In recent analyses mainly simple and robust algorithms are used based on these basic signatures, but also complex multi-variate techniques are in use.

All algorithms produce a single discriminator value per jet to distinguish b jets from others. Thresholds to separate the jets via this discriminator are optimised for the analysis goals. Three working points are commonly defined, based on the fraction of non-b jets contaminating the selected jets; they are estimated from simulation [114]. These are the loose (10% contamination), the medium (1% contamination) and the tight (0.1% contamination) working point. In Chapter 6 the simple secondary vertex algorithm (SSV) is employed, it is explained in the following.

SSV is a decay-length based algorithm. It requires the reconstruction of a primary and a displaced secondary vertex. The reference primary vertex for all secondary vertices is the one with the highest quadratic p_{T}-sum of its constituent tracks $\sum_{\mathrm{tracks}} p_{\mathrm{T}}^2$. If no secondary vertex is found, the discriminator is set to a negative value. The probability of reconstructing a secondary vertex in a weak b decay is about 60–70% [113]. If a secondary vertex is found, the discriminator value is a monotonous function of the three-dimensional distance—the working point defines the minimum value to tag a jet. There are two different versions of SSV concerning the secondary vertex reconstruction. The high-efficiency version (HE, SSVHE) requires that the secondary vertex is reconstructed from at least two tracks, which is anyway the minimal multiplicity for forming a secondary vertex. The high-purity version (HP, SSVHP) reduces the contamination of non-b jets by requiring at least three tracks to form a secondary vertex, which reduces on the other hand the efficiency of selecting b jets. In this work, both versions are studied. SSVHE is used with the medium working point, corresponding to a discriminator value of 1.74. SSVHP is used with the tight working point at a discriminator value of 2.0 [114].

3.5.7 Missing Transverse Energy

The missing transverse energy $\not{E}_{\mathrm{T}}$ is the measured imbalance of the energy in the transverse plane. Each particle which interacts with the detector deposes signals according to its energy. This energy can be summed and a possible imbalance can be found. Partly this imbalance occurs from energy mismeasurements, mainly from the jets, or from reconstruction inefficiencies missing some contributions. This is called fake $\not{E}_{\mathrm{T}}$. But it can be also due to particles which do not interact with the detector, like neutrinos or hypothetic supersymmetric particles, which leave the detector unobserved. This allows the indirect observation and measurement of such weakly interacting particles via real $\not{E}_{\mathrm{T}}$.

In analogy to the described jet types, also $\not{E}_{\mathrm{T}}$ can be reconstructed from different reconstructed objects, e.g. only energy deposits in the calorimeters or only the tracks can be used. In the presented analyses the particle flow $\not{E}_{\mathrm{T}}$ is in use, which is based on the PF candidates. The vectorial sum of the four-momenta of all PF candidates is formed. Its vectorial component in the transverse plane is the transverse energy $\vec{E}_{\mathrm{T}}$, and the missing transverse energy is defined in the opposite direction $\vec{\not{E}}_{\mathrm{T}} = -\vec{E}_{\mathrm{T}}$. The absolute value defines the $\not{E}_{\mathrm{T}}$, performance studies are in [107].

3.6 Luminosity Measurement

The instantaneous luminosity gives the number of collisions per time and per cross section of the given process—the proton-proton collisions at a centre-of-mass energy as given by the LHC. To translate measurements of specific processes for a given dataset into corresponding cross sections, a precise knowledge of the time-integrated luminosity is mandatory. The luminosity at CMS is measured both online in the hadronic forward calorimeters (HF) but also offline based on the production rate of primary vertices. The online measurement can be done in two ways. The first is based on zero counting, the average fraction of empty HF towers relates with the number of collisions per bunch crossing. The second exploits the linearity between the average transverse energy per tower and the luminosity. The linear relationship is best valid in the region $3.5 < |\eta| < 4.2$; only these towers are used. The offline measurement follows the same structure with two different measurements. Either a zero counting is applied, using the fraction of events where no vertex is found, or the mean number of vertices per event is the measure. The absolute calibration of the luminosity is gained from van der Meer scans [115]. In dedicated LHC fills, the beams are moved relative to each other, and the interaction rate is measured as a function of the transverse beam separation. This allows the estimate of shape and size of the interaction region. Luminosity studies can be found in the following documentations. The uncertainty for the reprocessed 2010 dataset used in Chapter 5 was primary given as 11% [116] and later updated using more advanced techniques as 4% [117]. The 2011 dataset of the prompt reconstruction as used in Chapter 4 and Chapter 6 got 4.5% uncertainty assigned [118], before a further update with 2.2% uncertainty was provided [119].

The uncertainty of the luminosity is a significant contribution to the systematic error of many analyses. Alternatively to the methods described above, the normalisation to the luminosity can be replaced by the normalisation to the cross section of a well measured and understood process. For instance electroweak processes can be used as standard candles. Such a cross-section ratio is calculated in Chapter 5 for the production cross section of $\mathrm{t\bar{t}}$ events relative to that of Z^0 events.

Chapter 4

Estimation of the Tracker Alignment Precision

An introduction to the tracker and the track reconstruction is given in Chapter 3.3. The tracker needs to provide excellent tracking performance in order to comply with the ambitious physics programme of CMS. For muons with $p_{\mathrm{T}} = 100\,\mathrm{GeV}$ the tracker is expected to achieve a transverse momentum resolution of about 1.5% and an impact parameter resolution of about $15\,\mu\mathrm{m}$ [2]. The latter is necessary especially for efficient b-tagging. The momentum scale should be known to an accuracy of 0.02% to 0.025%, to allow the $\mathrm{W}^{\pm}$ mass measurement with a precision of 15–20 MeV [120]. To reach this performance, it is crucial to know the absolute coordinates of the silicon sensors in the global CMS coordinate system (see Chapter 3.2) to very high precision, so that the resulting uncertainty on a measurement along a sensitive coordinate is less than $10\,\mu\mathrm{m}$. The values are taken from simulation studies based on the design geometry and simulated misalignment.

Using alignment procedures, the desired precision of the knowledge of the detector geometry can be achieved. The remaining misalignment can be quantified in the reconstruction framework with an uncertainty called the alignment precision, which is taken into account when the track errors are estimated. The track parameterisation becomes more accurate, thus the impact on physics analyses using tracker information is optimised. In this chapter, the CMS alignment procedures are introduced, and the alignment geometries as used in the 2011 data reconstruction and analysed in this chapter are explained. Furthermore, a method developed for the estimation of the alignment precision is described and results are presented. It is also documented in [121]. The results are submitted as potential contribution to the publication in preparation [122].

4.1 Influence of Misalignment on the Event Reconstruction

Modifiable conditions used in the reconstruction – like the ones describing the tracker geometry – are stored in and accessed from specific databases. The geometry assumptions influence the basic quantities of the track reconstruction, which are the hit residuals and the χ^2-value of the track fit. Also higher-level objects which are reconstructed using tracks as input depend consequently on these assumptions. This is of relevance for all physics analyses using tracker information.

4.1.1 Alignment and Calibration Database

All necessary information for the event reconstruction from alignment, concerning the detector geometry, and calibration, concerning the signal readout, are stored in databases. There are two databases; one is used for online event reconstruction during the data taking as used for triggering, the other one is applied offline in the full event reconstruction. However, the content for alignment and calibration is identical for both. Each alignment or calibration task provides a record where the relevant values are stored. For instance there are records for the Lorentz angle or the backplane corrections in the silicon modules or the magnetic field map. Parameters of a specific record are stored in so-called tags. Depending on the use case, several tags are provided for each record—there is always one for reconstructing simulated events and at least two for real data, one for online and one for the offline prompt full event reconstruction. Additional tags are produced for possible reprocessings of the data with improved conditions.

To account for possible changes with time, the tags are defined with respect to specific periods, which are e.g. for the beamspot CMS lumi sections, while for all alignment tasks CMS run numbers are chosen as granularity. The stored constants are used for runs within an interval of validity (IOV), the following runs use another set of constants. Each record can set its own IOVs, independent of the other records.

The performance of CMS can suffer from misalignment of each detector component. There can be intrinsic misalignments within the components, and misalignments of the components with respect to each other and relative to the global CMS coordinate system as defined in Chapter 3.2. For this reason, there is an own global $(r|r\phi|z)$ coordinate system for the tracker, one for the calorimeters, and another one for the muon system. Their origins are arbitrary, the transformation in the global CMS coordinate system needs to be adjusted. The absolute positions and orientations of the global coordinate systems of the subsystems are stored in the global position record. Within these global coordinate systems, the subsystems provide the intrinsic geometries, stored in individual records. The record of the tracker geometry is described in the following, and referred to as alignment parameters.

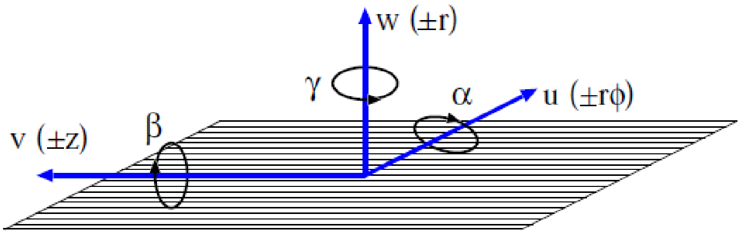

Figure 4.1: Local Cartesian $(u|v|w)$ coordinate system of a silicon module as used for tracking and for alignment [123]. Global orientations (in parentheses) are shown for modules in TIB and TOB.

Alignment Parameters and Local Cartesian Coordinate System

The global tracker coordinate system in tags used for data is defined as the centre of gravity of all modules of TOB, since TOB is expected to be more stable than other subdetectors. This means, the alignment parameters are fixed in a way that TOB as a whole does not rotate or move with respect to the design geometry. This coordinate system is not at the design position in the global position record, since TOB is shifted and rotated around the z-axis corresponding to survey measurements, and rotations around the other two Cartesian axes are measured using the influence of the magnetic field on the track reconstruction in case of non-parallel field with respect to the tracker z-axis. In simulation however, the global tracker coordinate system is defined by the pixel detector, and it is shifted in order to have the position of the beamspot with respect to the pixel detector at the correct place, but the following discussions are based on data and the real detector geometry.

For each silicon module of the tracker a local Cartesian $(u|v|w)$ coordinate system is defined as illustrated in Figure 4.1, the units are cm. The alignment parameters $\mathbf{p}$ are the positions and orientations of these local coordinate systems defined in the global tracker coordinate system.

The w-coordinate is given by the module's normal. The w-axis is always oriented in the direction of the design electric field within the sensor. Thus the strips or pixels are on the positive w-side, while the backplane of the module is on the negative w-side.

The u-v-plane of the local coordinate system is defined by the plane of the silicon sensors. It is placed in the middle of the sensor thickness. The origin is centred for each direction at the half width of the module, i.e. between the two innermost pixels or strips and at the half length of the strip.

For strip modules the v-axis is along the central strips, while the u-axis is orthogonal to it. This system is oriented on the readout electronics of the module. The v-axis points away from the direction of the readout cabling (the APV). The u-axis is then constrained to have a right-handed coordinate system. In rectangular barrel modules, only u has a sensitive measurement across the strips, while for the wedge-shaped forward sensors the measurements along these coordinates are more and more correlated for the strips when going to the edges of the modules.

For pixel modules, the u-axis is defined as the one which is more sensitive to Lorentz angle effects. In the barrel this is along the smaller pitch in the $\pm r\phi$-direction, in the forward it is along the wider pitch in the $\pm r$-direction. The v-direction is given by the orthogonal direction, forming a right-handed coordinate system. Measurements in the two coordinates are uncorrelated.

4.1.2 Hit Residuals and χ^2-Value of Track Fit

The hit residuals are the basic quantity in the track reconstruction, but also in the alignment, and the estimation of the alignment precision. For every hit measurement i, position coordinates $\mathbf{r}_{\text{hit}}$ and corresponding errors are estimated within the local coordinate frames of the modules. Hits which are assembled to tracks by the pattern recognition procedure get assigned the track parameters $\mathbf{q}$ for every track j as estimated by the final track fit. This depends strongly on the alignment parameters $\mathbf{p}$. The hit residual $\mathbf{r}$ is defined as the difference between the hit position measurement $\mathbf{r}_{\text{hit}}$ and of the associated track prediction, $\mathbf{r}_{\text{trk}}$,

$$\mathbf{r}_{ji}(\mathbf{p}, \mathbf{q}_j) = \mathbf{r}_{ji,\text{trk}}(\mathbf{p}, \mathbf{q}_j) - \mathbf{r}_{ji,\text{hit}} \,. \tag{4.1}$$

In case of the silicon modules, $\mathbf{r}_{\text{trk}}$ is the estimated intersection point of the particle trajectory and the two-dimensional module's plane. The residuals are the basis for the final fit of a particle track. The corresponding uncertainty depends strongly on characteristics like the shape of the module, the signal quality or the track incident angle.

The χ^2-value reflecting the goodness of the track fit is given by the sum of all residual contributions – normalised to their uncertainties – of all hits associated to the track,

$$\chi^2_j(\mathbf{p}, \mathbf{q}_j) = \sum_i^{\text{hits}} \mathbf{r}^{\text{T}}_{ji}(\mathbf{p}, \mathbf{q}_j) \mathbf{V}^{-1}_{ji} \mathbf{r}_{ji}(\mathbf{p}, \mathbf{q}_j) \,, \tag{4.2}$$

where $\mathbf{V}$ is the covariance matrix of the measurement uncertainties, and independence of measurements from different modules is assumed. Besides uncertainties originating from the intrinsic hit resolution and the track fit, the alignment precision can be taken into account. Details about the assigned uncertainties can be found later in this chapter.

The track reconstruction is based on this χ^2-formula. Given a set of alignment parameters $\mathbf{p}$, the track reconstruction fits the track parameters $\mathbf{q}_j$ by minimising the χ^2_j. The strip modules in TIB and TOB provide 1-dimensional measurements, while the pixel modules provide 2-dimensional measurements. Although the strip modules in TID and TEC provide only 1-dimensional measurements, they are treated as 2-dimensional measurements, since the Cartesian coordinate system which is used in the reconstruction does not reflect the

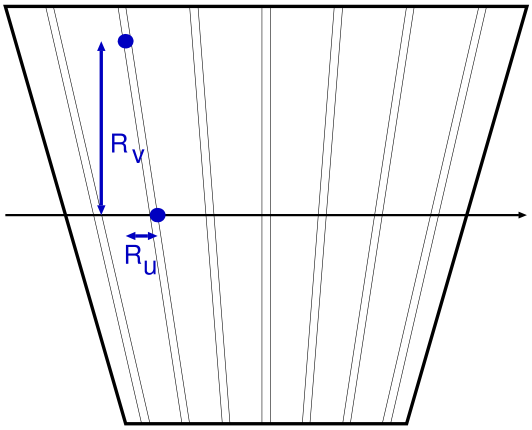

Figure 4.2: Wedge-shaped strip module in TID or TEC. If a particle crosses the module with a certain distance to the shown middle axis, the hit measurement is assigned to the middle of the strip. So even if the hit is reconstructed on the right strip, a finite residual in the u-direction occurs in the Cartesian $(u|v)$ coordinate system; it increases for strips closer to the module edges and with the distance of the particle crossing in the v-direction.

topology of the wedge-shaped modules and thus the sensitive coordinate (see Figure 4.2). In the pattern recognition procedure, hits on the two strip modules of a double-sided module are combined to a single 2-dimensional measurement. This was also done in the final track fit in early cosmic data analyses; alignment efforts with these combined hits can be found in [123], and the behaviour of their hit residuals, the χ^2, and the different alignment approaches in [124].

Within the track reconstruction all hit measurements are transformed to the local Cartesian $(u|v|w)$ coordinate system. This is done by a cluster parameter estimator algorithm (CPE) which translates the stored charge clusters to a hit measurement in the u-v-space. For the 2-dimensional measurements in TID and TEC the hit signals are set to the centre of the strips at $v = 0$. Also the track prediction on the module's surface is translated into the $(u|v|w)$ coordinate system. Details about the hit covariance matrices can be found in [125].

4.1.3 Influence of Misalignment and Alignment Precision on the Tracker Performance

It is clear that misalignment within the different detector systems, or of the systems relative to each other (e.g. tracker vs. muon system for muon reconstruction, tracker vs. ECAL for electron reconstruction), worsens the performance of CMS. The same holds for incorrect calibration conditions. The tracker is especially sensitive to misalignment due to its high resolution, and this is the main topic in this chapter. In the following misalignment means the internal misalignment of the tracker.

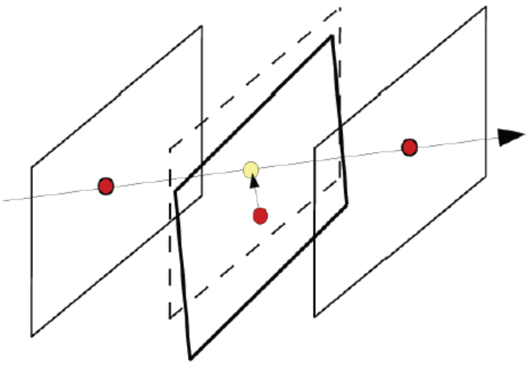

Figure 4.3: Displaced silicon module [126]. Displacements with respect to the assumed geometry lead to deviations between the hit measurement and the track prediction. As a consequence the residuals get systematically shifted and in general bigger.

The residuals and the χ^2 of the track fit depend strongly on the correct knowledge of the alignment parameters. In the presence of misalignment, which means deviations between the real geometry and the assumed geometry as given by the alignment parameters $\mathbf{p}$, the values of the residuals increase (see Figure 4.3). Thus those of the χ^2 increase also. Within the CMS software, there is the possibility to assign a corresponding uncertainty to the alignment parameters, the alignment precision. The uncertainties of the residuals are increased to balance the size of the misalignment. The χ^2-value should go back to the value with perfect alignment. Misalignment and the assignment of the alignment precision have consequences on both the pattern recognition procedure and the final track fit.

In the pattern recognition procedure misalignment causes tracking efficiency losses. Real hits migrate out of the search window due to the misplacement. This can lead to shortened or completely lost tracks. The alignment precision enlarges the size of the search window in the pattern recognition, and recovers the efficiency at the price of a small loss of purity. More fake hits are assigned to the tracks and the possibility for whole fake tracks is higher.

In the final track fit, the quality of the estimated track parameters suffers from misalignment. The central values are biased since the misalignment can differ throughout the detector volume. Also the final values for both the hit position and its uncertainty are affected slightly since they take track parameters into account—this effect is rather small, since the incident angle on the module changes only slightly, and this is the main parameter for the estimate. The errors of the track parameters do not describe correctly all uncertainties, they are too small. Again, this can be balanced with the alignment precision.

Besides the tracking efficiency and the detector resolution, there are also higher-level objects which are created from the tracks and hence are influenced directly by the tracking performance. Fake rates, inefficiencies and inaccuracies of the parameters and corresponding uncertainties depend on misalignment and the alignment precision. Important higher-level reconstruction steps are reconstruction of invariant masses of decaying particles, vertexing, impact-parameter based b-tagging, and beamspot estimation.

Almost all CMS physics analyses make use of the tracker and are thus sensible to misalignment and the alignment precision. But some are especially sensitive. Peaks of heavy resonances in dilepton mass spectra, can be degraded (e.g. the Z^0 peak) or even washed out (especially in the TeV mass region). Measurements like the estimation of the weak mixing angle θ_W using Z^0 events amongst others, suffer from this; corresponding studies are in [127]. An analysis about the impact on early quarkonium physics can be found in [128]. Also the influence on impact-parameter based b-tagging is studied in several analyses, since the lifetime signatures depend strongly on the correctness of the estimated track parameters (e.g. [129], [130] and [126]).

The physics analyses are sensitive to systematic biases or incorrect error estimates within the track reconstruction, which can also arise by miscalibration. Furthermore, the object parameterisation is strongly influenced by misalignment—a good knowledge of the alignment is necessary. The same holds for the knowledge of the achieved alignment precision.

4.2 Tracker Alignment

For the track reconstruction the local position measurements and corresponding uncertainties have to be transformed to a global coordinate system—actually the technical implementation is the other way around transforming the track prediction in the local frame, but this is equivalent. This requires precise knowledge about the position and orientation of the silicon modules within the tracker volume. The integration of the tracker is based on a hierarchical assembly of different mechanical sub-structures. Although it is done with highest possible accuracy, the uncertainties sum up with each hierarchical mounting structure to a relevant amount. The mounting precision is about $O(100\,\mu\text{m})$. It is clearly visible that this dominates the hit position uncertainty in the beginning of CMS. Alignment procedures determine the alignment parameters of the modules more precisely to reduce this impact. However, due to the complexity of the alignment challenge, the precision achieved has to be estimated in a separate step.

The alignment corrects the positions and orientations of alignment objects. Alignment objects are composite structures, which are treated as rigid non-deformable bodies. The alignment hierarchy of these sub-structures in the tracker is detailed in Figure 4.4. At the lowest level the modules themselves are the rigid bodies; the local parameterisation with 6 degrees of freedom, 3 translations u, v and w, and 3 rotations α, β and γ around these axes, is visualised in Figure 4.1. The higher-level structures are based on the mechanical mounting structure of the tracker, complemented by objects which are relevant for the track reconstruction. The full tracker is the highest level, and

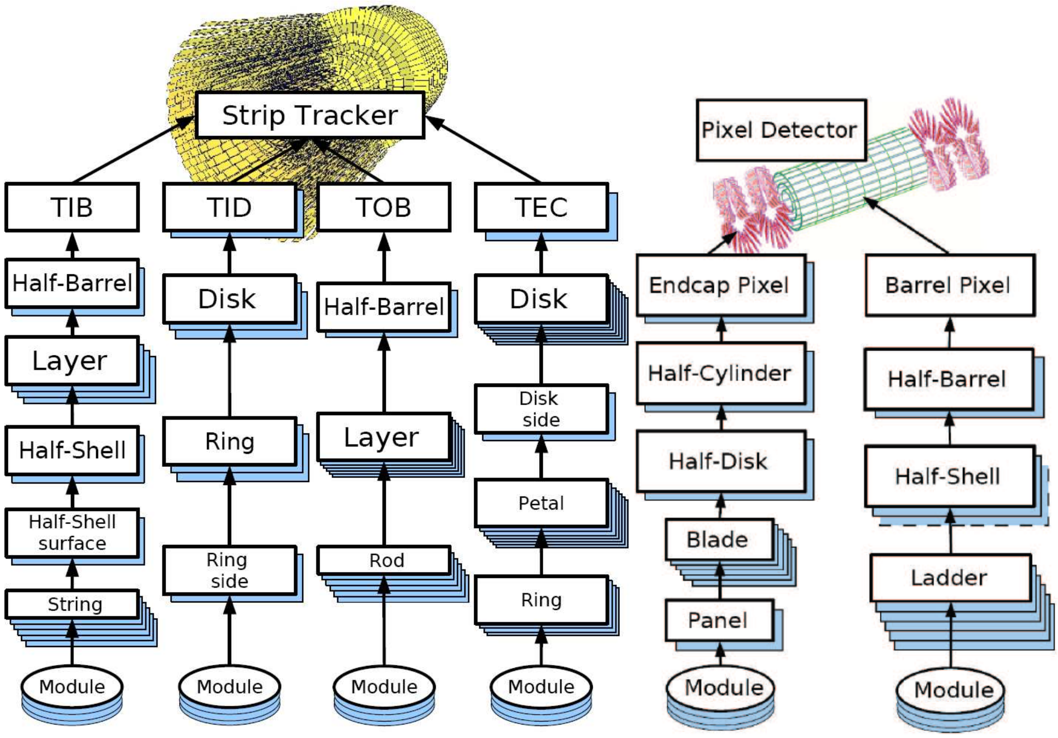

Figure 4.4: Alignment hierarchy of strip tracker [123] and pixel tracker [126]. The hierarchy is based on the mechanical mounting structure of the tracker, complemented by alignment objects which are relevant for the track reconstruction. For example TOB has no mechanical layers. The number of multilayers below the object names indicate the number of alignment objects of that type, i.e. TIB consists of 2 half barrels with 4 layers each—exceptions are made in case of different possible numbers or big numbers.

is used as alignment object in the cross-alignment between different detector components.

Different tracker alignment approaches exist in CMS. During the tracker integration, the mounting precision of several alignment objects was measured. These survey measurements can be used to improve the knowledge of the real geometry. In particular for alignment studies, a laser alignment system LAS is embedded in the strip tracker to monitor movements of larger substructures. But the main ingredient for efficient alignment is the track-based alignment, as explained in the next section.

It can be that there are time dependencies in the positions and orientations of alignment objects. For instance effects of the magnetic field, the cooling or even the beam itself can cause shifts and rotations of modules and higher-level structures. So the repeated estimation of the alignment and its precision is needed to exploit the intrinsic resolution of the modules in an optimal way.

4.2.1 Track-Based Alignment

Track-based alignment algorithms estimate the alignment parameters $\mathbf{p}$ in a statistical approach using millions of reconstructed particle tracks with track parameters $\mathbf{q}_j$. As already discussed, misalignment causes increased residuals and χ^2-values of the track fits. The alignment parameters are estimated by minimising the objective function χ^2_{tot} given by the sum of all χ^2-values of all tracks (see Equation 4.2),

$$\chi^2_{\text{tot}}(\mathbf{p},\mathbf{q}) = \sum_{j}^{\text{tracks}} \chi^2_j(\mathbf{p},\mathbf{q}_j) \quad \text{with} \quad \mathbf{q} = (\mathbf{q}_1, \mathbf{q}_2, \dots) \; . \tag{4.3}$$

Since the track fits depend on the alignment, sophisticated statistical approaches are needed. The big challenge is the huge number of degrees of freedom for the 16588 silicon modules, with 6 degrees of freedom each arising from the alignment parameters. In practice however, not all degrees of freedom are aligned, e.g. the v-direction of strip modules in TIB and TOB provides no measurement and changes of the corresponding alignment parameter have no influence. The algorithms need to be fast. Fully solving the equation without approximations for millions of tracks and $O(10^5)$ alignment parameters within a reasonable computing time is not feasible.

Three different alignment algorithms are implemented in the CMS software, but only two have been used to create the relevant alignment parameters. One is the Hit and Impact Point algorithm (HIP) [131], the other is the Millepede II algorithm [132]. In all methods the description is linearised in order to solve the complex equation. This leads to the fact, that the result depends on the starting geometry. But since the geometry is already close to the real one after the very first track-based alignment approaches and since the geometry seems to be rather stable with time, the dependence on the starting geometry is small. HIP is a local method and estimates the parameters for each module. Then iterations are needed to take the correlations between $\mathbf{p}$ and $\mathbf{q}$ with the track fit into account. It uses the same track model as the standard reconstruction. Millepede II is a global method, which fits all track and alignment parameters simultaneously. All correlations between $\mathbf{p}$ and $\mathbf{q}$ are considered. Specific track models are in use.

The procedures use constraints implied by the track model to estimate alignment corrections to the geometry. Tracks gathered from enough hit measurements to overconstrain the track fit are the basis. In principle additional constraints can be applied on all overconstrained parameters of reconstructed objects. Invariant masses of decaying particles or common vertices can be used to set constraints. This can be combined with two-body decay constraints, e.g. in decays $\mathrm{Z}^0 \rightarrow \mu^+\mu^-$. Furthermore an event-independent beamspot constraint can be applied. Since the beamspot estimation depends on the alignment parameters, it can also be included in the alignment procedures as an alignable object and be corrected.

To reach the ultimate precision, different track topologies are needed. In addition to tracks from collision events, cosmic muons are essential, and also beam halo tracks might be useful. Contrary to collision tracks, cosmic muons connect opposed parts of the tracker. In addition they penetrate the modules with very different incident angles.

A particular challenge are so-called weak modes. These are systematic distortions of the geometry, which influence the χ^2-distribution only slightly, but can cause a significant bias in physics results by shifting track parameters like p_{T} systematically. They depend on the track topology and thus can differ for different track sources. Constraining of weak modes is the main point why it is necessary to include cosmic muons in the track-based alignment. Partly weak modes can also be controlled by the additional constraints from higher-level reconstructed objects as explained above.

The algorithms are based on the χ^2_{tot}-minimisation using linearisations. The result of the alignment depends on the parameterisation of the input—the errors are required to be Gaussian and of correct size, and all underlying models need to be described properly. The tracks are influenced by the interactions with the detector material including some non-Gaussian effects, and the hit measurements are digitised and interpreted by CPEs. Sensitivity to the modelling is e.g. due to the track model, the magnetic field parameterisation or the correctness of the material description. Also miscalibration effects influence the alignment. For example incorrect estimates of the Lorentz angle or the backplane corrections of the silicon modules cause systematic shifts in the residuals, which translates to an additional shift of the corresponding alignment parameter in the alignment. For constant detector operation mode the effect is compensated by the alignment and the measured hit positions are correct. In principle they could be taken into account as own alignment object, being calibrated in one go with the alignment parameters. Especially global algorithms like Millepede II can take additional information and constraints into account, as long as the number of degrees of freedom is compatible with the available computing power and required speed.

Recent developments allow the treatment of the modules as deformable objects in Millepede II. In detail, the surface of the sensors is parametrised by 3 additional degrees of freedom, with orthogonal Legendre polynomials of second order, referred to as bows. For modules in TOB and TEC carrying two silicon sensors, each sensor is treated independently. These modules have an additional degree of freedom, allowing the sensors to be rotated around the axis defined by the gap between both sensors, called kinks. A description of these kinks and bows can be found in [133]. They are stored in an own record for the database (see Chapter 4.1.1), called surface deformations. Again, cosmic muons are helpful in the alignment, since they provide a wide range of incident angles on the modules. Evidence for these corrections are given by the gain in performance as demonstrated in Figure 4.5. In the track reconstruction the modules are still treated as flat modules, providing measurements in the 2-dimensional u-v-plane. Instead, the hit position measurements are shifted reflecting the deviations from flat modules.

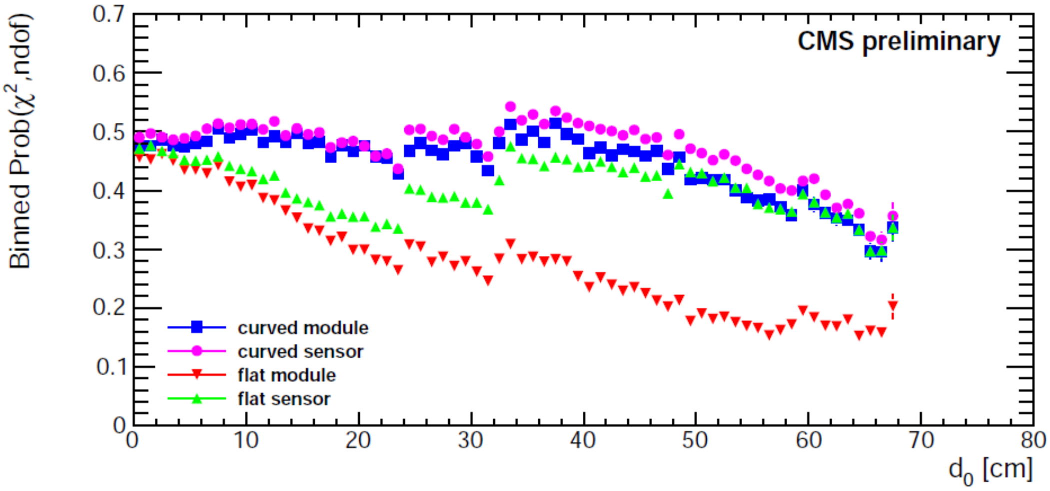

Figure 4.5: Effect of kinks and bows on χ^2-probability of tracks as a function of the impact parameter d_0. Shown are tracks from cosmic muons, giving a wide spread of impact parameters. Presuming correct error estimates for the tracks and hits, χ^2-probability values around 0.5 are expected. Misalignment leads to reduced probabilities. The incident angles on the modules grow with d_0 of cosmic tracks; those tracks are thus more sensitive to kinks and bows. Shown are results for flat modules (red triangles pointing downwards), modules described by two sensors allowing a kink angle (green triangles pointing upwards), bowed modules (blue squares), and bowed sensors (magenta dots) [133].

In this chapter the geometry as used for the data taking throughout 2011 (called "prompt") is compared to the one prepared for the reprocessing of the full 2011 dataset at the end of the year (called "reprocessing"). The reprocessing geometry uses much more data than the prompt one, and it is created on the 2011 dataset. The approach is in general more advanced, and for the first time also the kinks and bows are taken into account. One important finding are shifts of the pixel half barrels with respect to each other at specific points in time—they are accounted for in the reprocessing geometry. Details about all important sets of alignment parameters used for collision data taking are given in Appendix A.1.1, where also the alignment geometries as used in the data reconstruction for the physics analyses in Chapters 5 and 6 are explained.

4.3 Implementation of the Alignment Precision

The alignment precision is a record of the alignment and calibration database (see Chapter 4.1.1), similar to the record of the alignment parameters. The parameters of the alignment precision are defined per module in the same local Cartesian $(u|v|w)$ coordinate system as the alignment parameters—errors are assigned to translations only, and only those in the u-v-plane are used in the track reconstruction. More details concerning the contents of this section are given in Appendix A.2.

In the track reconstruction, position measurements and track predictions are translated into the two-dimensional Cartesian $(u|v)$ coordinate system of the module, which is the u-v-plane of the $(u|v|w)$-coordinate system. The uncertainties are fully described in the corresponding covariance matrix. The covariance matrix of the alignment precision is added to the one of the hit in order to reflect the effective hit resolution. Off-diagonal elements of the alignment precision are always set to 0 when producing parameters. Thus, the value σ_{align} in each coordinate is quadratically added to the value of the intrinsic hit resolution σ_{hit} in this direction, obtaining e.g. in the u-coordinate the effective resolution diagonal element $\sigma_{u,\text{eff}}$:

$$\sigma^2_{u,\text{eff}} = \sigma^2_{u,\text{hit}} + \sigma^2_{u,\text{align}} \, . \tag{4.4}$$

The local $(u|v)$ Cartesian system is not optimal for the description of the residuals—for this purpose, the local $(x|y)$ oriented system is used. Both are similar and they have the same origin, but two differences exist. The $(u|v)$ system is oriented on the architecture of the module, while the $(x|y)$ system has the directions of the coordinate axes according to the global coordinate system: the axes of all modules of a subdetector point in the same global direction (r, ϕ or z). The other difference affects only the wedge-shaped sensors of TID and TEC with the radial strip topology. Hit measurements are correlated in the $(u|v)$ system (see Figure 4.2). In the $(x|y)$ system, the inherent angular measurement is used, but it is multiplied with the distance of the origin to the virtual intersection point of the strips, in order to have all distances defined as lengths.

4.4 Basic Principle of Estimation of Alignment Precision

The main ingredient for the presented method to estimate the alignment precision is the distribution of normalised residuals in the oriented $(x|y)$ coordinate system. This requires the measured hit position and the track prediction on the module's surface. Within the CMS software the final track parameters are persistent, they are stored in the event. The trajectory however, and thus the track predictions on the module's surface, are transient, they are not stored. But the inspection of residuals requires the track predictions. They are made available using the track refit as explained in Chapter 3.3.4. The refit is also important to study changes in the alignment and calibration conditions, or in the hit or track model, which are configurable in the refit. This is used in this chapter to study the alignment precision for different alignment parameters, without the need of the full track reconstruction.

4.4.1 Normalised Hit Residual Distributions

To have the track prediction in the residual unbiased from the hit measurement itself, the track prediction is taken from a track fit excluding the hit under study, resulting in an addition of the covariance matrices of effective hit resolution and track prediction (details see Appendix A.3.1). In the $(x|y)$ oriented system all measurements are uncorrelated. In the strip modules there is only one sensitive coordinate x, in the pixel modules both coordinates are sensitive. For simplicity, the following descriptions are written with the coordinate x, but are valid for both x and y. The absolute and normalised residuals for uncorrelated measurements can be written in each coordinate as

$$r = x_{\text{trk}} - x_{\text{hit}} \qquad \text{and} \qquad r_{\text{norm}} = \frac{r}{\sigma_r}\,, \tag{4.5}$$

with the uncertainty given by

$$\begin{aligned} \sigma_r^2 &= \sigma_{\text{trk}}^2 + \quad \sigma_{\text{eff}}^2 \\ &= \sigma_{\text{trk}}^2 + \sigma_{\text{hit}}^2 + \sigma_{\text{align}}^2 \\ &= \qquad \sigma^2 \qquad + \sigma_{\text{align}}^2\,. \end{aligned} \tag{4.6}$$

The identity $\sigma^2 = \sigma_{\text{trk}}^2 + \sigma_{\text{hit}}^2$ defines the residual resolution σ which will be important later. It can be seen that the normalisation of the residual depends on

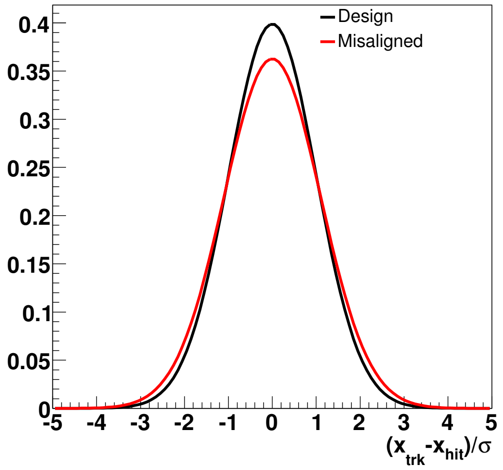

Figure 4.6: Influence of misalignment on normalised residual distribution. In an ideal measurement frame, a Gaussian distribution with standard deviation $\Delta_0 = 1$ is expected for perfect alignment (black). Misalignment (red) shifts the residuals, and thus broadens the distribution to an approximate Gaussian distribution of width Δ.

the correctness of the hit and track errors, and on the assumption of the misalignment, the alignment precision. Incorrect hit or track errors can broaden or narrow the distribution of normalised residuals.

Assuming perfect measurements without detector effects and correct error assignments, the r.m.s. value of the distribution of absolute residuals quotes the spatial resolution of the regarded detector. In case of perfect alignment the distribution is centred around zero for each module. Misalignment reduces the resolution of the module, the central value is shifted and the spread gets wider. The distribution of normalised residuals is described by a Gaussian distribution, assuming all errors to be Gaussian. The probability density φ of the normalised residuals r_{norm} for a Gaussian distribution, centred at $r_{0,\text{norm}}$ with standard deviation Δ, is

$$\varphi(r_{\text{norm}}) = \frac{1}{\Delta\sqrt{2\pi}} \cdot e^{-\frac{1}{2}\left(\frac{r_{\text{norm}} - r_{0,\text{norm}}}{\Delta}\right)^2} . \tag{4.7}$$

The distribution of the normalised residuals for perfect alignment is a Gaussian with standard deviation $\Delta_0 = 1$, centred around zero:

$$\varphi_0(r_{\text{norm}}) = \frac{1}{\sqrt{2\pi}} \cdot e^{-\frac{r_{\text{norm}}^2}{2}} . \tag{4.8}$$

In reality, the measurements are not perfectly Gaussian due to detector effects, as explained later. Also the normalisation does not need to be perfectly at $\Delta_0 = 1$. Nevertheless, the following descriptions are based on ideal measurements, but Δ_0 is kept variable and is called the nominal residual width in the following.

Table 4.1: Change of variables by assignment of finite value of the alignment precision $\sigma_{\mathrm{align}} > 0$. The value of σ_{align} is adjusted such, that $\Delta' = \Delta_0$.

Variable	$\sigma_{\mathrm{align}} = 0$	$\sigma_{\mathrm{align}} > 0$
Absolute residual	r	$r' = r$
Residual error	$\sigma_r^2 = \sigma^2$	${\sigma'_r}^2 = \sigma^2 + \sigma_{\mathrm{align}}^2$
Normalised residual	$r_{\mathrm{norm}} = \frac{r}{\sigma_r} = \frac{r}{\sigma}$	${r_{\mathrm{norm}}}' = \frac{r}{\sigma'_r} = \frac{\sigma}{\sigma'_r} \cdot r_{\mathrm{norm}}$
Probability density	$\varphi(r_{\mathrm{norm}})$	$\varphi'({r_{\mathrm{norm}}}') = \varphi'\left(\frac{\sigma}{\sigma'_r} \cdot r_{\mathrm{norm}}\right)$
Residual width	$\Delta > \Delta_0$	$\Delta' = \Delta_0$

In the presence of misalignment the distribution shows a broadened variance $\Delta^2 > \Delta_0^2$ as illustrated in Figure 4.6, as long as it is not accounted for with the σ_{align}. In fact the broadened distribution is not perfect Gaussian anymore, but for misalignments of the expected size, it can be approximated by a Gaussian with width Δ. This effect gives the basic idea of the method. The broadened width Δ is used as measure for the misalignment. And the alignment precision is estimated such, that the variance ${\Delta'}^2$ of the distribution with probability density φ' goes to ${\Delta'}^2 = \Delta_0^2$. Table 4.1 gives the changes of the variables when the alignment precision gets assigned a finite value $\sigma_{\mathrm{align}} > 0$. The ansatz for the probability density φ' is also a Gaussian with width $\Delta' = \Delta_0$:

$$\varphi'(r'_{\mathrm{norm}}) = \frac{1}{\Delta_0\sqrt{2\pi}} \cdot e^{-\frac{{r'_{\mathrm{norm}}}^2}{2\Delta_0^2}} . \tag{4.9}$$

The mean can also be shifted, but this is not important for the presented method, which is based exclusively on the width of the distribution.

The broadened distribution φ is a Gaussian for a fixed value of the residual resolution σ_i. Given the descriptions above, it is

$$\varphi(r_{\mathrm{norm}}) = \frac{1}{\Delta_i\sqrt{2\pi}} \cdot e^{-\frac{r_{\mathrm{norm}}^2}{2\Delta_i^2}} \qquad \text{with} \qquad \Delta_i = \frac{\sigma'_i}{\sigma_i}\Delta_0 . \tag{4.10}$$

Again, the mean value can be shifted, but is not important for the presented method. The variance Δ_i^2 of the distribution is given by

$$\Delta_i^2 = \frac{{\sigma'_i}^2}{\sigma^2}\Delta_0^2 = \frac{\sigma_i^2 + \sigma_{\mathrm{align}}^2}{\sigma_i^2}\Delta_0^2 . \tag{4.11}$$

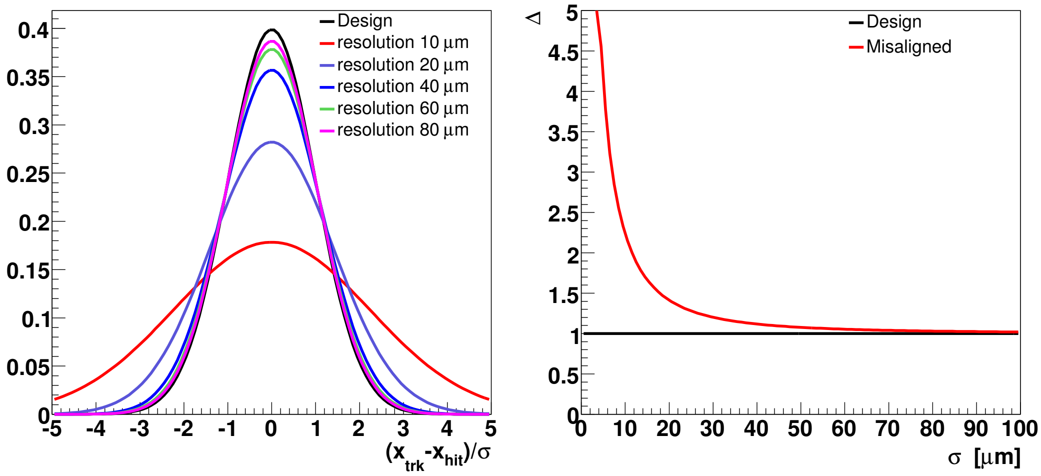

Figure 4.7: Dependence of the measurability of misalignment on the residual resolution σ. Left: normalised residual distributions for design geometry (black curve), and for distributions with a misalignment corresponding to $\sigma_{\text{align}} = 20\,\mu\text{m}$ (coloured curves). The distributions for misalignment are shown for 5 different values of σ; the misalignment is well measurable if it is at the same size, and gets less detectable with bigger values of σ. Right: dependence of Δ on σ for design geometry (black), where it is simply the nominal residual width $\Delta_0 = 1$, and for misalignment corresponding to $\sigma_{\text{align}} = 20\,\mu\text{m}$ (red).

Thus, the alignment precision for a given residual resolution σ_i can be calculated via

$$\sigma_{\text{align}} = \sigma_i \cdot \sqrt{\Delta_i^2 - \Delta_0^2}\,. \tag{4.12}$$

As Equation 4.12 shows, the alignment precision can be estimated based on the knowledge of the broadened residual width, the residual resolution and the nominal residual width. However this relation is only valid for a given value of the residual resolution σ_i and the corresponding width Δ_i. The influence of misalignment on the normalised residual distributions depends on the residual resolution as shown in Figure 4.7. If the residual resolution is of similar size as the misalignment, there is a big broadening of the distribution. With bigger values of the residual resolution the effect gets smaller and less measurable. This requires to study the distribution in small intervals of the residual resolution.

The normalised residual distribution is defined for each module, composed from the hit measurements corresponding to tracks which pass the active sensor area. However, there can be good reasons to group several modules and analyse their normalised residual distributions overlaid in one. This is necessary e.g. in case of insufficient statistical power per module or if statements for specific detector regions should be formulated. In this study modules are grouped in so-called sectors as they will be defined in Chapter 4.6.

4.4.2 Implementation of the Estimation Method

The basic principle of the alignment-precision estimation is as follows. The residual distributions are analysed in 10 different intervals of the residual resolution σ, where the interval size is small against the mean value. The borders of these intervals are $5\,\mu$m, $10\,\mu$m, $15\,\mu$m, $20\,\mu$m, $25\,\mu$m, $30\,\mu$m, $35\,\mu$m, $40\,\mu$m, $50\,\mu$m, $70\,\mu$m, $100\,\mu$m. The alignment precision is calculated in the $(x|y)$ oriented system separately for each independent measurement coordinate, i.e. x and y in pixel modules and x in strip modules. The alignment precision is determined for any given geometry from the following steps.

Calculation of Alignment Precision

First, for each interval in σ a separate value σ_{align_i} is calculated. It is estimated such that the total variance $\sigma^2_{r_i} = \sigma^2_i + \sigma^2_{\text{align}_i}$ reduces Δ_i to the nominal value Δ_0. According to Equation 4.12, this is done via the formula

$$\sigma^2_{\text{align}_i} = \left(\Delta^2_i - \Delta^2_0\right) \cdot \overline{\sigma}_i{}^2 \;, \tag{4.13}$$

which is valid for about constant values of σ_i, which means per interval. For each interval, the broadened width Δ_i is measured from data, together with the residual resolution $\overline{\sigma}_i$, which is the mean value of all residuals within the interval. In order to measure the broadening of the width, the refit of the tracks is used and all values of the alignment precision are set to 0. The residual width per interval is then measured with a Gaussian fit to the residual distribution, but each interval is only used when the normalised residual distribution spans at least 100 hits. Hence failures of the fits or bad fits due to a lack of statistical power are excluded.

Second, the alignment precision is calculated as the weighted mean from all intervals.

$$\sigma^2_{\text{align}} = \frac{1}{w} \sum w_i \cdot \sigma^2_{\text{align}_i} \quad \text{with} \quad w = \sum w_i \,. \tag{4.14}$$

The weight influences the outcome of the method. To cope with the residual resolution $\overline{\sigma}_i$ and the statistical power per interval, given by the number of measurements n_i, the weight is taken as

$$w_i\left(n_i, \overline{\sigma}^2_i\right) = \frac{n_i}{\overline{\sigma}^2_i} \,. \tag{4.15}$$

Iterative Procedure accounting for Correlations

Finally the procedure for estimating the alignment precision needs to be iterated, as can be seen from the total residual error. In the first estimate, named the iteration 0, every module gets assigned a value of the squared alignment precision $\sigma^2_{0,\text{align}} \geq 0\,\mu$m. The alignment precision of neighbouring layers influences the result of the track prediction, both the position and the error. And this is used for building the normalised residual distributions for the specific module under study. The errors of all hits per track are correlated. The estimated values are used for a refit called iteration 1, giving a correction $\Delta\sigma^2_{1,\mathrm{align}}$ with respect to the value of the previous iteration. The new value $\sigma^2_{j,\mathrm{align}}$ in iteration j is estimated as

$$\sigma^2_{j,\mathrm{align}} = \sigma^2_{j-1,\mathrm{align}} + c_{\mathrm{d}} \cdot \Delta\sigma^2_{j,\mathrm{align}} \geq 0\,\mu\mathrm{m} \tag{4.16}$$

The correction $\Delta\sigma^2_{1,\mathrm{align}}$ can now also be negative, to account for overestimated errors in the previous iteration ($\sigma_{j-1,\mathrm{align}}$), which lead to a residual width $\Delta < \Delta_0$. If $\sigma^2_{j,\mathrm{align}}$ gets negative – which would mean imaginary values of the alignment precision – it is set to zero. In principle negative values can occur if the resolution of the module is underestimated, which means the assigned errors of the intrinsic hit resolution are too big in general. But negative values are unphysical in the sense that the alignment precision reflects the knowledge of the module position and is thus a fixed value for a specific module, while the resolution of a module is a function of the track and hit parameters, and imaginary alignment-precision values would account only for the mean resolution given a specific dataset. Furthermore, imaginary values cannot be stored in the alignment precision record.

The procedure is repeated until convergence is reached. Especially in the iteration 0, the alignment precision tends to be overestimated. This is expected since the correlations of the alignment precision of modules from different layers are not taken into account. This is cured by the damping coefficient c_{d}, which is used for a smoothing of the iterations. The damping factor is also applied to the first estimate in iteration 0, $\sigma^2_{0,\mathrm{align}} \to c_{\mathrm{d}} \cdot \sigma^2_{0,\mathrm{align}}$. In fact it is necessary to avoid oscillations between huge values and zero, and slow convergence in general. The coefficient is tuned to take 40% information from the old result of the last iteration and 60% of the new result: $c_{\mathrm{d}} = 0.6$.

During the iterations after the first cycle, the tracks are fit including finite values of the alignment precision from the previous iteration. This cannot be separated from the track error $\sigma^2_{j,\mathrm{trk}} = \sigma^2_{j,\mathrm{trk}}(\sigma_{j-1,\mathrm{align}})$, which increases with bigger values. This means, that the squared residual resolution $\sigma^2_j = \sigma^2_{j,\mathrm{trk}} + \sigma^2_{j,\mathrm{hit}}$ itself depends on the recent estimate of the alignment precision. The intrinsic hit error stays untouched. The fluctuations of the residual resolution lead to migrations of the hits between different intervals in the interval-wise calculations at the beginning of an iteration cycle of the explained alignment-precision estimation.

Assignment of Values in Alignment Precision Record

The alignment precision is calculated in the oriented $(x|y)$-system in the sensitive coordinates, which means only the x-direction in strip modules, and the x- and y-direction in pixel modules. The two uncorrelated coordinates in pixel modules are treated independently as two separate measurements. The alignment precision record however needs to be stored in the Cartesian $(u|v)$-system.

In TIB and TOB the axes are identical; the calculated value is assigned to all three translational directions, i.e. the same absolute value in all directions resulting in spherical symmetry, called spherical assignment. In BPIX and FPIX the axes also agree between both coordinate systems. Thus, the result in each coordinate is directly assigned to the corresponding value in this coordinate. The w-direction gets assigned the square root of the mean value of the sum of the two squared values—the shape of the uncertainty is ellipsoidical.

In TID and TEC the axes are not exactly identical due to the radial strip topology. In principle, the estimated correction in each iteration step is not the correct one, since it is calculated in another coordinate system. This does not harm, since the iterations automatically lead to the best value which needs to be stored in the record—but potentially the convergence is slower than in the other subdetectors. The estimated value is assigned spherical as for TIB and TOB.

4.4.3 Estimation of Nominal Residual Width from Simulation

The nominal residual width Δ_0 should be close to 1 and the same across all intervals, and also the same for all modules of the tracker. With other words, in case of perfect alignment the measured residual width Δ should be the same across all intervals. This means that the determination should be independent from the input, the hits which are used for the determination. But even in simulation studies with perfect alignment this is not observed, since some hit or track error estimates are incorrect. And also the normalised residuals in data vary for different track topologies and throughout the detector regions. With the standard setup of the reconstruction, there have been observed distributions in the pixel detector with widths around 0.9, which means clearly below 1. Distributions in the strip detector often show the opposite behaviour, residuals are clearly bigger than 1 and the difference cannot be explained by misalignment only. This is mainly due to known deficits in the CPE parameterisation.

As solution an effective Δ_0 is determined from ideal simulation, which means using the refit with perfect alignment and calibration conditions as they were used for the simulation of events. Ideal conditions mean in particular the usage of the design geometry in the refit as used in simulation, and of the corresponding alignment precision where all values are set to 0, reflecting the perfect knowledge of the geometry. The nominal residual width Δ_0 is calibrated such that the calculation of the alignment precision – based on Equation 4.13 and Equation 4.14 – estimates for the design geometry exactly $\sigma_{\text{align}} = 0$. The same weight w_i as for the weighting of the σ_{align_i} is needed to estimate Δ_0 from simulation,

$$\Delta_0^2 = \frac{\sum w_i \cdot \overline{\sigma}_i^2 \Delta_i^2}{\sum w_i \cdot \overline{\sigma}_i^2} \,. \tag{4.17}$$

The mean value of the residual resolution $\overline{\sigma}_i$ and the width Δ_i per interval i is estimated in the same way as for the alignment-precision measurement in data. The usage of this information from simulation requires similar hit populations for data and simulation, which depend on the track sample. E.g. the hit error is mainly driven by the incident angle on the module, while the track error depends strongly on p_T. Modelling of data with simulated samples is indispensable.

4.5 Systematic Influences

It is observed that the quality of the normalised residual distributions varies with detector regions and intervals of the residual resolution. There are different types of systematic effects, which influence the normalised residuals and lead to deviations from Gaussian distributions in the $(u|v)$ coordinate system. The alignment precision estimation method requires a correct estimate of the residuals and especially of their errors. So both parametrisations have to be under control, the hit measurement and the track prediction. Especially influences on their uncertainty estimates are possible sources of error. The measured alignment precision does not reflect the misalignment in these two coordinates only, but all influences on the normalised residual distributions in this 2-dimensional projection.

One systematic effect is that misalignments in the other alignment parameters, which are not accounted for in the alignment precision, are absorbed into the two coordinates of the u-v-plane. Several other systematic influences enter the measurement, they are listed in Appendix A.5. Their influences are mainly small, except of the two described in the following.

Biases from Track Reconstruction

Due to the hit and track models in use, wrong position and uncertainty estimates can occur, leading to non-Gaussian behaviour. Wrong uncertainties are very dangerous, since they can broaden and narrow the residual distribution. The uncertainties of the track depend on the track model and on the effects described so far. The uncertainty of the hit itself is estimated together with the track parameters by a cluster parameter estimator (CPE). Huge variations of the residual width could be observed, several errors are systematically over- or underestimated, depending on the track and hit parameters (see e.g. [134]). This requires a stringent track and hit selection, however this can cure the effect only partly. More details about the implemented CPEs and the choice for this work can be found in Appendix A.4.

Incorrect Modelling of Data

Due to discrepancies amongst normalised residual distributions in different detector regions and for different hit and track topologies arising from the biases in the track reconstruction, the behaviour cannot be described assuming a constant nominal residual width Δ_0 throughout the different intervals of the residual resolution and all detector regions. The described solution is the determination of an effective Δ_0 for each regarded detector region, which is determined from simulation based on the design geometry. The basic idea is to have the same non-ideal descriptions in data and simulation, and to use the same problematic input from hits and tracks with the same statistical power in both cases. This requires an accurate modelling of the data, which means similar hit and track topologies—the track and hit selection needs to be optimised. In addition, possible systematic deviations between real and simulated hits can bias the results.

4.6 Detector Granularity for Estimate of Alignment Precision

Theoretically the method described in Chapter 4.4 could be used to estimate the alignment precision of each module. However this is not possible due to the requirement of enough statistical power in face of the stringent track and hit selection, which in the first place allows the comparison to simulation.

Instead, modules are grouped to one entity called sector. The normalised residual distributions for all modules of a sector are analysed altogether, and the identical parameters of the alignment precision are assigned. The modules are arranged in sectors turning the attention on grouping modules with the same resolution and with a similar expected alignment precision. The sector definitions, together with their names (keys) and the number of spanned modules, are detailed in Table 4.2 and Table 4.3. Each interval of the residual resolution in the given sector is used for the alignment precision calculation, if at least 100 hits are used for the estimation of the residual width Δ within this interval.

The modules for the sectors in the barrel detectors BPIX, TIB and TOB are grouped by layers (3, 4, and 6 each), which separates already the different module topologies. These sectors are further separated by $r\phi$- and stereo-modules in the layers which are equipped with double-sided strip modules. Finally a further separation is based on the global orientation of the modules. Either the sensor side with the pixels respectively strips points into the direction of the beam pipe (inwards), or away from the beam pipe (outwards). This separation reduces the impact of Lorentz angle miscalibrations: since the orientation of the electric fields with respect to the magnetic field is inverted between inwards and outwards pointing modules, the residuals are systematically shifted to opposite directions, as it shows up in the used globally oriented

Table 4.2: Granularity for alignment precision estimate in BPIX, FPIX, TIB and TOB. The separation criteria for sectors of a given subdetector are indicated by column 'Description', which is mainly based on the separation via layers or rings. In forward detectors, it is important, which side is used (minus, plus); in strip detectors for double-sided modules, which one is used ($r\phi$, stereo); in barrel detectors, whether the module's surface points in direction of the beamline, or away (inwards, outwards).

Subdetector	ID	# modules	Key	Description
BPIX	1	80	BPIX L1o	layer 1, outwards
	2	80	BPIX L1i	layer 1, inwards
	3	128	BPIX L2o	layer 2, outwards
	4	128	BPIX L2i	layer 2, inwards
	5	176	BPIX L3o	layer 3, outwards
	6	176	BPIX L3i	layer 3, inwards
FPIX	7	168	FPIXm L1	minus side, layer 1
	8	168	FPIXm L2	minus side, layer 2
	9	168	FPIXp L1	plus side, layer 1
	10	168	FPIXp L2	plus side, layer 2
TIB	11	180	TIB L1Ro	layer 1, $r\phi$, outwards
	12	156	TIB L1So	layer 1, stereo, outwards
	13	156	TIB L1Ri	layer 1, $r\phi$, inwards
	14	180	TIB L1Si	layer 1, stereo, inwards
	15	228	TIB L2Ro	layer 2, $r\phi$, outwards
	16	204	TIB L2So	layer 2, stereo, outwards
	17	204	TIB L2Ri	layer 2, $r\phi$, inwards
	18	228	TIB L2Si	layer 2, stereo, inwards
	19	276	TIB L3o	layer 3, outwards
	20	264	TIB L3i	layer 3, inwards
	21	336	TIB L4o	layer 4, outwards
	22	312	TIB L4i	layer 4, inwards
TOB	23	504	TOB L1So	layer 1, stereo, outwards
	24	504	TOB L1Ri	layer 1, $r\phi$, inwards
	25	576	TOB L2Ro	layer 2, $r\phi$, outwards
	26	576	TOB L2Si	layer 2, stereo, inwards
	27	324	TOB L3o	layer 3, outwards
	28	324	TOB L3i	layer 3, inwards
	29	360	TOB L4o	layer 4, outwards
	30	360	TOB L4i	layer 4, inwards
	31	396	TOB L5o	layer 5, outwards
	32	396	TOB L5i	layer 5, inwards
	33	444	TOB L6o	layer 6, outwards
	34	444	TOB L6i	layer 6, inwards

Table 4.3: Granularity for alignment precision estimate in TID and TEC. The separation criteria for sectors of a given subdetector are indicated by column 'Description', which is mainly based on the separation via layers or rings. In forward detectors, it is important, which side is used (minus, plus); in strip detectors for double-sided modules, which one is used ($r\phi$, stereo); in barrel detectors, whether the module's surface points in direction of the beamline, or away (inwards, outwards).

Subdetector	ID	# modules	Key	Description
TID	35	72	TIDm R1R	minus side, ring 1, $r\phi$
	36	72	TIDm R1S	minus side, ring 1, stereo
	37	72	TIDm R2R	minus side, ring 2, $r\phi$
	38	72	TIDm R2S	minus side, ring 2, stereo
	39	120	TIDm R3	minus side, ring 3
	40	72	TIDp R1R	plus side, ring 1, $r\phi$
	41	72	TIDp R1S	plus side, ring 1, stereo
	42	72	TIDp R2R	plus side, ring 2, $r\phi$
	43	72	TIDp R2S	plus side, ring 2, stereo
	44	120	TIDp R3	plus side, ring 3
TEC	45	72	TECm R1R	minus side, ring 1, $r\phi$
	46	72	TECm R1S	minus side, ring 1, stereo
	47	144	TECm R2R	minus side, ring 2, $r\phi$
	48	144	TECm R2S	minus side, ring 2, stereo
	49	320	TECm R3	minus side, ring 3
	50	504	TECm R4	minus side, ring 4
	51	360	TECm R5R	minus side, ring 5, $r\phi$
	52	360	TECm R5S	minus side, ring 5, stereo
	53	504	TECm R6	minus side, ring 6
	54	720	TECm R7	minus side, ring 7
	55	72	TECp R1R	plus side, ring 1, $r\phi$
	56	72	TECp R1S	plus side, ring 1, stereo
	57	144	TECp R2R	plus side, ring 2, $r\phi$
	58	144	TECp R2S	plus side, ring 2, stereo
	59	320	TECp R3	plus side, ring 3
	60	504	TECp R4	plus side, ring 4
	61	360	TECp R5R	plus side, ring 5, $r\phi$
	62	360	TECp R5S	plus side, ring 5, stereo
	63	504	TECp R6	plus side, ring 6
	64	720	TECp R7	plus side, ring 7

$(x|y)$ coordinate system. The selection on the global orientation does not effect an additional separation of the sectors in TOB layer 1 and 2. All $r\phi$-modules of TOB layer 1 point in the same direction, all stereo-modules point in the opposite direction. The same is valid for TOB layer 2. Overall the definition leads to 6 sectors in BPIX, 12 sectors in TIB, and 12 sectors in TOB.

The modules in FPIX have all the same resolutions. The modules of the sectors are separated by forward (plus side) and backward subdetector (minus side). They are further separated by layers, which are the discs with modules at constant longitudinal z-position. 4 sectors are defined in FPIX.

Also the modules for the sectors in TID and TEC need to be divided between plus and minus side. The wedge-shaped sensors have the same topology if they are placed at the same radial positions, which means in one of the up to seven rings. Thus modules are grouped by rings, 3 in TID and 7 in TEC. The rings which are equipped with double-sided modules are separated by $r\phi$- and stereo-modules. The separation adds up to 10 sectors in TID and 20 sectors in TEC.

4.7 Results

The measurement of the alignment precision with the method explained in this chapter is performed on about $250\,\mathrm{pb}^{-1}$ of 2011 data, and modelled with simulation. The modelling and the basic event selection are described in Appendix A.6. In order to minimise detector effects on the measurements, both in data and for deviations between data and simulation, isolated muons which have to fulfil the identification and isolation criteria as described in Chapter 3.5.3 are selected. Their kinematic range is restricted to $p_{\mathrm{T}} \in [25\,\mathrm{GeV}, 150\,\mathrm{GeV}]$ and $|\eta| < 2.5$. Furthermore, a more stringent track and hit selection is applied, in order to exclude badly described residuals; it is detailed in Appendix A.7. While the track parameter distributions show reasonable agreement, several hit parameter distributions show significant deviations.

Given the final event, track and hit selection and the setup of the method as described in this chapter, several sets of alignment precision parameters for different geometries are produced. Setting the nominal residual width for each defined sector individually from simulation with design geometry requires to run on the simulated samples only once. This is used as the reference for all geometries which are studied on real data. The alignment-precision estimation is done using 15 iterations, called iteration 0 to iteration 14. First, the geometry as used during the 2011 data taking, and as it is used for the prompt event reconstruction, is analysed. Second, it is compared to the improved alignment parameters as they are used for the reprocessing of the whole year's dataset. Finally, systematic studies about the sensitivity of the method to misalignment are performed. The figures showing the hit or track parameter distributions compare the simulation to the data before the iterations (where the alignment precision is set to 0), and after iteration 14 which reflects the final estimate.

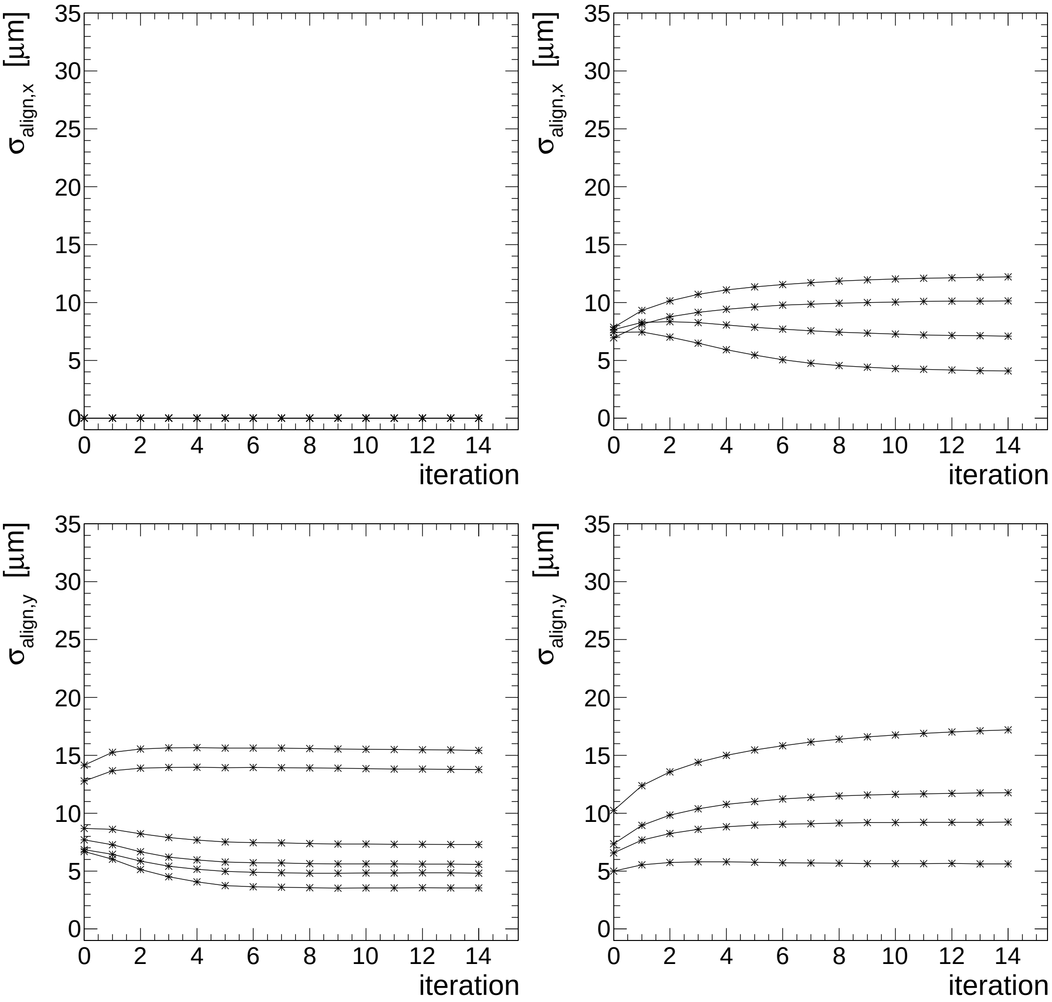

Figure 4.8: Alignment precision during iterations in pixel detector. Left: both coordinates in BPIX. Right: both coordinates in FPIX. Each line represents one sector.

4.7.1 Geometry of Prompt Reconstruction

The geometry as it was used during data taking and for the prompt reconstruction is identical for the whole year. Since the analysed data is composed from different periods spanning several IOVs, the observed time-dependent pixel movements are expected to show up in the alignment precision. Figure 4.8 shows the development of the estimated alignment precision during the iterations in the pixel detector, Figure 4.9 illustrates the same for the strip detector.

It is visible, that convergence is reached quickly in most sectors. The corrections in the last steps are clearly below 1 μm, which is negligible compared to the intrinsic resolution. The estimated values are all smaller than 15 μm, except for the outermost rings of both sides of TEC, where the result is close to 30 μm. In general, the alignment is already of good precision, which veri-

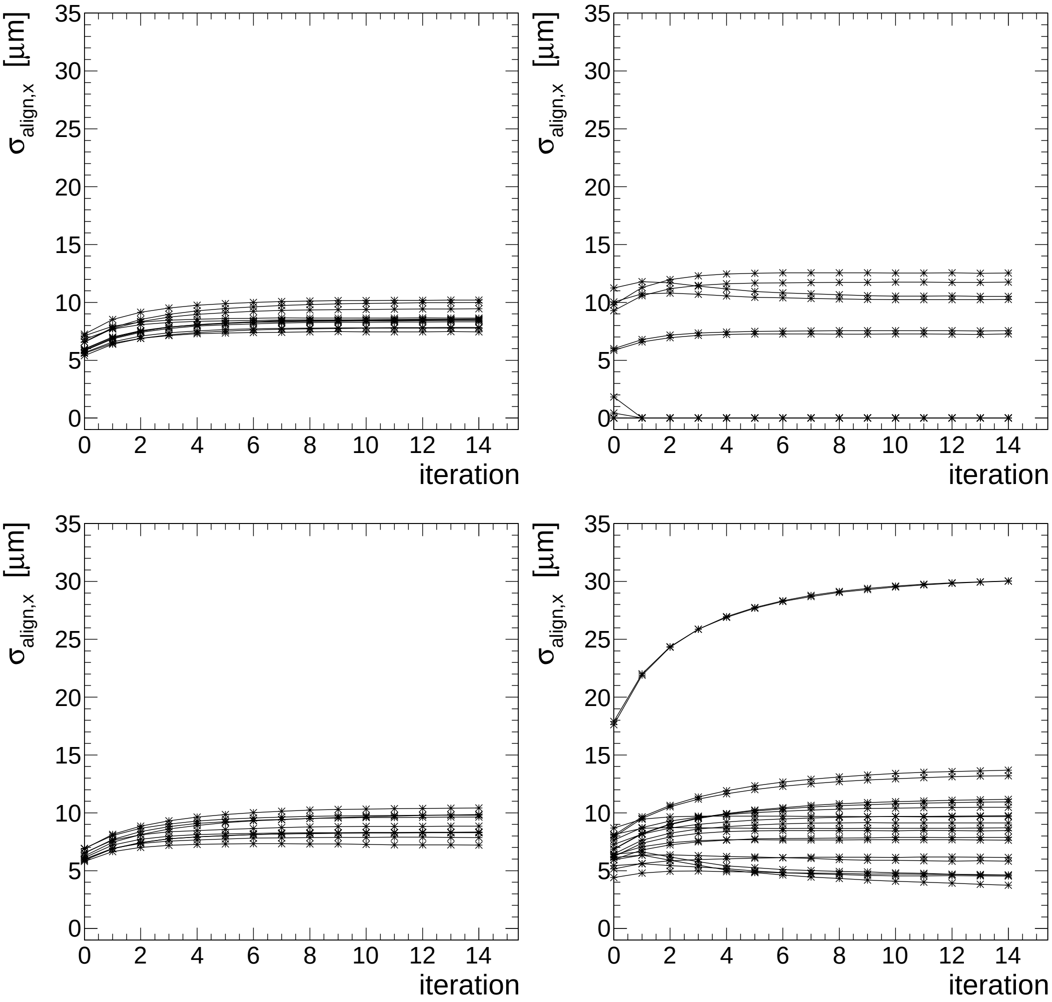

Figure 4.9: Alignment precision during iterations in strip detector, for TIB (top left), TOB (top right), TID (bottom left) and TEC (bottom right). Each line represents one sector.

fies the assumption that the geometry is good enough for online data taking throughout the whole year. However, there are some sectors, where the estimated squared correction would be negative, thus the alignment precision imaginary. As described, those sectors get assigned $\sigma_{\mathrm{align}} = 0\,\mu\mathrm{m}$. The effect shows up in all sectors of BPIX in the x-direction, where already in iteration 0 the values are imaginary, and in some sectors of TOB, beginning at iteration 0 or iteration 1. To understand this behaviour, a closer look at the residual distributions of the individual sectors is necessary.

Figure 4.10 shows important hit parameters for one of the problematic sectors of BPIX, while Figure 4.11 shows the same for a well described sector of TIB, further examples can be found in Appendix A.8.1. Although the track parameter distributions are well modelled and the number of selected tracks is similar for data (1336357 tracks in iteration 0) and simulation (1245913 tracks), the hit parameter distributions show significant differences, as already discussed. This leads to the fact, that the number of selected hits for each sector can deviate between data and simulation. Another effect is, that the values of the residual resolution can deviate—as a consequence the amount of hits within the defined intervals of the residual resolution show deviations, and the weights for the individual intervals in the alignment precision estimation differ. Due to the increase of the track parameter uncertainty during the iterations, some of the hits in data migrate to intervals with bigger values of the residual resolution, thus are analysed in different normalised residual distributions.

The main problem gets visible when looking at the residual distributions. The simulation does not describe the behaviour very well in the problematic sectors in BPIX and layers 1–4 in TOB, while the modelling in the other sectors is much better. The TOB sectors in layer 5 and 6 are better described than the other TOB sectors, it might be that this comes from the smaller strip pitch in these two outermost layers, compared to the other four. The example in BPIX shows, that even the absolute residuals can show a better behaviour in data than the simulation with perfect alignment, as the values are clearly more centred around 0. This is different for the well described sectors like for the one in TIB. The same effect can be seen for the normalised residual distributions, which are the basis for the method. The example in TIB illustrates also, that a good residual description is not necessary, the normalised residual distribution is obviously not Gaussian—the important point is that data and simulation agree, that the incorrect values with certain track and hit errors are used with the same fraction in data and simulation. An interesting observation is, that the mean values of the normalised residual distributions in the x-direction of BPIX are not centred around 0 in simulation. For the sectors spanning inwards pointing modules, it is shifted slightly to positive values, while for the outwards pointing modules they are shifted to negative values. Such an effect could be seen in data when the Lorentz angle calibration was imperfect. But in simulation with ideal conditions there is no obvious explanation for this behaviour. The data does not show this behaviour, the normalised residuals are all centred around 0 for the x-direction of BPIX.

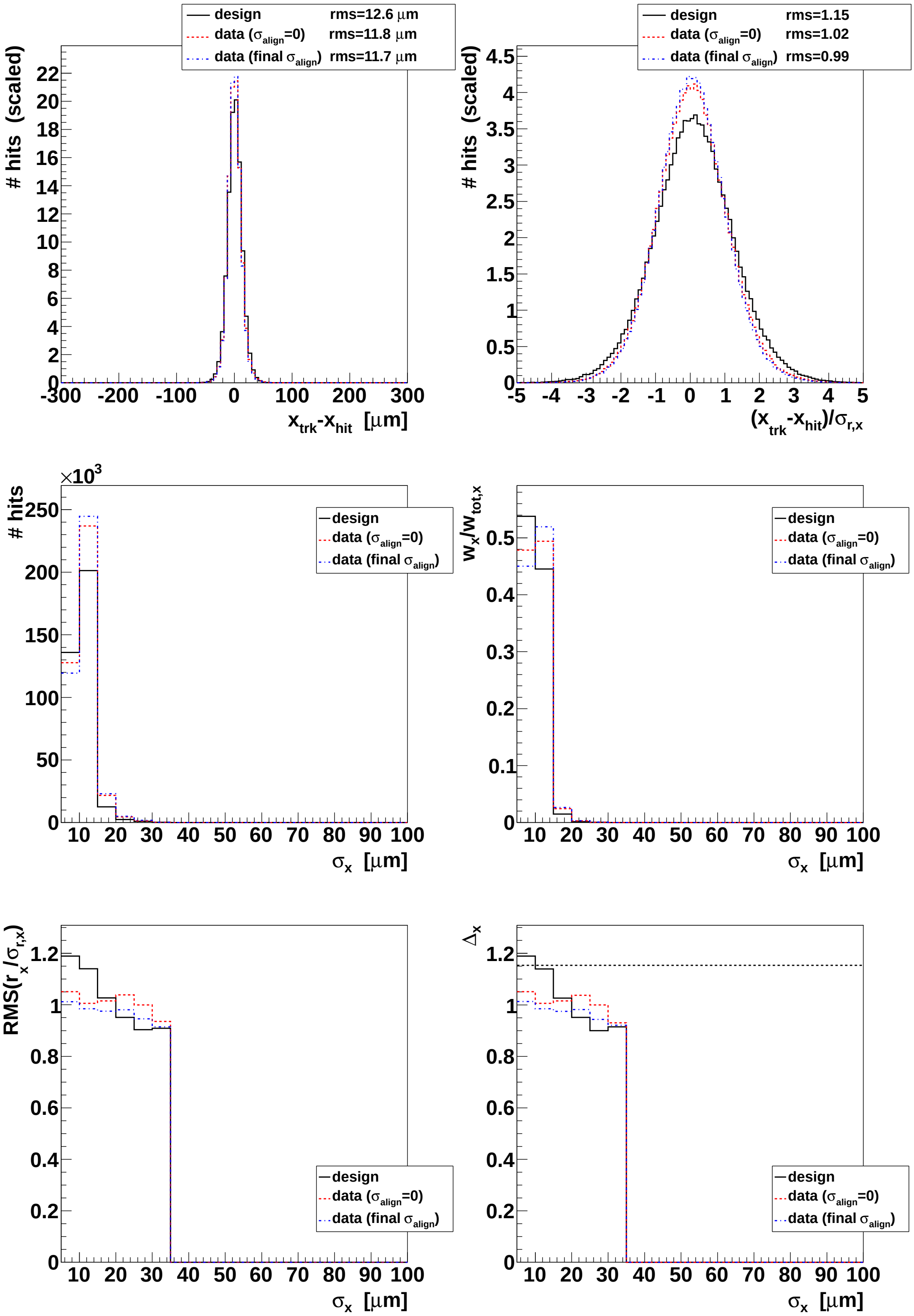

Figure 4.10: Figures for alignment-precision measurement in sector "BPIX L3i". Top: absolute (left) and normalised (right) residuals, scaled to their integral. Middle: number of hits (left) and corresponding weight (right) per interval of residual resolution. Bottom: r.m.s. value (left) and residual width (right) per interval of residual resolution.

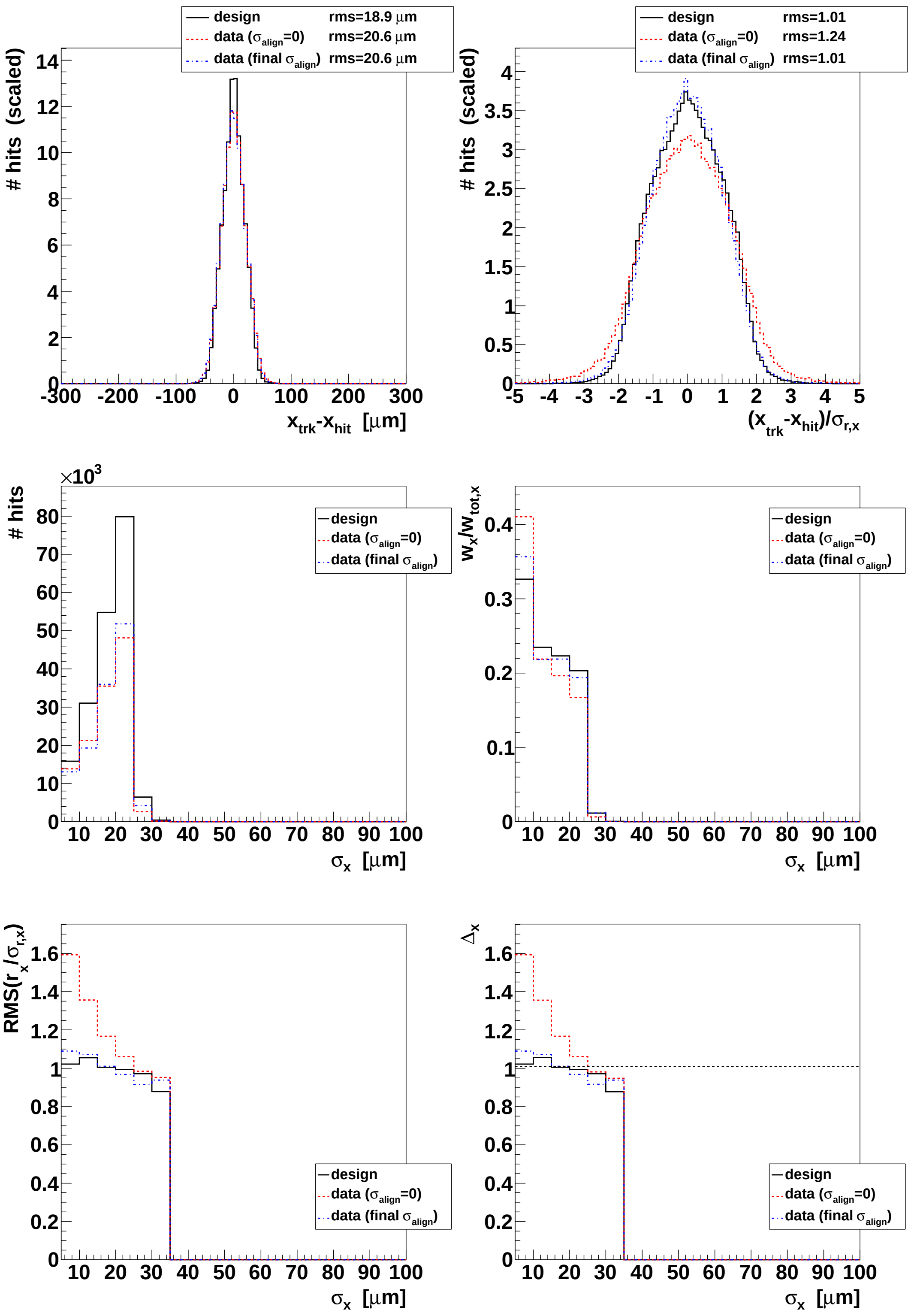

Figure 4.11: Figures for alignment-precision measurement in sector "TIB L1Ro". Top: absolute (left) and normalised (right) residuals, scaled to their integral. Middle: number of hits (left) and corresponding weight (right) per interval of residual resolution. Bottom: r.m.s. value (left) and residual width (right) per interval of residual resolution.

Comparing the behaviour of the estimated residual width Δ from a Gaussian fit to the RMS value indicates only slight deviations. This is due to the outlier rejection of the refit, omitting big values of the normalised residuals. While the BPIX example shows that the nominal residual width as gained from simulation, illustrated by the constant dashed line, is clearly too big, the TIB example shows perfectly the principle of the method. In the bins with small values of the residual resolution, the misalignment is clearly visible before the iterations. Using the estimated alignment precision, the distribution agrees with the simulated one, although the distribution is neither in simulation nor in data flat at the end. The estimated nominal residual width however is close to 1, as it should be with perfect error estimates.

The impact of the estimated alignment precision on the track reconstruction is visualised for important quantities in Figure 4.12. The distributions of the central values of the track parameters stay mainly identical, since the estimated values of the alignment precision are small in general, and the small differences for different sectors do not have a big influence on the track reconstruction. The uncertainties of the track parameters however show significant changes to bigger values; data and simulation show similar shapes, but also discrepancies. A very important quantity is the transverse impact parameter with respect to the beamspot $d_{0,\mathrm{BS}}$, which is the basis for b-tagging based on lifetime signatures. The uncertainty increases only slightly with the finite values for the alignment precision, since the uncertainty is dominated by the uncertainty of the beamspot. And the beamspot in simulation has a different size and position as the real beamspot.

The three parameters in Figure 4.13 show clearly the improvement when assigning values of the correct order to the alignment precision. Before the iterations, the χ^2-distribution indicates clearly bad fits, reflected by big values; the probability of the track fits also shows a big fraction of bad track fits in the peak close to 0; and the significance of the impact parameter is too wide. With the final values of the alignment precision these distributions change in the desired way. The χ^2-distribution peaks below 1, the mean value is close to 1, but slightly too small. The peak in the probability distribution gets significantly reduced, the mean value gets closer to 0.5, but slightly too big, and it is clearly not flat. The impact parameter significance distribution gets more narrow closer to 1, but is still bigger than 1 and than in the simulation. In general, it is visible that the agreement in the track parameters between data and simulation gets better, but due to the deviations in the modelling, differences remain.

4.7.2 Comparison to Geometry of Reprocessing

As already described, the geometry which is used for the reprocessing of the whole 2011 dataset is much improved compared to the one of the prompt reconstruction—on one hand the alignment parameters are estimated directly on this dataset, on the other hand the introduction of different IOVs reflecting

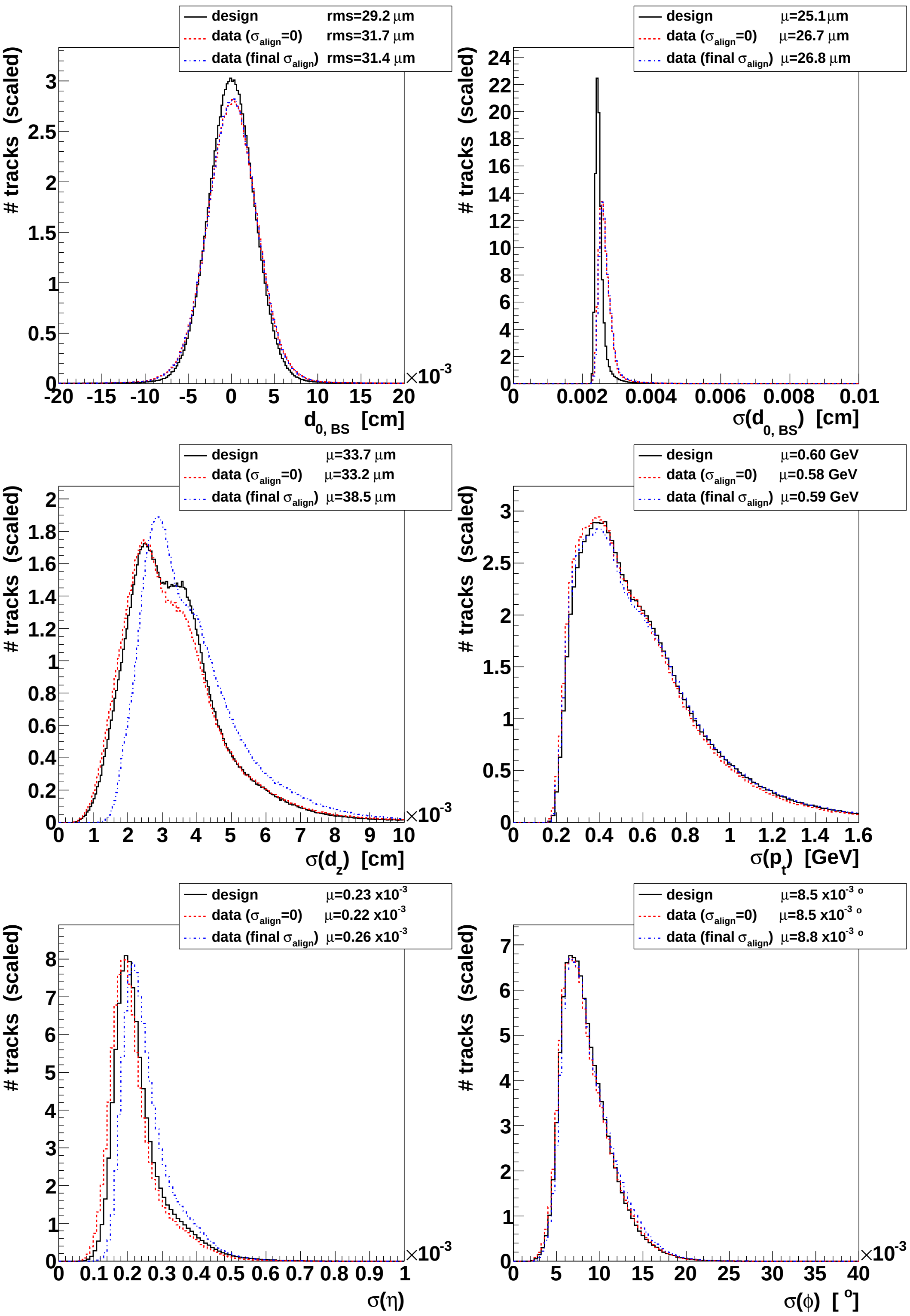

Figure 4.12: Influence of alignment precision for prompt geometry on track impact parameter with respect to the beamspot $d_{0,\mathrm{BS}}$ (top left), and on uncertainties of track parameters. All distributions are scaled to their integral.

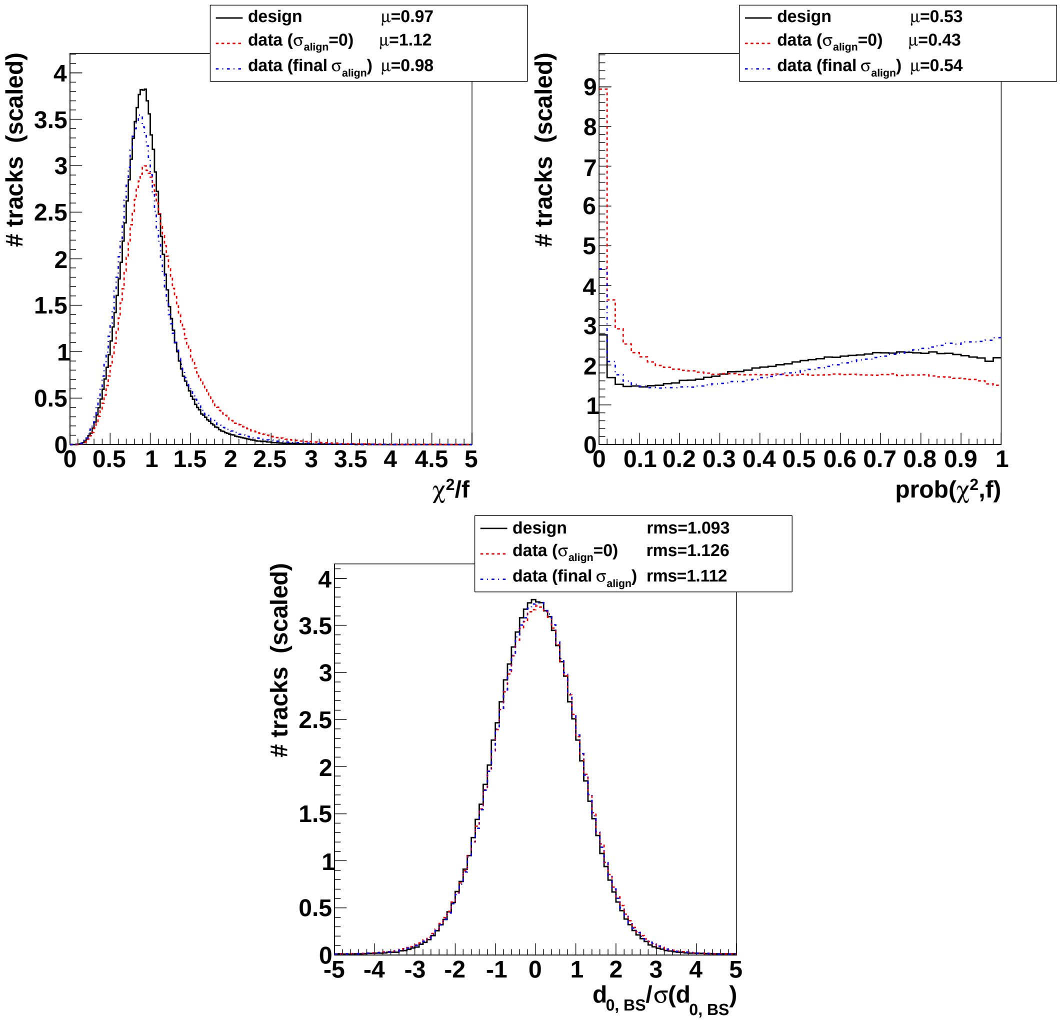

Figure 4.13: Track quantities sensitive to alignment precision for prompt geometry: normalised χ^2 (top left), track fit probability (top right), and significance of impact parameter with respect to the beamspot. All distributions are scaled to their integral.

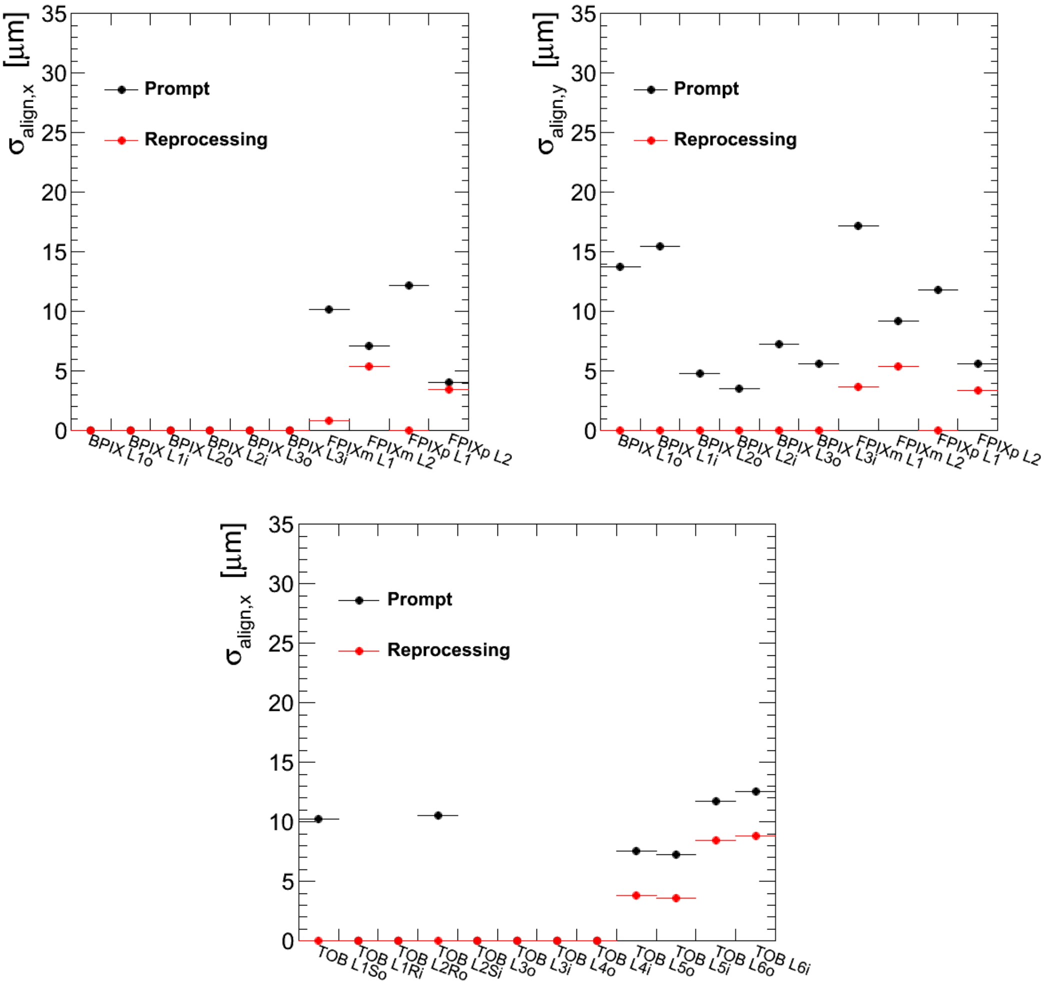

Figure 4.14: Alignment-precision results for pixel (top left: x-coordinate, top right: y-coordinate) and TOB (bottom) sectors, shown for prompt and reprocessing geometry.

the pixel movements and the assignment of finite values to the kinks and bows reflecting the module deformations describe the geometry more accurately. The results for all sectors are compared in Figure 4.14 and Figure 4.15 for both geometries. However, the dataset in use is reconstructed with the prompt geometry and all other conditions are also like in the prompt reconstruction. For the analysis of the geometry of the reprocessing, the geometry is changed in the refit only, and all other conditions are unchanged.

First, it is visible that the new geometry is clearly an improvement, all sectors show smaller values of the estimated alignment precision. Second, the biggest change is in the y-direction in BPIX; now also these values end up at 0. It is similar in FPIX. Most probably this is due to the pixel shifts, which are accounted for in the new geometry. Third, the behaviour is similar for both sides in the two-piece forward detectors, the patterns agree—and the behaviour during the iterations is almost identical. The same is also valid for the inwards

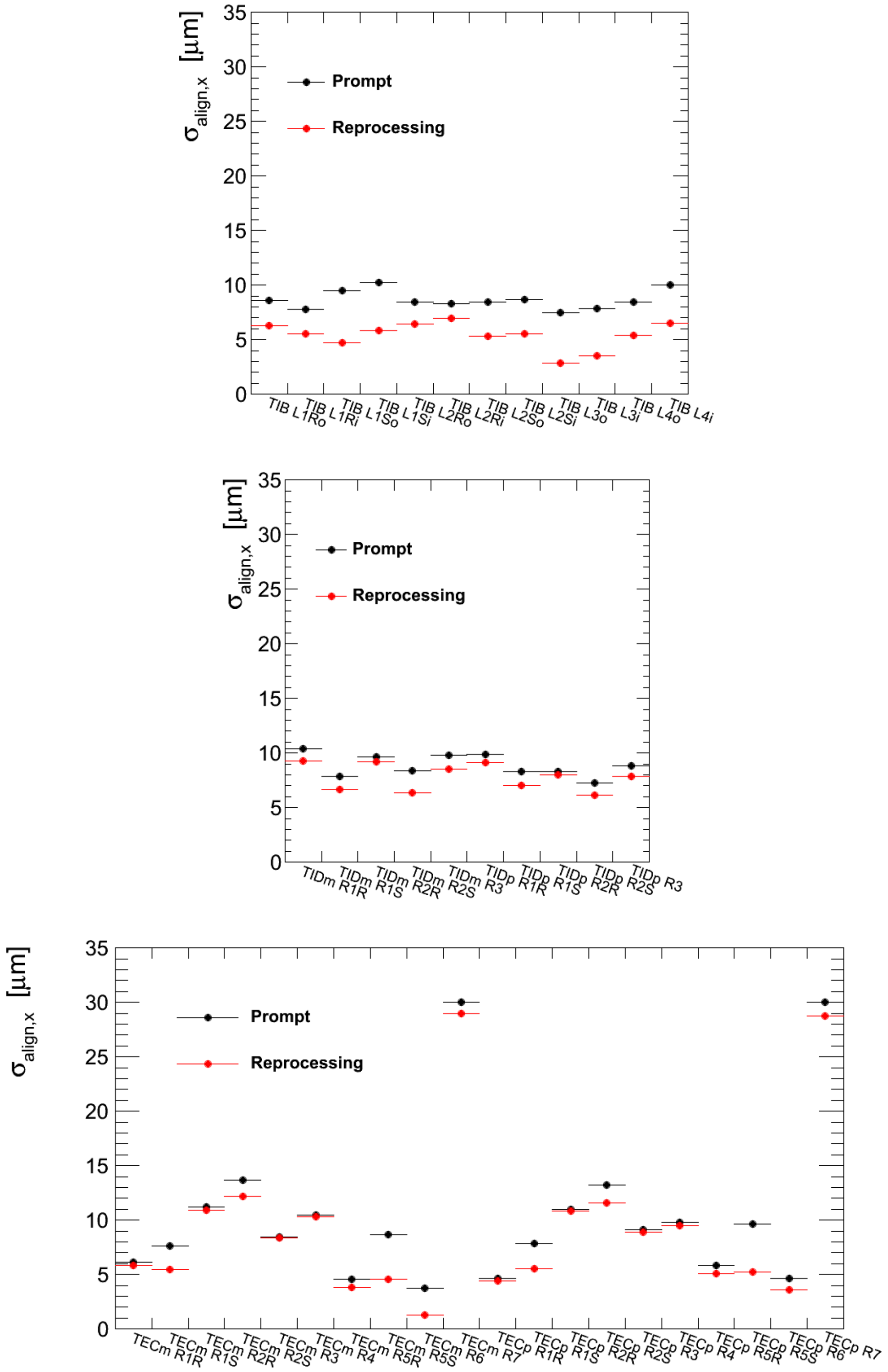

Figure 4.15: Alignment-precision results for TIB (top), TID (middle), and TEC (bottom) sectors, shown for prompt and reprocessing geometry.

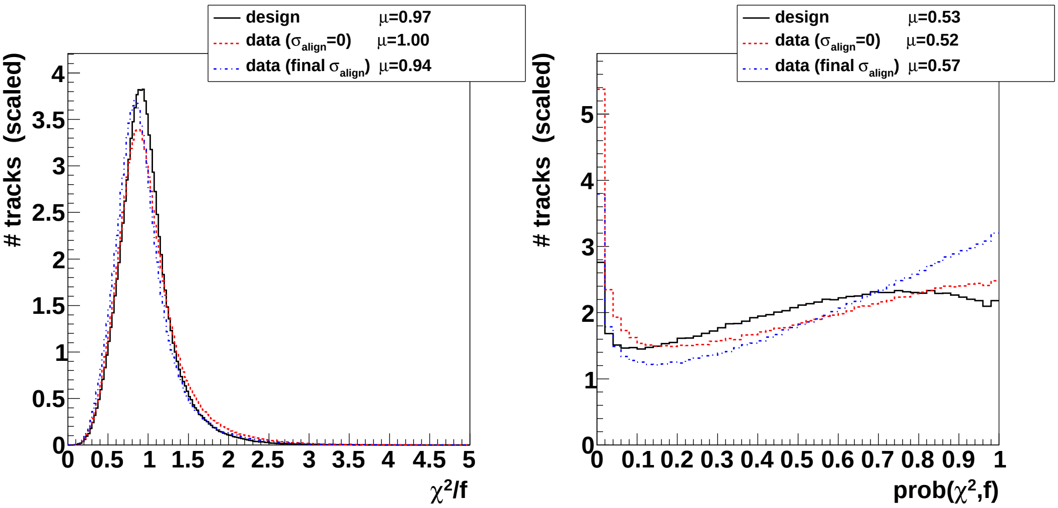

Figure 4.16: Track quantities sensitive to alignment precision for reprocessing geometry: normalised χ^2 (left), and track fit probability (right). All distributions are scaled to their integral.

and outwards pointing sublayers of a layer in the barrel detectors, deviations are small, even throughout the iterations. Finally, all values are below $10\,\mu$m, except some sectors in TEC. Especially the outermost TEC rings on both sides stay with big values around $30\,\mu$m.

The influence on the track parameter distributions gets less significant, since the small alignment precision values lead only to small changes. However, many sectors do have imaginary values which are set to 0 and have smaller residual widths than in simulation, while the other sectors get values assigned to fit the simulation. This leads to the fact, that the final results seem to be too good, the errors are overestimated in general, as can be seen in Figure 4.16.

4.7.3 Systematic Studies introducing Misalignments

In order to understand better the behaviour in the sectors with imaginary values and to set upper limits for the remaining misalignment, systematic studies are performed. The studies are based on the misalignment tools of CMS—additional misalignment can be added to a given geometry. The basis is the geometry of the reprocessing. Since the method seems to work well in TIB, TID and TEC, these subdetectors stay untouched. For BPIX, FPIX and TOB, additional misalignment is introduced in several steps to see how the results change. The misalignment is introduced only in the sensitive coordinates, i.e. x- and y-direction in the pixel detector, and the x-direction in TOB. The individual module positions of these subdetectors are shifted in these coordinates, using a Gaussian smearing of increasing standard deviations with values $5\,\mu$m, $10\,\mu$m, $15\,\mu$m and finally $20\,\mu$m. Assuming that the original remaining misalignment can also be described with a Gaussian of a given width,

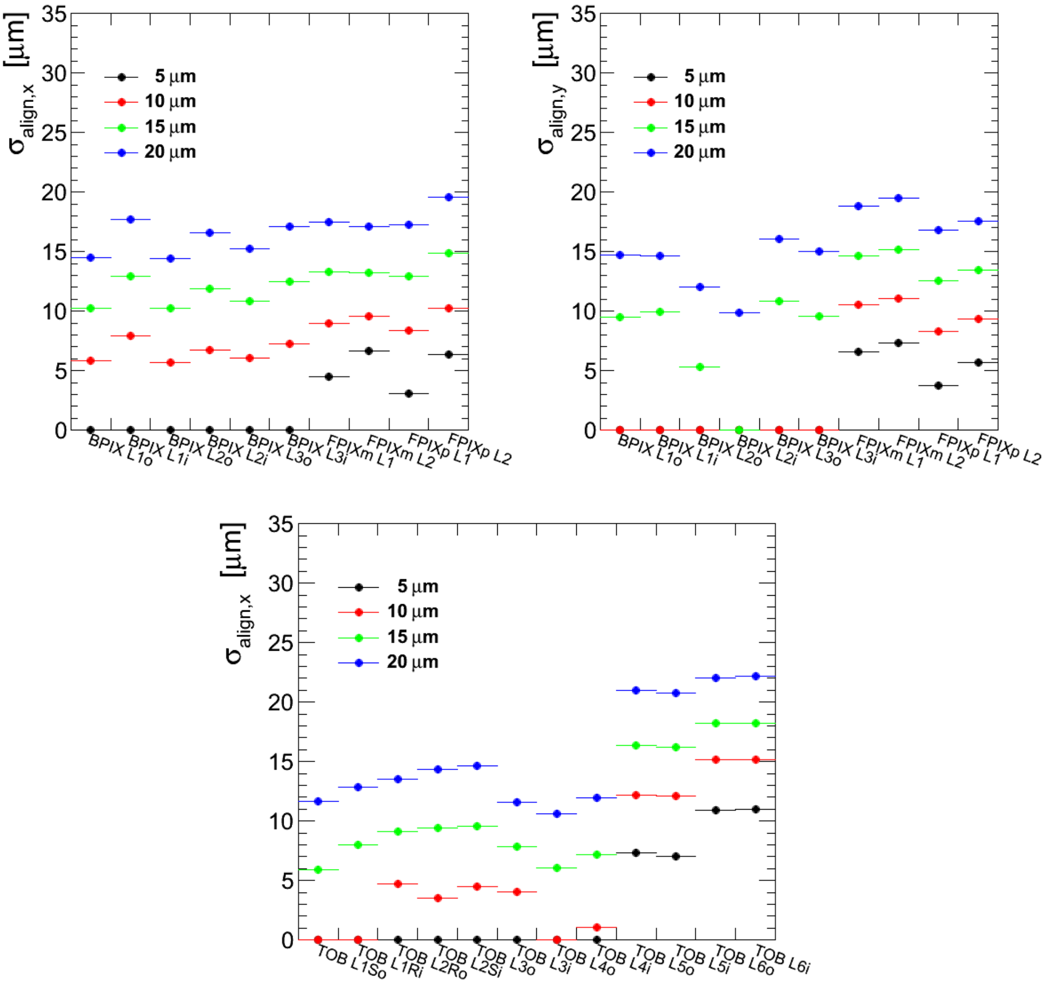

Figure 4.17: Alignment-precision results in systematic studies for pixel (top left: x-coordinate, top right: y-coordinate) and TOB (bottom) sectors. Misalignment of increasing size is added to the shown sectors, others stay unchanged.

the width of the squared misalignment is the sum of the squared original misalignment and the quadratic additionally introduced misalignment.

The results of the alignment precision estimates are given in Figure 4.17. It can be seen that the outermost TOB layers, layer 5 and 6, show the desired behaviour—the measured original misalignment gets overlaid by the introduced one. Also in FPIX the situation is well under control in both coordinates, the introduced misalignment is mainly reflected in the results, although the absolute values are mostly slightly too small. In these sectors, misalignments of 5 μm can be measured. In the x-direction of BPIX, a misalignment of 5 μm is not measurable, but 10 μm clearly is; as a consequence all values are slightly too small. In TOB, some but not all sectors show finite values for 10 μm—with 15 μm additional misalignment all sectors have finite values. Analogous to the other cases, the values are always too small, but the difference gets more pronounced. The worst case is the y-direction of BPIX. While $10\,\mu$m are not measurable at all, $15\,\mu$m are measurable in most sectors and show directly values of about $10\,\mu$m. But in layer 2, and especially for the inwards pointing modules, the sensitivity is even worse and only the case with $20\,\mu$m additional misalignment gives finite values. An interesting observation is, that already with $10\,\mu$m four of the six BPIX sectors have finite starting values after iteration 0 of up to $7\,\mu$m, but at latest after iteration 2 they end up at imaginary values. This might be an indication, that the iterative process is not optimal for the y-direction in BPIX, and that perhaps a smaller damping factor should be used in Formula 4.16.

In Figure 4.18 the influence of the introduced misalignment on the sectors which stay unchanged is shown. The results are rather stable, the differences are below $1\,\mu$m, although e.g. the tracks crossing TIB also have hits in the misaligned subdetectors, starting mainly in BPIX, and ending in TOB. This shows, that the misalignment is really measured at its origin, neighbouring layers are not sensitive. The same could also be verified in studies based on simulation purely, where introduced misalignment was measured exactly in the misaligned sectors and only with small impact on the neighbouring sectors.

Given these artificially large misalignments, the usefulness of the alignment precision can be visualised perfectly. The results for the biggest misalignment scenario show clearly how the track parameters are influenced by the alignment precision, illustrated in Figure 4.19. The χ^2-distribution and the probability distribution of the track fits show significant misalignment before the iterations, and are almost identical to the simulation after the iterations. The track parameter errors show a significant increase. The influence on the central values of the track parameters is still small for most quantities. But for the given distribution of the impact parameter with respect to the beamspot it is obvious, that also the central values get much better due to the correct weights of the individual hits of the track—hit and track parameters are improved by more correct error assignments. And also the significance of the impact parameter shows clearly, that unaccounted misalignment leads to bad results and influences especially the b-tagging—of course, the same is also valid for wrong error assignments, like too big values of the alignment precision.

4.8 Conclusions

Summarising, the alignment precision achieved with the Millepede II algorithm is very good and significantly below the intrinsic hit resolution of the silicon sensors. Taking the estimated alignment precision into account improves the track reconstruction and thus all object reconstructions which depend on it, like the vertexing or the estimation of the beamspot. During prompt reconstruction the effect is much more pronounced, since time dependencies and possible other changes – e.g. updates of the calibration conditions – are not reflected in the geometry. The detailed alignment record as it is produced

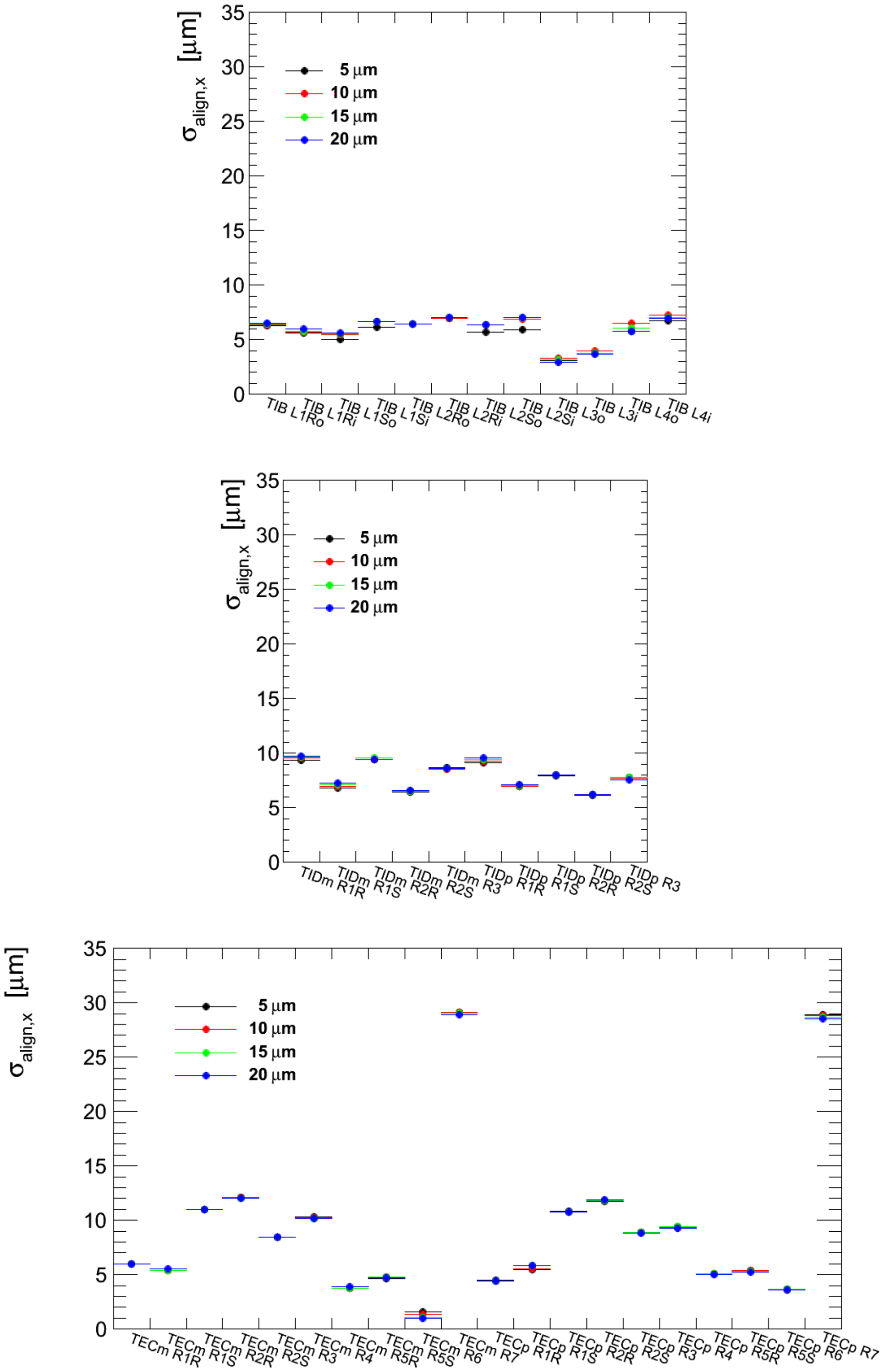

Figure 4.18: Alignment-precision results in systematic studies for TIB (top), TID (middle), and TEC (bottom) sectors. Misalignment of increasing size is added to the other sectors not shown here, the shown sectors stay unchanged.

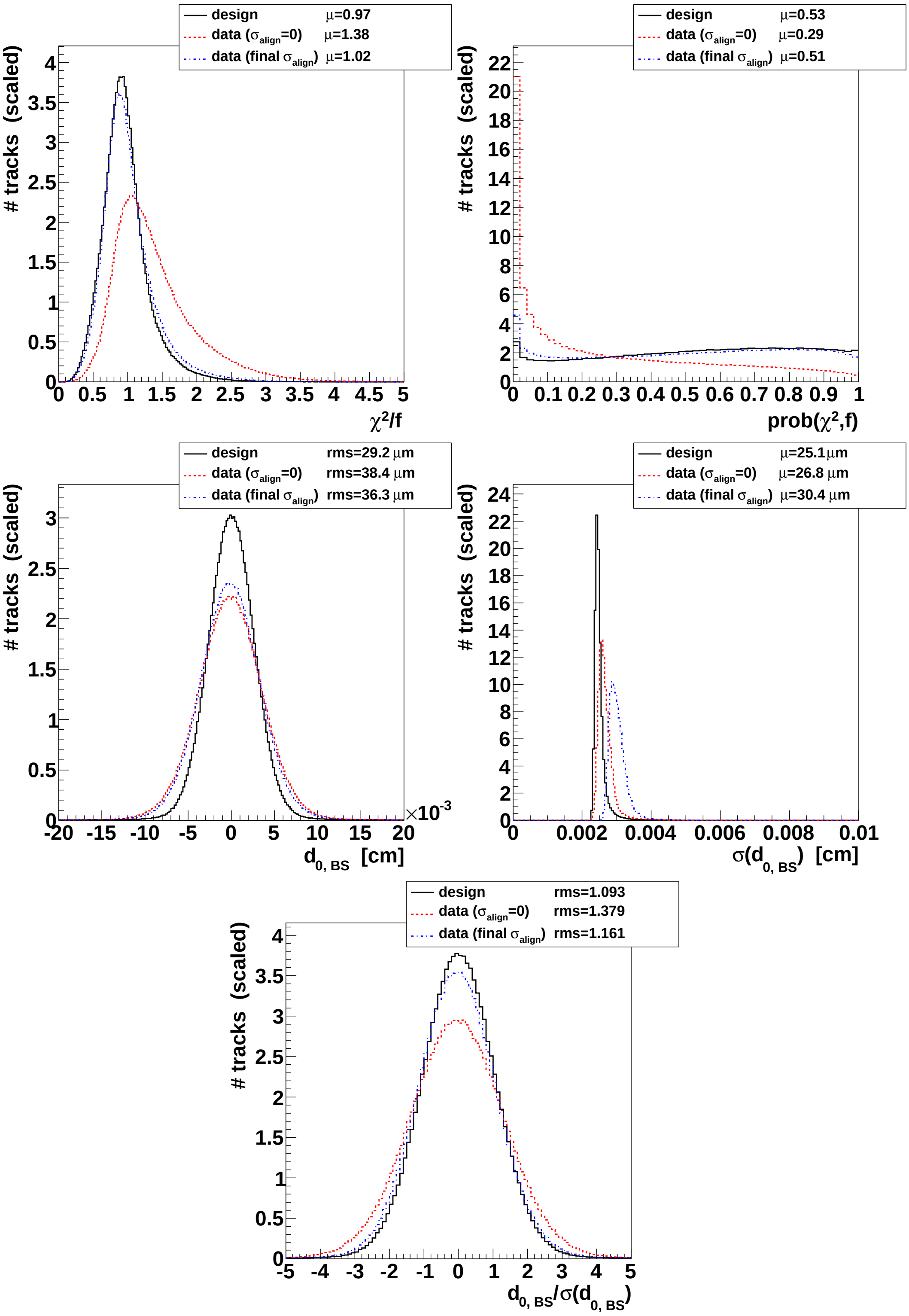

Figure 4.19: Influence of alignment precision on track quantities for the biggest misalignment scenario (20 μm): normalised χ^2 (top left) and track fit probability (top right), as well as central value (middle left) and uncertainty (middle right) and significance (bottom) of impact parameter with respect to the beamspot. All distributions are scaled to their integral.

for the reprocessing takes these effects into account, the influence from the alignment precision is still visible but small.

The described method for the alignment-precision estimation can detect and quantify big misalignments as it is shown in the systematic studies. In some detector regions the method works well since the simulation describes the data adequately, and precise estimates are possible. In some other regions however, for small remaining misalignments like in the geometry of the reprocessing, the method is limited by systematic effects which cannot be eliminated within the alignment framework.

The main problem is, that the position and error estimates of the hits do not describe well the individual hit measurements, but only their parameters on average. An improvement of the CPE would be necessary. The second big problem is the disagreement between data and simulation on hit level—cluster sizes, shapes and further parameters do not agree, some distributions show clear differences. Thus the estimated hit parameters are also differing. The ansatz to handle the deficits from the CPE is to use the simulation as baseline, taking the nominal residual width from simulation, which leads to excellent results is specific detector regions. But due to the disagreement in the modelling of hits, the nominal residual width also does not reflect the perfect target for the residual width corresponding to perfect alignment as it would be expected in data, leading to an indetectability of small remaining misalignments in some detector regions, and in general to underestimation of the alignment precision. The track and hit error estimates are in some regions in general too big, which would require imaginary values of the alignment precision for compensation.

Chapter 5

Cross-Section Ratio of Top-Pair and Z^0-Boson Production

The uncertainty of the integrated luminosity constitutes an irreducible experimental uncertainty to cross section measurements. However, in measurements of ratios of cross sections using the same datasets, the integrated luminosities, as well as other common systematic errors cancel out, leading to significantly reduced systematic errors. The measurement of the top-pair-to-Z^0 cross section ratio thus offers tests of the Standard Model with improved accuracy. Furthermore it gives the possibility to extract the top-pair cross section with improved accuracy from the well-known Z^0 cross section predictions of the Standard Model. This was successfully applied earlier by the CDF collaboration [135].

Alternatively, each cross section can be normalised to the ratio of the theoretical and the measured cross section for Z^0 production on the same dataset. This ratio is a correction factor that substitutes the use of the integrated luminosity. Thus it allows the normalisation of cross-section measurements, performed on the same amount of data, to the Z^0 production cross section. Depending on the given estimate on the uncertainty of the luminosity, this normalisation can improve the accuracy.

This chapter describes the measurement of the ratio of cross sections of top-pair production ($t\bar{t}$) and Z^0-boson production on the full 2010 dataset. The processes are explained in Chapter 2.3.1 and Chapter 2.3.2. The measurement of the $t\bar{t}$-to-Z^0 cross section ratio requires a study of top-pair production, called "top analysis" in the following, and a study of Z^0 production, referred to as "Z^0 analysis". Both, the top analysis and the Z^0 analysis, are performed on the same dataset, using the dimuon final states and applying the same triggers and muon identification criteria. Thus, the luminosity cancels completely, and the muon trigger and reconstruction efficiencies cancel partly, depending on the differences in the event topology. A more technical description of the presented analysis can be found elsewhere [136]. The results of the Z^0 analysis as presented in this work were used in the publication [137]. A similar later analysis, using the technique on the 2011 dataset, can be found elsewhere [53].

The measurement was performed with a certain luminosity estimate. However, the estimate was updated with a more advanced technique (see Chapter 3.6) – giving smaller uncertainties and a small change of the central value – in time to adjust the results. The descriptions before the Chapter 5.4 “Results” are based on the primary estimate. This results chapter is updated to the ultimate values including a discussion about the influence of the update on the results.

Although the analysis aims for the ratio of cross sections, the cross sections of both processes are also calculated, allowing comparisons to other measurements and theory. The top analysis, presented here, is identical to the measurement described in full detail in [138] and [5], thus only the relevant points are mentioned. In contrast, the Z^0 analysis presented here is somewhat different from existing and official CMS results of the Z^0 cross section, as it is optimised for the determination of the $\mathrm{t\bar{t}}$-to-Z^0 cross section ratio.

At the time this measurement was performed, the published CMS Z^0 cross section results, referred to in the following as VBTF (vector boson task force), were based on early data with an integrated luminosity of about $\int \mathcal{L}\mathrm{dt} = 2.9\,\mathrm{pb}^{-1}$ [139], while being superseded by an update using the full 2010 dataset [140][141]. In order to justify the correctness of the Z^0 analysis with setups optimised for $\mathrm{t\bar{t}}$ measurements, results are compared to VBTF, and methodic differences with respect to VBTF are emphasised throughout the chapter. Furthermore, systematic uncertainties as estimated by VBTF are used whenever possible.

5.1 Data and Simulated Samples

The signal process in the top analysis is the production of $\mathrm{t\bar{t}}$ quark pairs followed by top quark decays $\mathrm{t} \rightarrow \mathrm{W}^+\mathrm{b}$ and $\mathrm{\bar{t}} \rightarrow \mathrm{W}^-\mathrm{\bar{b}}$, and subsequent leptonic $\mathrm{W}^\pm$ boson decays into muons. Also decays via intermediate τ leptons with subsequent muonic decay are considered as signal, since they cannot be separated well. The signal process in the Z^0 analysis is the production of a Z^0/γ^* and its decay into muons—only the direct muonic decay is used. Thus the same muon triggers can be used in both analyses. Data samples collected on single muon triggers during the 2010 runs are used to select signal dimuon events, spanning the run range 135821–149294. The events have to be certified to have good quality (see Chapter 3.2.3), and correspond to an integrated luminosity of $36.1\,\mathrm{pb}^{-1}$ with an uncertainty of $11\,\%$. The advantage of identical input samples for both analyses is that the uncertainty on the integrated luminosity cancels completely in the ratio measurement.

The signal process of the top analysis is a background process for the Z^0 analysis and vice versa. Further backgrounds are common for both analyses. Hence both analyses use the same simulated data samples, which minimises the systematic uncertainties arising from simulation. These samples comprise the two signal and the relevant background processes. The simulated background

Table 5.1: Summary of simulated data samples used in this analysis, together with the cross sections assigned to the processes. The cross sections of $W \to l\nu$ and $Z^0/\gamma^* \to ll$ samples are in NNLO, the QCD sample is LO, the others are NLO. The POWHEG sample does not need to be normalised, since it is used only in kinematic acceptance studies on generator-level.

Sample	cross section [pb]
$t\bar{t}$	157.5
tW	10.6
$WW \to ll\nu\nu$	4.51
$WZ^0 \to lll\nu$	0.61
Z^0Z^0	7.4
$W \to \mu\nu_\mu$	10438
$W \to \tau\nu_\tau$	10438
$Z^0/\gamma^* \to \mu^+\mu^-$ ($M_{Z^0/\gamma^*} > 10\,\text{GeV}$)	5123
$Z^0/\gamma^* \to \tau^+\tau^-$ ($M_{Z^0/\gamma^*} > 10\,\text{GeV}$)	5123
QCD (μ enriched, $p_T(\mu) > 15\,\text{GeV}$)	84679
$Z^0/\gamma^* \to \mu^+\mu^-$ ($M_{Z^0/\gamma^*} > 20\,\text{GeV}$) – POWHEG sample	(1666)

contributions stem from Z^0/γ^*, tW, W+jets and dibosons (W^+W^-, $W^\pm Z^0$ and Z^0Z^0). For the simulation of the multijet background (referred to as QCD) a muon enriched sample ($p_T(\mu) > 15\,\text{GeV}$) is used—at least one muon arises from the semileptonic decay of b or c quarks. The $t\bar{t}$ and the tW and Drell–Yan (generated Z^0 mass $> 50\,\text{GeV}$) samples are generated with MadGraph and interfaced with PYTHIA (see Chapter 3.4.2). Additional Drell–Yan samples generated with PYTHIA are used to cover the low dilepton invariant mass range ($10\,\text{GeV} < M_{Z^0} < 50\,\text{GeV}$). The diboson samples are produced with PYTHIA, as well as the QCD sample. For the Z^0 analysis an additional Drell–Yan sample is regarded, and used for acceptance corrections. It is an NLO simulation produced with POWHEG and interfaced with PYTHIA; the generated boson mass is constrained to $M_{Z^0} > 20\,\text{GeV}$.

For comparisons between data and simulation and for those background estimates which are based on simulation only the simulated samples are scaled in order to match the luminosity of the data. The cross sections used for these samples are given in [142], and are shown in Table 5.1. One significant difference between data and simulation is the fact, that the simulated samples were generated without pileup while in the data there are about 2.2 collisions per event. This influences the $\not{E}_T$ distribution—especially Z^0 events without natural $\not{E}_T$ show an increased $\not{E}_T$ when adding pileup. So the Z^0 background estimate for the $t\bar{t}$ analysis is scaled to experimental measurements.

VBTF uses samples which are generated with POWHEG for the signal process and all background processes with single vectorboson production, and for systematic studies also samples generated with PYTHIA. All other background samples are generated with PYTHIA.

5.2 Event Selection

Both analyses are based on the same muon triggers. Also the selections based on muons are identical, as described in this section. The benefit is that several systematic uncertainties and corrections arising from muons cancel in the ratio measurement.

In a first step, events for which a proton-proton collision occurred are selected with the following criteria. Processes like interactions of a proton with the remaining gas in the beam pipe are rejected by selecting a significant fraction of high-purity tracks with respect to the total number of tracks ($> 25\%$) if the event has at least 10 tracks. In addition, at least one primary vertex (see Chapter 3.5.1) is required. Besides, events with significant noise in the hadronic calorimeters are also removed.

Table 5.2: Single muon triggers used to select data events for all run ranges certified as good for physics analyses.

Run range	Trigger threshold	Integrated luminosity [pb]
136035–145000	$p_{\mathrm{T}} > 9\,\mathrm{GeV}$	3.2
145000–147120	$p_{\mathrm{T}} > 11\,\mathrm{GeV}$	5.1
147120–149294	$p_{\mathrm{T}} > 15\,\mathrm{GeV}$	27.9

The trigger configuration during the 2010 runs evolved with the increasing instantaneous luminosity. As a result, a run-dependent trigger selection is applied to the data. In this analysis, only events selected by the single muon triggers are considered. The list of the used triggers, based on increasing p_{T} thresholds $(9, 11, 15\,\mathrm{GeV})$, is shown in Table 5.2, together with the run range and the corresponding integrated luminosity. In the simulated samples, events are selected according to the trigger with $p_{\mathrm{T}} > 9\,\mathrm{GeV}$. Deviations due to the different trigger are compensated in the calculations, estimating the trigger efficiency for each of them and scaling the simulation to match the average on data [5].

5.2.1 $\mathrm{t\bar{t}}$ Selection

The $\mathrm{t\bar{t}}$ signal in the dimuon final state presents a characteristic signature, which consists of two isolated muons with unlike charge and high transverse momentum, large missing transverse momentum $\not{E}_{\mathrm{T}}$ due to the neutrinos from the W boson decays, and two energetic b jets from the t and $\bar{\mathrm{t}}$ quark decays. The analysis uses a unique set of requirements to disentangle signal from background, exploiting the topology of the reconstructed objects. This event selection is applied both to the data and simulation samples and corresponds to the reference selection described in [142]. A summary is given in the following.

Muons, jets and $\not{E}_{\mathrm{T}}$ are identified as described in Chapter 3.5, where also the isolation criterion for muons can be found. The muons are required to fulfil

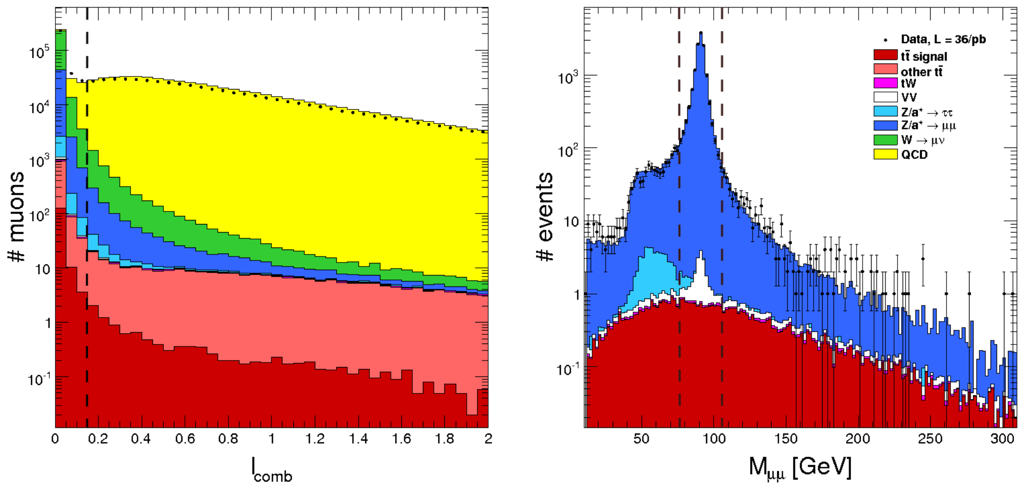

Figure 5.1: Muon isolation (left) and dimuon mass (right) distributions. The isolation is shown for all muons fulfilling the identification criteria and kinematical selection; the isolation is selected as $I_{\text{comb}} < 0.15$. The mass is shown for the full dimuon selection excluding the separative mass cut for both analyses; the Z^0 analysis selects $76\,\text{GeV} < M_{\mu^+\mu^-} < 106\,\text{GeV}$, the top analysis vetos this Z^0 window.

the phase space selections $p_T > 20\,\text{GeV}$ and $|\eta| < 2.4$. The momentum is well above the trigger thresholds, minimising effects from these thresholds. The pseudorapidity corresponds to the coverage of the muon system. The muon isolation criterion strongly suppresses the QCD background, as can be seen in Figure 5.1. These selected muons are the basis for the dimuon selection. However in the cutflow presented later, the isolation is applied at a later step during the dimuon selection, in order to check the correctness of the modelling for samples with less than two isolated muons (QCD, W, non-signal $t\bar{t}$).

The dimuon selection is based on the requirement of at least two selected muons. A dimuon pair is built using the two highest-p_T muons. They need to be oppositely-charged. Both muons are required to be associated to the same primary vertex, i.e. their longitudinal distance to a common vertex need to be smaller than 1 cm each. A further selection is applied to ensure a good trigger efficiency: events should have at least one muon in the fiducial region of the trigger ($|\eta| < 2.1$). Events with a dimuon mass below 12 GeV are excluded to reject low-mass Drell–Yan events and muons from low-mass resonances. Since the fake rate of these well identified and isolated muons is very small, all contributions without two isolated muons in the final state are almost completely deselected. All criteria mentioned so far are also applied to the Z^0 analysis, then both analyses are split (see Figure 5.1). In order to reduce the contribution from Drell–Yan background, events with dimuon invariant mass compatible with the Z^0-boson mass are rejected by applying a veto on events for which $76\,\text{GeV} < M_{\mu^+\mu^-} < 106\,\text{GeV}$. Instead, these events are used as signal in the Z^0 analysis.

Table 5.3: Number of expected signal and background events in the $t\bar{t}$ analysis, compared to the event yields in the $36.1\,\mathrm{pb}^{-1}$ data, after each selection step. Since the QCD sample used in the analysis is already preselected on generator level for muons with $p_{\mathrm{T}} > 15$ GeV, the comparison between data and simulation is performed only after the muon identification requirement.

sample	1 muon	2 muons	iso muons	Z^0 veto	1 jet	2 jets	$\not\!\!E_{\mathrm{T}}$
$t\bar{t}$ signal	85.9	48.0	41.5	32.0	31.0	23.5	19.8
other $t\bar{t}$	1044.9	20.0	0.2	0.1	0.1	0.1	0.1
tW	71.6	4.1	3.0	2.4	2.1	0.8	0.7
Diboson	92.3	23.7	22.3	8.8	2.4	0.6	0.3
W	198107.9	13.8	0.7	0.6	0.2	–	–
QCD	684340.4	527.5	0.3	0.3	0.1	–	–
$Z^0 \to \tau^+\tau^-$	1768.1	44.7	41.3	38.3	5.7	1.3	0.6
$Z^0 \to \mu^+\mu^-$	29150.5	15891.7	15224.1	1373.7	219.0	40.7	3.1
Sum	914661.5	16573.5	15333.4	1456.2	260.9	67.2	24.4
Data	854708	16472	15057	1463	290	83	28

The $t\bar{t}$ signal is characterised by the presence of energetic hadronic jets corresponding to b jets and additional softer jets from initial and final state radiation. Therefore, the further event selection requires the presence of at least two jets with $p_{\mathrm{T}} > 30$ GeV and within $|\eta| < 2.5$. The selected jet collection is cleaned to remove possible lepton candidates reconstructed as jets: jets overlapping with the muon candidates of the pair within $\Delta R < 0.4$ are rejected. Most background events are not expected to have such strong hadronic activity, therefore the requirement of jets in the event selection further suppresses the background contribution.

Another characteristic feature of the $t\bar{t}$ signal is the presence of natural $\not\!\!E_{\mathrm{T}}$ arising from the neutrinos of the W decays. Therefore, selecting events with significant $\not\!\!E_{\mathrm{T}}$ further suppresses the Drell–Yan and QCD background contributions, where no real source of $\not\!\!E_{\mathrm{T}}$ is present. The final selection criterion for the events is $\not\!\!E_{\mathrm{T}} > 30\,\mathrm{GeV}$. 28 events are selected.

Event Yields

The number of observed events in the data compared to the number of expected events from the simulation is given in Table 5.3 after each sequential selection step defined as follows:

- 1 muon: events with at least 1 muon passing the trigger, p_{T}, η and muon identification requirements.
- 2 muons: events with at least 2 oppositely-charged muons and $M_{\mu^+\mu^-} > 12\,\mathrm{GeV}$.
- iso muons: events passing the muon isolation requirements and the full dimuon selection except the Z^0 veto.

- Z^0 veto: events passing the full dimuon selection, including the veto on the Z^0 mass.
- 1 jet: fully selected dimuon events with at least 1 jet fulfilling the jet p_T and η requirements.
- 2 jets: same as the previous one, but requiring at least 2 jets.
- $\not{E}_T$: events surviving the full selection, including the requirement on the missing energy.

There is a good agreement between data and the sum of simulated samples, which further improves after applying a data-driven correction to the Drell–Yan background contribution as described in the top analysis [5]. Also Figure 5.1 showing comparisons between data and simulation for several distributions show good, but not perfect agreement. Many more comparisons for muon properties, but also for jets and $\not{E}_T$ can be seen in [5].

5.2.2 Z^0 Selection

The characteristic signature of the $Z^0 \to \mu^+\mu^-$ events is given by two opposite-charged muons with high transverse momentum p_T, adding up to an invariant mass close to the Z^0 peak.

The criteria for muon identification, isolation and kinematic selection are the same as for the $t\bar{t}$ selection. Also, the dimuon selection is identical except for the Z^0 veto. Both analyses identically follow the cut flow in table 5.3 up to the step 'iso muons'. Contrary to the $t\bar{t}$ analysis, the invariant mass of the muon pairs is required to be between 76 GeV and 106 GeV, narrower than the one selected in the VBTF analysis (60 GeV to 120 GeV). The choice of this narrow mass window is motivated by the fact that it corresponds exactly to the Z^0 veto cut in the top analysis. As a consequence, the data samples for top and Z^0 analysis are completely independent, and their statistical errors are uncorrelated. Another advantage of the narrow mass window is that the background from $Z^0 \to \tau^+\tau^-$ is strongly suppressed. As can be observed in Figure 5.1, the peak of the distribution is still well included within this narrow mass window, and the shape of the dimuon mass spectrum is well reproduced by the simulation. In contrast to the $t\bar{t}$ analysis, the Z^0 analysis requires no further selection on e.g. jets or $\not{E}_T$. The kinematical distributions of the muons are given in Figure 5.2, they show good agreement between data and simulation. The number of selected events corresponding to an integrated luminosity of $\int \mathcal{L}\mathrm{d}t = 36.145\,\mathrm{pb}^{-1}$ in the full data sample is $N_{\mathrm{obs}} = 13594 \pm 117$ events.

Systematic checks performed using the bigger mass window of VBTF show only small deviations, and are assigned as systematic uncertainty to the final measurement. The VBTF analysis also uses other slightly different identification criteria on the muons. One is that the distance of closest approach to

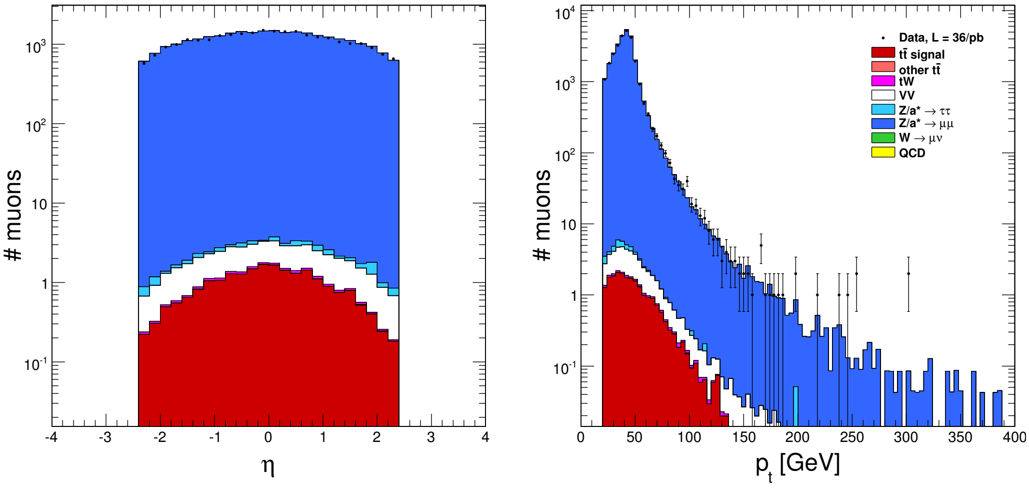

Figure 5.2: Muon pseudorapidity (left) and transverse momentum (right) distributions for the final selection of the Z^0 analysis.

the beamspot is $|d_{0,\mathrm{BS}}| < 0.2\,\mathrm{cm}$, which is a factor 10 bigger. The pseudorapidity values of both muons are required to be $|\eta| < 2.1$. So, the kinematical acceptance region is smaller and clearly less events are selected. The isolation criterion is not a relative, but the absolute tracker isolation $I_{\mathrm{trk}} < 3.0\,\mathrm{GeV}$. It has different systematic uncertainties. Furthermore, in the VBTF analysis, if more than two muons survive the selection, all combinations for building a Z^0 candidate are considered, and not only the ones leading in p_{T}. An additional selection criterion requires that at least one of the two selected muons must match geometrically a HLT muon that triggered the event. Also the trigger selection of VBTF is different and leads to some more events. They do not select data events with the trigger threshold $p_{\mathrm{T}} > 11\,\mathrm{GeV}$ and use the trigger with $p_{\mathrm{T}} > 9\,\mathrm{GeV}$ continuous for those (up to event 147116). But the VBTF analysis requires on all runs a reconstructed HLT muon above a transverse momentum threshold of $p_{\mathrm{T}}(\mathrm{HLT}) > 15\,\mathrm{GeV}$, in order to achieve better uniformity. Since the analysis selects events with at least one selected muon with $p_{\mathrm{T}}(\mathrm{selected}) > 20\,\mathrm{GeV}$, the difference to the presented analysis is negligible.

The presented event selection and the one of VBTF is based on similar characteristics, but differs in many aspects. So there are systematic differences in the analyses that can lead to other results and different uncertainties. The VBTF selection comprises 12261 selected events in the almost full dataset corresponding to an integrated luminosity of $36.09\,\mathrm{pb}^{-1}$.

Table 5.4: Number of expected signal and background events in the Z^0 analysis, compared to the event yields in the 36.1 pb^{-1} data.

Sample	Final Z^0 selection
$t\bar{t}$	9.58
tW	0.66
Diboson	13.51
W	0.07
QCD	–
$Z^0 \to \tau^+\tau^-$	3.03
$Z^0 \to \mu^+\mu^-$	13850.43
Sum of all events	13877.28
Sum of background for Z^0 analysis	26.91
Data	13594

5.3 Background Estimation

Z^0 Analysis

The background estimation of the Z^0 analysis is based on simulation, the samples are scaled to the data luminosity. The corresponding expected number of events after the full event selection are shown in Table 5.4. The overall background is small, and almost negligible. The main contribution comes from double-vectorboson events, which constitute about half of the background yield (see Figure 5.1). This background peaks in the Z^0 mass window as it mostly consists of real muonic Z^0 decays. Also, the contributions from top events are shown. Possible contamination from cosmic muons is strongly suppressed by the requirement that the muons are compatible with the beamspot in x-y and with a primary vertex in z. To be consistent with the top analysis a rescaling of the $t\bar{t}$ sample with the measured cross section might be appropriate. But since the central value is well within the theoretical uncertainty, and the uncertainty of the measurement is much bigger, the theoretical value is kept.

The uncertainty on the background for the simulated samples is estimated from the statistical error, the uncertainty on the theoretical cross section and the luminosity uncertainty. In accordance with the common agreement on systematics [143], the errors on the cross sections for the single-top and diboson processes are set to 30%. The number of background events is estimated to be $N_{\text{bkg}} = 27 \pm 3$ events. Given the number of 13594±117 observed events in data, the signal consists of about $N_{\text{sig}} = 13567$ events and the relative background contamination is about 0.2 %.

VBTF estimates the background to be about 0.4 %. But this value corresponds to the bigger invariant mass window, which increases the relative amount of $t\bar{t}$ events and especially those from $Z^0 \to \tau^+\tau^-$. Cosmic muons are also more probable since the allowed maximum distance to the beam line is bigger. However, the cosmic muons are only a small contribution to the overall small background. VBTF estimates the signal and background contribution from a simultaneous fit to the measured event yield in the dimuon invariant mass distribution (also outside the mass selection window), together with all reconstruction efficiencies. A second degree polynomial function models the background shape. A signal template is estimated from the measured data. The yield is obtained together with the trigger and muon reconstruction and isolation efficiencies on data. This leads to the number of observed events, already corrected for the selection efficiency on data events, of $N_{\mathrm{obs}}/\epsilon_{\mathrm{data}} = 13728$. Segregating the number of observed events reveals $\epsilon_{\mathrm{data}} = 89.3\,\%$. Only the geometrical and kinematical acceptance is excluded from this number. Furthermore, the irreducible background in the selection is estimated from simulation to be 0.4 %, as stated above. VBTF and the presented analysis estimate signal and background in different ways, but the introduced systematic uncertainties are small in both cases.

Top Analysis

In the top analysis the backgrounds are estimated from simulation except of Drell–Yan, which contributes the main background [5]. The $\mathrm{Z}^0 \to \mu^+\mu^-$ contribution is scaled such that the peak in the Z^0 veto window is best described. In other words, the $\mathrm{Z}^0 \to \mu^+\mu^-$ contribution measured in the veto window – where it dominates – is extrapolated to the region outside the window using the simulation. However, since $\mathrm{t\bar{t}}$ events are also inside the window, this needs to be considered and the estimation method is more complex. Especially the $\not{E}_{\mathrm{T}}$ selection requires a big scale factor since pileup is not modelled, thus especially events without natural $\not{E}_{\mathrm{T}}$ are influenced. The $\mathrm{Z}^0 \to \tau^+\tau^-$ contribution is scaled with the value of $\mathrm{Z}^0 \to \mu^+\mu^-$ before the $\not{E}_{\mathrm{T}}$ selection, since $\mathrm{Z}^0 \to \tau^+\tau^-$ with muonic tau decays have natural $\not{E}_{\mathrm{T}}$. The QCD background is completely eliminated in simulation, an upper limit is calculated using events with muons of same instead of opposite charge, fulfilling all other selection criteria. The uncertainty of the $\mathrm{Z}^0 \to \mu^+\mu^-$ estimate dominates the background description and is the main systematic uncertainty for the cross-section measurement. The number of selected data events is 28 ± 5.29 events, the expectation of the background is $10.44^{+4.79}_{-4.75}$ events.

5.4 Results

The cross sections are calculated using the basic formula

$$\sigma = \frac{N_{\mathrm{sig}}}{\epsilon_{\mathrm{tot}} \cdot \int \mathcal{L}\mathrm{dt}}\,, \tag{5.1}$$

where N_{sig} is the number of signal events, ϵ_{tot} is the total efficiency, and $\int \mathcal{L}\mathrm{dt}$ is the integrated luminosity. The number of signal events is obtained using the background estimate as explained above $N_{\mathrm{sig}} = N_{\mathrm{obs}} - N_{\mathrm{bkg}}$, the luminosity is measured directly by CMS. Several cross sections are introduced in the following, and so are their total efficiencies, which link the number of measured signal events to the number of all events defining the signal of the corresponding cross section. Systematic uncertainties for each analysis separate and possible cancellations in the cross-section ratio are discussed. Finally, cross sections and ratios are calculated and used together with the theoretical Z^0 cross section for estimates of the $\mathrm{t\bar{t}}$ cross section independent of the luminosity.

As mentioned before, all parts of the analysis presented so far were based on the primary luminosity estimate. The descriptions in the following are based on the corrected value, described by a scale factor of 0.993 and 4% uncertainty, resulting in $\int \mathcal{L}\mathrm{dt} = 35.9\,\mathrm{pb}^{-1}$. The presented background estimates, using partly the data luminosity for scaling of simulated samples, change only marginally; nevertheless the updated values are taken into account in the following.

5.4.1 Definition of Cross Sections

Several different cross sections are defined in this analysis. First there is the “total cross section”, describing the production of the regarded processes in proton-proton collisions at a centre-of-mass energy of $\sqrt{s} = 7\,\mathrm{TeV}$. For $\mathrm{t\bar{t}}$ production it is without further restriction:

$$\sigma^{\mathrm{t\bar{t}}}_{\mathrm{total}} = \sigma\left(\mathrm{pp} \to \mathrm{t\bar{t}} + X\right) . \tag{5.2}$$

For Z^0 production all processes with a mass constraint $60\,\mathrm{GeV} < M_{\mathrm{Z}^0(\gamma^*)} < 120\,\mathrm{GeV}$ are considered:

$$\begin{aligned} \sigma^{\mathrm{Z}^0}_{\mathrm{total}} &= \sigma\left(\mathrm{pp} \to \mathrm{Z}^0(\gamma^*) + X\right) , \\ 60\,\mathrm{GeV} &< M_{\mathrm{Z}^0(\gamma^*)} < 120\,\mathrm{GeV} . \end{aligned} \tag{5.3}$$

The mass window is chosen in accordance with the VBTF definition and the general choice in CMS electroweak measurements. This allows direct comparisons to the corresponding CMS results and theoretical calculations.

For the presented analysis, the selection is restricted to the dimuonic decay channels. Therefore, the “inclusive cross section” which will be measured is defined including the direct branching ratio to dimuons. For the top analysis intermediate taus with muonic decays are also treated as signal. The top quark is assumed to decay purely to bottom quarks, $\mathrm{t} \to \mathrm{bW}$. This leads to the definition

$$\sigma^{\mathrm{t\bar{t}}}_{\mathrm{inc}} = \sigma^{\mathrm{t\bar{t}}}_{\mathrm{total}} \times \left[\mathrm{BR}\left(\mathrm{W}^{\pm}\left(\to \tau^{\pm}\right) \to \mu^{\pm}\right)\right]^2 . \tag{5.4}$$

In the Z^0 analysis the decay via intermediate taus is mostly removed by the dimuon mass cut as pointed out in Chapter 5.3. Identical to the VBTF definition, only the direct muonic decay is evaluated as signal:

$$\sigma^{\mathrm{Z}^0}_{\mathrm{inc}} = \sigma^{\mathrm{Z}^0}_{\mathrm{total}} \times \mathrm{BR}\left(\mathrm{Z}^0 \to \mu^+\mu^-\right) . \tag{5.5}$$

The branching ratios needed to calculate the total cross sections are given in Chapter 2.3.1 and 2.3.2, needing in addition the $\mathrm{BR}(\tau^\pm \to \mu^\pm) = (17.36 \pm 0.05)\,\%$ [6] for the W case, resulting in

$$\mathrm{BR}\left(\mathrm{Z}^0 \to \mu^+\mu^-\right) = (3.366 \pm 0.007)\,\%\,, \tag{5.6}$$

$$\left[\mathrm{BR}\left(\mathrm{W}^\pm\left(\to \tau^\pm\right) \to \mu^\pm\right)\right]^2 = (1.616 \pm 0.023)\,\%\,. \tag{5.7}$$

A third definition is the “visible cross section”, which includes similar kinematic cuts as they are applied on the reconstruction level. Thus, extrapolations to the unmeasured phase space are avoided and the uncertainties from theory on the quoted measurement are minimised. It includes cuts on the pseudorapidity η and the transverse momentum p_T of both muons, as well as cuts on the dimuon invariant mass. For both analyses the selection is $p_\mathrm{T}^\mu \geq 20\,\mathrm{GeV}$, identical to the reconstruction level. Similar to the reconstruction level for both muons $|\eta^\mu| \leq 2.4$ is required:

$$\sigma_\mathrm{vis} = \sigma_\mathrm{inc} \qquad \text{with} \quad |\eta^\mu| \leq 2.4\,, \quad p_\mathrm{T}^\mu \geq 20\,\mathrm{GeV}\,, \quad \text{constraint on } M_{\mu^+\mu^-}\,. \tag{5.8}$$

The constraints on the invariant dimuon mass $M_{\mu^+\mu^-}$ can be chosen in two different ways. One is to keep those from the total cross section, i.e. to set no further constraint on this, but the focus lies on the other variant: the invariant mass is selected with the same values as on reconstruction level. For the top analysis these are $12\,\mathrm{GeV} \leq M_{\mu^+\mu^-} \leq 76\,\mathrm{GeV}$ or $M_{\mu^+\mu^-} \geq 106\,\mathrm{GeV}$. For the Z^0 analysis it is the complementary mass window $76\,\mathrm{GeV} \leq M_{\mu^+\mu^-} \leq 106\,\mathrm{GeV}$.

The cut flow for the Z^0 analysis on the simulated values is illustrated in the following figures. Figure 5.3 shows the simulated invariant mass distribution of the boson of the Drell–Yan process in the muonic decay channel in the signal sample. In Figure 5.4 pseudorapidity and transverse momentum distribution of the muons which are relevant for the further cuts are shown. Mainly the pseudorapidity criterion deselects events.

5.4.2 Estimates for Total Efficiency

The total efficiency ϵ_tot is defined as the ratio of the measured signal events to the number of all events which are produced for a given process. It is factorised into the kinematical acceptance A, and the event selection efficiency on data ϵ_data,

$$\begin{aligned} \epsilon_\mathrm{tot} = \epsilon_\mathrm{data} \times A \;&=\; \rho_\mathrm{eff} \times \epsilon_\mathrm{MC} \times A \\ &=\; \rho_\mathrm{eff} \times \left(\frac{N^\mathrm{reco}_\text{all cuts}}{N^\mathrm{gen}_\text{kin. cuts}}\right) \times \left(\frac{N^\mathrm{gen}_\text{kin. cuts}}{N^\mathrm{gen}}\right)\,. \end{aligned} \tag{5.9}$$

The event selection efficiency on data is estimated from the event selection efficiency on simulated events ϵ_MC, and a scale factor ρ_eff. The values of ϵ_MC and

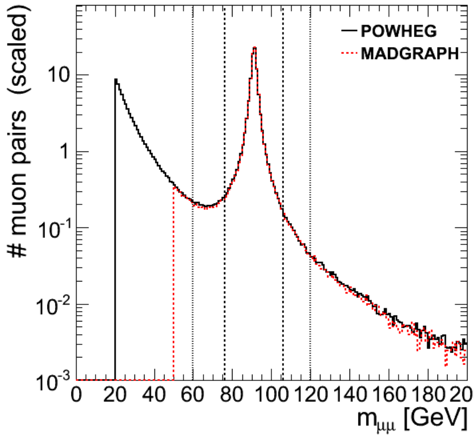

Figure 5.3: Generated $Z^0(\gamma^*)$ boson mass of Drell–Yan process in signal samples of Z^0 analysis (POWHEG and MADGRAPH). Only bosons with dimuonic decay are considered. The distributions are normalised to the number of events above 50 GeV (in %).

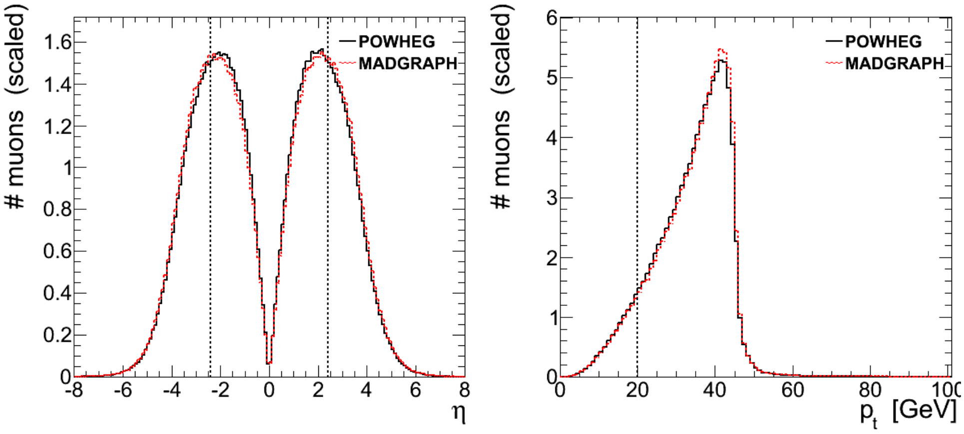

Figure 5.4: Properties of muons from $Z^0(\gamma^*)$ decay (POWHEG and MADGRAPH). Left: generated pseudorapidity of muon with higher absolute value for selected mass window $76\,\text{GeV} \leq M_{Z^0} \leq 106\,\text{GeV}$. Right: generated transverse momentum of muon with lower value for the final Z^0 signal selection. The distributions are normalised to the number of events (in %).

A are obtained from simulation using the signal sample. The scale factor ρ_{eff} is necessary to account for differences of the efficiency in data and simulation, it is described in Chapter 5.4.3.

The acceptance is estimated on generator-level from all signal events N^{gen}, given by the definition of the cross section, and those events surviving the kinematic selection corresponding to the acceptance definition $N^{\text{gen}}_{\text{kin. cuts}}$. The efficiency ϵ_{MC} is the ratio of all signal events fulfilling all selection criteria of the measurement on detector-level $N^{\text{reco}}_{\text{all cuts}}$ and all signal events being selected by the kinematic cuts on generator-level. The separation between A and ϵ_{data} is arbitrary—A should mainly separate measured and unmeasured phase space (theory), while ϵ_{data} should mainly reflect the efficiency of the detector (measurement). The separation is needed to apply different simulated samples in the Z^0 analysis, while it is not relevant in the top analysis.

$\mathbf{Z^0}$ Analysis

The Z^0 analysis on generator-level is performed on the MadGraph and on the powheg sample. For the estimation of the kinematic acceptance the powheg sample is used, since it is a NLO simulation. The pseudorapidity distribution becomes more central going from LO to NLO predictions. The signal is defined as all $\text{Z}^0 \to \mu^+\mu^-$ events with the corresponding mass constraint defining the Z^0 window. For the visible cross section the choice of the acceptance is such that the full phase space is selected $N^{\text{gen}} = N^{\text{gen}}_{\text{kin. cuts}}$, which means $A(\text{visible}) = 1$ by definition. For the acceptance of the inclusive cross section, the generated muons need to fulfil $|\eta| < 2.4$ and $p_{\text{T}} > 20\,\text{GeV}$: the number of signal events on generator-level is $N^{\text{gen}}(\text{inclusive}) = 1143944$, the number of events fulfilling the kinematical cuts is $N^{\text{gen}}_{\text{kin. cuts}}(\text{inclusive}) = 554296$. The value for the acceptance is then about

$$A(\text{inclusive}) = \frac{N^{\text{gen}}_{\text{kin. cuts}}}{N^{\text{gen}}} = 48.4\,\%\,. \tag{5.10}$$

The acceptance calculated from the MadGraph sample with an absolute value of $A = 47.2\,\%$ shows a clear deviation of $2.7\,\%$ for the calculation of the cross section (see Figure 5.3 and Figure 5.4). The difference arises mainly because it is only a LO simulation. The value of VBTF is significantly lower, $A(\text{inclusive}) = (39.8 \pm 0.2)\,\%$. But this is due to the different threshold of $|\eta| < 2.1$ for both muons. Systematic effects are expected to be small since the same generator is used.

For the event selection efficiency ϵ_{MC} estimation the MadGraph sample is used. It is the standard sample of the top analysis. Furthermore, the estimates of the muon efficiency corrections ρ_{eff}, as given in Chapter 5.4.3, are relative to this sample. The number of Z^0 events in the acceptance region on generator-level for the visible and the inclusive cross sections are $N^{\text{gen}}_{\text{kin. cuts}}(\text{visible}) = 378847$ and $N^{\text{gen}}_{\text{kin. cuts}}(\text{inclusive}) = 393877$. The number of all reconstructed $\text{Z}^0 \to \mu^+\mu^-$ (no selection on generator-level, except that muonic decay is verified) events surviving all selection criteria on reconstruction-level is $N^{\text{reco}}_{\text{all cuts}} = 327442$. The event selection efficiency for the inclusive cross section is slightly smaller than the one for the visible cross section:

$$\epsilon_{\text{MC}}(\text{visible}) = \frac{N^{\text{reco}}_{\text{all cuts}}}{N^{\text{gen}}_{\text{kin. cuts}}(\text{visible})} = 86.4\%\,, \tag{5.11}$$

$$\epsilon_{\text{MC}}(\text{inclusive}) = \frac{N^{\text{reco}}_{\text{all cuts}}}{N^{\text{gen}}_{\text{kin. cuts}}(\text{inclusive})} = 83.1\%\,. \tag{5.12}$$

These factors are expected to be clearly smaller than one, not only due to reconstruction efficiencies. The more restrictive selection of at least one muon with $|\eta| < 2.1$ on reconstruction level, but both muons with $|\eta| < 2.4$ on generation level, reduces the measured phase space. The difference between both values is due to the further restriction of the visible cross section to the smaller Z^0 mass window. The inclusive event selection efficiency has this further contribution from unmeasured phase space.

The resulting total efficiencies are then:

$$\epsilon_{\text{tot}}(\text{visible}) = \rho^{\text{Z}^0}_{\text{eff}} \times 86.4\%\,, \tag{5.13}$$

$$\epsilon_{\text{tot}}(\text{inclusive}) = \rho^{\text{Z}^0}_{\text{eff}} \times 40.3\%\,. \tag{5.14}$$

Estimated corrections ρ_{eff} between data and simulation are discussed later and will be applied to the estimated cross sections. The statistical uncertainty of the simulation is negligible compared to the systematic uncertainties, which are assigned in Chapter 5.4.3.

Top Analysis

Muons from t$\bar{\text{t}}$ are in general more central as those of Z^0 events, and the difference between LO and NLO is not that large. The product $A \times \epsilon_{\text{MC}}$ is estimated directly from the MadGraph sample. In the top analysis described in [5], there is nothing documented for the visible cross section. The total efficiency is $\epsilon_{\text{tot}}(\text{visible}) = \rho^{\text{t}\bar{\text{t}}}_{\text{eff}} \times 47.8\%$ with the muon kinematics and invariant dimuon mass restriction identical to the cross-section definition. The value is dominated by the further selection steps on jets and $\not\!\!E_{\text{T}}$, which are not considered in the definition of the visible cross section. The total efficiency for the inclusive cross section is about $\epsilon_{\text{tot}}(\text{inclusive}) = \rho^{\text{t}\bar{\text{t}}}_{\text{eff}} \times 20.8\,\%$.

5.4.3 Systematic Uncertainties

For the cross sections measured in this chapter, the systematic uncertainties can arise from luminosity, background subtraction, branching ratio, event reconstruction efficiency and kinematic acceptance considering the specific set of requirements for the event selection. The systematic uncertainties are discussed in detail in this section. For all measurements the uncertainty of the

Table 5.5: Scale factors and systematic uncertainties of the measured cross sections of the Z^0 analysis. The sums are given without the influence of the luminosity, which is always stated separately.

Source	Scale factor	Uncertainty	Cancel in ratio
Luminosity		(0.04)	X
Trigger efficiency	0.9956	0.0074	X
Pre-trigger losses	0.995^2	$2 \cdot 0.003$	X
Muon overall efficiency	0.9920^2	$2 \cdot 0.0054$	X
Muon momentum scale & resolution		0.0035	X
Dimuon mass cut, Z^0 mass resolution		0.003	
Background subtraction		0.0003	
Theoretical uncertainties		0.016	
Sum for cross section (σ_{vis})	0.970	0.022	
Sum for ratio (σ_{vis})	—	0.016	
PDF uncertainty for acceptance		0.012	
Sum for cross section (σ_{inc})	0.970	0.025	
Sum for ratio (σ_{inc})	—	0.020	
Branching ratio		0.0021	
Sum for cross section (σ_{total})	0.970	0.025	
Sum for ratio (σ_{total})	—	0.020	

luminosity is provided centrally as 4% (see Chapter 3.6). In the cross-section ratio, uncertainties common to both processes cancel; they are discussed afterwards. Finally, a theoretical calculation of the inclusive Z^0 cross section and its uncertainty are discussed, since it is also used in the results.

Z^0 Analysis

For the Z^0 analysis several kinds of experimental systematics have to be considered; all contributions to the measured Z^0 cross sections are quantified and can be found in Table 5.5.

One is the trigger efficiency of the used muon triggers. The used muon trigger with $p_T > 15\,\text{GeV}$ is not simulated, but used for the selection of the major amount of data. In the simulated samples the one with $p_T > 9\,\text{GeV}$ is used instead. But since the muon momenta are selected to be $p_T \geq 20\,\text{GeV}$, which is quite above the threshold, the efficiency behaves almost identically. The small scale factor and uncertainty are taken from the top analysis [5]. The values are estimated with a tag-and-probe approach on Z^0 events.

An additional contribution to the trigger efficiency not covered by this method comes from the pre-triggering problem. In about 0.5 ± 0.3 of the events a L1 muon trigger is wrongly assigned to one or a few bunch crossings before the actual collision. The consequence is that inner tracker hits and muon system hits are assigned to different events and the muon cannot be reconstructed. The value of 0.995 ± 0.003 per muon is taken in accordance to [144].

The second systematic source is the overall muon efficiency, including reconstruction, identification and isolation. A scale factor and uncertainty of 0.9920 ± 0.0054 per muon [137] is applied, so it enters twice. Also these values are estimated with a tag-and-probe approach on Z^0 events. The influence from wrong charge assignments is negligible. The third is the effect of the muon momentum scale and resolution. Several studies show that no scale factor has to be applied, e.g. [143]. The uncertainty is taken as 0.35 %, like VBTF implies [141]. The fourth is the influence of the Z^0 mass selection window due to the mass resolution. This is taken from the difference of the central cross section values for the Z^0 analysis with a dimuon mass window of [76 GeV, 106 GeV] resp. [60 GeV, 120 GeV], as mentioned in Chapter 5.2.2.

Further contributions to the measured cross sections come from backgrounds (see Chapter 5.3) and from branching ratios for the dimuonic final states (see Chapter 5.4.2). Finally, systematic effects from PDF uncertainties on the acceptance and other remaining theoretical uncertainties are considered. The latter ones are associated with the treatment of initial-state radiation, final-state QED radiation, missing electroweak effects, and renormalisation and factorisation scale assumptions. The values are taken from VBTF.

The estimated scale factor for the cross sections originating from the total efficiency – correcting the efficiency estimate based on simulation for differences between data and simulation – is the ratio of the selection efficiency on data events and the selection efficiency on simulated events. The value is

$$\rho_{\text{eff}} = \frac{\epsilon_{\text{data}}}{\epsilon_{\text{MC}}} = (97.0 \pm 1.5)\,\%\,, \tag{5.15}$$

as stated in Table 5.5. The updated result of VBTF is lower, but within the assigned uncertainties. The value of about 95.5% is also estimated from the simultaneous fit together with the event yield.

Top Analysis

For the top analysis the same considerations as for the Z^0 analysis apply. The muon efficiencies (trigger and others) are calculated from the same tag-and-probe approach on Z^0 events. Since the muon kinematics are similar in both processes, most of these efficiencies are similar as verified by comparisons to the $\mathrm{t\bar{t}}$ sample. However, since the hadronic activity in the top analysis is in general bigger, the muons are in general less isolated. This effect is studied in [145]. The central value is taken identical, but the top analysis gets an additional uncertainty of 2% per muon, according to [137]. Theoretical uncertainties are obtained using specific $\mathrm{t\bar{t}}$ samples with systematic variations, and contribute as well as background subtraction and branching ratio to the systematic uncertainty.

Table 5.6: Scale factors and systematic uncertainties of the measured cross sections of the top analysis. The sums are given without the influence of the luminosity, which is always stated separately.

Source	Scale factor	Uncertainty	Cancel in ratio
Luminosity		(0.04)	X
Trigger efficiency	0.9956	0.0074	X
Pre-trigger losses	0.995^2	$2 \cdot 0.003$	X
Muon overall efficiency	0.9920^2	$2 \cdot 0.0054$	X
Muon momentum scale & resolution		0.0035	X
Muon isolation difference to T&P		$2 \cdot 0.02$	
Jet energy scale		$+0.055-0.044$	
Unclustered $\not{E}_\mathrm{T}$ scale		$+0.0035-0.0004$	
$\not{E}_\mathrm{T}$ for $\mathrm{t\bar{t}}$ signal	1.011	0.011	
Background subtraction		$+0.270-0.273$	
Theoretical uncertainties		0.048	
Sum for cross section (σ_vis)	0.981	$+0.283-0.284$	
Sum for ratio (σ_vis)	1.011	$+0.283-0.284$	
Sum for cross section (σ_inc)	0.981	$+0.283-0.284$	
Sum for ratio (σ_inc)	1.011	$+0.283-0.284$	
Branching ratio		0.0144	
Sum for cross section (σ_total)	0.981	$+0.283-0.284$	
Sum for ratio (σ_total)	1.011	$+0.283-0.284$	

The scale factor for muon efficiencies is identical to Equation 5.15, but the uncertainty due to isolation comes along in addition. Furthermore experimental systematics originating from selections on jets and $\not{E}_{\mathrm{T}}$ need to be quantified for the top analysis. These are corrections or uncertainties for the jet energy scale and resolution, as well as for $\not{E}_{\mathrm{T}}$. The values are obtained as described in [138] and summarised in Table 5.6.

Cross-Section Ratio

The advantage of the cross-section ratio is that several systematics cancel as indicated in Table 5.5 and Table 5.6. Since the same dataset is used for both analyses, the luminosity cancels completely. Due to the similar muon topology and identical trigger and muon selection, efficiencies resulting from those cancel almost. These are the trigger efficiency, the pre-trigger losses and all contributions to the overall muon efficiency except for the difference in isolation. Since the overall muon efficiency is from tag-and-probe on a Z^0 sample, it is immediately appropriate for the Z^0 analysis, while the top analysis gets an additional uncertainty of 4% due to isolation. The other listed contributions from muons are treated as being exactly identical, thus cancelling in the ratio. Also the trigger and muon efficiency scale factors cancel and have no influence on the result. Since the pseudorapidity distribution of the muons is more centred around 0 for the top analysis, the trigger efficiency can differ slightly, but is also negligible. Due to the complementary dimuon mass selection, both analyses are statistically independent.

For the cross-section ratio also correlations for the cross-section uncertainties arising from PDFs have to be considered in principle. At TeVatron, both production processes are dominated by annihilation of valence quarks (u and d). At LHC, the top pairs are mainly produced in gluon-gluon fusion, while there are significant contributions from s, c and b quarks to the Z^0 production (see Figure 2.9). Although the Z^0 production is still dominated by light quarks, the PDF uncertainty gets dominated by the other flavours, since the light quark PDFs are notedly constrained by measurements, compared to the charm or the beauty quark PDF, and since the relative uncertainty of s, c, and b is significantly bigger due to the smaller amplitude. Anticorrelations arising from PDFs degrade the usefulness of a specific process as standard candle for another one, while positive correlations are a clear benefit. A study of correlations between both processes (and also between others) is in [146] for TeVatron, and LHC with a centre-of-mass energy of 14 TeV. For $\mathrm{t\bar{t}}$ and Z^0 at TeVatron, there is no significant correlation found. But at LHC, depending on the collision conditions, there can appear anticorrelations, e.g. between the gluon PDF and the strange quark PDF, which can lead to anticorrelations for both processes. But compared to the other systematic uncertainties of the top analysis, this effect is negligible.

Table 5.7: Cross section and corresponding uncertainties as assigned to the theoretical prediction of the Drell–Yan process with muonic decay. The values correspond to the invariant boson mass interval of [60 GeV, 120 GeV].

σ_{NNLO} [pb]	$\Delta\sigma_{\mathrm{PDF}+\alpha_s}$ [pb]	$\Delta\sigma_{\mathrm{scale}}$ [pb]	$\Delta\sigma_{\mathrm{(N)NLO}}$ [pb]
972	±41	±11	±42

Theoretical Z^0 Cross Section

Together with the cross-section ratio measurement, the theoretical Z^0 production cross section can be used to extract the $t\bar{t}$ cross section. This method leads to another systematic uncertainty coming from theory, the uncertainty of the theory value of the Z^0 cross section. The NNLO prediction for the inclusive cross section with a central value of 972 pb has an assigned uncertainty of 42 pb as determined in [147] and reflected in Table 5.7. This value includes scale uncertainties, determined by varying the factorisation and renormalisation scales. This is dominated by the numerical precision of the integration. Furthermore, uncertainties originating from the PDFs and the value of α_s are included. However, the relative error of the NLO calculation is assigned to them. Thus the central value is in NNLO, but the uncertainty not completely.

5.4.4 Cross Sections and Cross-Section Ratios

For the cross section measurements the integrated luminosity of $\int \mathcal{L}\mathrm{dt} = 35.9 \pm 1.4\,\mathrm{pb}^{-1}$ is used. The cross sections are calculated via the formula

$$\sigma = \frac{N_{\mathrm{sig}}}{\epsilon_{\mathrm{tot}} \cdot \int \mathcal{L}\mathrm{dt}} = \frac{N_{\mathrm{obs}} - N_{\mathrm{bkg}}}{\rho_{\mathrm{eff}} \cdot \epsilon_{\mathrm{MC}} \cdot A \cdot \int \mathcal{L}\mathrm{dt}} \,. \tag{5.16}$$

It is not needed to study corrections or uncertainties on luminosity in detail, since they cancel completely in the final ratio. The same holds almost for trigger and muon systematics, as they are based on identical selection criteria and similar muon topologies. However all effects are taken into account in order to compare the absolute cross sections with other results as a cross-check. Furthermore it is needed to compare the $t\bar{t}$ cross section normalised to luminosity with the usage of the Z^0 as standard candle.

The Z^0 cross sections defined in Chapter 5.4.1 are obtained to be

$$\sigma_{\mathrm{vis}}^{Z^0} = 451 \pm 4\,(\mathrm{stat.}) \pm 10\,(\mathrm{syst.}) \pm 18\,(\mathrm{lumi.})\,\mathrm{pb}\,, \tag{5.17}$$

$$\sigma_{\mathrm{inc}}^{Z^0} = 967 \pm 8\,(\mathrm{stat.}) \pm 24\,(\mathrm{syst.}) \pm 39\,(\mathrm{lumi.})\,\mathrm{pb}\,, \tag{5.18}$$

$$\sigma_{\mathrm{total}}^{Z^0} = 28742 \pm 247\,(\mathrm{stat.}) \pm 722\,(\mathrm{syst.}) \pm 1150\,(\mathrm{lumi.})\,\mathrm{pb}\,. \tag{5.19}$$

The uncertainty is dominated by theoretical uncertainties and especially the luminosity estimate. The value of the inclusive cross section is in good agreement with the NNLO theory prediction of $\sigma^{\mathrm{Z}^0}_{\mathrm{inc}} = 972 \pm 42\,\mathrm{pb}$. Furthermore, it can be compared to other CMS results from VBTF. The definition of the cross section is identical, but the analysis differs slightly. Different event generators are used for some samples. The event selection on reconstruction level is similar, but not identical. The signal yield and the muon efficiencies are taken from a simultaneous fit. The published result [141] is

$$\sigma^{\mathrm{Z}^0}_{\mathrm{inc,\ CMS}} = 968 \pm 8\,(\mathrm{stat.}) \pm 20\,(\mathrm{syst.}) \pm 39\,(\mathrm{lumi.})\,\mathrm{pb}\,, \tag{5.20}$$

in excellent agreement with the result obtained above. Since almost the same data is used, the statistical and the luminosity uncertainty are correlated with the presented analysis. Some systematic uncertainties are also correlated, like the acceptances which are estimated from the same sample. But the method to determine the cross section differs in various aspects, leading to slightly different systematic corrections and uncertainties.

The results obtained for the $\mathrm{t\bar{t}}$ cross sections defined in Chapter 5.4.1 are:

$$\sigma^{\mathrm{t\bar{t}}}_{\mathrm{vis}} = 1.0 \pm 0.3\,(\mathrm{stat.}) \pm 0.3\,(\mathrm{syst.}) \pm 0.04\,(\mathrm{lumi.})\,\mathrm{pb}\,, \tag{5.21}$$

$$\sigma^{\mathrm{t\bar{t}}}_{\mathrm{inc}} = 2.4 \pm 0.7\,(\mathrm{stat.}) \pm 0.7\,(\mathrm{syst.}) \pm 0.1\,(\mathrm{lumi.})\,\mathrm{pb}\,, \tag{5.22}$$

$$\sigma^{\mathrm{t\bar{t}}}_{\mathrm{total}} = 148 \pm 45\,(\mathrm{stat.}) \pm 42\,(\mathrm{syst.}) \pm 6\,(\mathrm{lumi.})\,\mathrm{pb}\,. \tag{5.23}$$

The value of the total cross section is in good agreement with the NLO theory prediction of $\sigma^{\mathrm{t\bar{t}}}_{\mathrm{inc}} = 157.7^{+23.2}_{-24.4}\,\mathrm{pb}$, assuming the top mass to be 172.5 GeV. The result is dominated by the statistical error and the background uncertainty, which arises mainly from the data-driven Drell–Yan estimate, and is thus also statistically limited.

Finally, the results for the cross-section ratios are given. These contain no uncertainty from luminosity which cancels completely in the ratio. Also several uncertainties from the muons cancel, as stated in Section 5.4.3. The values for the ratios are:

$$\begin{aligned}\frac{\sigma^{\mathrm{t\bar{t}}}_{\mathrm{vis}}}{\sigma^{\mathrm{Z}^0}_{\mathrm{vis}}} &= (2.3 \pm 0.7\,(\mathrm{stat.}) \pm 0.7\,(\mathrm{syst.})) \cdot 10^{-3} \\ &= (432 \pm 179)^{-1}\,,\end{aligned} \tag{5.24}$$

$$\begin{aligned}\frac{\sigma^{\mathrm{t\bar{t}}}_{\mathrm{inc}}}{\sigma^{\mathrm{Z}^0}_{\mathrm{inc}}} &= (2.5 \pm 0.7\,(\mathrm{stat.}) \pm 0.7\,(\mathrm{syst.})) \cdot 10^{-3} \\ &= (403 \pm 167)^{-1}\,,\end{aligned} \tag{5.25}$$

$$\begin{aligned}\frac{\sigma^{\mathrm{t\bar{t}}}_{\mathrm{total}}}{\sigma^{\mathrm{Z}^0}_{\mathrm{total}}} &= (5.2 \pm 1.6\,(\mathrm{stat.}) \pm 1.5\,(\mathrm{syst.})) \cdot 10^{-3} \\ &= (194 \pm 80)^{-1}\,.\end{aligned} \tag{5.26}$$

About 400 times more Z^0 events than $\mathrm{t\bar{t}}$ events occur in dimuonic decay modes, corresponding to about 200 times more Z^0 bosons than top pairs produced at LHC with $\sqrt{s} = 7\,\mathrm{TeV}$.

Using this ratio measurement, a top-pair cross section can be extracted from the theory value of the Z^0 cross section, thus effectively using Z^0 production as a luminosity standard candle:

$$\sigma^{\mathrm{t\bar{t}}}_{\text{inc, extr}} = \left(\frac{\sigma^{\mathrm{t\bar{t}}}_{\mathrm{inc}}}{\sigma^{\mathrm{Z}^0}_{\mathrm{inc}}} \right)_{\text{measured}} \times \left(\sigma^{\mathrm{Z}^0}_{\mathrm{inc}} \right)_{\text{theory}} = 2.4 \pm 0.7\,(\text{stat.}) \pm 0.7\,(\text{syst.})\,\mathrm{pb}\,. \tag{5.27}$$

The uncertainty is dominated by the $\mathrm{t\bar{t}}$ analysis. Within its large uncertainty, this result shows consistency with Standard Model expectations.

Another interpretation of the latter formula and especially the incorporated uncertainties can be seen when it is grouped as follows:

$$\sigma^{X}_{\mathrm{norm}} = \left(\sigma^{X} \right)_{\text{measured}} \times \frac{\left(\sigma^{\mathrm{Z}^0}_{\mathrm{inc}} \right)_{\text{theory}}}{\left(\sigma^{\mathrm{Z}^0}_{\mathrm{inc}} \right)_{\text{measured}}}\,. \tag{5.28}$$

Any measured cross section can be normalised to the Z^0 production cross section instead of the measured luminosity. The ratio of theoretical and measured value is a correction factor for luminosity. However, in order to exclude influences from time-dependent systematic effects on the direct luminosity measurement, the method guarantees absolute independence of luminosity only in case of a dataset based on these $35.9\,\mathrm{pb}^{-1}$. Using this formula, all defined cross sections and measured decay channels can be renormalised. Other systematic uncertainties than luminosity will not cancel in this case. It should be remarked that the uncertainty of the used NNLO calculation was inflated by taking the NLO uncertainty of the PDF and α_{s} dependence (see Chapter 5.4.3), and thus dominates this normalisation. The inverse theory-to-measurement ratio is

$$\frac{\left(\sigma^{\mathrm{Z}^0}_{\mathrm{inc}} \right)_{\text{measured}}}{\left(\sigma^{\mathrm{Z}^0}_{\mathrm{inc}} \right)_{\text{theory}}} = 1.00 \pm 0.01\,(\text{stat.}) \pm 0.02\,(\text{exp.}) \pm 0.04\,(\text{theo.})\,. \tag{5.29}$$

This can be compared to the value using directly the MadGraph sample for the theory prediction, as a crosscheck of the correct modelling of data. This needs the estimated number of signal events in data, the corresponding number of selected signal events on simulation, and the estimated correction factor for the selection efficiency difference in data and simulation. Furthermore, it has to be corrected for the 2.7 % difference in the acceptance to the next-to-leading order powheg expectation. Both values are in agreement:

$$\left[\frac{(N_{\mathrm{sig}})_{\text{measured}}}{\rho_{\mathrm{eff}} \cdot (N_{\mathrm{sig}})_{\text{simulated}}} \right]_{\text{acceptance corrected}} = 0.99\,. \tag{5.30}$$

The result for the total cross section of the top-pair production normalised to the Z^0 cross section is obtained as

$$\sigma^{\mathrm{t\bar{t}}}_{\text{total, norm}} = 149 \pm 45\,(\text{stat.}) \pm 42\,(\text{syst.}) \pm 7.6\,(\text{norm.})\,\mathrm{pb}\,. \tag{5.31}$$

Good agreement is observed compared to the result using the measured luminosity in Equation 5.23. Both normalisation methods can be combined. They are not completely uncorrelated, since the luminosity estimate includes also a method based on tracker information, but the correlations are small and here neglected. The combination as weighted arithmetic mean results in higher accuracy:

$$\sigma^{\mathrm{t\bar{t}}}_{\text{total, comb}} = 149 \pm 45\,(\text{stat.}) \pm 42\,(\text{syst.}) \pm 4.7\,(\text{comb.})\,\text{pb}\,. \tag{5.32}$$

The cancellation of the trigger and muon efficiencies could still be used for the normalisation to the Z^0 cross section. But then, the combination of both normalisations is not trivial, and the gain in precision is marginal.

5.5 Conclusions

The cross section ratio of top-pair and Z^0 (i.e. Drell–Yan) production has been measured in the proton-proton collisions of 2010, using the decay channels of top-pairs and Z^0 into two muons. The measurement of the ratio provides a reduced systematic uncertainty in comparison to absolute cross section measurements, since the luminosity and common muon efficiencies cancel. The dataset at hand remains dominated by the statistical error of the top analysis, and is thus not yet competitive with theory predictions. However, within these large uncertainties of the experiment, consistency is found with Standard Model predictions. With the drastic increase of luminosity for the LHC data taking in 2011 and beyond the statistical uncertainties are bound to decrease very quickly, and the method presented here is going to provide valuable benefits to the testing of the Standard Model and the precision determination of its parameters.

Furthermore, the ratio of the theoretical prediction and the measured cross section of Z^0 production was obtained. It can replace the luminosity measurement and thus reduce the total normalisation uncertainty for the top-pair production cross section or any other measured cross section. At the time the analysis was initiated, the luminosity uncertainty of 11% contributed significantly, and the usage of Z^0 as a standard candle gave clearly the better normalisation, and even more when combining both methods. With the better luminosity estimate this method is less impressive, especially since the other systematic and the statistical uncertainties are huge in comparison. Nevertheless it still was a significant cross-check with slightly reduced uncertainty. But since many of the systematic uncertainties are de facto also limited by statistics used for their estimation, and since the understanding of the detector naturally gets better with time, the method will become more relevant again.

Chapter 6

Measurement of Associated Z^0-Boson and b-Jet Production

Chapter 5 presents a measurement of the Z^0 production cross section in the muonic decay mode. Here, the measurement of the same process is performed with a more exclusive initial state selection—the Z^0 needs to be produced in association with b quarks, which are identified by the resulting b jets, referred to as bZ^0 or in figures often labelled as Z+b. The process and the relevance of this measurement are explained in Chapter 2.3.3. It is a test of QCD calculation schemes, and it is an important benchmark and background process, e.g. for some Higgs analyses.

Furthermore, for $t\bar{t}$ measurements in dileptonic decay modes as also presented in Chapter 5, bZ^0 is a background—and it becomes the dominant one in analyses where also the b jets of the top decays are tagged in order to reduce other background contributions. This is the case in recent measurements with 2011 data, e.g. measurements of differential cross sections in dileptonic final states [148][149]. Vice versa for the bZ^0 ($Z^0 \rightarrow \mu^+\mu^-$) measurement the $t\bar{t}$ process with dimuonic final state is the main background. This is due to the similar topology of both processes with two isolated muons and two b jets in the final state and their similar cross sections. The muons have similar kinematic topologies, but can be separated by the invariant dimuon mass in comparison with the Z^0 peak. The b jets however show bigger deviations of the topologies; in $t\bar{t}$ events both b jets have in general high transverse energies, in bZ^0 events the transverse energy is in general lower and often only one hard jet is produced. An important difference for the separation of both processes is the $\not{E}_T$ distribution, which shows a wide range of values for $t\bar{t}$ due to the neutrinos in the final state, while in bZ^0 events there is in general no natural $\not{E}_T$.

The main contribution of this thesis to the bZ^0 measurement is the estimation of the $t\bar{t}$ background, making use of results from the differential $t\bar{t}$ cross section measurement mentioned above. The $t\bar{t}$ estimate is also described in more technical detail in [150], and is used in the publication [151]. The publication contains analyses in $Z^0 \rightarrow e^+e^-$ and $Z^0 \rightarrow \mu^+\mu^-$ decay modes and the combination of both. This chapter however focuses on $Z^0 \to \mu^+\mu^-$. The measurement is based on parts of the 2011 dataset and the requirement of at least one b jet. In order to study additional selections for future bZ^0 analyses, also additional criteria are analysed, like requiring two b jets and a selection on $\not\!\!E_T$.

Before the LHC era the process could be measured only at the TeVatron [62][63]. Preparatory studies for CMS based on simulation are presented in [152][153][154], an observation of the process in the 2010 data is described in [56]. An analysis of ATLAS can be found elsewhere [155]. A main difference between the TeVatron and LHC measurements is the different probability of the initial state production channels, dominated by quark-antiquark interactions at the TeVatron and dominated by gluon-gluon processes at LHC.

6.1 Data and Simulated Samples

The signal process is extracted by identifying the Z^0 via its muonic decay and requiring at least one hard b jet. Dimuon triggers are used to collect data samples during the 2011 runs. The events have to be certified as being of good quality (see Chapter 3.2.3). The analysis was first performed on the first parts of the 2011 data with run range 160404–167913, corresponding to an integrated luminosity of $1.143\,\mathrm{fb}^{-1}$ with a relative uncertainty of 4.5%. Several parts of the analysis and the final results are updated taking also the subsequent periods of 2011 data up to run number 173692 into account, corresponding to $2.11\,\mathrm{fb}^{-1}$ at the time the analysis was performed—however the luminosity estimate was updated with a more precise technique – giving $2.22\,\mathrm{fb}^{-1}$ and 2.2% uncertainty – in time to adjust the final results (see Chapter 3.6).

The analysis is very similar to the one described in Chapter 5 concerning the dimuon selection. For this reason, the presented analysis focuses mainly on the subsequent steps—only two simulated samples are in use for the modelling of the data. One is the inclusive Z^0/γ^* production, which contains the signal process bZ^0 but also important background contributions from Z^0 production associated with non-b jets. The other is $t\bar{t}$ production which contributes the main background. Both samples are generated with MadGraph and interfaced with pythia (see Chapter 3.4.2). The MadGraph simulation is based on the variable-flavour scheme using massless b quarks.

The invariant mass range of the Z^0/γ^* sample is restricted to $M_{Z^0/\gamma^*} > 50\,\mathrm{GeV}$. All leptonic decay modes are simulated, thus a filter for the simulated muonic decay is applied. The signal process bZ^0 is separated from the background processes of associated Z^0 and c quark production, labelled cZ^0, and the Z^0 events produced in association with light quarks, labelled lZ^0, by the following criteria. An event is assigned to

- bZ^0, if at least one b quark occurs in the list of generated particles,

Table 6.1: Summary of simulated data samples used in this analysis, together with the cross section assigned to the process. The cross section of the $t\bar{t}$ sample is in NLO, the $Z^0/\gamma^* \to \mu^+\mu^-$ sample is NNLO.

Sample	cross section [pb]
$t\bar{t}$	$157.5^{+23.2}_{-24.4}$
Z^0/γ^* ($M_{Z^0/\gamma^*} > 50\,\text{GeV}$, $Z^0/\gamma^* \to \mu^+\mu^-$)	3048 ± 132

- cZ^0, if it does not belong to bZ^0 and at least one c quark occurs in the list of generated particles,
- lZ^0, for all remaining events not assigned to bZ^0 or cZ^0.

There are no selections on kinematics applied apart from the Z^0/γ^* mass threshold.

For comparisons between data and simulation the simulated samples are scaled in order to match the luminosity of the data. The assigned theoretical cross sections are shown in Table 6.1. They are taken from [156] and are identical to the ones used in Chapter 5. The inclusive Z^0 sample is normalised to the NNLO cross section—for bZ^0 however, this corresponds to NLO. The samples are simulated with pileup.

6.2 Event Selection

In order to select events for which a proton-proton collision occurred, at least one primary vertex – using the identification criteria described in Chapter 3.5.1 – is required. The distribution of the number of primary vertices per event reflects the pileup. In the data, there are about 6 vertices per event on average. In the simulation, the distribution is flat and spans a wide range, and has a Poissonian tail; this allows a reweighting of events in order to match the distribution in the data, thus taking pileup correctly into account. The reweighting is applied to the simulated samples.

The trigger selection for data events is based on the loosest unprescaled dimuon triggers, for which the requirements are tightened with an increase of the instantaneous luminosity. For the first about $200\,\text{pb}^{-1}$ symmetric triggers are used, requiring two muons with $p_T > 6\,\text{GeV}$ in the very beginning, then $p_T > 7\,\text{GeV}$ in the following. The rest of the data is based on an asymmetric trigger setup, requiring one muon with $p_T > 13\,\text{GeV}$ and a second muon with $p_T > 8\,\text{GeV}$. In the simulation no trigger selection is applied because the simulated triggers differ from the ones used in data; the trigger efficiency is thus 100% in the simulation. A corresponding correction is applied later.

Muons, jets and $\not{E}_T$ are identified as described in Chapter 3.5, where also the isolation criterion for muons can be found. For the 2011 data analysis, additional muon identification criteria are applied compared to the analysis in Chapter 5, the muon fake rate is absolutely negligible. Also the pseudorapidity selection is more stringent with $|\eta| < 2.1$, having both muons in the efficient trigger region. The momentum selection is identical, $p_{\mathrm{T}} > 20\,\mathrm{GeV}$, which is well above the trigger threshold. Furthermore, both muons need to be matched to a HLT muon which triggered the event. A muon is rated as matched if the differences to the HLT muon are smaller than $\Delta R < 0.3$ and $\Delta p_{\mathrm{T}}/p_{\mathrm{T}} < 0.5$.

The dimuon combination is based on at least two of the selected muons. They need to be of opposite charge. In case of more than one possible combination, the one closest to the nominal Z^0 mass is chosen. Since the muon fake rate is negligible, the remaining events really contain two isolated muons of opposite charge. As can be seen in Figure 5.1, where the selection is very similar, apart from $\mathrm{Z}^0 \to \mu^+\mu^-$ and $\mathrm{t\bar{t}}$ events there remain small contributions from $\mathrm{Z}^0 \to \tau^+\tau^-$, tW, and dibosons. The Z^0 invariant mass window is defined as $60\,\mathrm{GeV} < M_{\mu^+\mu^-} < 120\,\mathrm{GeV}$.

The measurement of jet energies needs to be corrected for the pileup contribution, which is estimated for each event using the jet-area method described in [157], and subtracted from the p_{T} response. Jets are selected to be in the kinematic range $p_{\mathrm{T}} > 25\,\mathrm{GeV}$ and $|\eta| < 2.1$. The pseudorapidity is chosen such that most of the tracks belonging to a jet with cone $\Delta R < 0.5$ can be reconstructed. Furthermore the jets need to be separated from both muons belonging to the Z^0 decay by at least $\Delta R > 0.5$. At least one of these selected jets is required for each event.

Finally a selection of b jets is applied, the selected jets are the basis for this. The b jets are identified by secondary vertices in a high-efficiency (HE) and a high-purity (HP) variant, as described in Chapter 3.5.6. The tight jet pseudorapidity selection ensures optimal b-tagging performance. Both variants are studied, but the HP version is chosen for the cross-section calculation. At least one b jet is required. The reference primary vertex for the secondary vertex is in more than 99.9% of the events identical to the Z^0 vertex, thus the effect from misassignment can be neglected [158].

Additional studies span a selection on $\not{E}_{\mathrm{T}} < 40\,\mathrm{GeV}$ to suppress $\mathrm{t\bar{t}}$ background, and the requirement of a second jet and a second b-jet. In different parts of the analysis, some of these additional selection criteria are also studied, which can lead to a better understanding of the bZ^0 process and its measurement, and might be the basis for future analyses with different selections.

6.2.1 Selection Efficiencies and Simulation Scale Factors

To calculate a cross section, each criterion described above requires an estimation of the selection efficiency. This will be discussed later since this requires the exact definition of the cross section as given in Chapter 6.3. Here, the intention is a corresponding weighting of the simulated samples in order to match the efficiencies in data.

All efficiencies concerning the selection on a muon including the trigger selection are summarised in one variable, the muon efficiency ϵ_μ. It is factorised into five sequential relative measurements corresponding to the five

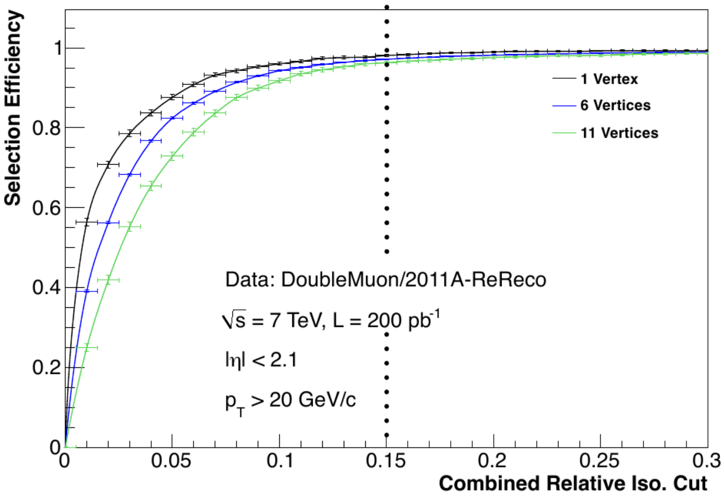

Figure 6.1: Dependency of muon isolation on pileup [159]. The selection efficiency is shown for 1, 6 and 11 selected primary vertices. Indicated is the muon selection criterion $I_{\text{comb}} < 0.15$.

steps: tracking, reconstruction, identification, isolation and the trigger efficiency,

$$\epsilon_\mu = \epsilon_{\text{trk}} * \epsilon_{\text{reco/trk}} * \epsilon_{\text{ID/reco}} * \epsilon_{\text{iso/ID}} * \epsilon_{\text{trig/iso}} \,. \tag{6.1}$$

Each term is estimated with a tag-and-probe method using the two muons of Z^0 decays [159]. All efficiencies have been estimated in data and in simulation on the inclusive Z^0 sample. The efficiency estimates are based on dimuon events including the jet selection requirement in order to reflect the topology of the signal events. In order to estimate the efficiencies with the tag-and-probe method [160], the dimuon triggers cannot be used. Instead, single muon triggers are used, and it is checked that the muon transverse momentum and pseudorapidity distributions are similar for both trigger variants. The trigger efficiency for all applied dimuon triggers is similar since the muon p_{T} selection is well above the trigger thresholds. The stability of the isolation against pileup is also verified, see Figure 6.1. A set of correction factors has been extracted in order to properly rescale simulation events for matching data. The values are calculated for different intervals in the 2-dimensional η-p_{T}-space. The simulated samples are scaled correspondingly to the muon distributions: The uncertainty on the scale factor per muon is less than 1%. The reconstruction and selection efficiency for the jets is close to 100% in data and simulation [159], thus no weights are applied.

The remaining selection efficiency is due to the b-tagging. Besides the efficiency of correctly tagging a b jet $\epsilon_{\text{b-tag}}$, the mistag rate of non-b jets is required, and is separated between efficiencies for c jets $\epsilon_{\text{c-tag}}$ and all other jets $\epsilon_{\text{o-tag}}$. The general methods in use called pTrel and System8 – which are extensions of the tag-and-probe technique – are described in [161]. Both methods show good agreement. Results are given as estimated on inclusive jet samples, and are binned in the 2-dimensional η-p_{T}-space. Since the efficiency depends on the

Table 6.2: Number of expected signal and background events, compared to the event yields in 2.2 fb^{-1} data. All default selection steps are listed, supplemented with additional steps.

Selection	$t\bar{t}$	bZ^0	cZ^0	lZ^0	Sum	Data
Dimuons	969 ± 9	38877 ± 83	178210 ± 179	466801 ± 289	684857 ± 350	696786
1 jet	948 ± 9	10769 ± 44	39203 ± 84	86088 ± 124	137007 ± 156	134725
1 b (HE)	700 ± 8	3303 ± 24	1706 ± 18	814 ± 12	6523 ± 33	6734
2 b (HE)	217 ± 4	154 ± 5	16 ± 2	2 ± 1	388 ± 7	412
1 b (HP)	537 ± 7	2128 ± 20	502 ± 10	51 ± 3	3218 ± 23	3362
2 b (HP)	106 ± 3	67 ± 4	1 ± 1	0 ± 0	175 ± 5	172

specific event selection, scale factors between data and simulation are provided for general usage instead of absolute efficiencies; but absolute values are also provided. Scale factors for c jets are assumed to be the same as for b jets. The scale factors are provided for both, HE and HP b-tags. Due to huge statistical power, $\epsilon_{\text{o-tag}}$, or the mistagging fraction $1-\epsilon_{\text{o-tag}}$, can be estimated in very fine bins, thus it is used directly in the presented analysis. The other two contributions are estimated as explained in the following. The efficiency $\epsilon_{\text{b-tag}}$ ($\epsilon_{\text{c-tag}}$) in simulation has been calculated for the bZ^0 (cZ^0) sample in the 2-dimensional η-p_T-space of the jets [150], and are multiplied with the provided scale factors between data and simulation to estimate the efficiency in data. These efficiencies are estimated on all events fulfilling the dimuon and jet selection. The simulated samples are scaled using the scale factors mentioned above in order to model the data, depending on the generator-level flavour.

6.2.2 Selection Steps and Event Yields

In order to compare the event yields and differential distributions between simulation and data, several steps are performed as described above. Summarising, after scaling the samples to the data luminosity a reweighting on the number of primary vertices is required in order to account for pileup, and phase-space dependent scaling factors are applied due to the lepton efficiencies and b-tagging efficiencies. The number of observed events in data compared to the expected events from simulation is given in Table 6.2 after each sequential selection step described above:

- Dimuons: Full dimuon selection with $60\,\mathrm{GeV} < M_{\mu^+\mu^-} < 120\,\mathrm{GeV}$
- 1 jet: dimuons with at least one selected jet
- 1 b (HP): dimuons with at least one HP b jet

Additional steps can be found in different parts of the analysis as additional information. These are:

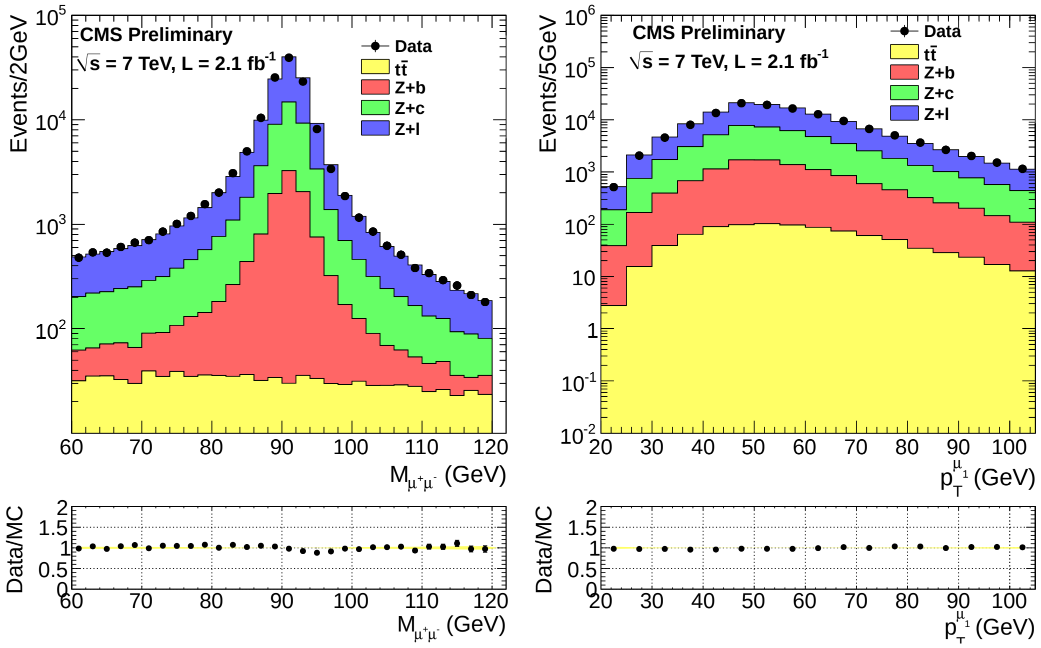

Figure 6.2: Dimuon mass distribution and p_{T}-distribution of muon with bigger p_{T} [150]. Distributions are shown for full dimuon+jet selection.

- 1 b (HE): dimuons with at least one HE b jet
- 2 b (HE): dimuons with at least two HE b jets
- 2 b (HP): dimuons with at least two HP b jets
- 1 b (HE) & $\not\!\!E_{\mathrm{T}}$: dimuons with at least one HE b jet and $\not\!\!E_{\mathrm{T}}$ selection
- 1 b (HP) & $\not\!\!E_{\mathrm{T}}$: dimuons with at least one HP b jet and $\not\!\!E_{\mathrm{T}}$ selection
- + 2nd jet: dimuons with at least one HP b jet and $\not\!\!E_{\mathrm{T}}$ selection and at least one additional jet
- + 2nd b (HE): dimuons with at least one HP b jet and $\not\!\!E_{\mathrm{T}}$ selection and at least one additional HE b jet
- + 2nd b (HP): dimuons with at least two HP b jets and $\not\!\!E_{\mathrm{T}}$ selection

It can be seen, that the requirement of at least one b-tag makes the signal the dominant contribution. However, future analyses requiring two b-tags need to suppress the $\mathrm{t\bar{t}}$ background, which e.g. can be done using the mentioned selection on $\not\!\!E_{\mathrm{T}} < 40\,\mathrm{GeV}$. This is due to the presence of in general two hard b jets in $\mathrm{t\bar{t}}$ events, while there is often only one in $\mathrm{bZ^0}$ events. The agreement between data and simulation is good but not perfect, as also demonstrated by the following distributions. Figure 6.2 shows comparisons for the selection step “1 jet”.

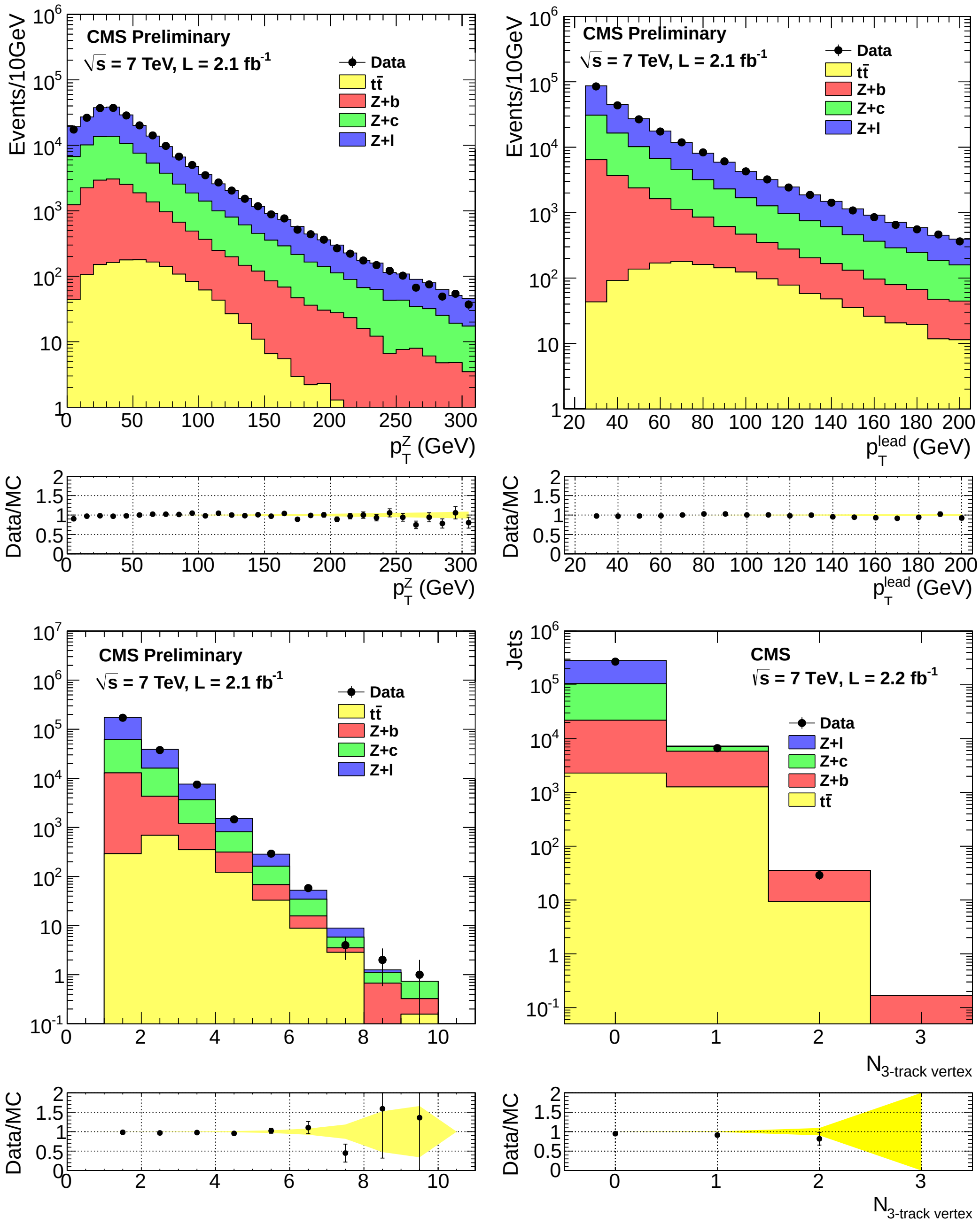

Figure 6.3: Data-to-simulation comparison for selection "1 jet" [159] [151]. Top left: p_T-distribution of Z^0. Top right: p_T-distribution of leading jet. Bottom left: multiplicity of selected jets. Bottom right: Multiplicity of selected HP secondary vertices.

The results in the electronic decay mode of the Z^0 are similar [150][159]. The following set of comparison images is thus produced for both decay channels together, making use of the maximum statistical power for the distributions. Figure 6.3 shows several distributions again for the selection "1 jet" for the reconstructed Z^0 and the selected jets. The jet multiplicity shows good agreement even for large values, and also the description of p_{T} of the Z^0 and the leading jet is excellent. The secondary vertex multiplicity is also well described and illustrates the background suppression power of requiring one or two b jets. Figure 6.4 shows the modelling of pileup and $\not{E}_{\mathrm{T}}$. The multiplicity of selected primary vertices shows that despite the reweighting the pileup is systematically underestimated. This might be due to different selection efficiencies in data and simulation as a function of pileup, since the events are reweighted before any selection is applied, but it is more probably due to the reference distribution for data in use which is provided centrally and does not reflect perfectly the distribution for each amount of data used in a specific analysis. Another point is the fact that pileup arising from the previous and the following bunch crossing is not taken into account in the simulation for weighting. The $\not{E}_{\mathrm{T}}$-distribution shows a systematic underestimation in the Z^0 samples, where in principle no natural $\not{E}_{\mathrm{T}}$ is expected at all—the mismatch might be correlated with the mismatch of pileup. Figure 6.5 shows distributions for selection "1 b (HP)". The p_{T}-distributions of the Z^0 and of the leading b jet are slightly underestimated. The expectation of selected events from simulation is smaller than the data yield (5194/5352) [150], the excess seems to be for Z^0 in the interval $50\,\mathrm{GeV} < p_{\mathrm{T}}^{\mathrm{Z}^0} < 120\,\mathrm{GeV}$ and for the jet around $p_{\mathrm{T}}^{\mathrm{b}} \approx 70\,\mathrm{GeV}$. This hardening of the spectrum in data could come from higher-order corrections [162][163]. The azimuth angle distance between the Z^0 and the leading b jet shows a deficit in the region $2 < \Delta\phi(\mathrm{Z}^0, \mathrm{b}) < 2.7$. However, a part of the lack of simulated events comes from the fact, that the $\mathrm{t\bar{t}}$ contribution is underestimated as detailed in Chapter 6.5.3, but it cannot explain the full difference between data and simulation yields.

6.3 Definition of Cross Section and Generalities of Measurement

The presented analysis aims for the cross-section measurement of bZ^0, and for comparison to predictions, which requires a definition of the cross section feasible for both. Corrections to a common level of consideration need to be made. This section comprises the cross-section definition and generalities of a measurement, but first some general thoughts about their common level of consideration.

6.3.1 General Thoughts

The process bZ^0 is defined as the production of a Z$^0/\gamma^*$ boson in association with at least one b jet. The measurement is by nature performed on detector-

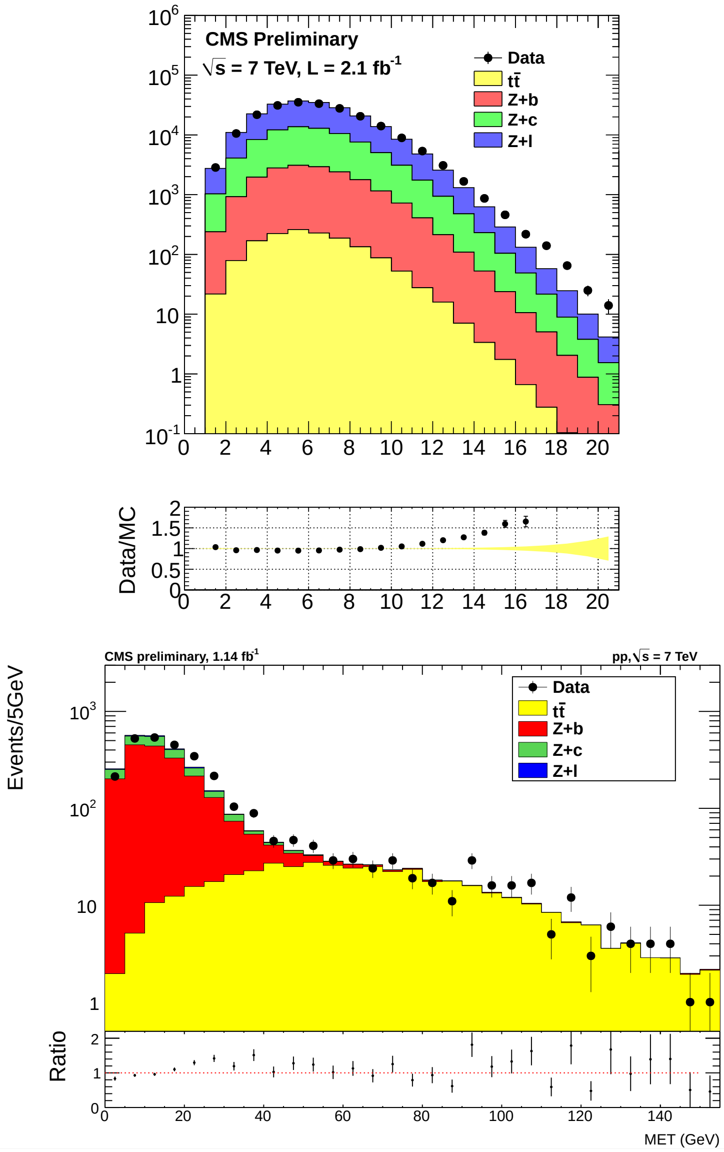

Figure 6.4: Modelling of pileup and $\not\!\!E_{\rm T}$ [159]. Top: multiplicity of selected vertices for selection "1 jet". Bottom: $\not\!\!E_{\rm T}$-distribution for selection "1 b (HP)".

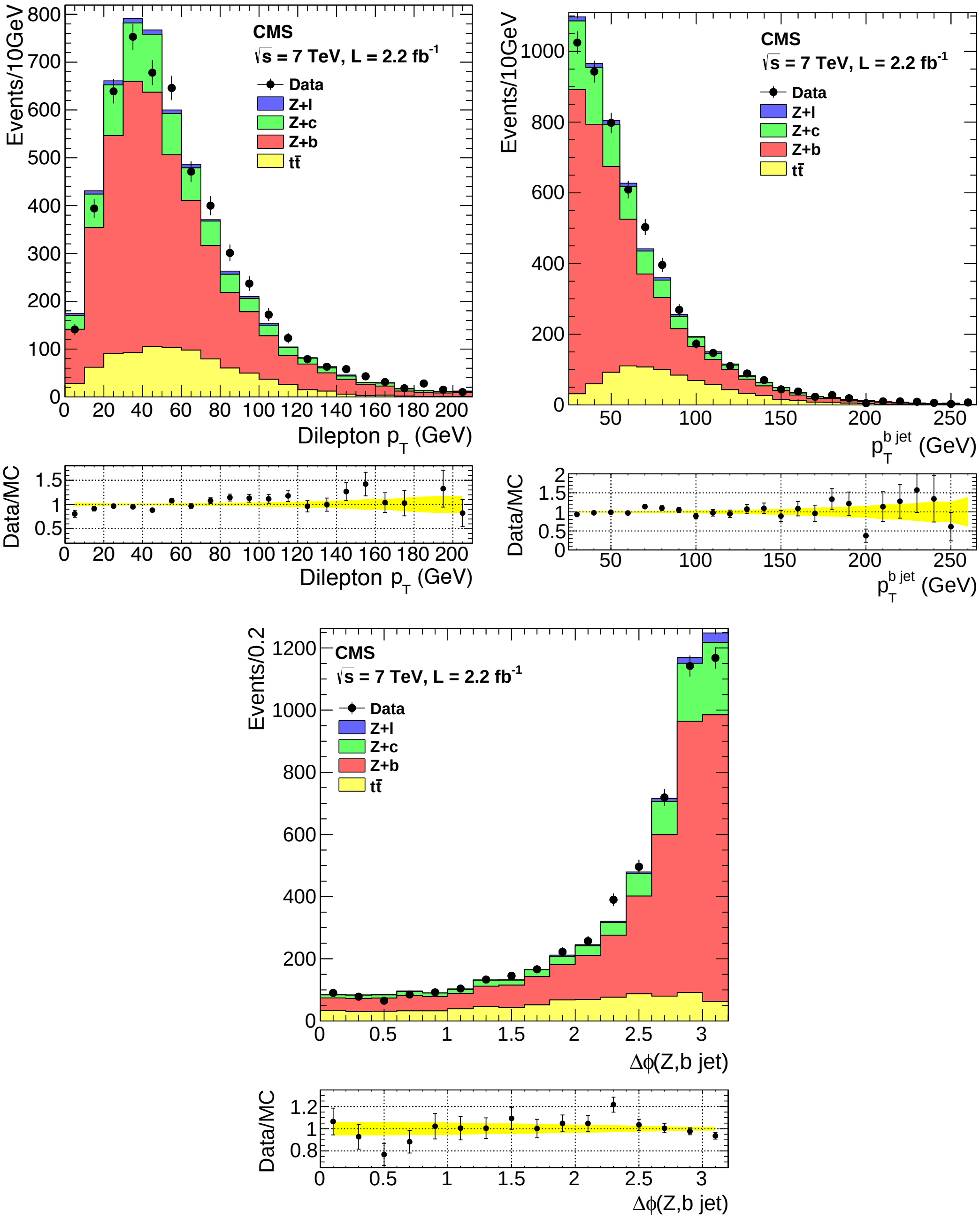

Figure 6.5: Data-to-simulation comparison for selection “1 b (HP)” [151]. Top left: p_T-distribution of Z^0. Top right: p_T-distribution of leading b jet. Bottom: $\Delta\phi$-distribution between Z^0 and leading b jet.

level. The cross section however must be defined on hadron-level (also called generator-level), requiring a correction factor C_h from detector-level to hadron-level for the measurement, or even at parton-level, requiring an additional correction factor C_p between hadron-level and parton-level. These two levels allow comparisons to theory predictions. Furthermore the process can be defined as a visible cross section, restricting the interactions in phase space close to the measured one, or as inclusive cross section spanning the whole available phase space requiring an acceptance correction A to extrapolate into the unmeasured phase space.

The criteria on the Z^0/γ^* are chosen as follows: the mass of the boson is restricted to $60\,\mathrm{GeV} < M_{\mathrm{Z}^0(\gamma^*)} < 120\,\mathrm{GeV}$, and only the muonic decay mode $\mathrm{Z}^0 \to \mu^+\mu^-$ is considered. The muons can be defined on hadron-level, i.e. muons before electromagnetic FSR, resulting in a contribution to C_h. They can be defined for a visible cross section with selections on p_T and η identical to the phase space selected for the measurement, or inclusive spanning the whole phase space requiring an acceptance correction A_l.

Jets can be defined at hadron-level (contributing to C_h) or parton-level (contributing to $C_\mathrm{h}{\cdot}C_\mathrm{p}$). Parton-level jets are built from all quarks and gluons after showering before hadronisation. Hadron-level jets are built from all showered particles after hadronisation (treated as stable by the event generator) but neutrinos, since neutrinos do not contribute to the jet measurement. The association of the b flavour to a parton jet is simply requiring at least one b quark as jet constituent. The b-flavour association for hadron jets is done with geometrical matching of an object identifying the flavour to the jet within $\Delta R < 0.5$, the object can be chosen in several ways: either it is based on b quarks or on B hadrons. The former can be separated again into the latest b quark before hadronisation or a parton jet of b flavour, the latter is based on the latest B hadron, the one with the b decay. In order to define bZ^0 as a measurable process – i.e. it can be distinguished from inclusive Z^0 production – the cross section cannot be taken inclusively in jet kinematics. The straightforward choice is to restrict the phase space to be identical to the measured one, thus avoiding extrapolations into unmeasured phase space, which means jet kinematics of a visible cross section.

Finally the origins of the Z^0 and the b quark need to be defined. They can occur from the same process (as described in Chapter 2.3.3), or they can arise in MPI, one parton-parton interaction producing the Z^0 and another one resulting in b jets. The two possibilities are not separated in the measurement; and MPI is also contained in all simulated samples in use. A rough estimate results in about 2% contribution from MPI [158]. However, the theory prediction used later for comparisons does not contain MPI.

6.3.2 Definition of Cross Section

Two cross sections are defined, the visible and the inclusive cross section. Both are defined as proton-proton cross sections including contributions from MPI.

The inclusive cross section $\sigma_{\mathrm{inc}}^{\mathrm{bZ}^0}$ is defined at hadron-level as

$$\begin{gathered}\sigma_{\mathrm{inc}}^{\mathrm{bZ}^0} = \sigma\left(\mathrm{pp} \to \mathrm{bZ}^0 + X\right) \times \mathrm{BR}(\mathrm{Z}^0 \to \mu^+\mu^-)\,, \\ 60\,\mathrm{GeV} < M_{\mathrm{Z}^0} < 120\,\mathrm{GeV}\,,\end{gathered} \tag{6.2}$$

with the following additional restrictions. At least one b jet needs to be in the process, chosen is the variant with hadron jets being geometrically matched to a B hadron. The jet is constrained to the visible phase space as it is selected in the measurement: $p_{\mathrm{T}}^{\mathrm{b}} > 25\,\mathrm{GeV}$, $|\eta^{\mathrm{b}}| < 2.1$ and $\Delta R(\mathrm{jet,muons}) > 0.5$. This definition of the inclusive cross section is chosen such, that comparisons to theoretical calculations, but also to measurements in the $\mathrm{Z}^0 \to \mathrm{e}^+\mathrm{e}^-$ decay mode with independent lepton selections, are feasible.

The definition of the visible cross section $\sigma_{\mathrm{vis}}^{\mathrm{bZ}^0}$ is kept as close to the phase space of the measurement as possible, reducing the uncertainty of theoretical model assumptions to a minimum. Thus, in addition to all selections of $\sigma_{\mathrm{inc}}^{\mathrm{bZ}^0}$ – which are identically applied – the leptons are restricted:

$$\sigma_{\mathrm{vis}}^{\mathrm{bZ}^0} = \sigma_{\mathrm{inc}}^{\mathrm{bZ}^0} \qquad \text{with} \qquad |\eta^\mu| < 2.1\,,\; p_{\mathrm{T}}^{\mu} > 20\,\mathrm{GeV}\,. \tag{6.3}$$

The acceptance to extrapolate the visible to the inclusive cross section is then given by the lepton acceptance A_{l},

$$A_{\mathrm{l}} = \frac{\sigma_{\mathrm{vis}}^{\mathrm{bZ}^0}}{\sigma_{\mathrm{inc}}^{\mathrm{bZ}^0}}\,. \tag{6.4}$$

The selection of b jets with the given thresholds guarantees that the difference of the cross sections for the different possible b jet definitions is kept small, since big differences between true and reconstructed jet values – in p_{T} as well as in the three-dimensional direction – but also between the different flavour-matching schemes are mainly in the rejected phase space. Correlation studies are performed in [158]. The migration effects are smaller for hadron-level than for parton-level jets.

6.3.3 Generalities of Cross-Section Measurement

A cross section σ from a measurement is calculated from the basic formula

$$\sigma = \frac{N_{\mathrm{sig}}}{\epsilon_{\mathrm{tot}} \cdot L}\,, \tag{6.5}$$

where N_{sig} is the number of signal events, ϵ_{tot} the total event selection efficiency, and L the integrated luminosity. The luminosity is measured directly by CMS. The number of signal events requires an estimate of the contained background in the number of observed events. The background estimates are emphasised in this thesis and described in Chapter 6.4, Chapter 6.5 and Chapter 6.6. The total event selection efficiency spans the discussed corrections from detector-level to hadron-level C_{h} and acceptance corrections in the unmeasured phase space A_{l}, but also corrections due to the efficiencies of the lepton selection ϵ_{l} and the b-jet selection ϵ_{b}. These efficiencies and correction factors are determined in Chapter 6.7.

6.4 Purity of b Jets

The b-jet purity of events P defines the fraction of selected events where the event really contains b jets and not only misidentified jets of other flavour—it is used as the estimate of all backgrounds which do not comprise real b jets. The purity estimate employs the secondary vertex mass m_{SV} distribution [150], which can be also used to estimate mistagging rates [161]. The definition of m_{SV} is given by the invariant mass of all tracks originating from the secondary vertex, assuming the pion mass for each track. The separation power is given by the fact, that the reconstructed secondary vertex mass reflects the mass of the decaying hadron—vertices originating from B mesons show in general bigger masses than those arising from D mesons, which themselves have bigger masses then the mesons originating from lighter flavours only.

At least one b jet is required in the final state, thus m_{SV} is built for the tagged jet leading in p_{T}. The estimation is based on a fit of templates, gained from simulation, to the data distribution. The final values are based on a multijet sample (QCD) and the inclusive Z^0 sample as used throughout this chapter. The flavour of the reconstructed jet is determined from the flavour of the corresponding generated jet. The advantage of the Z^0 sample is the correct description of the jet kinematics compared to data, but the drawback is the limited size leading to distinctive statistical errors. For the QCD sample, there is no limitation in statistical power, but especially the p_{T}-distribution disagrees—the events are scaled as a function in the 2-dimensional η-p_{T}-space, and additionally in the number of selected primary vertices, in order to model the data distributions. In fact the m_{SV}-distribution depends on the kinematics, e.g. in general it gets bigger with increasing p_{T}. The template fit on the rescaled QCD sample is shown in Figure 6.6, the effects explained in the figure are similar for both template sets. The HP b-tag has the higher purity, as expected; a main difference to the HE b-tag is the requirement of at least 3 tracks to form a secondary vertex, which removes all two-body decays like the $\mathrm{K_S} \to \pi^+\pi^-$ from the distributions. The fit uncertainty due to data is assigned as statistical uncertainty.

Different systematic effects are studied. The difference between both template sets is the basis for the uncertainty arising from the specific sample. The central value is taken as the weighted mean of both, and the systematic uncertainty is conservatively set to the envelope of both uncertainties. Furthermore, the statistical power of the simulation sample and the template parameterisation are of importance; the parameterisation was varied, the influence is negligible. Another effect is due to the size of the contribution from b quarks originating from gluon splitting and not from the association to the Z^0 production, i.e. processes where the Z^0 does not couple directly to the b quark (like in Figure 2.10, middle). The kinematics and thus potentially the m_{SV}-distribution of such b jets is in general different—however no difference of the purity estimate shows up when using b-from-gluon templates instead, neither in the presented analysis, nor in [164]. Finally the variation as a function of

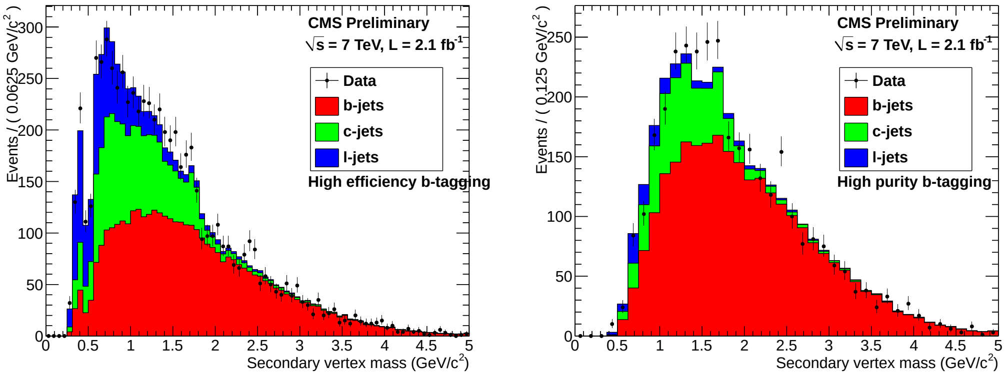

Figure 6.6: Template fit of secondary vertex mass distribution with QCD sample [150]. Left: selection with HE b tag. Right: selection with HP b tag. The peak around $m_{\mathrm{SV}} \approx 0.5\,\mathrm{GeV}$ stems from $\mathrm{K_S} \rightarrow \pi^+\pi^-$. The edge around 2 GeV is due to D-meson decays, the region above is dominated by B mesons. The bump in the b-jet template at the $\mathrm{K_S}$ mass hypothetically arises from kaons originating from B decays.

pileup is checked; fluctuations are observed, but within the statistical uncertainty and no clear trend is visible. Except for the uncertainty arising from the choice of the sample, no additional systematic uncertainty is assigned. The values are in agreement with simulation predictions and with the 2010 data analysis [56].

The described purity is the purity of the b-tagged jet leading in p_{T}. However the desired quantity is the event purity. Multiple jets can occur per event, and if more than one jet is tagged, the chance of having actually a true b jet in the event increases. Allowing also two b-tagged jets lead to the final event purity for at least one HP b-tag [151]:

$$P = (81.5 \pm 2.9)\,\% \,. \tag{6.6}$$

Events with more than two HP b-tags are not yet expected and not observed. The event purity for at least one HE b-tag is significantly lower at $P = (60.2 \pm 2.2)\,\%$ [150].

6.5 Estimation of the $\mathrm{t\bar{t}}$ Background

The purity indicates the signal contamination due to mistagging of non-b jets. The $\mathrm{t\bar{t}}$ background however needs to be determined independently, since there are in general two hard b jets in the event; they are part of the estimated purity. The probability of having none of both b jets but an additional jet of different flavour selected is assumed to be negligible, thus there is no double-counting of events. This section describes a method to estimate the signal contamination from $\mathrm{t\bar{t}}$ events, using the dilepton invariant mass spectrum, and the results. Besides the presented description of the dimuon final state, also results produced with the same method in the electron decay channel and correlations between both channels can be found in Appendix B.2, since both are used in the publication [151].

6.5.1 Description of the Method

The signal is defined as events from $\mathrm{Z}^0/\gamma^* \to \mu^+\mu^-$, which are produced in association with b quarks. Although the final signal definition is reduced to the mass interval [60 GeV, 120 GeV], this is not taken into account in this section, since the behaviour outside the mass window is the crucial ingredient for this method. The selection is optimised to have the signal as dominant contribution within this window, and the peak from the Z^0 and its tails are almost completely contained in this window. In this section the distinction between the different flavours of the associated jets is not taken into account—all Drell–Yan processes with decay $\mathrm{Z}^0/\gamma^* \to \mu^+\mu^-$ are treated collectively, and are labelled as Z^0.

There are two sideband regions, one below the mass window [60 GeV, 120 GeV], and one above. After the full event selection including b-tags the remaining Z^0 events are mainly signal events (bZ^0). In the upper sideband, there are only few Z^0 events left. In the lower sideband the "Z^0" contribution is still a notable part of the remaining events, since the contribution from γ^* increases with lower invariant masses. However, selections of a minimum p_T at trigger level and also on the analysis level for both muons reduce the contributions at low invariant masses. This is due to the strong correlation of the invariant mass and the p_T of the muons, since the kinematics of the muons depend directly on the decay of the Z^0/γ^*.

For the top-pair background, the two muons come from the different three-body decay chains of the top and the antitop quark. Thus, they are almost uncorrelated in p_T and η. As a consequence, the shape in the invariant mass spectrum is a smooth curve, and the muon p_T selection has only a small influence in the low mass region. Also high values of the mass are possible, if the muons have large momenta and the opening angle between both muons is big. Summarising, the top-pair contribution is similar in all three regions (signal region, lower and upper sideband). Hence it is the dominating contribution in the sidebands, especially in the upper one.

The basic principle of estimating the $\mathrm{t\bar{t}}$ contamination in the signal region is to measure the $\mathrm{t\bar{t}}$ contribution in the sidebands and to extrapolate to the signal region. In the following formulas the signal region is defined as inside ("in"), and the sideband region as outside ("out"). The number of $\mathrm{t\bar{t}}$ events outside is given by

$$N_{\mathrm{t\bar{t}}}^{\mathrm{out}} = N_{\mathrm{obs}}^{\mathrm{out}} - N_{\mathrm{other}}^{\mathrm{out}} - N_{\mathrm{Z}^0}^{\mathrm{out}} \,. \tag{6.7}$$

The number of observed events $N_{\mathrm{obs}}^{\mathrm{out}}$ is measured from data. $N_{\mathrm{other}}^{\mathrm{out}}$ is the number of all other backgrounds together, excluding $\mathrm{t\bar{t}}$ and Z^0. In principle it can be taken from simulation, but as shown in Chapter 6.6 it is only a small contribution of about 1–2% of all events. Thus, it is set to zero. $N^{\mathrm{out}}_{\mathrm{Z}^0}$ is the number of the Drell–Yan events. This number is not known a priori, but the following will show how it can be replaced.

The extrapolation from outside to inside is then done via

$$N^{\mathrm{in}}_{\mathrm{t\bar{t}}} = R^{\mathrm{in/out}}_{\mathrm{t\bar{t}}} \times N^{\mathrm{out}}_{\mathrm{t\bar{t}}} \,, \tag{6.8}$$

where the ratio $R^{\mathrm{in/out}}_{\mathrm{t\bar{t}}}$ is defined as the quotient of the event selection efficiencies for an event to be inside $\epsilon^{\mathrm{in}}_{\mathrm{t\bar{t}}}$ and outside $\epsilon^{\mathrm{out}}_{\mathrm{t\bar{t}}}$, where these efficiencies are the probability of a $\mathrm{t\bar{t}}$ event to end in the respective region. It is abbreviated as $R_{\mathrm{t\bar{t}}}$:

$$\begin{aligned} R_{\mathrm{t\bar{t}}} = R^{\mathrm{in/out}}_{\mathrm{t\bar{t}}} &= \frac{\epsilon^{\mathrm{in}}_{\mathrm{t\bar{t}}}}{\epsilon^{\mathrm{out}}_{\mathrm{t\bar{t}}}} \\ &= \frac{n^{\mathrm{in}}_{\mathrm{t\bar{t}}}}{n^{\mathrm{out}}_{\mathrm{t\bar{t}}}} \,. \end{aligned} \tag{6.9}$$

It is taken from simulation, but is corrected with measurements as explained later. $n^{\mathrm{in}}_{\mathrm{t\bar{t}}}$ and $n^{\mathrm{out}}_{\mathrm{t\bar{t}}}$ are the number of selected simulated $\mathrm{t\bar{t}}$ events inside and outside, but not scaled to luminosity in order to get an idea about their statistical power.

Given an estimate of the $\mathrm{t\bar{t}}$ contamination, the number of Z^0 events inside can be obtained using

$$N^{\mathrm{in}}_{\mathrm{Z}^0} = N^{\mathrm{in}}_{\mathrm{obs}} - N^{\mathrm{in}}_{\mathrm{other}} - N^{\mathrm{in}}_{\mathrm{t\bar{t}}} \,. \tag{6.10}$$

Like for the sideband region, $N^{\mathrm{in}}_{\mathrm{obs}}$ is measured from data, and $N^{\mathrm{in}}_{\mathrm{other}}$ is about 5% of all events and could be taken from simulation, but is set to zero. The influence of neglecting the other backgrounds in this $\mathrm{t\bar{t}}$ estimate is discussed in Chapter 6.6.

The estimated value $N^{\mathrm{in}}_{\mathrm{Z}^0}$ is inserted in the following formula,

$$N^{\mathrm{out}}_{\mathrm{Z}^0} = \left(R^{\mathrm{in/out}}_{\mathrm{Z}^0}\right)^{-1} \times N^{\mathrm{in}}_{\mathrm{Z}^0} \,, \tag{6.11}$$

where the ratio $R^{\mathrm{in/out}}_{\mathrm{Z}^0}$ is defined analogous to $\mathrm{t\bar{t}}$, and also taken from simulation:

$$\begin{aligned} R_{\mathrm{Z}^0} = R^{\mathrm{in/out}}_{\mathrm{Z}^0} &= \frac{\epsilon^{\mathrm{in}}_{\mathrm{Z}^0}}{\epsilon^{\mathrm{out}}_{\mathrm{Z}^0}} \\ &= \frac{n^{\mathrm{in}}_{\mathrm{Z}^0}}{n^{\mathrm{out}}_{\mathrm{Z}^0}} \end{aligned} \,. \tag{6.12}$$

Finally, this description of the Z^0 sideband contribution is used to replace the unknown value $N^{\mathrm{out}}_{\mathrm{Z}^0}$ in equation 6.7. The formula for calculating the $\mathrm{t\bar{t}}$ contamination in the signal region is obtained putting all these Equations 6.7–6.12 together. This leads to

$$N^{\mathrm{in}}_{\mathrm{t\bar{t}}} = \frac{R_{\mathrm{t\bar{t}}}}{R_{\mathrm{Z}^0} - R_{\mathrm{t\bar{t}}}} \times \left[R_{\mathrm{Z}^0} \cdot \left(N^{\mathrm{out}}_{\mathrm{obs}} - N^{\mathrm{out}}_{\mathrm{other}}\right) - N^{\mathrm{in}}_{\mathrm{obs}} + N^{\mathrm{in}}_{\mathrm{other}}\right] \,. \tag{6.13}$$

Thus, the estimation depends on $N^{\mathrm{in}}_{\mathrm{t\bar{t}}} = N^{\mathrm{in}}_{\mathrm{t\bar{t}}}\left(N^{\mathrm{in}}_{\mathrm{obs}}, N^{\mathrm{out}}_{\mathrm{obs}}, N^{\mathrm{in}}_{\mathrm{other}}, N^{\mathrm{out}}_{\mathrm{other}}, R_{\mathrm{t\bar{t}}}, R_{\mathrm{Z^0}}\right)$.

The lower sideband has several disadvantages. As already mentioned, the contribution from $\mathrm{Z}^0/\gamma^* \to \mu^+\mu^-$ is a notable part there, and the $\mathrm{Z}^0/\gamma^* \to \tau^+\tau^-$ contribution with muonic decay of the taus is mainly in this region. Systematic effects due to trigger efficiencies or the p_{T}-thresholds of the final muon selection show up mainly in the low-mass region. Furthermore, the Z^0 sample has an invariant mass cut on generator-level of $M^0_{\mathrm{Z}}/\gamma^* > 50\,\mathrm{GeV}$. In principle one could add the missing region in the invariant dimuon mass range $[12\,\mathrm{GeV}, 50\,\mathrm{GeV}]$ using additional PYTHIA samples for $\mathrm{Z}^0/\gamma^* \to \mu^+\mu^-$, as it is done in Chapter 5. Since the PYTHIA samples start with generated masses $M^0_{\mathrm{Z}}/\gamma^* > 10\,\mathrm{GeV}$, they can be added in the interval $[12\,\mathrm{GeV}, 50\,\mathrm{GeV}]$. Below 12 GeV one would have to deal also with the Υ resonances. The PYTHIA sample can be normalised to the MadGraph sample in the overlapping region above $M^0_{\mathrm{Z}}/\gamma^* > 50\,\mathrm{GeV}$. This could also be applied separately for the different flavours of the associated jet production, normalising every subset to the corresponding MadGraph subset.

Due to the mentioned reasons, only the upper sideband is used for the definition of the outside region. It has an upper mass limit in order to use results from a top analysis produced in the same mass window. The interval defining the sideband region covers the dimuon invariant mass $[120\,\mathrm{GeV}, 400\,\mathrm{GeV}]$. Using the lower sideband in addition would select more data events in the outside region, but the gain in statistical precision would be faced by additional systematic effects. The method described in this section is equivalent to a template fit using two bins.

6.5.2 Ingredients and Corresponding Uncertainties

Recapitulating, with the assumption of fixed other backgrounds $N^{\mathrm{in}}_{\mathrm{other}}$ and $N^{\mathrm{out}}_{\mathrm{other}}$, especially with setting them to zero, there is a system of four equations,

$$\begin{array}{rcl} N^{\mathrm{in}}_{\mathrm{obs}} & = & N^{\mathrm{in}}_{\mathrm{Z^0}} + N^{\mathrm{in}}_{\mathrm{t\bar{t}}} \\ N^{\mathrm{out}}_{\mathrm{obs}} & = & N^{\mathrm{out}}_{\mathrm{Z^0}} + N^{\mathrm{out}}_{\mathrm{t\bar{t}}} \\ N^{\mathrm{in}}_{\mathrm{t\bar{t}}} & = & R_{\mathrm{t\bar{t}}} \times N^{\mathrm{out}}_{\mathrm{t\bar{t}}} \\ N^{\mathrm{in}}_{\mathrm{Z^0}} & = & R_{\mathrm{Z^0}} \times N^{\mathrm{out}}_{\mathrm{Z^0}} \end{array} , \tag{6.14}$$

for estimating the four unknowns $N^{\mathrm{in}}_{\mathrm{Z^0}}$, $N^{\mathrm{in}}_{\mathrm{t\bar{t}}}$, $N^{\mathrm{out}}_{\mathrm{Z^0}}$ and $N^{\mathrm{out}}_{\mathrm{t\bar{t}}}$. Thus, it is analytically solvable and the error propagation can be done in the analytical way using the derivatives. The final formula shows the dependency on the four input parameters

$$N^{\mathrm{in}}_{\mathrm{t\bar{t}}}\left(N^{\mathrm{in}}_{\mathrm{obs}}, N^{\mathrm{out}}_{\mathrm{obs}}, R_{\mathrm{t\bar{t}}}, R_{\mathrm{Z^0}}\right) = \frac{R_{\mathrm{t\bar{t}}}}{R_{\mathrm{Z^0}} - R_{\mathrm{t\bar{t}}}} \times \left[R_{\mathrm{Z^0}} \cdot N^{\mathrm{out}}_{\mathrm{obs}} - N^{\mathrm{in}}_{\mathrm{obs}}\right] . \tag{6.15}$$

The number of observed data events $N^{\mathrm{in}}_{\mathrm{obs}}$ and $N^{\mathrm{out}}_{\mathrm{obs}}$ are needed. They are displayed in Table 6.3. The uncertainties are given by their statistical errors.

Table 6.3: Number of observed events in data inside and outside the signal region. Results are given for the dataset corresponding to $\int \mathcal{L}\mathrm{dt} = 1.1\,\mathrm{fb}^{-1}$.

Selection	$N^{\mathrm{in}}_{\mathrm{obs}}$	$N^{\mathrm{out}}_{\mathrm{obs}}$
Dimuons	373611	5211
1 jet	71185	1554
1 b (HE)	3568	311
1 b (HE) & $\not{E}_{\mathrm{T}}$	3221	133
1 b (HP)	1789	233
1 b (HP) & $\not{E}_{\mathrm{T}}$	1540	92
+ 2nd jet	648	67
+ 2nd b (HE)	116	24

Table 6.4: Relevant input values from simulation for estimation of $\mathrm{t\bar{t}}$ contribution. Shown are the event yields in the signal region and in the sideband. Z^0 and $\mathrm{t\bar{t}}$ yields are not scaled to luminosity, because only their ratio is needed.

Selection	$n^{\mathrm{in}}_{\mathrm{t\bar{t}}}$	$n^{\mathrm{out}}_{\mathrm{t\bar{t}}}$	$n^{\mathrm{in}}_{\mathrm{Z^0}}$	$n^{\mathrm{out}}_{\mathrm{Z^0}}$
Dimuons	10456.0	7553.8	3812094.0	45851.2
1 jet	10229.5	7337.1	752470.7	12013.4
1 b (HE)	7832.1	5435.0	34724.7	474.8
1 b (HE) & $\not{E}_{\mathrm{T}}$	1840.8	1434.4	34089.8	460.4
1 b (HP)	6348.5	4306.4	16812.3	224.8
1 b (HP) & $\not{E}_{\mathrm{T}}$	1507.8	1130.3	16501.7	219.6
+ 2nd jet	1305.7	943.4	6191.5	87.3
+ 2nd b (HE)	558.8	396.9	880.8	13.2

Since the integrated luminosity is not used directly, the value is not relevant. But certainly the used amount of data limits the statistical precision.

Table 6.4 shows the needed input variables from simulation and their values for different steps of the event selection. The resulting ratios $R_{\mathrm{t\bar{t}}}$ and $R_{\mathrm{Z^0}}$ and their statistical errors are given in Table 6.5. The dependency of Equation 6.15 on $R_{\mathrm{t\bar{t}}}$ is about linear, since $R_{\mathrm{Z^0}} \gg R_{\mathrm{t\bar{t}}}$. The dependency on $R_{\mathrm{Z^0}}$ is much weaker. The statistical errors are limited by the size of the simulated samples. Since the ratios are taken from simulation, systematic uncertainties and potential corrections need to be estimated in addition. The values of the ratios $R_{\mathrm{t\bar{t}}}$ and $R_{\mathrm{Z^0}}$ among the different selection steps form a check of systematic effects.

The ratio $R_{\mathrm{t\bar{t}}}$ should not depend strongly on additional jet selections. Two b-jets are produced in every event, and in general they have high momenta, since they originate from the decay of the heavy top quark. There are slight deviations amongst the selection steps due to additional jet or b-tag selections. But compared to their statistical errors, there is no big systematic deviation visible.

Table 6.5: Ratios $R^{\text{in/out}}$ and corresponding statistical errors as taken from simulation.

Selection	$R^{\text{in/out}}_{\text{t}\bar{\text{t}}}$	$R^{\text{in/out}}_{\text{Z}^0}$
Dimuons	1.384 ± 0.021	83.14 ± 0.39
1 jet	1.394 ± 0.021	62.64 ± 0.58
1 b (HE)	1.441 ± 0.025	73.13 ± 3.38
1 b (HE) & $\not{E}_{\text{T}}$	1.283 ± 0.045	74.04 ± 3.47
1 b (HP)	1.474 ± 0.029	74.80 ± 5.02
1 b (HP) & $\not{E}_{\text{T}}$	1.334 ± 0.052	75.13 ± 5.10
+ 2nd jet	1.384 ± 0.059	70.91 ± 7.64
+ 2nd b (HE)	1.408 ± 0.092	66.58 ± 18.44

An additional $\not{E}_{\text{T}}$ antiselection reduces $R_{\text{t}\bar{\text{t}}}$, muon pairs with higher mass are preferred. But the $\not{E}_{\text{T}}$, originating from the two neutrinos, is correlated with the dimuon mass spectrum. The muon and the neutrino from each of the two W decays are strongly correlated. If the two neutrinos have opposite directions the value of $\not{E}_{\text{T}}$ is small, and the event is not deselected. In this case, the muons have bigger opening angles in general, which leads to bigger masses of the dimuon combination. If the neutrinos point in the same direction, the situation is inverted. Lower dimuon masses are reduced by the requirement on $\not{E}_{\text{T}}$. Due to the huge mass of the top quark, which predefines the decay chains, these correlations are not very strong. The method seems to be rather stable against $R_{\text{t}\bar{\text{t}}}$.

For R_{Z^0}, the situation is different. The different selection steps correspond to different event topologies and different couplings. After the dimuon selection, most Z^0 bosons should be produced without additional jets, thus with small p_{T}. When requiring the presence of a jet, most of these events should contain exactly one radiative gluon jet. Since this jet balances the Z^0 in p_{T}, the muons from the decay have different properties. When a jet is b-tagged, the probability that it originates from a quark of flavour b or c is high. This means, that at least one heavy quark jet and possibly two of them have been produced. The Z^0 is potentially not fully balanced by one jet, also if only one is found. If a looser b-tag discriminant (HE) is used, the contamination from light and c flavours is bigger. If the tighter b-tag discriminant (HP) is applied, mainly real b-jets are selected.

The difference between the selection steps can be explained when the components of the inclusive Z^0 production are separated into bZ^0, cZ^0 and lZ^0. For each component separately the ratios are more stable. The ratio is in general bigger for bZ^0 than for cZ^0 and lZ^0. This could be due to the smaller charge of the b quarks and the resulting smaller coupling to the γ^* contribution, which dominates outside the Z^0 peak region. The ratios of bZ^0 lie around 80–95. The ratios of cZ^0 lie around 55–65, and differ only slightly from the ones for lZ^0. For the first selection step (dimuons), all ratios are significantly higher. For the last steps with 2 jets the statistical precision in the sideband gets poor.

The selection on $\not{E}_\mathrm{T}$ should have only a small influence on R_{Z^0}. There is no real $\not{E}_\mathrm{T}$ present, it can only be a fake measurement, except for possible small contributions of neutrinos from semileptonic b and c decays. The topology of the Z^0 decay does not depend on it. Pileup is a potential source for fake $\not{E}_\mathrm{T}$. Also mis-measured lepton momenta will fake $\not{E}_\mathrm{T}$. This is associated to a mis-measured dimuon mass, leading mainly to migrations out of the Z^0 peak. The estimated ratio R_Z^0 shows only small changes with the $\not{E}_\mathrm{T}$ selection.

The $\mathrm{t\bar{t}}$ cross section as estimated in Chapter 5 suffers from the uncertainty of the Drell–Yan background estimate, which is the dominant systematic uncertainty. The estimation is the inverse of the method described: the Z^0 background contribution is measured in the Z^0 peak window and then extrapolated to the sideband regions, which are in fact the signal region of the measurement. However the experimental difference is, that the whole region $M_{\mu^+\mu^-} > 12\,\mathrm{GeV}$ excluding the Z^0 veto is used, and that the window itself is smaller (76 GeV–106 GeV). Another difference is the simulation without pileup. The ratio R_{Z^0} as taken from simulation shows a large difference of about a factor 2 when applying the $\not{E}_\mathrm{T}$ selection, and is the main uncertainty of the method. In the results presented here the behaviour is clearly more stable. This is probably due to the bigger Z^0 window, spanning also the tails – migrations out of the window are reduced – and due to the disregard of the lower sideband which is more sensitive to systematic effects as explained before. Furthermore, the $\not{E}_\mathrm{T}$-distribution is better simulated taking pileup into account. And very important is the different $\not{E}_\mathrm{T}$ selection of $\not{E}_\mathrm{T} < 40\,\mathrm{GeV}$ selecting the core of the distribution – having only small differences of selection efficiencies in data and simulation – instead of $\not{E}_\mathrm{T} > 30\,\mathrm{GeV}$ which selects the tail and thus the effect is bigger (see Figure 6.4).

Summarising, the description of R_{Z^0} seems to be rather good. A systematic uncertainty of 10 % is assigned in addition to the statistical uncertainty to cover the deviations of the different selection steps, and of the composition of bZ^0, cZ^0 and lZ^0 components. The resulting uncertainty for the final estimate of the $\mathrm{t\bar{t}}$ contamination is small compared to others.

The value of $R_{\mathrm{t\bar{t}}}$ can be corrected with a $\mathrm{t\bar{t}}$ measurement performed on the same amount of data. This correction is described in the following.

Correction Factor for Estimate of $R_{\mathrm{t\bar{t}}}$

The $\mathrm{t\bar{t}}$ measurement used for the correction of $R_{\mathrm{t\bar{t}}}$ is described in detail in [148][149]. This will be referred to as “top analysis” in the following, contrary to the presented “Z^0 analysis”. The relevant information is outlined here.

In the top analysis, differential $\mathrm{t\bar{t}}$ cross sections are measured in different dileptonic decay modes, characterised by the final lepton states ee, eμ and $\mu\mu$. Intermediate τ states with leptonic decays are also part of the signal. The two leptons need to be of opposite charge. The same simulated samples as in the Z^0 analysis are used for Z^0 and $\mathrm{t\bar{t}}$, but also others are needed in addition.

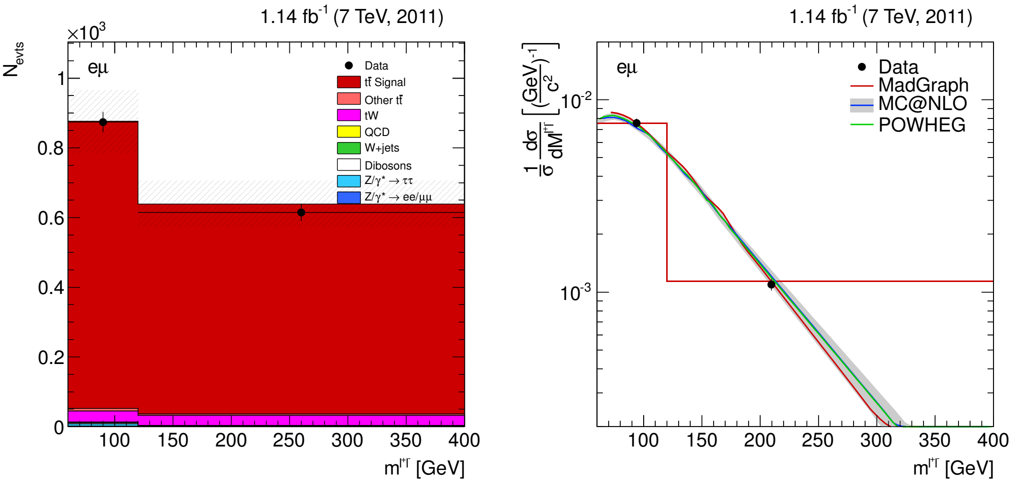

Figure 6.7: Top analysis measurement in the decay channel with eμ final states [165]. The intervals are identical to the signal window and the sideband. Left: Event yield. Right: Normalised differential cross sections, and comparison to unbinned theory predictions. The MadGraph prediction is also shown as binned histogram.

In the decay channel with eμ final states the t$\bar{\text{t}}$ signal is very clean. The Z^0 contribution is very small and results from Z^0 $\to \tau^+\tau^-$ decays. The event yield differential in the dilepton mass is shown in Figure 6.7. The results are produced for the two interesting intervals, the signal and the sideband region. The top analysis uses several different reconstruction and identification criteria as the Z^0 analysis. Also lepton isolation criteria and b-tag algorithms are different. In the eμ channel there are additional differences in the trigger efficiency (eμ trigger), and in the lepton efficiencies, compared to the ee and $\mu\mu$ channels. Thus it is not possible to use the yield plot for controlling the correctness of $R_{\text{t}\bar{\text{t}}}$.

The final results of the top analysis are normalised differential cross sections, differential in different lepton, dilepton, jet and combined parameters, like top properties and properties of the full t$\bar{\text{t}}$ system. The relevant distribution for the Z^0 analysis is the dilepton invariant mass, as given in Figure 6.7. The differential cross sections are normalised to the total cross section in a way that the integral over the full range of the regarded quantity equals 1. The full range is given by all possible values of the regarded quantity, and not only analysed ones—for the dilepton mass, this is $[0, \infty]$. These cross sections are corrected for detector effects, all relevant efficiencies are taken into account. Since these cross sections are differential and normalised, many uncertainties, e.g. from luminosity, cancel completely or partially. Thus, the measurements in the separate bins and the assigned errors are uncorrelated. It might be that very small correlations remain. But taking them into account when building a ratio $R_{\text{t}\bar{\text{t}}}$ could only reduce the corresponding uncertainty, i.e. it is conservative to treat the errors as uncorrelated. The remaining systematic uncertainties are

Table 6.6: Normalised cross sections $\frac{1}{\sigma}\frac{d\sigma}{dM^{l^+l^-}}$ in $\left[\left(\frac{\mathrm{GeV}}{c^2}\right)^{-1}\right]$ from the top analysis, differential in dilepton mass $M^{l^+l^-}$ [165]. Results are shown for the eμ channel, and for the MadGraph prediction. The last row gives the in/out ratio $R_{\mathrm{t\bar{t}}}^{\mathrm{top}}$ for the two cases. Statistical and systematic errors are given separate. The values are scaled by a factor 1000.

$M^{l^+l^-}$	$\frac{1}{\sigma}\frac{d\sigma}{dM^{l^+l^-}}$ $(e\mu)$	$\frac{1}{\sigma}\frac{d\sigma}{dM^{l^+l^-}}$ (MadGraph)
$[60\,\mathrm{GeV}, 120\,\mathrm{GeV}]$	$7.55 \pm 0.27 \pm 0.35$	7.55
$[120\,\mathrm{GeV}, 400\,\mathrm{GeV}]$	$1.09 \pm 0.05 \pm 0.07$	1.14
$R_{\mathrm{t\bar{t}}}^{\mathrm{top}}$	$1.484 \pm 0.083 \pm 0.113$	1.419

given by experimental uncertainties dominated by the jet selection, originating e.g. from the jet energy scale or b-tagging, and by theoretical uncertainties due to hadronisation, parton-shower matching in MadGraph, the top mass and the Q^2-scale. However the theoretical uncertainties are partly limited by the size of specific simulated samples from which they are estimated. They could be largely reduced having bigger samples.

The needed ratio $R_{\mathrm{t\bar{t}}}$ for the Z^0 analysis depends on the different selection efficiencies in the two bins. It cannot be directly compared to the one taken from these differential cross sections. But the top analysis cross sections are compared to the same MadGraph sample as used for the Z^0 analysis. This allows to calculate a correction factor for the difference between data and simulation. Since different final states are measured (ee and $\mu\mu$ in Z^0 analysis; eμ in top analysis), the measurements are statistically independent. Table 6.6 shows the values of the differential cross sections, and the resulting ratios $R_{\mathrm{t\bar{t}}}^{\mathrm{top}}$ for the $e\mu$ channel and for MadGraph. A correction factor is estimated from the difference of the ratios, and yields

$$\rho_{R_{\mathrm{t\bar{t}}}} = \frac{R_{\mathrm{t\bar{t}}}^{\text{top, data}}}{R_{\mathrm{t\bar{t}}}^{\text{top, simu}}} = 1.046 \pm 0.059\,(\text{stat.}) \pm 0.080\,(\text{syst.})\,. \tag{6.16}$$

The values are not the final ones of the t$\bar{\mathrm{t}}$ analysis, an update with the latest values is shown in Appendix B.1. The systematic uncertainty is reduced, the mean value changes only marginally. However the value of Equation 6.16 is used throughout this work, since it is used for the results which entered the publication [151]. The final precision of the cross-section measurement is not affected.

To verify the independence from the lepton flavour, Table 6.7 shows the behaviour of the cross sections for all three decay modes; the table is the only one showing results of the final update. In the ee and the $\mu\mu$ channel, the invariant mass interval $[76\,\mathrm{GeV}, 106\,\mathrm{GeV}]$ needs to be excluded to get rid of the overwhelming amount of Z^0 decays. So the comparison can only be done excluding this region. For these two channels, there is also an additional selection on $\not{E}_{\mathrm{T}} > 30\,\mathrm{GeV}$ applied to further reduce the Z^0 contribution. The results are statistically independent, all values agree within the statistical errors. The

Table 6.7: Normalised cross sections $\frac{1}{\sigma}\frac{d\sigma}{dM^{l^+l^-}}$ in $\left[\frac{\text{GeV}}{c^2}^{-1}\right]$ from the top analysis, differential in dilepton mass $M^{l^+l^-}$ [165]. Results are shown for the eμ, $\mu\mu$ and ee channels. Statistical and systematic errors are given separate. The values are scaled by a factor 1000.

$M^{l^+l^-}$	$\frac{1}{\sigma}\frac{d\sigma}{dM^{l^+l^-}}$ $(e\mu)$	$\frac{1}{\sigma}\frac{d\sigma}{dM^{l^+l^-}}$ $(\mu\mu)$	$\frac{1}{\sigma}\frac{d\sigma}{dM^{l^+l^-}}$ (ee)
[60 GeV, 76 GeV]	$8.47 \pm 0.56 \pm 0.43$	$7.97 \pm 0.86 \pm 0.80$	$7.49 \pm 0.85 \pm 0.54$
[76 GeV, 106 GeV]	$8.13 \pm 0.40 \pm 0.37$	—	—
[106 GeV, 120 GeV]	$5.30 \pm 0.46 \pm 0.33$	$5.74 \pm 0.79 \pm 0.82$	$4.77 \pm 0.68 \pm 0.41$
[120 GeV, 400 GeV]	$1.09 \pm 0.05 \pm 0.06$	$0.96 \pm 0.07 \pm 0.07$	$1.02 \pm 0.07 \pm 0.06$

systematic errors are highly correlated and not important here, but there are also differences from the lepton flavour, the $\not{E}_\text{T}$ selection and the background composition.

The estimated correction factor is valid for the phase space defined for the cross section in the top analysis. The measured cross sections are visible cross sections, which means they are defined in a phase space close to the measured one. The definition requires the two leptons to be in $|\eta| < 2.4$ and $p_\text{T} > 20\,\text{GeV}$, independent of the flavour. Further the two (anti)b quarks from the (anti)top decays have to be in $|\eta| < 2.4$ and $p_\text{T} > 30\,\text{GeV}$. Since the b quarks are boosted, there is not a big difference in the cross-section definition when restricting the phase space for b jets instead of the b quarks—nevertheless the cross section is defined for the kinematic selection applied on the b quarks.

The measured phase space of the Z^0 analysis, which is the relevant one for $R_{\text{t}\bar{\text{t}}}$, differs slightly in several points. Muons are measured within $|\eta| < 2.1$. The b jets are selected within $|\eta| < 2.1$ and $p_\text{T} > 25\,\text{GeV}$, and only one is required. Thus, there could occur slight deviations of the correction factor $\rho_{R_{\text{t}\bar{\text{t}}}}$ when extrapolating between these phase spaces. However, the simulations show a good description of the data in these quantities (η and p_T of leading and second leading lepton or jet, number of jets), both in the top analysis and in the Z^0 analysis. This allows the assumption that no relevant additional systematic effects are present. The ratios $R_{\text{t}\bar{\text{t}}}$ as used in the Z^0 analysis are similar to the MadGraph one from the differential cross section. This means that the selection efficiency is similar in both intervals.

6.5.3 t$\bar{\text{t}}$ Contamination Results and Discussion

The t$\bar{\text{t}}$ contamination in the signal region of the bZ^0 measurement is estimated using Equation 6.15 and all ingredients described in Chapter 6.5.2. The corrected ratio $R_{\text{t}\bar{\text{t}}} \to R_{\text{t}\bar{\text{t}}} \cdot \rho_{R_{\text{t}\bar{\text{t}}}}$ gets the full uncertainty of the correction factor $\rho_{R_{\text{t}\bar{\text{t}}}}$ assigned as systematic uncertainty, i.e. the statistical uncertainty arises from the uncorrected estimate on the simulated sample only. The resulting absolute ($N^\text{in}_{\text{t}\bar{\text{t}}}$) and relative ($f^\text{in}_{\text{t}\bar{\text{t}}}$) values of t$\bar{\text{t}}$ events inside the signal region are given in Table 6.8 together with their errors, where also the absolute ($N^\text{out}_{\text{t}\bar{\text{t}}}$) and relative ($f^\text{out}_{\text{t}\bar{\text{t}}}$) values of t$\bar{\text{t}}$ events outside the signal region and the fractions

Table 6.8: Absolute estimated (N) and relative fractions (f) of $\mathrm{t\bar{t}}$ events inside and outside, and corresponding errors. Also resulting fractions of Z^0 events are shown.

Selection	$N^{\mathrm{in}}_{\mathrm{t\bar{t}}}$	$N^{\mathrm{out}}_{\mathrm{t\bar{t}}}$	$f^{\mathrm{in}}_{\mathrm{t\bar{t}}}$ (%)	$f^{\mathrm{out}}_{\mathrm{t\bar{t}}}$ (%)	$f^{\mathrm{in}}_{\mathrm{Z}^0}$ (%)	$f^{\mathrm{out}}_{\mathrm{Z}^0}$ (%)
Dimuons	1057 ± 677	730	0.28 ± 0.18	14.0	99.7	86.0
1 jet	623 ± 189	428	0.88 ± 0.27	27.5	99.1	72.5
1 b (HE)	404 ± 49	268	11.31 ± 1.36	86.1	88.7	13.9
1 b (HE) & $\not{E}_{\mathrm{T}}$	122 ± 21	91	3.80 ± 0.66	68.5	96.2	31.5
1 b (HP)	329 ± 41	214	18.40 ± 2.27	91.6	81.6	8.4
1 b (HP) & $\not{E}_{\mathrm{T}}$	102 ± 18	73	6.60 ± 1.14	79.2	93.4	20.8
+ 2nd jet	86 ± 15	59	13.19 ± 2.35	88.2	86.8	11.8
+ 2nd b (HE)	34 ± 8	23	28.89 ± 7.23	94.8	71.1	5.2

of Z^0 events inside ($f^{\mathrm{in}}_{\mathrm{Z}^0}$) and outside ($f^{\mathrm{out}}_{\mathrm{Z}^0}$) are listed. For the selection of the cross-section measurement ("1 b (HP)"), the method results in a fraction of $\mathrm{t\bar{t}}$ events in the signal region $f_{\mathrm{t\bar{t}}}$ of

$$f_{\mathrm{t\bar{t}}} = f^{\mathrm{in}}_{\mathrm{t\bar{t}}} = \frac{N^{\mathrm{in}}_{\mathrm{t\bar{t}}}}{N^{\mathrm{in}}_{\mathrm{obs}}} = (18.40 \pm 2.27)\,\%\,. \tag{6.17}$$

The results especially for the first selection step ("dimuons") in the table, but also for the second selection step ("1 jet"), should not be interpreted as the best result achievable. The $\mathrm{t\bar{t}}$ contamination there is not a very big contribution, and other backgrounds are also existent. Since the other backgrounds are neglected, the result obtained is biased. For example after the dimuon selection, there is a contribution from diboson events, which should be about the same as the one from $\mathrm{t\bar{t}}$. Also a contamination of the same size from tauonic decays of the Z^0, and some single-top events, are present. However, for the selection "dimuons", all non-Z^0 backgrounds are almost negligible. The contributions from other backgrounds and also from non-signal Z^0 events get smaller with tighter selection steps. Thus, their influence gets closer to negligible, and the obtained results are close to the best possible solutions.

It is clearly visible, that the relative $\mathrm{t\bar{t}}$ contamination increases with tighter selection steps. The $\mathrm{t\bar{t}}$ events always contain two b-jets which have in general high momenta. Thus, the selection of one jet deselects almost no events, and also the requirement of one b-tag and even of two b-tags does not reduce the $\mathrm{t\bar{t}}$ yields much. The Z^0 component, and all other backgrounds are significantly reduced with every tighter selection step, since only few events have at least one high-energetic b jet or even two of them. Due to these reasons, the relative $\mathrm{t\bar{t}}$ contamination for events with exactly one b-tag is lower than for the inclusive measurement with at least one b-tag. Application of the $\not{E}_{\mathrm{T}}$ selection however reduces the amount of $\mathrm{t\bar{t}}$ events drastically, since there is real $\not{E}_{\mathrm{T}}$ originating from the neutrinos, while Z^0 events have a big value of fake $\not{E}_{\mathrm{T}}$ only in few cases.

The mass spectra with the fitted contributions are shown in Figure 6.8. The simulated samples are scaled such, that the estimated fraction of the

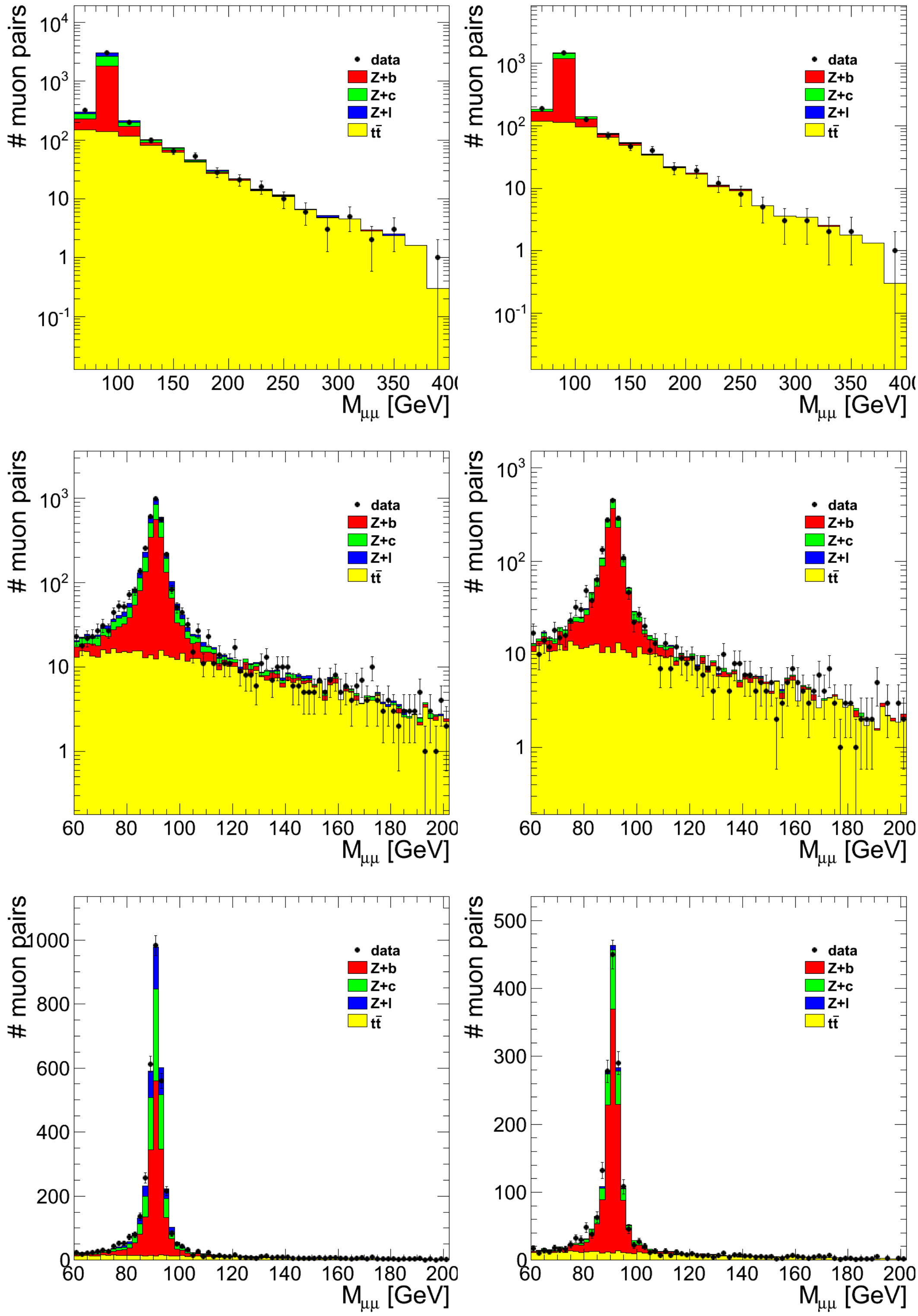

Figure 6.8: Invariant dimuon mass spectrum from data and fitted contributions. The data correspond to 1.1 fb^{-1}. The left column has at least one HE b-tag. The right column has at least one HP b-tag. All plots of a column show the same distribution with different binning or y-axis scale.

Table 6.9: Influence of the different uncertainties of the ingredients on the relative uncertainty $\sigma_f = \frac{\Delta f^{\mathrm{in}}_{\mathrm{t\bar{t}}}}{f^{\mathrm{in}}_{\mathrm{t\bar{t}}}}$ of the estimated $\mathrm{t\bar{t}}$ fraction $f^{\mathrm{in}}_{\mathrm{t\bar{t}}}$. Shown are the influences from the statistical errors of $N^{\mathrm{in}}_{\mathrm{obs}}$ and $N^{\mathrm{out}}_{\mathrm{obs}}$, the influences from the statistical errors of the simulated samples for $R_{\mathrm{t\bar{t}}}$ and $R_{\mathrm{Z^0}}$, and all other uncertainties for $R_{\mathrm{t\bar{t}}}$ and $R_{\mathrm{Z^0}}$ gathered in the systematic error. All values are relative uncertainties of the estimated $\mathrm{t\bar{t}}$ fraction and are given in %.

Selection	σ_f $[N^{\mathrm{in}}_{\mathrm{obs}}]$	σ_f $[N^{\mathrm{out}}_{\mathrm{obs}}]$	σ_f $[R_{\mathrm{t\bar{t}}}\,(\mathrm{stat.})]$	σ_f $[R_{\mathrm{Z^0}}\,(\mathrm{stat.})]$	σ_f $[R_{\mathrm{t\bar{t}}}\,(\mathrm{syst.})]$	σ_f $[R_{\mathrm{Z^0}}\,(\mathrm{syst.})]$
Dimuons	1.0	10.1	1.5	2.9	9.6	62.5
1 jet	1.0	9.4	1.6	2.5	9.7	27.0
1 b (HE)	0.3	6.7	1.8	0.8	9.7	1.7
1 b (HE) & $\not{E}_{\mathrm{T}}$	0.9	12.9	3.6	2.2	9.6	4.7
1 b (HP)	0.3	7.3	2.0	0.6	9.7	0.9
1 b (HP) & $\not{E}_{\mathrm{T}}$	0.7	13.4	4.0	1.8	9.6	2.7
+ 2nd jet	0.6	14.1	4.4	1.5	9.7	1.4
+ 2nd b (HE)	0.7	22.0	6.7	1.5	9.7	0.6

data yield in the signal region equals the integral of the sample in the signal region. Scaling the sideband region would be almost equivalent, except for the correction factor $\rho_{R_{\mathrm{t\bar{t}}}}$ on $R_{\mathrm{t\bar{t}}}$. The histograms show good agreement between data and simulation. This is true also for other selection steps, some further examples can be found elsewhere [150]. Variations of the sideband size show only small changes of the result, no systematic effect is visible.

Table 6.9 shows the influence of the uncertainties of the ingredients on the uncertainty of the estimated $\mathrm{t\bar{t}}$ fraction $f^{\mathrm{in}}_{\mathrm{t\bar{t}}}$. The first two steps with very small values of $f^{\mathrm{in}}_{\mathrm{t\bar{t}}}$ show a large dependence on $R_{\mathrm{Z^0}}$, which is expected, since these are completely dominated by the Z^0 contribution. But these steps are not important for the analysis. If one would like to use the described method for these steps, the accuracy of $R_{\mathrm{Z^0}}$ has to be determined much better, in contrast to the conservative error assignment which is used here. As already mentioned, one would have to take also the other backgrounds into account. The uncertainty of $R_{\mathrm{Z^0}}$ is almost negligible for the presented cross-section measurement, because it gets only big when the $\mathrm{t\bar{t}}$ contamination $f^{\mathrm{in}}_{\mathrm{t\bar{t}}}$ is small. And the dependence of the cross section on $f^{\mathrm{in}}_{\mathrm{t\bar{t}}}$ is small for small values of $f^{\mathrm{in}}_{\mathrm{t\bar{t}}}$.

For the steps with requirement on $\not{E}_{\mathrm{T}}$, and especially for the step with two b-tags, the statistical error increases drastically. This is due to the small statistics for the observed events $N^{\mathrm{out}}_{\mathrm{obs}}$ in the sideband. For the important selection steps, the dominant contributions to the uncertainty arise from $N^{\mathrm{out}}_{\mathrm{obs}}$ and the systematic error of $R_{\mathrm{t\bar{t}}}$. With increasing integrated luminosity, the contribution from $N^{\mathrm{out}}_{\mathrm{obs}}$ will decrease. Also the contribution from the systematic error of $R_{\mathrm{t\bar{t}}}$, which is given by the top analysis, will slightly decrease with more data, as the statistical error of $\rho_{R_{\mathrm{t\bar{t}}}}$ is still valuable (see Equation 6.16).

The overall relative uncertainty $\sigma_f = \frac{\Delta f^{\mathrm{in}}_{\mathrm{t\bar{t}}}}{f^{\mathrm{in}}_{\mathrm{t\bar{t}}}}$ of the estimated $\mathrm{t\bar{t}}$ fraction $f^{\mathrm{in}}_{\mathrm{t\bar{t}}}$ is

Table 6.10: Comparison of estimated $\mathrm{t\bar{t}}$ fraction $f^{\mathrm{in}}_{\mathrm{t\bar{t}}}$ amongst the result of sideband extrapolation (based on $1.1\,\mathrm{fb}^{-1}$) and as taken from simulation (based on $2.1\,\mathrm{fb}^{-1}$) and the result from the template fit (based on $1.1\,\mathrm{fb}^{-1}$). The sideband results include also systematic uncertainties. The values of simulation are gained dividing the $\mathrm{t\bar{t}}$ expectation by the expectation of all regarded samples summed up. The error of the template fit is statistical only. All values are in %.

Selection	$f^{\mathrm{in}}_{\mathrm{t\bar{t}}}$ (sideband)	$f^{\mathrm{in}}_{\mathrm{t\bar{t}}}$ (simulation)	$f^{\mathrm{in}}_{\mathrm{t\bar{t}}}$ (template)
Dimuons	0.28 ± 0.18	0.14	
1 jet	0.88 ± 0.27	0.69	
1 b (HE)	11.31 ± 1.36	10.73	10.6 ± 0.8
1 b (HE) & $\not{E}_{\mathrm{T}}$	3.80 ± 0.66		4.9 ± 0.6
1 b (HP)	18.40 ± 2.27	16.68	16.8 ± 1.3
1 b (HP) & $\not{E}_{\mathrm{T}}$	6.60 ± 1.14		8.1 ± 1.1

lower than 20% in all relevant selection steps. The relative uncertainty of the $\mathrm{bZ^0}$ cross section $\frac{\Delta\sigma_{\mathrm{bZ^0}}}{\sigma_{\mathrm{bZ^0}}}$ is about the same as the absolute uncertainty $\Delta f^{\mathrm{in}}_{\mathrm{t\bar{t}}}$ as listed in Table 6.8. It depends also on the purity P of events with real b-tag, and scales with the inverse of $P - f^{\mathrm{in}}_{\mathrm{t\bar{t}}}$:

$$\frac{\Delta\sigma_{\mathrm{bZ^0}}}{\sigma_{\mathrm{bZ^0}}} = \Delta f^{\mathrm{in}}_{\mathrm{t\bar{t}}} \times \frac{1}{P - f^{\mathrm{in}}_{\mathrm{t\bar{t}}}} = \Delta f^{\mathrm{in}}_{\mathrm{t\bar{t}}} \times \frac{1}{f^{\mathrm{in}}_{\mathrm{bZ^0}}} \,. \tag{6.18}$$

$f^{\mathrm{in}}_{\mathrm{bZ^0}}$ is the fraction of selected $\mathrm{bZ^0}$ events, the amount of signal events in the candidate events. Given the purity estimates as shown in Chapter 6.4, the relative uncertainty of $\sigma_{\mathrm{bZ^0}}$ yields less than 3% for the HE b-tag. For the HP b-tag the values are bigger, but less than 4%.

Cross Checks

The results of the $\mathrm{t\bar{t}}$ contamination can be compared to the estimates taken purely from simulation, scaling the sample to the integrated luminosity and the theoretical cross section, as they are listed in Table 6.2. Values can be found in Table 6.10. Deviations are visible, but not huge—they are all within the uncertainty of the given estimate. The values from simulation are in general smaller, but also the sum of all simulated events is in general below the observed data events.

Furthermore, a template fit to the dimuon mass distribution in the interval $[60\,\mathrm{GeV}, 200\,\mathrm{GeV}]$ is performed [150]. Two templates are generated from the simulated $\mathrm{Z^0}$ and $\mathrm{t\bar{t}}$ samples with a fine binning of $2\,\mathrm{GeV}$. The results without $\not{E}_{\mathrm{T}}$ selection are in agreement, but smaller and closer to simulation. The results with additional $\not{E}_{\mathrm{T}}$ selection show bigger deviations and the values are higher. The statistical errors are highly correlated.

Table 6.11: Dependence of $R_{t\bar{t}}$ on pileup. Values are shown for the default analysis with number of vertices $N_{\text{vtx}} \geq 1$, and for dedicated selections on the number of vertices. This table shows results obtained without pile-up reweighting. Errors are statistical.

Selection	$R_{t\bar{t}}$(Default)	$R_{t\bar{t}}(N_{\text{vtx}} \in [1,4])$	$R_{t\bar{t}}(N_{\text{vtx}} \in [5,7])$	$R_{t\bar{t}}(N_{\text{vtx}} \geq 8)$
Dimuons	1.371 ± 0.020	1.397 ± 0.031	1.369 ± 0.039	1.333 ± 0.037
1 jet	1.383 ± 0.021	1.409 ± 0.032	1.380 ± 0.040	1.345 ± 0.038
1 b (HE)	1.433 ± 0.025	1.473 ± 0.038	1.398 ± 0.047	1.402 ± 0.046

Table 6.12: Dependence of R_{Z^0} on pileup. Values are shown for the default analysis with number of vertices $N_{\text{vtx}} \geq 1$, and for dedicated selections on the number of vertices. This table shows results obtained without pile-up reweighting. Errors are statistical.

Selection	R_{Z^0}(Default)	$R_{Z^0}(N_{\text{vtx}} \in [1,4])$	$R_{Z^0}(N_{\text{vtx}} \in [5,7])$	$R_{Z^0}(N_{\text{vtx}} \geq 8)$
Dimuons	82.75 ± 0.38	83.05 ± 0.58	83.46 ± 0.74	81.65 ± 0.70
1 jet	63.08 ± 0.56	62.05 ± 0.87	63.16 ± 1.09	64.32 ± 1.01
1 b (HE)	74.83 ± 3.41	74.09 ± 5.09	69.77 ± 5.98	81.25 ± 7.06

6.5.4 Systematic Influence of Pileup

It could be observed, that pileup influences parts of the analysis, which makes the pileup reweighting of the simulation necessary. In order to study the influence of pileup on the $t\bar{t}$ estimate, the analysis is divided into three subanalyses via the number of selected primary vertices N_{vtx}. All samples are divided into subsamples with 1–4 vertices, 5–7 vertices, and at least 8 vertices. The non-overlapping subsamples are analysed with the standard analysis – i.e. as described for the full samples in the last sections – and their results for the $t\bar{t}$ estimate are compared. The studies are performed exemplarily on the selection with 1 b-tag (HE). The results for the tighter b-tag (HP), or additional selection on $\not{E}_{T}$ are similar, and certainly statistically highly correlated. A dependence is visible, the relative $t\bar{t}$ contamination depends on the pileup (see Table 6.13). The three subsamples are statistically independent, but the differences are not within the statistical error. In order to study this observation, the pileup reweighting of events based on N_{vtx} is not applied in the following—instead of having mainly events with $N_{\text{vtx}}^{\text{mean}} = 6.2 \pm 2.9$ in all three subsamples, a wide spread of equally distributed values is available. The possible pileup effect gets more pronounced, also the statistical errors are more similar for the three subsamples, while the final results of the estimated $t\bar{t}$ fraction change only by less than 1%. The fit results of the dimuon mass within the subsamples in general look good, no hint of systematic deviations is visible; exemplary distributions are documented elsewhere [150].

Tables 6.11 and 6.12 show the dependence of the ratios $R_{t\bar{t}}$ and R_{Z^0} on the vertex selections. Looking at $R_{t\bar{t}}$ in the first two selection steps ("dimuons", "1 jet"), a clear drop with increasing pileup is visible, i.e. lower values of the invariant mass are suppressed more and more. For R_{Z^0} this is not the case, the ratio stays about constant. This can be explained with the isolation criterion (see Chapter 3.5.3). The identification and the momentum estimate of the muons are in general not affected by the pileup. However, the used isolation criterion is a relative isolation, the muon p_{T} relative to the other energy deposits. This leads to the fact that muons with lower momenta are less isolated, compared to an all-over energy deposit from pileup. The effect is illustrated in Figure 6.9, where the isolation is studied on events with at least two muons fulfilling all identification and kinematic selection criteria. The figures are produced with the isolation requirement $I_{\mathrm{comb}} < 0.15$ applied to only one muon (upper two rows), and in comparison for both muons representing the full muon selection (bottom row). They show the mean value of the isolation as a function of the muon p_{T} —but since the isolation distributions are smooth curves, they reflect the fraction of muons with isolation above threshold to some extent. In $\mathrm{t\bar{t}}$ events (top left), there is by nature more hadronic activity than in Z^0 events. Thus, the isolation is in general much worse. For $p_{\mathrm{T}} < 60\,\mathrm{GeV}$ the mean values are above the threshold, while the mean values of inclusive Z^0 events are in the full range below the threshold. Looking on the subprocesses, the isolation in bZ^0 (top right) is slightly worse than in cZ^0 (centre left), which is itself slightly worse than for the lZ^0 (centre right). This is due to the bigger hadronic activity, more events with hard jets are contained. But for the Z^0 the situation still stays different when additional jets are required. This is due to the fact, that the jets need to balance the boost of the Z^0, thus they do not overlap much with the muons in general. The figure shows also the different pileup subsamples; if there is more pileup with additional energy deposits, than less muons with low energy exceed the relative isolation criterion. This is visible in all but the top left plot, where the huge values of the isolation suppress the visibility.

The effect on the p_{T}-distribution of the muons is given in Figure 6.10, showing that the distribution for Z^0 is mainly independent of the pileup, and so is the dimuon mass distribution, while for $\mathrm{t\bar{t}}$ the low momenta are suppressed, thus in general the lower values of dimuon masses—R_{Z}^{0} stays constant, $R_{\mathrm{t\bar{t}}}$ decreases. In addition, the p_{T} of the muons of the Z^0 decay peaks around 45 GeV, and values around 20 GeV are rare, and they increase when additional jets are required due to the balancing. The muons of the $\mathrm{t\bar{t}}$ decays are more spread and have more tracks in the lower but also in the higher p_{T} range. The muon momenta of $\mathrm{t\bar{t}}$ in the upper sideband are in general higher than in the signal region; again the influence of pileup on the isolation is smaller than in the signal region, and $R_{\mathrm{t\bar{t}}}$ gets smaller.

An important conclusion is that pileup suppresses the relative $\mathrm{t\bar{t}}$ contamination due to the influence on the isolation. But this effect can be well explained and is reflected in simulation, thus there should be no systematic effect present for the $\mathrm{t\bar{t}}$ estimate after pileup reweighting of the simulation.

When an additional b-tag is required, the situation changes. Both ratios $R_{\mathrm{t\bar{t}}}$ and R_{Z^0} show a significant increase in the sub-sample with $N_{\mathrm{vtx}} \geq 8$. It seems to be an additional effect coming from the b-tag selection. The samples

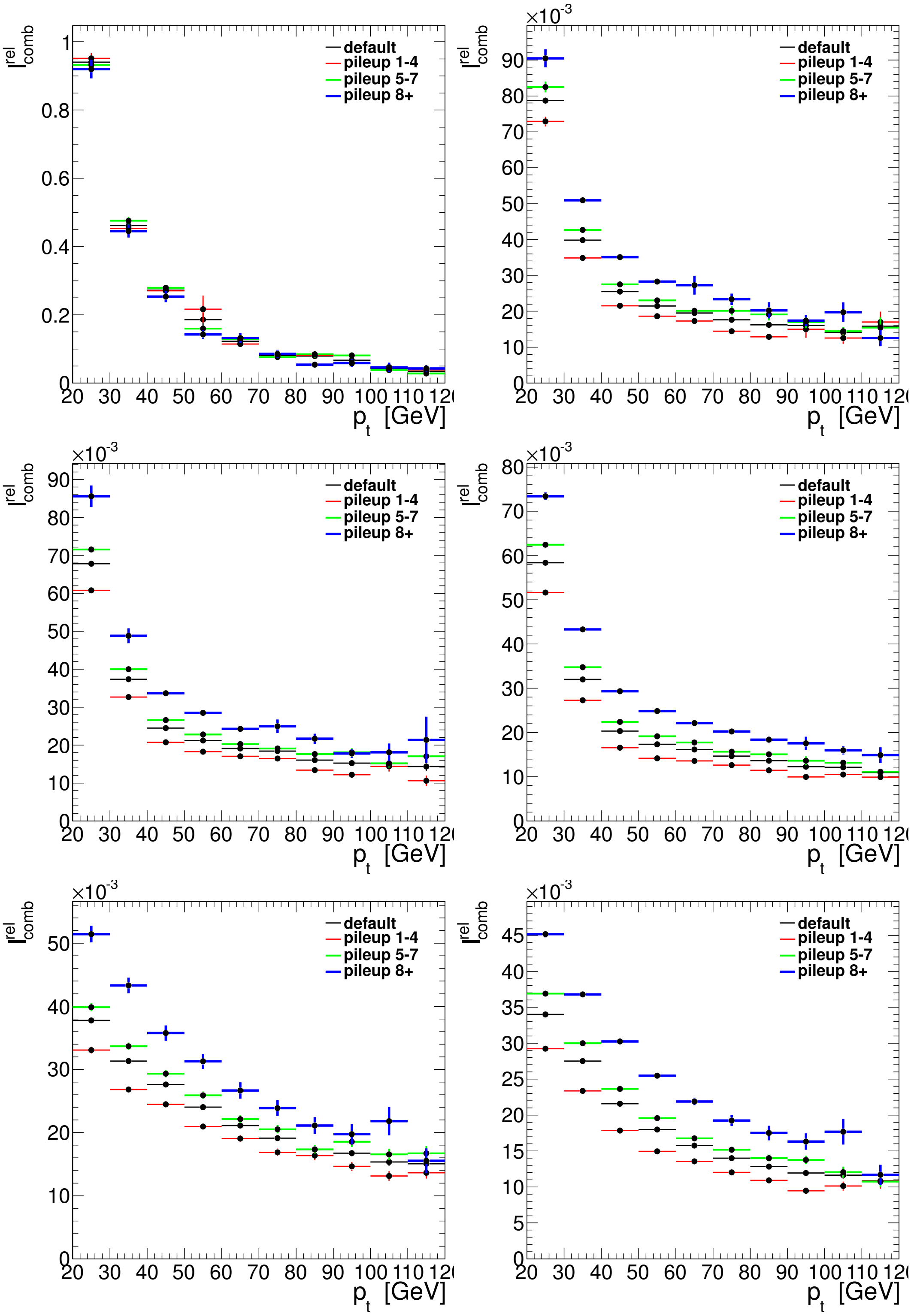

Figure 6.9: Average of relative isolation of muons $I^{\mathrm{rel}}_{\mathrm{comb}} = I_{\mathrm{comb}}$ as function of muon p_{T} for different pileup selections. The y-axis scale is much larger in the top left plot. The upper two rows are requiring at least two muons with full selection criteria except isolation selection on the second muon, the lower row requires isolation also on the second muon. The plots show from upper left to lower right: t$\bar{\mathrm{t}}$, bZ^0; cZ^0, lZ^0; t$\bar{\mathrm{t}}$, bZ^0.

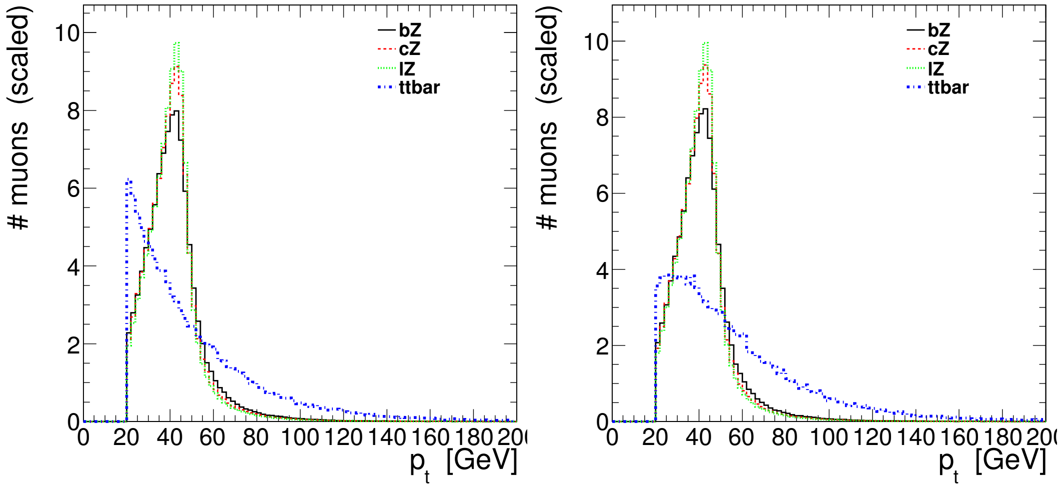

Figure 6.10: Transverse momentum of selected muons in events with at least 2 muons. Left: full muon selection excluding isolation on second muon. Right: full muon selection including isolation on second muon.

Table 6.13: Dependence of estimates of the relative fraction of $\mathrm{t\bar{t}}$ events inside the signal region $f^{\mathrm{in}}_{\mathrm{t\bar{t}}}$ for step "1 b (HE)" on pileup. Values are shown for the default analysis with number of vertices $N_{\mathrm{vtx}} \geq 1$, and for dedicated selections on the number of vertices. The sideband method shows the full errors, the template method only statistical ones. All values are in %.

Method	$f^{\mathrm{in}}_{\mathrm{t\bar{t}}}$(Default)	$f^{\mathrm{in}}_{\mathrm{t\bar{t}}}(N_{\mathrm{vtx}} \in [1,4])$	$f^{\mathrm{in}}_{\mathrm{t\bar{t}}}(N_{\mathrm{vtx}} \in [5,7])$	$f^{\mathrm{in}}_{\mathrm{t\bar{t}}}(N_{\mathrm{vtx}} \geq 8)$
Sideband	11.3 ± 1.4	13.6 ± 1.9	9.5 ± 1.5	10.1 ± 2.2
Template	10.6 ± 0.8	11.7 ± 1.5	9.8 ± 1.2	10.2 ± 1.9

as used for the $\mathrm{t\bar{t}}$ estimate are not scaled for b-tagging efficiencies, which means scaling to match the efficiencies in data; this could thus introduce small biases.

The final results of $f^{\mathrm{in}}_{\mathrm{t\bar{t}}}$ for the different subsamples, but now using pileup reweighting, is listed in Table 6.13, together with cross-check values of the template fit [150] as already used for cross-checks in Chapter 6.5.3. The sideband and the template fit method show similar behaviour and only the values in the first interval deviate. The differences between intervals are mainly compatible with statistical fluctuations. In fact, using this subsample scheme for pileup studies, there are also small deviations of lepton and b-tagging efficiency as well as of parton-to-hadron correction factors observed using simulation only [158].

Assuming that the dependence on pileup is described correctly in the simulation, no additional systematic uncertainty on the $\mathrm{t\bar{t}}$ estimate has to be taken into account. All dimuon mass distributions of the fits in the subanalyses divided by N_{vtx} behave well, they are documented in [150]. But it is clear that pileup influences the $\mathrm{t\bar{t}}$ contamination and thus also the b-tag event purity introduced in Chapter 6.4. The uncertainty arising from the uncertainty of the measurement of real pileup in data – and thus possible mismodelling in simulation – needs to be considered. The data-driven correction of $R_{\mathrm{t\bar{t}}}$ as taken from the top analysis contains a small contribution from the uncertainty of the pileup modelling in the systematic uncertainty. For $R_{\mathrm{Z^0}}$ the conservatively assigned systematic uncertainty should also be big enough to cover pileup effects.

6.6 Final Background Estimate

In this section, the final background estimate for the bZ^0 cross-section measurement – taking all relevant backgrounds into account – is presented and discussed, but first a simplified study is presented in order to get an idea of additional backgrounds not considered so far.

6.6.1 Appraisal of All Backgrounds

The behaviour of all possible backgrounds of bZ^0 is analysed based on a study on the first 191 pb^{-1} of 2011 data, and all relevant simulation samples. The samples are mainly identical to the ones used in Chapter 5, but from a later production. They include pileup and contain slightly more events. However they span significantly less events than the Z^0 and $\mathrm{t\bar{t}}$ samples used in the present chapter, thus they are not of sufficient size for sophisticated background studies, but they reflect the approximate size. The simulated muon enriched multijet (QCD), W→ $\mu\nu$ and W→ $\tau\nu$ contributions are negligible even at the dimuon selection step. Also the different channels – s-channel, t-channel and tW – of single top production are considered (single t), but mainly the tW sample contributes. Furthermore the separate diboson samples (WW, WZ^0, Z^{0}Z^0) are taken into account. The inclusive Z^0 sample is separated into contributions from tauonic decay (Z^0 $\rightarrow \tau\tau$) and the different muonic decay contributions (bZ^0, cZ^0, lZ^0). Finally the top-pair sample ($\mathrm{t\bar{t}}$) is added.

This background analysis was performed at an earlier stage of the analysis, the setup is different to the main analysis described in this thesis. The event selection is identical in terms of kinematics with the one stated in Chapter 6.2 and is very similar in all other points. There are small differences in the final muon and dimuon identification criteria. The only big difference is that in simulation also a trigger requirement is employed—dimuon triggers with $p_{\mathrm{T}} > 5\,\mathrm{GeV}$ for each muon are used. The trigger selection is similar to the one in the used data, where the threshold is set to $p_{\mathrm{T}} > 6\,\mathrm{GeV}$ in the very first data and later to $p_{\mathrm{T}} > 7\,\mathrm{GeV}$. The simulated samples are scaled to the data luminosity, but without any efficiency corrections. The event yields for all relevant simulation samples are listed in Table 6.14, while their sum and the comparison to data is shown in Table 6.15.

All contributions without two real isolated muons are negligible after the dimuon selection. Due to the b-tag, the contributions from WW and WZ^0

Table 6.14: Comparison of event yields for all relevant simulation samples separately for different selection steps, scaled according to 191 pb^{-1}.

Selection	single t	$t\bar{t}$	WW, WZ^0	Z^0Z^0	$Z^0 \to \tau\tau$	lZ^0, cZ^0	bZ^0
Dimuons	6.33	86.73	34.73	38.05	74.48	56452.91	3311.91
1 jet	5.61	85.00	14.76	27.65	13.75	11441.48	923.20
1 b (HE)	3.20	60.75	0.35	4.06	0.75	184.69	248.17
1 b (HE) & $\not{E}_T$	0.95	15.50	0.15	3.90	0.75	181.44	242.92
1 b (HP) & $\not{E}_T$	0.72	12.23	0.06	2.45	0.25	41.74	161.45
+ 2nd jet	0.30	10.38	0.02	1.69	0.25	15.00	61.48
+ 2nd b (HP)	0.03	2.31	0.00	0.27	0.00	0.25	4.75

Table 6.15: Comparison of event yields for simulation and data corresponding to 191 pb^{-1} for different selection steps, shown with the statistical errors.

Selection	Simulation	Data
Dimuons	60006.07 ± 122.30	60269 ± 245.50
1 jet	12511.45 ± 55.64	12310 ± 110.95
1 b (HE)	501.96 ± 10.48	550 ± 23.45
1 b (HE) & $\not{E}_T$	445.61 ± 10.33	491 ± 22.16
1 b (HP) & $\not{E}_T$	218.89 ± 7.15	258 ± 16.06
+ 2nd jet	89.11 ± 4.41	108 ± 10.39
+ 2nd b (HP)	7.62 ± 1.14	8.00 ± 2.83

are negligible. Also the $Z^0 \to \tau\tau$ contamination with muonic tau decays is irrelevant, although it can be produced associated with b jets. The only contributions besides $t\bar{t}$, cZ^0 and lZ^0 are small amounts of tW and Z^0Z^0 events, since they can have the same topology as the measured one: two isolated muons and one b jet. Figure 6.11 shows the $\not{E}_T$-distribution after requesting 1 HE b-tag. The Z^0 shows in general slightly underestimated values, but the overall shape is well reflected. Contributions from tW and $t\bar{t}$ behave similar and on the other hand the behaviour of $Z^0 \to \mu^+\mu^-$ and Z^0Z^0 is similar, due to the similar topologies. When applying a selection on $\not{E}_T$, mainly tW and $t\bar{t}$ are suppressed, which would make Z^0Z^0 more relevant. Since in tW only one jet is produced at LO, the selection of a second jet and especially two b-tags remove almost the entire component. The second b-tag also removes the cZ^0 and lZ^0 contamination. Z^0Z^0 is the only relevant irreducible background besides $t\bar{t}$ since it also reproduces the topology of two isolated muons and two b jets, and since the b jets arise from Z^0 decays they are in general of high momenta. Compared to the signal sample bZ^0, the contamination is at the few percent level. Another estimate of Z^0Z^0 events [158] using a recent production of the identical sample estimates 28 events in 3293 signal events as estimated from the full dataset (0.9%) for selection “1 b (HE)”, and 20 in 2121 events (0.9%) for selection “1 b (HP)”.

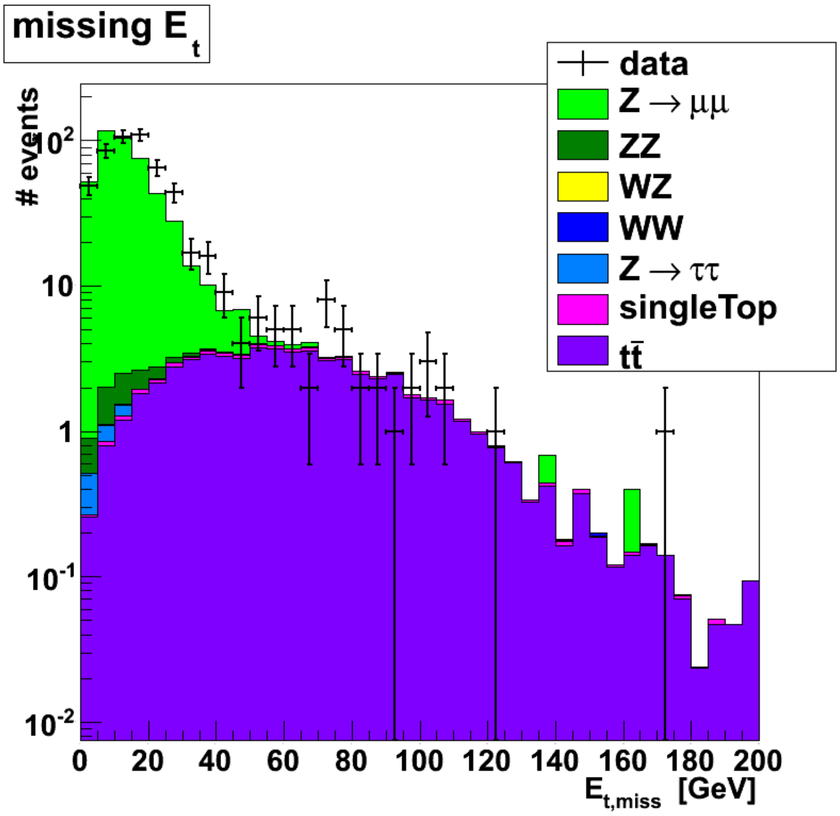

Figure 6.11: Comparison of $\not{E}_{\mathrm{T}}$-distribution between all relevant simulation samples and data corresponding to $191\,\mathrm{pb}^{-1}$, for selection step “1 b (HE)”.

6.6.2 Background Calculation and Discussion

Given the estimates of the b-tag event purity P as stated in Chapter 6.4 and the $\mathrm{t\bar{t}}$ background fraction $f_{\mathrm{t\bar{t}}}$ as shown in Chapter 6.5.3, the signal events are estimated from the number of observed events N_{obs} following

$$N_{\mathrm{sig}} = N_{\mathrm{obs}} \cdot (P - f_{\mathrm{t\bar{t}}}) \ . \tag{6.19}$$

This estimate accounts for almost all backgrounds due to the following reasons. All contributions with mistagged non-b jets are absorbed in the purity estimate, which includes $\mathrm{lZ^0}$ and $\mathrm{cZ^0}$ and possible small other contributions, like WW and $\mathrm{WZ^0}$ but also $\mathrm{Z^0Z^0}$ with one muonic decay and one hadronic non-b decay. The small remaining tW contribution behaves similar to the $\mathrm{t\bar{t}}$ background in the dimuon mass spectrum and is mainly absorbed in the $\mathrm{t\bar{t}}$ contamination estimate. Thus only the small $\mathrm{Z^0Z^0} \to \mu^+\mu^-\mathrm{b\bar{b}}$ component, which also peaks at the $\mathrm{Z^0}$ mass, shows up irreducibly in the signal estimate. Given the intended precision of the presented measurement and the small $\mathrm{Z^0Z^0}$ yield (see Chapter 6.6.1), it is not relevant and not taken into account. For the selection used in the cross-section calculation ("1 b (HP)"), the result is $N_{\mathrm{sig}} = 2121 \pm 130$ based on $N_{\mathrm{obs}} = 3362 \pm 58$ (see Table 6.2), which means the selection results in 63.1% signal events.

6.7 Selection Efficiencies and Correction Factors

As explained in Chapter 6.3, the cross-section measurement requires an estimate of the total event selection efficiency ϵ_{tot} for each of the defined cross sections. The total efficiency contains the corrections and uncertainties due to the cross-section definition and the measurement effects, which is in case of the inclusive cross section:

$$\epsilon_{\mathrm{tot}} = A_{\mathrm{l}} \cdot C_{\mathrm{h}} \cdot \epsilon_{\mathrm{l}} \cdot \epsilon_{\mathrm{b}} \ . \tag{6.20}$$

For the visible cross section it is identical, but without the lepton acceptance term A_{l}.

The lepton acceptance A_{l} accounts for the extrapolation of the muons in the unmeasured phase space. The hadron-level correction C_{h} is used to translate between hadron-level and detector-level. Here, the detector-level is given by muons and jets as reconstructed by the standard CMS reconstruction, fulfilling all kinematic selections of the measured phase space. All other effects are absorbed in the lepton efficiency ϵ_{l} accounting for the full muon and dimuon selection, and in the b-jet efficiency ϵ_{b} for the full jet and b-tag selection.

The total event selection efficiency ϵ_{tot} is estimated from the $\mathrm{bZ^0}$ signal sample [158], which is scaled in order to match the muon and b-tagging efficiencies in data as explained earlier. The different components are defined and calculated as

$$\epsilon_\mathrm{b} = \frac{N^\mathrm{reco}_{\mathrm{bZ}^0}}{N^\mathrm{reco}_{\mathrm{Z}^0}}\,, \tag{6.21}$$

$$\epsilon_\mathrm{l} = \frac{N^\mathrm{reco}_{\mathrm{Z}^0}}{N^\mathrm{reco}}\,, \tag{6.22}$$

$$C_\mathrm{h} = \frac{N^\mathrm{reco}}{N^\mathrm{gen}_{\mu+\mathrm{b}}}\,, \tag{6.23}$$

$$A_\mathrm{l} = \frac{N^\mathrm{gen}_{\mu+\mathrm{b}}}{N^\mathrm{gen}_\mathrm{b}}\,. \tag{6.24}$$

The different number of events are defined by their restriction to the bZ^0 sample as

- $N^\mathrm{gen}_\mathrm{b}$: events defining the signal of the inclusive cross section, i.e. all signal events having at least one hadronic b jet in the given kinematic range.
- $N^\mathrm{gen}_{\mu+\mathrm{b}}$: events defining the signal of the visible cross section, i.e. all signal events having both muons from the Z^0 and at least one hadronic b jet in the given kinematic ranges.
- N^reco: events having two muons and at least one jet in the given kinematic ranges, which are reconstructed by the standard CMS reconstruction, and are matched to generator objects, and fulfilling the selections on $M_{\mu^+\mu^-}$ and ΔR(jet,muons).
- $N^\mathrm{reco}_{\mathrm{Z}^0}$: all events of N^reco, which fulfil the full muon and dimuon selection on reconstruction level.
- $N^\mathrm{reco}_{\mathrm{bZ}^0}$: all events of $N^\mathrm{reco}_{\mathrm{Z}^0}$, which fulfil the full jet and b jet selection on reconstruction level, i.e. events fulfilling the final event selection.

In order to ensure that only real signal events of the bZ^0 sample are considered and thus having the correct event topology for C_h, the muons and jets reconstructed with the CMS standard reconstruction are required to be matched to hadron-level objects, the muons within $\Delta R < 0.3$ to muons of the Z^0 decay and the jets within $\Delta R < 0.5$ to hadron-level b jets. In principle, the matching reduces the total event selection efficiency ϵ_tot, but the matching efficiency is close to 100% and thus negligible. For each of the factors mentioned above the estimate including systematic uncertainties is outlined in the following.

Lepton Efficiency ϵ_l

The lepton efficiency ϵ_l is conditioned by the muon efficiency estimates ϵ_μ described in Chapter 6.2.1. It spans the efficiency from trigger, identification and isolation criteria, and on the dimuon selection. Since these estimates use the same tag-and-probe approach as for the standard CMS muon reconstruction – which is absorbed in C_h – the uncertainty of the reconstruction efficiency is also assigned to ϵ_l instead of C_h. The estimate of the global lepton efficiency yields [151]

$$\epsilon_\mathrm{l} = (84.4 \pm 1.7)\,\%\,. \tag{6.25}$$

The uncertainty has 0.5% relative contribution from statistics in simulation and 2.0% from the tag-and-probe method.

B-Jet Efficiency ϵ_b

Jet reconstruction and selection efficiencies are close to 100% in data and simulation, as stated in Chapter 6.2.1—possible very small deviations between data and simulation are not taken into account. The b-jet efficiency ϵ_b – which contains in principle also the jet identification criteria – is given by the efficiency estimates due to the b-tagging $\epsilon_\text{b-tag}$ and the mistagging of c jets $\epsilon_\text{c-tag}$ and of other jets $\epsilon_\text{o-tag}$ explained in Chapter 6.2.1. It depends on the chosen b-jet multiplicity, which is at least one HP b jet, and yields [151]

$$\epsilon_\mathrm{b} = (34.9 \pm 3.5)\,\%\,. \tag{6.26}$$

Dominant is the systematic uncertainty of the simulation-to-data scale factor for the correct b-tags (9.7% relative error), those of mistagging of other flavours contribute only 0.04% relative uncertainty, the rest is statistical uncertainty. The central value is considerably larger for HE b jets, resulting in about 52%—but as shown earlier, HE leads to a smaller b-tag event purity P.

Hadron-Level Correction C_h

C_h corrects for detector resolution and reconstruction effects from reconstructed objects to generator-level objects, the determination is described in [158]. As stated above, the uncertainty due to reconstruction efficiencies of muons is already absorbed in ϵ_l. For C_h, the statistical uncertainty of the sample (±0.2% relative error) is small compared to systematic uncertainties. The latter arise mainly from the uncertainty of the generator model. It is estimated by comparison to SHERPA [166] (LO, variable-flavour) and aMC@NLO+HERWIG [167][168][57] (NLO, fixed-flavour), giving $^{+6.9}_{-0.0}\%$ relative uncertainty. C_h contains for the muons a correction due to electromagnetic FSR. An experimental uncertainty arising from the jet energy resolution (JER) is estimated being about ±0.5% relative error. The final result is [151]

$$C_\mathrm{h} = \left(95.0^{+6.6}_{-0.5}\right)\,\%\,. \tag{6.27}$$

Dependencies on the flavour-matching method of generated jets are found to be negligible.

Lepton Acceptance Correction A_l

In order to extrapolate the measurement to the full phase space in terms of lepton kinematics, the acceptance correction A_l is estimated as described in [158]. The lepton properties are defined before FSR. Besides the statistical uncertainties of the sample, the uncertainties arise from the PDF and scale uncertainties. In order to allow comparisons of A_l with values from MCFM, it needs to be calculated on parton-level. Since the b jets of the signal definition are restricted in phase space, the result of A_l can depend on their definition, especially since neutrinos are excluded in hadron-level jets. But differences of A_l between hadron-level and parton-level are found to be small, so the uncertainty of MCFM is applied to the hadron-level acceptances. It is evaluated on MCFM (NLO, variable-flavour) for parton-level varying the factorisation and renormalisation scale – defined with the Z^0 mass of 91 GeV – by factors 2 up and down, and by varying the PDFs. Furthermore, the systematic effect by the choice of the generator model is estimated by comparing results of MadGraph with MCFM, sherpa and aMC@NLO+HERWIG. The acceptance yields [151]

$$A_\mathrm{l} = \left(57.2^{+3.7}_{-2.4}\right)\,\% \,. \tag{6.28}$$

Parton-Level Correction C_p

The correction between hadron-level jets and parton-level jets C_p can be used to define the cross-section on parton-level, but this is not of importance in this chapter. Alternatively, it can be used to transform a theoretical prediction on parton-level to hadron-level. This is used later to allow a direct comparison with MCFM that produces b jets with NLO correction, i.e. with the potential emission of an additional gluon. The estimate as explained in [158] is calculated as

$$C_\mathrm{p} = \frac{N^\mathrm{gen}_{\mu+\mathrm{b}}}{N^\mathrm{parton}_{\mu+\mathrm{b}}} \,, \tag{6.29}$$

where $N^\mathrm{parton}_{\mu+\mathrm{b}}$ is the number of events fulfilling the kinematic muon and b jet selections on parton-level. Differences due to the flavour-matching method used for hadron jets are small. The statistical uncertainty is again small. The model dependence is estimated by averaging the result of the bZ^0 signal sample with a factor computed by aMC@NLO+HERWIG, using the envelope as systematic uncertainty (relative error 3.6%). A small additional uncertainty arises from differences estimated on the muonic and electronic decay channels (relative error 0.5%). The method results in [151]

$$C_\mathrm{p} = (84 \pm 3)\,\% \,. \tag{6.30}$$

6.8 Measurement of Cross Section

In this section, first all ingredients as estimated for the cross-section calculation and the systematic uncertainties arising are recapitulated. Afterwards, the

Table 6.16: Ingredients of the cross-section calculation and corresponding uncertainties, subdivided by the number of observed events, the background estimates, selection efficiencies, theoretical correction factors, and integrated luminosity.

N_{obs}	3362 ± 58
P (%)	81.5 ± 2.9
$f_{\mathrm{t\bar{t}}}$ (%)	18.4 ± 2.3
ϵ_{b} (%)	34.9 ± 3.5
ϵ_{l} (%)	84.4 ± 1.7
C_{h} (%)	$95.0^{+6.6}_{-0.5}$
A_{l} (%)	$57.2^{+3.7}_{-2.4}$
L (fb^{-1})	2.22 ± 0.05

results are presented.

6.8.1 Cross-Section Calculation and Systematic Uncertainties

As mentioned earlier, the cross section is calculated from the basic formula

$$\sigma^{\mathrm{bZ}^0} = \frac{N_{\mathrm{sig}}}{\epsilon_{\mathrm{tot}} \cdot L}\,, \tag{6.31}$$

where N_{sig} is the number of signal events, ϵ_{tot} the total event selection efficiency, and L the integrated luminosity. The number of signal events N_{sig} is calculated as explained in Chapter 6.6.2 from the number of selected events N_{obs}, the b-tag event purity P and the fraction of $\mathrm{t\bar{t}}$ events $f_{\mathrm{t\bar{t}}}$. The total event selection efficiency for the two defined cross sections is estimated from the efficiency and acceptance corrections as described in Chapter 6.7 from the b-jet efficiency ϵ_{b}, the lepton efficiency ϵ_{l}, the hadron-level correction C_{h}, and in case of the inclusive cross section also the lepton acceptance A_{l}; the values are $\epsilon_{\mathrm{tot}}(\text{visible}) \approx 28\%$ and $\epsilon_{\mathrm{tot}}(\text{inclusive}) \approx 16\%$. All relevant ingredients for the cross-section calculation are summarised in Table 6.16. The statistical uncertainty is given by the uncertainty of N_{obs}.

The influence of the systematic uncertainties considered on the uncertainty of the cross-section measurement is listed in Table 6.17. The uncertainty of C_{h} is separated into the experimental part arising from the jet energy resolution (JER) and the theoretical part originating from the uncertainty of the generator model and the statistical uncertainty of the simulation. The contribution from ϵ_{b} is separated for efficiencies of mistagging (tagging of non-b jets) and correct b-tagging. Besides the uncertainty on the ingredients stated above, the table shows also the remaining relevant uncertainties which are not considered so far, arising from the jet-energy scale (JES) and the pileup; they are evaluated as described in the following.

Table 6.17: Influence of all systematic effects considered on the measured cross section, separated for experimental uncertainties, theoretical uncertainties, and a summary of the full uncertainty of the measurement for the inclusive cross section.

Source	Fractional uncertainty (%)
ϵ_b (b-tagging)	±10.0
P	±4.6
$f_{\mathrm{t\bar{t}}}$	±3.6
JES	±2.5
L	±2.2
ϵ_l	±2.0
C_h (JER)	±0.5
Pileup	±0.5
ϵ_b (mistagging)	±0.04
A_l (theory)	$^{+4.2}_{-6.5}$
C_h (theory)	$^{+0.2}_{-6.9}$
Experimental systematic	±12.3
Theoretical systematic	$^{+4.2}_{-9.5}$
Statistical	±1.7

The jet energy corrections applied can systematically over- or underestimate the true jet energy. The jet selection with $p_\mathrm{T} > 25\,\mathrm{GeV}$ thus can have an effect on the fraction of selected jets—the uncertainty on JES leads to a systematic uncertainty on the cross section. The influence of the (p_T, η)-dependent JES uncertainty on the event yields is calculated on the bZ^0 sample [159]. The scale in simulation is well known, so all correction factors should not be affected, but only the data yield. The influence on the cross section is about 2.5% [151]. The uncertainty on the pileup is estimated in the way recommended by CMS [169], shifting the mean of the expected distribution in simulation up and down by 0.6 interactions, i.e. number of primary vertices, giving a small uncertainty on the cross section of about 0.5% [151].

Not all ingredients are estimated on the full dataset used for the final cross-section measurement. For example the $\mathrm{t\bar{t}}$ contamination estimate is estimated on about the first half of the data, and as explained in Chapter 6.5.4 pileup can change the result. The uncertainty of the cross section due to pileup is covered by the estimate as stated above, but the central values are potentially not perfect. However the pileup rate was stable for the majority of the events, only the very last part of the data in use shows a slight increase [158]. Given the precision of the measurement, this effect can be neglected.

6.8.2 Results

Given all the ingredients, the visible and inclusive cross sections as defined in Chapter 6.3 follow

$$\begin{aligned}\sigma_{\text{vis}}^{\text{bZ}^0} &= \frac{N_{\text{obs}} \cdot (P - f_{\text{t}\bar{\text{t}}})}{C_{\text{h}} \cdot \epsilon_{\text{l}} \cdot \epsilon_{\text{b}} \cdot L} \\ &= 3.41 \pm 0.06\,(\text{stat.})^{+0.42}_{-0.48}\,(\text{syst.})\,\text{pb}\,,\end{aligned} \tag{6.32}$$

$$\begin{aligned}\sigma_{\text{inc}}^{\text{bZ}^0} &= \frac{N_{\text{obs}} \cdot (P - f_{\text{t}\bar{\text{t}}})}{A_{\text{l}} \cdot C_{\text{h}} \cdot \epsilon_{\text{l}} \cdot \epsilon_{\text{b}} \cdot L} \\ &= 5.97 \pm 0.10\,(\text{stat.})^{+0.78}_{-0.93}\,(\text{syst.})\,\text{pb}\,.\end{aligned} \tag{6.33}$$

The statistical uncertainty is well below the systematic uncertainties. The measurement is dominated by the experimental systematic uncertainties arising from the b jets, more precisely the b-jet efficiency ϵ_{b} and the b-jet event purity P. But also theoretical uncertainties contribute significantly, they are strongly reduced in the visible cross section. The uncertainty of the described $\text{t}\bar{\text{t}}$ estimate is only a minor contribution.

The inclusive bZ^0 cross section can be compared to the inclusive Z^0 cross section calculated in Chapter 5 in Equation 5.18. About 0.6% of all events of Z^0-boson production with muonic decay contain at least one hadronic b jet within the kinematic acceptance of the presented measurement.

In addition, the inclusive bZ^0 cross section can be compared to the result obtained in the electronic Z^0 decay channel, which yields $\sigma_{\text{inc}}^{\text{bZ}^0,\text{Z}^0\to\text{ee}} = 5.61 \pm 0.13\,(\text{stat.})^{+0.77}_{-0.90}\,(\text{syst.})\,\text{pb}$ [151]. The two channels are statistically uncorrelated. The dominant systematic errors are correlated, but some – in particular the lepton efficiencies, but e.g. also parts of the $\text{t}\bar{\text{t}}$ background estimate – are uncorrelated. The results of both channels are in agreement.

Furthermore, using some simplifications, the cross-section ratio $R_{\text{b/j}}$ of bZ^0 production and inclusive Z^0 production with any jet in the kinematic acceptance, labelled jZ^0, can be calculated for the visible cross section. It is assumed that the lepton kinematics are similar, thus ϵ_{l} cancels out. Furthermore, the hadron-level corrections C_{h} are assumed to be identical, which is valid due to the small deviation from unity. The last assumption is, that the background for jZ^0 is small, thus $N_{\text{sig}}^{j\text{Z}^0} = N_{\text{obs}}^{j\text{Z}^0} = 134725$ can be taken from Table 6.2. Using Equation 6.19, it is $N_{\text{sig}}^{\text{bZ}^0} = 2121 \pm 37\,(\text{stat.}) \pm 124\,(\text{syst.})$. The ratio is then calculated as

$$\begin{aligned}R_{\text{b/j}} &= \frac{\sigma_{\text{vis}}^{\text{bZ}^0}}{\sigma_{\text{vis}}^{j\text{Z}^0}} = \frac{N_{\text{sig}}^{\text{bZ}^0}}{N_{\text{sig}}^{j\text{Z}^0} \cdot \epsilon_{\text{b}}} \\ &= (4.4 \pm 0.1\,(\text{stat.}) \pm 0.5\,(\text{syst.}))\,\%\,.\end{aligned} \tag{6.34}$$

However, the precision of such a ratio is not much better than the absolute cross section given the dominant uncertainties on ϵ_{b} and P entering the calculation.

The value is in good agreement with the one of the analysis on 2010 data of $R_{\mathrm{b/j}} = (4.6 \pm 0.8\,(\mathrm{stat.}) \pm 1.1\,(\mathrm{syst.}))\,\%$ [56]. Actually, the definitions are identical, but the 2010 data analysis uses also the selection on $\not{E}_{\mathrm{T}} < 40\,\mathrm{GeV}$ for bZ^0 events and corrects for it with simulation yields, but it is shown in this chapter that the influence on bZ^0 events is only marginal and deselects only few percent (see Table 6.14).

Finally, the inclusive bZ^0 cross section is compared to theory, to NLO calculations in the variable-flavour scheme with massless b quarks obtained with the MCFM tool. The inclusive cross section at parton-level, using identical acceptance requirements for the parton jets, is found to be $\sigma^{\mathrm{MCFM}}_{\mathrm{parton}} = 4.73 \pm 0.54\,\mathrm{pb}$ [151]. The uncertainty is estimated with the CTEQ6M PDF set [170] and variations of the renormalisation and factorisation scales around the Z^0 mass with factor 2 up and down, considering correlated and anticorrelated combinations [171]. For a direct comparison, the cross section is corrected to hadron-level with C_{p} (see Chapter 6.7), and found to be smaller than the measurement:

$$\sigma^{\mathrm{bZ}^0,\mathrm{MCFM}}_{\mathrm{inc}} = 3.97 \pm 0.47\,\mathrm{pb}\,. \tag{6.35}$$

6.9 Conclusions

The production cross section of $\mathrm{Z}^0(\gamma^*)$ bosons associated with b jets has been measured in the first parts of the proton-proton collisions of 2011 at $\sqrt{s} = 7\,\mathrm{TeV}$, using the muonic decay mode to identify the Z^0 in the mass range $60\,\mathrm{GeV} < M_{\mathrm{Z}^0} < 120\,\mathrm{GeV}$. The cross section requires at least one b jet in the kinematic regime of $p_{\mathrm{T}} > 25\,\mathrm{GeV}$ and $|\eta| < 2.1$, and $\Delta R(\mathrm{jet,muons}) > 0.5$. Corrections from detector-level to hadron-level are estimated with simulated samples produced with MadGraph. The distributions from data and simulation are in fair agreement. Remaining differences may be a consequence of the higher order terms absent in the tree-level simulation by MadGraph with massless b quarks. The background contamination is estimated first on measuring the b-tag event purity of selected events, i.e. the fraction of events containing real b jets. The remaining relevant background are $\mathrm{t\bar{t}}$ events with dimuonic final state, which have a similar topology and a similar cross section. It is estimated by extrapolation from the sideband in the invariant dimuon mass spectrum $120\,\mathrm{GeV} < M_{\mu^+\mu^-} < 400\,\mathrm{GeV}$, which is dominated by $\mathrm{t\bar{t}}$. Information based on simulation is corrected with a $\mathrm{t\bar{t}}$ cross-section measurement differential in the dilepton mass for the almost background free $\mathrm{e}\mu$ final state. The uncertainty has only a small effect on the cross-section measurement, but this may be more important in future measurements based on two b jets. The measured cross section is somewhat above the NLO prediction. This can be a hint that cross sections for the postulated Higgs boson in association with b jets could also have a bigger cross section than the one expected from NLO theory calculations.

Chapter 7

Summary

This thesis describes three analyses evaluating proton-proton collisions at a centre-of-mass energy of $\sqrt{s} = 7\,\mathrm{TeV}$, provided by LHC, and recorded with the CMS experiment in 2010 and 2011. One is a technical analysis concerning the CMS tracker, the other two are physics analyses. All of them use events containing isolated muons of high momentum in the final state, and these muons are also used for triggering these events. The two physics analyses have directly contributed to CMS results which have been published [137][151], the technical analysis is submitted as potential contribution to the publication in preparation [122].

Technical Analysis
Estimation of the Tracker Alignment Precision

The only active detector elements of the tracker are silicon strip and pixel modules. Their alignment parameters – positions and orientations of all modules in the global tracker coordinate system – need to be known very precisely in the track reconstruction, in order to exploit best the intrinsic resolution, and to achieve the precision required for the ambitious physics programme of CMS. The desired knowledge is gained using alignment—sophisticated algorithms recalculate the alignment parameters from millions of reconstructed tracks on a statistical basis. However, due to the complexity of the corresponding system of equations, the simultaneous estimation of the achieved precision for a certain set of alignment parameters is not feasible. The uncertainties, reflecting the remaining misalignment, need to be estimated in a separate approach.

The technical analysis describes the development and the results of a method for estimating the uncertainty corresponding to the alignment parameters, which is called the alignment precision. Similar to the alignment parameters, the alignment precision is a parameter set defining the uncertainty of each module in the global tracker coordinate system. However, only translations in the plane defined by the module are considered. The alignment precision is taken into account in the track reconstruction, correcting the intrinsic hit resolution to an effective hit resolution.

The method is based on the width of normalised residual distributions. The residual is defined as the difference of hit measurement and track prediction on the module's surface; this is normalised to the intrinsic hit and track uncertainty estimates. The distribution is approximately Gaussian, and in case of correct error assignment, the width (defined as the standard deviation of a Gaussian fit to the distribution) is a measure for the misalignment. In the case of perfect alignment, the nominal residual width Δ_0 is expected to be around 1, while misalignment broadens the distribution, and thus can be measured from the broadening. The alignment precision is estimated such, that the broadened width Δ goes back to Δ_0 when taking the effective hit resolution, including the alignment precision, into account.

The main challenge is given by the fact, that the uncertainty estimates of the hits are obviously incorrect when looking at individual residuals, while they are on average good enough to describe the whole tracks. The method is very sensitive to incorrect error estimates, since they can broaden or narrow the nominal residual distribution. The solution is based mainly on two steps. First, a stringent track and hit selection is applied, in order to reduce the influence from very badly described residuals. Second, instead of using the expectation of $\Delta_0 \approx 1$, the nominal residual width is estimated from simulation. The latter requires accurate modelling, but allows independence from correct error estimates, as long as the same incorrect estimates are used with the same frequency in data and simulation. However, this solution cannot remove systematic effects completely, since the modelling of track parameters works quite well, but several hit parameters show significant deviations between data and simulation.

In several regions of the tracker where the modelling is good, the method gives precise results. But some regions suffer from the fact, that the nominal residual width as taken from simulation is above the value measured in data, which would mathematically lead to imaginary values of the alignment precision. Systematic studies are applied in order to get an idea about the upper limit of the misalignment in such regions. Results are estimated for the geometry as it is used throughout the 2011 data taking and in the prompt reconstruction, and for a second geometry which was prepared for the final reprocessing of the data at the end of the year. The result of the alignment precision does not reflect the misalignment in the corresponding coordinate only, but also all other misalignments, e.g. from shifts along the module's normal or rotations. It is a projection of all influences on this two-dimensional space, thus represents the best value for the alignment precision given the recent implementation in the reconstruction. It is found, that the prompt geometry is already of good quality and that it is stable enough in time for the whole year. However, the reprocessing geometry shows significant improvement, since all present effects are accounted for and due to the advanced alignment strategy. The estimated values are mainly below $10\,\mu$m confirming the excellent performance of the alignment procedures, i.e. the demands of physics analyses are fulfilled.

Finally, the influence on the track reconstruction is analysed. Of course, it is more visible for bigger misalignment, and the reprocessing geometry is already close to the truth. Due to the more correct weight of individual hits, the central values get slightly better, and the uncertainties are described much better. Since almost all physics analyses require tracker information, their results get better when including the alignment precision of correct size. Especially impact parameter based b-tagging algorithms, like the one used in the second physics analysis presented, can profit a lot.

Physics Analysis
Cross-Section Ratio of Top-Pair and Z^0-Boson Production

Reporting measurements in terms of cross-section ratios instead of absolute cross sections can result in higher precision, since common systematic effects – both from the experimental measurement and from the underlying theory – cancel out. In this work, the measurement of the cross-section ratio of top-pair ($t\bar{t}$) and inclusive Z^0-boson production is performed on 2010 data, using their leptonic decay modes with muons in the final state. The ratio offers a more precise scrutiny of the Standard Model compared to absolute cross sections. Furthermore, the ratio permits – in conjunction with the theoretical Z^0 cross section – an extraction of the $t\bar{t}$ cross section independent of the luminosity estimate. The muon triggers and the muon selections chosen are identical for both analyses. Uncertainties arising from the muons (trigger and selection efficiencies) cancel partly, depending on the difference of the event topology of both processes. The same dataset is used for both processes, thus the luminosity cancels completely. The analyses are separated by a complementary selection in the dimuon invariant mass, choosing events around the Z^0 peak for the Z^0 analysis, and those vetoing this window for the top analysis. The top analysis requires in addition the presence of at least two jets and significant missing transverse energy originating from the indetectability of the neutrinos. Due to the similar topology, both processes are main backgrounds for each other.

While the Z^0 cross section can be measured precisely with this data, the $t\bar{t}$ cross section suffers from the small statistical power and systematic uncertainties uncorrelated with the ones of the Z^0 analysis. The cross-section ratio is thus dominated by the uncertainty of the top analysis, but the cancellation of several experimental uncertainties lead to a gain in precision. Within the large uncertainties of the experiment, consistency is found with the Standard Model predictions. The method will provide valuable benefit in future analyses with bigger datasets and better understanding of the detector for testing the Standard Model and the precise determination of its parameters. The presented measurement results in about 400 Z^0 events per $t\bar{t}$ event for their dimuon final states:

$$\begin{aligned}\frac{\sigma_{\mathrm{inc}}^{t\bar{t}}}{\sigma_{\mathrm{inc}}^{Z^0}} &= (2.5 \pm 0.7\,(\mathrm{stat.}) \pm 0.7\,(\mathrm{syst.})) \cdot 10^{-3} \\ &= (403 \pm 167)^{-1}\,.\end{aligned}$$

Furthermore, using the theoretical prediction of the Z^0 cross section, the luminosity measurement is replaced by the ratio of measured and theoretical cross section for the estimate of the $t\bar{t}$ production cross section—the Z^0 is used as a standard candle. Depending on the uncertainties of the direct luminosity measurement and of the theoretical cross section, this can reduce the total normalisation uncertainty. Since they are of similar size, the precision is similar; results are found to be in good agreement. The ultimate precision is reached combining both normalisation methods. The total production cross section of $t\bar{t}$ events with the combined normalisation is found to be in good agreement with the NLO theory prediction of $\sigma^{t\bar{t}}_{\text{total, theory}} = 158^{+23}_{-24}\,\text{pb}$:

$$\sigma^{t\bar{t}}_{\text{total, comb}} = 149 \pm 45\,(\text{stat.}) \pm 42\,(\text{syst.}) \pm 4.7\,(\text{comb.})\,\text{pb}\,.$$

Physics Analysis
Measurement of Associated Z^0-Boson and b-Jet Production

Z^0-boson production is a well understood and precisely measured process of the Standard Model. However, the production in association with b quarks (bZ^0) was difficult to access for experimental particle physics so far. A precise measurement of the cross section of this specific process is essential e.g. for various Higgs analyses, since it is a direct irreducible background for some of them, and an important benchmark process for some others. The latter is due to the sensitivity on the b quark fraction of the protons, which is known with big uncertainties only. Furthermore, different schemes of theoretical calculations show big deviations of the central values, which are still compatible due to the huge uncertainties. Thus, the process is also relevant for the refinement of theoretical calculations. In this thesis, the cross-section measurement of bZ^0 is detailed using 2011 data. The Z^0 is identified by its muonic decay mode, and in addition at least one b jet is required.

Given the leptonic Z^0 decay in association to b jets, the topology of the process is very similar to $t\bar{t}$ in the dilepton final state, which thus constitutes the dominant background. In this work special emphasis is placed on the estimation of the $t\bar{t}$ background, using the synergy with the local top group. Similar to the separation of the two processes in the $t\bar{t}$-to-Z^0 ratio measurement, $t\bar{t}$ is measured in the sideband above the Z^0 peak of the dimuon invariant mass distribution, and is then extrapolated to the signal region enclosing the peak. Results of $t\bar{t}$ cross-section measurements differential in the dilepton mass performed in the clean $e\mu$ final state are used to correct the extrapolation, which is based in first place on the dimuon mass spectrum as taken from simulation. The fraction of $t\bar{t}$ events in the bZ^0 signal region is found to be

$$f_{t\bar{t}} = (18.4 \pm 2.3)\,\%\,.$$

Thanks to the well-understood $t\bar{t}$ measurement, the uncertainty on this background estimate is a small contribution to the uncertainty of the cross section, which is dominated by experimental systematic effects concerning the b-tagging. Further backgrounds are found to be negligible except for Z^0 events associated with non-b jets which are mistagged. The estimated cross section is defined for all Z^0 events with muonic decay which also contain at least one b jet in the kinematic range $p_{\mathrm{T}}^{\mathrm{b}} > 25\,\mathrm{GeV}$, $|\eta^{\mathrm{b}}| < 2.1$ and $\Delta R(\mathrm{jet,muons}) > 0.5$. The result is:

$$\sigma_{\mathrm{inc}}^{\mathrm{bZ^0}} = 5.97 \pm 0.10\,(\mathrm{stat.})^{+0.78}_{-0.93}\,(\mathrm{syst.})\,\mathrm{pb}\,.$$

The value is above the NLO prediction of $\sigma_{\mathrm{inc,\ theory}}^{\mathrm{bZ^0}} = 3.97 \pm 0.47\,\mathrm{pb}$. This result can be of relevance for searches of the Higgs boson in association to b jets, being an indication that cross sections for this process might as well be above the prediction.

Appendix A

Appendix for Chapter 4

A.1 Tracker Alignment

A.1.1 Important Sets of Alignment Parameters

When LHC started to provide collisions for its physics programme, the tracker alignment was already in a good shape. CMS took data of cosmic muons in several periods starting in September 2008, and repeated in 2009 and 2010. The data was used to commission the detector and collect experience in the operation of the detector systems [172]. It was also used for alignment purely based on cosmic muons (see [173] or [174]). The alignment constants were obtained with a hybrid approach. First, the geometry was aligned with Millepede II, then the resulting geometry was used as starting geometry for HIP, producing the final alignment parameters. At this time, Millepede II used a simple 5-parameter helix as track model and the number of parameters in the implementation was restricted to at most 46320, thus the final precision was limited. In the later alignment campaigns more sophisticated track models are used, and the limitation on the number of parameters is removed.

The small amount of low-energy data taken in late 2009 is not used in alignment. Since March 2010, LHC has been providing collisions at $\sqrt{s} = 7\,\mathrm{TeV}$. The collision data is used in combination with cosmic ray data for all following alignments. In order to gather enough cosmic ray data, possible periods of cosmic ray data taking before the 2010 collision runs are used, with special settings maximising the efficiency of cosmic muon reconstruction ("cosmics run at four Tesla CRAFT"). Due to the small number of colliding proton bunches at that time, also cosmic rays during collision runs could be recorded for empty bunches ("cosmics during collisions CdC"). In addition, special regional tracking algorithms are introduced to take cosmic rays within collisions, but in fact this was never used ("regional cosmics"); the same holds for cosmic ray recordings in between collision runs ("interfill cosmics"). The 2010 data as used in Chapter 5 was reprocessed at the end of 2010 with improved alignment and calibration conditions. The tracker alignment was produced by Millepede II. Tracks from collision events taken with a minimum bias trigger, thus with mainly low momenta, are combined with cosmics. Movements of the pixel half-barrels – which are real mounting structures – with respect to each other could be observed. For this reason, the alignment parameter tag is subdivided in 8 IOVs defining consecutive run ranges (see Chapter 4.1.1). The strip tracker and the intrinsic pixel alignment have the same geometry in all IOVs, but the pixel half-barrels are determined individually for each IOV. The results are achieved in one single alignment procedure using all tracks in all IOVs instantaneously. Details about the alignment strategy and validation can be found elsewhere [126].

In 2011 the amount of collision data recorded exceeds the 2010 dataset by far. Since the alignment was well understood, the whole collision data of the year was taken with the same alignment constants. This data is used for the analysis in Chapter 6 and for the estimation of the alignment precision in this chapter. Again, a reprocessing of the dataset of the whole year is done at the end of 2011 with improved alignment and calibration conditions. The basic tracker alignment strategy is similar to the one of 2010, but more information is used and more degrees of freedom are aligned as stated in the following. The tracker alignment tag is provided by Millepede II. This time it is subdivided in 12 IOVs to account for the observed pixel movements, presented in Table A.1. For the first time, also the kinks and bows of the sensors were estimated. Data taken with the minimum bias trigger is combined with cosmic ray data and this time also with isolated muons based on muon triggers, while the used isolated muon dataset exceeded the minimum bias dataset by far. It was found that the whole tracker shows a weak mode in shape of a twist along the z-axis. Additional datasets based on muon triggers providing $Z^0 \to \mu^+\mu^-$ decays are used with two-body decay constraints to get a handle on this weak mode. The achieved precision of the resulting alignment parameters of this approach is studied in this chapter. Documentation can be found in [175][122].

In order to provide accurate modelling of the data with simulation, misalignment and miscalibration needs to be introduced in the reconstruction of simulated events. During the simulation itself, all conditions are set to the ideal values. But in the reconstruction specific tags are used to reflect the conditions in real data. Realistic misalignment and miscalibration tags were obtained in comparison to data, and were updated several times in order to comply with recent developments. The physics analyses in Chapter 5 and Chapter 6 use these samples with realistic conditions. These simulated event samples are also used in the present chapter, reconstructed with the realistic conditions as they were estimated for the 2011 data taking period. However, since the simulated samples are used to understand the behaviour of the hit and track reconstruction in case of perfect conditions, the simulation on design geometry needs to be studied. This is achieved with the refit is use, it is again based on the ideal alignment and calibration conditions, thus the design geometry – which is the true geometry in this case – is applied.

Table A.1: Tracker alignment periods in 2011 for data reprocessing, defined by their interval of validity (IOV) [176]. The IOV sets the run range, for which the same set of alignment parameters from the database record are used. The alignment parameters can change from IOV to IOV. Here, only the larger pixel structures are allowed to change between the IOVs to account for the observed pixel movements.

IOV	Run range	Remark
A	157866–158383	Cosmic data taking
B	158384–161406	
C	161407–163044	Since 26.03.
D	163045–164161	Since 19.04.
E	164162–165414	Since 05.05.
F	165415–165999	Since 21.05.
G	166000–166398	Since 29.05.
H	166399–167043	Since 03.06.
I	167044–170248	Since 16.06.
P1	170249–171875	
P2	171876–173664	
P3	173665–end	

A.2 Implementation of the Alignment Precision

It is desirable to take all experimental uncertainties into account and to describe them in the best possible way. This holds for the errors of the reconstructed track parameters from the tracker. In addition, processes like b-tagging need very precise track errors to keep the best possible balance between efficient tagging of real b-jets and minimal mis-tagging rates of jets without real b-hadrons. The results are influenced by systematic effects, like misalignment. Within the CMS software, misalignment can be quantified with an uncertainty assignment, the alignment precision. In this framework it is also called the alignment position error (APE).

The tracker has a complex design. There are regions of very different intrinsic hit resolutions. The module-wise alignment as derived in the alignment algorithms is based on different track and hit distributions. E.g. every alignment approach uses cosmic muons in addition to other track sources, like collision tracks. And the nature of the cosmic rays give an asymmetric illumination for the different silicon modules. In addition, there can occur time-dependent movements of substructures, e.g. due to the magnetic field or the observed pixel shifts. Summarising, the alignment precision can vary over the modules and over the detector regions. To get the best possible results, high granularity of the alignment precision is needed. This is also needed to build realistic misalignment scenarios for the reconstruction of simulated samples.

A.2.1 Alignment Precision Record

The alignment precision is a record of the alignment and calibration database (see Chapter 4.1.1), similar to the record of the alignment parameters. The parameters of the alignment precision are defined per module in the same local Cartesian $(u|v|w)$ coordinate system as the alignment parameters. To each module, errors are assigned for the three translations in u-, v- and w-direction taking correlations between them into account. However, the parameters in the record are stored in global tracker coordinates, like it is done for the alignment parameters. There are no explicit uncertainties for the other alignment parameters, neither for the rotation angles around the local coordinate axes, nor for the kinks and bows describing the sensor shape on the modules.

There are different tags in use, one for the reconstruction of data and one for the reconstruction of simulated events. To this day, the uncertainty is always assigned spherical, which means the same absolute value in all three translations. The values assigned in the data tag are shown in Figure A.1. The values are obtained as described in [128]. The record for the simulation was in earlier days adjusted to the developed misalignment scenario, the alignment precision is set according to the smearing amplitudes used for the misalignment. Meanwhile they are estimated identical to data—the identical alignment procedure

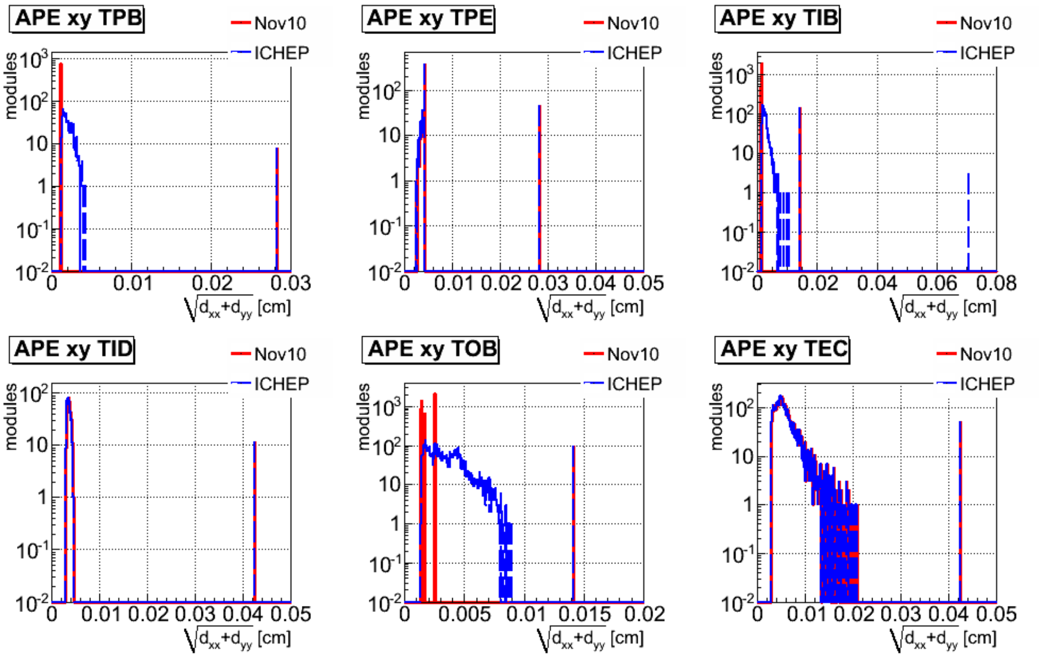

Figure A.1: Alignment precision as used for data reconstruction [177]. Shown are the values for each module, separated by subdetector. These are from top left to bottom right BPIX, FPIX, TIB, TID, TOB and TEC. The blue line shows the values as they were set for the beginning of the collision data taking, the red line shows an update as it is in use for the data reprocessings of 2010 and for all reconstructions (prompt and reprocessings) of 2011 data. The spike on the right in each plot shows huge values as they are assigned to inactive or problematic modules, where no measurement can be performed.

is run on a misalignment scenario, the resulting alignment parameters get the corresponding alignment precision assigned with the cited method.

A.2.2 Implementation in the Track Reconstruction

The first step in the track reconstruction chain is the hit reconstruction, based on the induced charges from charged particles penetrating the active area of the silicon modules. Clusters are formed with a specific algorithm, assembling neighbouring strips or pixels above the noise threshold, based on the calibration and the knowledge of inefficiencies of channels. The hit reconstruction uses algorithms called cluster parameter estimator (CPE). They translate a one-dimensional (two-dimensional) measurement in a strip (pixel) module for hit i into a position

$$\mathbf{x}_{\text{hit}} = \begin{pmatrix} u_{\text{hit}} \\ v_{\text{hit}} \end{pmatrix} \tag{A.1}$$

and corresponding uncertainty given by the covariance matrix $\mathbf{V}_{\text{hit}}$ in the local Cartesian $(u|v)$ coordinate system, assuming flat modules. This coordinate system is the u-v-plane of the $(u|v|w)$ coordinate system, lying in the plane of the module. The positions are corrected for deviations of the module shape from a flat sensor in w-direction, using the track prediction on the module. As explained, these deviations are parameterised in the kinks and bows database record.

The whole track reconstruction is based on this $(u|v)$ coordinate system. The intrinsic hit resolution is given by

$$\mathbf{V}_{\text{hit}} = \begin{pmatrix} \sigma^2_{u,\text{hit}} & c \cdot \sigma_{u,\text{hit}}\sigma_{v,\text{hit}} \\ c \cdot \sigma_{u,\text{hit}}\sigma_{v,\text{hit}} & \sigma^2_{v,\text{hit}} \end{pmatrix} . \tag{A.2}$$

Correlations between both coordinates are taken into account and are given by the correlation coefficient $c \in [-1, +1]$. In the pixel detector and in the rectangular strip modules of TIB and TOB, both coordinates are uncorrelated, $c = 0$, since they reflect the module topology. Since the track reconstruction is based on this Cartesian system, the measurements in TIB and TOB are treated as 1-dimensional, only the u-coordinate is regarded. In the wedge-shaped sensors of TID and TEC however, both coordinates are correlated as illustrated in Figure 4.2.

The alignment precision is used to correct the intrinsic uncertainty of a hit measurement $\mathbf{x}_{\text{hit}}$ in the local coordinate frame, when translating the track parameterisation into a track prediction in this local coordinate, where the misalignment affects the precision. Although the alignment precision is stored in the record as the full covariance matrix for module translations in three dimensions, only the two in $(u|v)$ are used in the reconstruction. Their correlations are in principle incorporated, but not regarded in the production of constants, where they are always set to 0—thus, within the reconstruction the alignment precision is defined as

$$\mathbf{V}_{\text{align}} = \begin{pmatrix} \sigma^2_{u,\text{align}} & 0 \\ 0 & \sigma^2_{v,\text{align}} \end{pmatrix} . \tag{A.3}$$

In TIB and TOB, only the value $\sigma^2_{u,\text{align}}$ is relevant. Neglecting off-diagonal elements of the alignment precision has no influence. For the other modules the correlations are expected to be small with negligible off-diagonal elements. The errors for each coordinate independently are added in quadrature to the hit errors. The effective hit resolution $\mathbf{V}_{\text{eff}}$ is then given by

$$\mathbf{V}_{\text{eff}} = \mathbf{V}_{\text{hit}} + \mathbf{V}_{\text{align}} = \begin{pmatrix} \sigma^2_{u,\text{hit}} + \sigma^2_{u,\text{align}} & c \cdot \sigma_{u,\text{hit}}\sigma_{v,\text{hit}} \\ c \cdot \sigma_{u,\text{hit}}\sigma_{v,\text{hit}} & \sigma^2_{v,\text{hit}} + \sigma^2_{v,\text{align}} \end{pmatrix} . \tag{A.4}$$

The effective hit error consists of the alignment precision of the module and the individual intrinsic hit error depending on the specific cluster parameters but also on the track parameters.

The effective hit resolution is used in the second step of the track reconstruction, the global reconstruction. First, the pattern recognition procedure builds tracks assembling clusters from consecutive silicon layers. The search window for the clusters depends on the effective hit uncertainties. Then, after the tracks are formed, the final track fit is performed, incorporating the effective hit uncertainties. The track prediction on the module's surface $\mathbf{x}_{\text{trk}}$ and the corresponding uncertainty $\mathbf{V}_{\text{trk}}$ transformed in the (u, v) coordinate system are

$$\mathbf{x}_{\text{trk}} = \begin{pmatrix} u_{\text{trk}} \\ v_{\text{trk}} \end{pmatrix}, \qquad \mathbf{V}_{\text{trk}} = \begin{pmatrix} \sigma^2_{u,\text{trk}} & k \cdot \sigma_{u,\text{trk}}\sigma_{v,\text{trk}} \\ k \cdot \sigma_{u,\text{trk}}\sigma_{v,\text{trk}} & \sigma^2_{v,\text{trk}} \end{pmatrix}, \tag{A.5}$$

where $k \in [-1, +1]$ is the correlation coefficient, which is $k = 0$ for TIB, TOB and pixel modules.

The track prediction $\mathbf{x}_{ji,\text{trk}} = \mathbf{x}_{ji,\text{trk}}(\mathbf{x}_{j,\text{hit}})$ of track j for hit i with position $\mathbf{x}_{ji,\text{hit}}$ depends on all positions and errors of all N hits used in the track fit $\mathbf{x}_{j,\text{hit}} = (\,\mathbf{x}_{j1,\text{hit}}\,, \ldots, \,\mathbf{x}_{jN,\text{hit}}\,)$. Thus it depends on the alignment precision of all used modules and on the specific intrinsic hit resolutions. As already discussed, it also depends on the alignment parameters $\mathbf{p}$ of the used modules and the track model leading to the track parameterisation $\mathbf{q}_j$. The hit residuals follow

$$\mathbf{r}_{ji} = \mathbf{x}_{ji,\text{trk}} - \mathbf{x}_{ji,\text{hit}} = \begin{pmatrix} u_{ji,\text{trk}} - u_{ji,\text{hit}} \\ v_{ji,\text{trk}} - v_{ji,\text{hit}} \end{pmatrix} \tag{A.6}$$

with the covariance matrix depending on $\mathbf{V} = \mathbf{V}(\mathbf{V}_{\text{eff}}, \mathbf{V}_{\text{trk}})$.

A.2.3 Coordinate Systems

As discussed, the hit residuals get in general bigger by misalignment. The same is valid for the residuals normalised to their errors, since the errors are underestimated. This can be balanced by the alignment precision. The basic alignment validations visualise the quality of derived alignment parameters with distributions of absolute and normalised hit residuals. Moreover, normalised residual distributions are the main ingredient for estimating the alignment precision with the presented method.

To get useful statements from the residual distributions, a coordinate system has to be chosen which is oriented on the geometrical design and on the global orientation of the modules. In the following, local coordinate systems are presented which lead to the alignment $(x|y)$ coordinate system fulfilling these requirements. These two-dimensional local coordinate systems are defined in the same plane as the local $(u|v)$ Cartesian system described in Chapter A.2.2. Furthermore, their origins all coincide, except for the $(m_1|m_2)$ measurement system.

The Local $(m_1|m_2)$ Measurement System

The local $(m_1|m_2)$ measurement system is the native measurement frame of the silicon sensors. The readout channels are numerated, beginning from 0 for the strip or pixel at one edge of the sensor. For strip modules there is only one sensitive coordinate (m_1), while m_2 goes from $-1/2$ to $+1/2$ along the strip with the origin in the middle of the strip—for the pixel modules both coordinates ($m_1|m_2$) are sensitive and numerated. The orientation of both axes in ($m_1|m_2$) is identical to the orientation of the axes in the local ($u|v$) Cartesian system. It is the only system whose units are not absolute lengths, but lengths normalised to the channel pitch, thus number of strips or pixels.

The coordinate system coincides with the shape of the charge clusters. Clusters are built from neighbouring channels above the noise threshold, and the position and signal strength of each regarded channel is stored. But this system is not used in the tracking procedure, all hits are transformed in the Cartesian ($u|v$) coordinate system. This is done by a cluster parameter estimator (CPE) which calculates positions and uncertainties from the stored clusters, and translates them from the ($m_1|m_2$) system to a hit measurement in the ($u|v$) system.

The Local ($x^{\mathrm{T}}|y^{\mathrm{T}}$) Topological System

The topological ($x^{\mathrm{T}}|y^{\mathrm{T}}$) system takes the topology of the modules into account to have two uncorrelated coordinates. The system is identical to the ($u|v$) system for the rectangular modules in BPIX, FPIX, TIB and TOB. It only differs for the wedge-shaped sensors in TID and TEC, where it is a radial coordinate system instead of a Cartesian. The x^{T}-axis is along the sensitive measurement coordinate, it is equivalent to an angular coordinate, translated in a length. The y^{T} axis is along the strips, orthogonal to x^{T}, and has no sensitivity. Given the measurement in the ($m_1|m_2$) system, an angle ϕ with its uncertainty σ_ϕ is defined as

$$\phi = \pm 1 \cdot A \cdot m_1 + \phi_0\,, \qquad \sigma_\phi = A \cdot \sigma_{m_1}\,. \tag{A.7}$$

In this equation, A is the angular width giving the angular distance between two strips, and ϕ_0 is the negative signed angle spanned by the module edge and the centre of the module, corresponding to the v-axis. This definition leads to the fact that $\phi = 0^\circ$ coincides with the v-axis. The ± 1 depends on the orientation of the m_2-axis, whether it points into the direction of the virtual intersection point of the strips, or away from it.

To get conclusive information about the quality of the alignment, the angle and its error is translated into a length and error by multiplying with the radius:

$$x^{\mathrm{T}} = r_0 \cdot \phi\,, \qquad \sigma_{x^{\mathrm{T}}} = r_0 \cdot \sigma_\phi\,. \tag{A.8}$$

A constant value r_0 needs to be chosen to keep the linearity of the hit residuals in the angular measurement. Chosen is the distance of the virtual intersection point of the strips to the origin of the module, which is for the design geometry the distance of the origin to the beam line. If the distance would be kept variable like referring to the penetration point of the individual track instead of the module's origin, residuals corresponding to the same distance in number of strips would differ driven by their distance on the sensor in y^{T}-direction. Measurements close to the origin are similar for the coordinates of the $(u|v)$ and the $(x^{\mathrm{T}}|y^{\mathrm{T}})$ system. Differences become bigger for bigger angular distances ϕ, since the correlations of both coordinates in the $(u|v)$ system rise. The values of x^{T} are only correct lengths when the track penetrates the sensor in a distance from the virtual intersection point equal to r_0. But the resulting differences are small, since the modules are small compared to the distance to the intersection point. The system is not used at any place, it is another step towards the most important coordinate system for alignment studies.

The Local $(x|y)$ Oriented System

The oriented $(x|y)$ system is identical to the $(x^{\mathrm{T}}|y^{\mathrm{T}})$ system except for the signs of the axes. It takes the orientation of the modules in the global $(r|r\phi|z)$ tracker system into account, which differs among the modules. To do so, 3 local points are defined in $(u|v)$, the origin $O(0|0)$ plus the points $P_u(1|0)$ and $P_v(0|1)$. They are transformed via the alignment parameters in global points in $(r|r\phi|z)$. Each axis is compared to the corresponding axis in the global coordinate system. It is checked whether their positive directions are the same, or whether the axes point in opposite directions. The positive x-axis is decided to point in the positive $r\phi$-direction in all subdetectors except FPIX, where the axis point in the positive r-direction,

$$x = \begin{cases} \begin{array}{lll} +x^{\mathrm{T}} & \text{for} & \phi_{P_x} - \phi_O \geq 0 \\ -x^{\mathrm{T}} & \text{for} & \phi_{P_x} - \phi_O < 0 \end{array} & \text{in all except FPIX} \\ \\ \begin{array}{lll} +x^{\mathrm{T}} & \text{for} & r_{P_x} - r_O \geq 0 \\ -x^{\mathrm{T}} & \text{for} & r_{P_x} - r_O < 0 \end{array} & \text{in FPIX} \end{cases} . \tag{A.9}$$

The positive y-axis is mapped to the positive z-direction in the barrel subdetectors BPIX, TIB and TOB. In FPIX it points into the positive $r\phi$-direction, and in TID and TEC it is oriented in positive r-direction:

$$y = \begin{cases} \begin{array}{lll} +y^{\mathrm{T}} & \text{for} & z_{P_y} - z_O \geq 0 \\ -y^{\mathrm{T}} & \text{for} & z_{P_y} - z_O < 0 \end{array} & \text{in BPIX, TIB, TOB} \\ \\ \begin{array}{lll} +y^{\mathrm{T}} & \text{for} & \phi_{P_y} - \phi_O \geq 0 \\ -y^{\mathrm{T}} & \text{for} & \phi_{P_y} - \phi_O < 0 \end{array} & \text{in FPIX} \\ \\ \begin{array}{lll} +y^{\mathrm{T}} & \text{for} & r_{P_y} - r_O \geq 0 \\ -y^{\mathrm{T}} & \text{for} & r_{P_y} - r_O < 0 \end{array} & \text{in TID, TEC} \end{cases} . \tag{A.10}$$

Due to the orientation of the coordinate axes, the residuals are also oriented in the same global directions.

All measurements are uncorrelated in this $(x|y)$ coordinate system, just as in $(m_1|m_2)$ and $(x^{\mathrm{T}}|y^{\mathrm{T}})$. Thus, the residuals can be written 1-dimensional. In the strip modules, there is only one sensitive coordinate across the strips, in the pixel modules both coordinates are uncorrelated. The residual in x-direction r_x and its error σ_{r_x} depends only on the parameters along this direction, the hit position x_{hit} with error $\sigma_{x_{\mathrm{eff}}}$ and the track prediction x_{trk} with error $\sigma_{x_{\mathrm{trk}}}$:

$$r_x = x_{\mathrm{trk}} - x_{\mathrm{hit}}\,, \qquad \sigma_{r_x} = \sigma_{r_x}(\sigma_{x_{\mathrm{eff}}}, \sigma_{x_{\mathrm{trk}}})\,. \tag{A.11}$$

The same uncorrelated relation is valid for the y-direction in the pixel modules:

$$r_y = y_{\mathrm{trk}} - y_{\mathrm{hit}}\,, \qquad \sigma_{r_y} = \sigma_{r_y}(\sigma_{y_{\mathrm{eff}}}, \sigma_{y_{\mathrm{trk}}})\,. \tag{A.12}$$

In this description, also the normalised residuals can be regarded independently in each coordinate, since the errors are uncorrelated. The normalised residuals can be written as:

$$r_x^{\mathrm{norm}} = \frac{r_x}{\sigma_{r_x}}\,, \qquad r_y^{\mathrm{norm}} = \frac{r_y}{\sigma_{r_y}}\,. \tag{A.13}$$

The modules are mounted in the detector with different global orientations of their axes. When regarding residual distributions for a single module, there is no preference for one of the systems $(x|y)$ and $(x^{\mathrm{T}}|y^{\mathrm{T}})$. Misalignment shifts the central value to one side, and the distribution gets broader. But the difference gets clear, when residual distributions of several modules with different orientations are analysed together, e.g. when looking at the modules mounted on the same rod. Common misalignment of a region, e.g. a shift of the rod, would not show up as a shift in the central value with the corresponding broadening, but as two overlaid distributions, symmetrically shifted to each side. The central value would not shift at all, while the broadening of the distribution gets too big.

The system is used to analyse the residual distributions in uncorrelated coordinates, as it is the basis for the presented estimation of the residual resolution, and as it is used in the basic alignment validation (see [178]). Since the track reconstruction uses the $(u|v)$ Cartesian system, the hits and the track predictions need to be converted. They are first converted back into the native $(m_1|m_2)$ measurement system, then transformed into the $(x^{\mathrm{T}}|y^{\mathrm{T}})$ topological system, and finally translated in the $(x|y)$ oriented system.

A.3 Basic Principle of Estimation of Alignment Precision

A.3.1 Unbiased Track Prediction

In the track reconstruction and in the track-based alignment, the track prediction $\mathbf{x}_{\text{trk}}$ is made from all hits of the track, containing the hit under study itself. It is clear that it is used in the track reconstruction, since the influence of each hit needs to be regarded in the final fit. Also in the alignment it is necessary to include the hit under study, since its influence is the basis for the minimisation procedure. In order to study the misalignment though, the track prediction should not contain the hit on the module under study itself, since it would bias the track prediction in its direction. If a module is displaced with respect to the others, the displacement only crystallises fully in the residual, if the hit on the module is excluded from the track fit. This can be done in the refit. As explained in Chapter 3.3.3, the trajectory consists of three parts. There is the full smoothed trajectory, but there are also the two predictions from each side, the forward prediction $\mathbf{x}_{\text{forward}}$ and the backward prediction $\mathbf{x}_{\text{backward}}$. The forward prediction is built from all hits on the one side of the module, those who are closer to the interaction point. The backward prediction is built from all hits on the other side of the module. The track prediction $\mathbf{x}_{\text{trk}}$ which is used in this chapter, is the weighted combination of these two predictions,

$$\mathbf{x}_{\text{trk}} = \mathbf{x}_{\text{trk}}(\mathbf{x}_{\text{forward}}, \mathbf{x}_{\text{backward}})\,. \tag{A.14}$$

In this way, the hit under study is excluded from the track prediction. The parameters of the hit and those of the track are fully uncorrelated. It is clear, that for the two hits at the very ends of the track only the track prediction from one side can be used. For those hits the precision of the track prediction is worse, since the prediction is an extrapolation, contrary to the both-sided interpolation for the other hits.

Uncorrelated hit measurement and track prediction lead to the fact, that the positions $\mathbf{x}_{\text{hit}}$ and $\mathbf{x}_{\text{trk}}$ as used for the calculation of the residuals, but also their uncertainties given by the covariance matrices $\mathbf{V}_{\text{eff}}$ and $\mathbf{V}_{\text{trk}}$, become uncorrelated. The full uncertainty of the residuals $\mathbf{V}$ can then be written as

$$\mathbf{V} = \mathbf{V}_{\text{eff}} + \mathbf{V}_{\text{trk}} = \mathbf{V}_{\text{hit}} + \mathbf{V}_{\text{align}} + \mathbf{V}_{\text{trk}}\,. \tag{A.15}$$

A.4 Cluster Parameter Estimators

A cluster parameter estimator (CPE) transforms the charge clusters on neighbouring channels of the silicon sensors into a hit measurement (position and corresponding uncertainty) in the Cartesian $(u|v)$-system. It is subdivided into a CPE for the pixel modules and a CPE for the strip modules, which can be chosen separately. As explained in Chapter 3.3.2, systematic shifts of the charge carriers with respect to the real particle position are taken into account, like the Lorentz angle or the backplane corrections. The pixel CPE and the strip CPE can be changed for the used refit of the tracks, independent of the ones which are used during reconstruction. In the following they are explained shortly and the choice for the described method is motivated.

A.4.1 Pixel CPE

The default pixel CPE in the reconstruction is based on templates, which are developed using test beam measurements. The incident angle on the module's surface is used to control the compatibility of the template with the track prediction—depending on the goodness, a value of the so-called cluster probability is assigned. The templates which were used in the reconstruction gave too big errors in data in general; the width of the normalised residual distributions is clearly lower than 1 in most cases. In simulation however, the normalised residual distributions seem to be well described, their widths are mainly close to 1.

This default CPE is also used in the refit in this chapter. But the overestimated errors in data are problematic, since the residual distributions are too narrow and consequently the χ^2-values of the track fits are too small. For this reason, newly developed templates are used. The new templates show a better behaviour in data, the normalised residual distributions get broader with widths close to 1, thus also the mean of the χ^2-values gets closer to 1. But these templates also change the results in simulation, for these the normalised residual distributions are too wide, the width is mainly bigger than 1. Since the alignment precision estimate is based on a comparison between data and simulation, where the difference does not vary much between the different templates, the estimated values of the alignment precision do change only marginally. The motivation to use these new templates is, that the description of the data gets better, thus the weights of the individual hits stemming from pixel measurements and strip measurements are in better agreement.

A.4.2 Strip CPE

The default strip CPE as used in the reconstruction is explained in the following. The hit position u is estimated as the barycentre of the charges on the strips belonging to the cluster. The assigned uncertainty σ_u depends on the

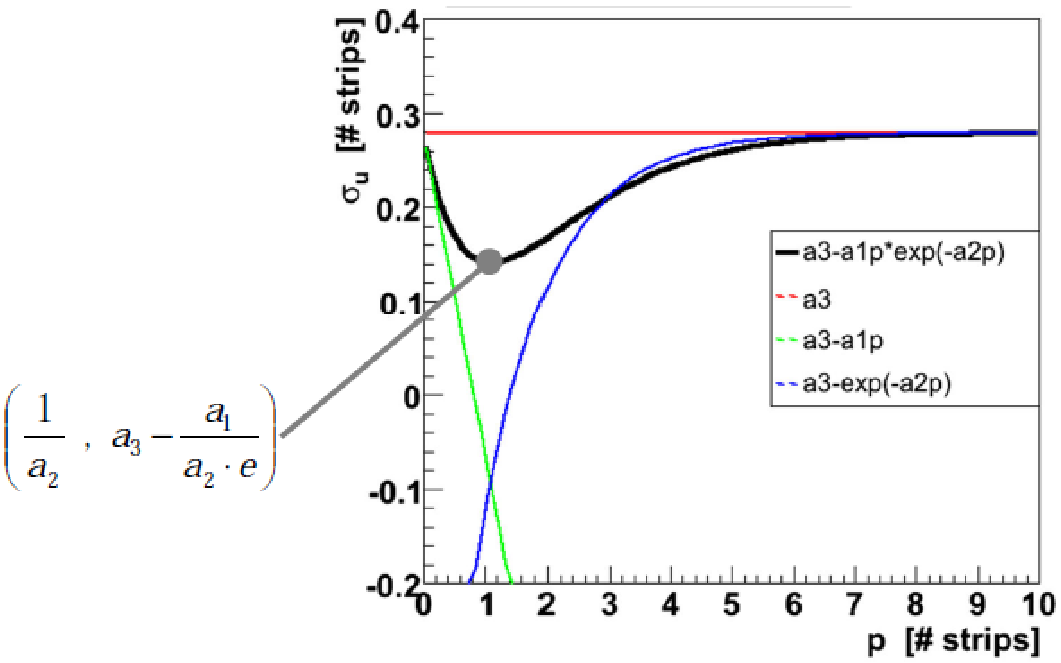

Figure A.2: Default strip CPE.

corrected track length projected on the module p and the cluster width w_{cl}, and is given by the formula

$$\sigma_u(p, w_{\text{cl}}) = \begin{cases} w_{\text{cl}}/\sqrt{12} & \text{for} \quad w_{\text{cl}} - p > 3.5 \\ \sigma_u(p) & \text{for} \quad w_{\text{cl}} - p \leq 3.5 \end{cases} \tag{A.16}$$

with all units given as number of strips. The projected track length p depends on the incident angle on the module, corrected for the charge carrier drift in the silicon sensors and the possible partial signal readout in deconvolution mode. From geometrical aspects, the projection length p is compatible with the cluster width w_{cl} for $0 \leq w_{\text{cl}} - p_{\text{cl}} < 2$. However, due to crosstalk, the next neighbouring strips show often increased signals. Thus, the track projection is assigned as matched for $w_{\text{cl}} - p_{\text{cl}} \leq 3.5$. If it is incompatible with the cluster width, huge errors are assigned. In case of compatibility, the uncertainty is calculated depending only on p—the cluster size and shape is ignored:

$$\sigma_u(p) = -a_1 p \cdot e^{-a_2 p} + a_3 \,. \tag{A.17}$$

The tunable coefficients are set to $a_1 = 0.339$, $a_2 = 0.90$ and $a_3 = 0.279$. The function and the individual components are illustrated in Figure A.2. The position and the error estimate are uncorrelated.

Since the cluster size and shape are neglected in the uncertainty estimate, all cluster sizes and shapes are described as good or bad as others. Applying a cluster selection would be mainly meaningless; a good agreement between cluster parameters and hit measurements cannot be guaranteed. Thus, an improvement of the behaviour of normalised residuals with application of a cluster selection is only partly achievable. The uncorrelated position and error estimate forbids the selection of hits with well described normalised residuals. But the method for the alignment precision estimation depends on correct hit positions and especially hit uncertainties. Furthermore, such a function can only describe the hit errors correctly on average; but studies showed that even this is not the case, the normalised residual width shows a strong dependence on the incident angle (e.g. see [134]). For this reason, another strip CPE is chosen, which is also implemented in the official CMS software. It is explained in the following.

The alternative strip CPE is based on geometric aspects, details can be found in [179]. The basic idea is, that only the two strips on both edges of the cluster contain the information of the position, since their active silicon areas are partly illuminated, while those in between are crossed completely. Thus, the position estimate is an average of the two edge strips. However, this hypothesis can only be valid, if projected track length and cluster width are compatible. In case of compatibility, the corresponding uncertainty is calculated with error propagation, using the uncertainties of the projected track length and the influences on the signal shapes on the strips within the module. The cluster is corrected for crosstalk. Clusters of width $w_{\mathrm{cl}} = 1$ need a special treatment, the position is assigned to the strip's centre, the uncertainty depends on the projected track length p, given by $(1-p)/\sqrt{12}$. In case of incompatibility of cluster width and projected track length, there are two different cases to distinguish. If the cluster is too small, the procedure of the default strip CPE is used. If the cluster is too wide, this can be due to merged clusters, which can be reflected by an evidence of multiple peaks—the position is given by the geometrical centre of the cluster, the uncertainty is given as $w_{\mathrm{cl}}/\sqrt{12}$. But if the cluster is too wide and there is no evidence for multiple peaks, it is assumed that it arises from noise and crosstalk. Two thresholds of the signal strength on the edge strips are defined, one defines where it is clearly noise, a higher one defines where it is clearly an induced signal. If the lower charge of the two edge strips lies in between, it is removed from the cluster, and the procedure is repeated iteratively until compatibility is reached.

A.5 Systematic Influences

It is observed that the quality of the normalised residual distributions varies with detector regions and intervals of the residual resolution. There are different types of systematic effects, which influence the normalised residuals and lead to deviations from Gaussian distributions in the $(u|v)$ coordinate system. The alignment precision estimation method requires a correct estimate of the residuals and especially of their errors. So both parametrisations have to be under control, the hit measurement and the track prediction. Especially influences on their uncertainty estimates are possible sources of error. The measured alignment precision does not reflect the misalignment in these two coordinates only, but all influences on the normalised residual distributions in this 2-dimensional projection.

A.5.1 Misalignment

The misalignment itself gets quantified by the method. However, only the uncertainties in the local Cartesian u- and v-coordinates are taken independently into account in the track reconstruction. The other possible uncertainties are not parameterised. They correspond to remaining misalignment in the estimated alignment parameters, which are u-v-correlations and the translations involving the w-direction, the rotations α, β and γ around these axes, and deformations of the module leading to deviations from a flat module, parameterised in alignment by the kinks and bows. The influence of these misalignments on the normalised residuals is absorbed in an enlarged estimate of the alignment precision. However, the strip modules in TIB and TOB have no sensitivity in v-direction—the corresponding alignment parameter and its precision is not relevant.

Misalignments biasing the assumed position of the hit measurement in w-direction – corresponding to misalignment in w, but also in the angles α and β and in the surface deformations – lead to slight dependencies of the result on the track topology, thus on the dataset. For example the amount of positively versus negatively charged tracks is relevant, but also the other track parameters since they define the incident angles on the modules. Since the modules in FPIX (TIB) are tilted around the u-axis (v-axis) for the optimisation of the tracking performance, and thus their v-axes (u-axes) do not point exactly along the global ϕ-direction, in principle also the estimate of the alignment precision in this direction is slightly sensitive to the dataset.

A.5.2 Miscalibration

There are systematic effects from miscalibration, resulting in systematic shifts of the residuals. These are incorrect estimates of the Lorentz angle or of the backplane corrections, but also shifts of the beamspot parameters. As already described in Chapter 4.2.1, they are absorbed in the alignment parameters.

However, if they are not absorbed in the alignment, they show up in an increase of the calculated alignment precision. This happens also in case of time-dependent changes, whose mean influence is absorbed in the alignment. All data which is reconstructed without individual alignment, in particular during data taking, can suffer from misalignment and miscalibration.

A.5.3 Coordinate System

The $(x|y)$ oriented coordinate system which is used for the normalised residual description in the alignment precision estimation coincides in TIB, TOB and the pixel detector with the $(u|v)$ Cartesian system as used for the alignment precision parameterisation in the track reconstruction; both measurement directions are uncorrelated. In TID and TEC however this is not the case. The radial x component is similar but not identical to the u component. But the estimated value in x direction is assigned to the alignment record as the value for the u direction. This is unproblematic, since the iterative process finds the optimal value for the u direction, by possibly requiring more iterations. The assignment of spherical uncertainties in strip modules is not ideal in TID and TEC, since the $(u|v)$ coordinates in the reconstruction are slightly correlated for the radial measurements. The spherical assignment does not reflect the truth, but the difference is expected to be small.

A.5.4 Detector Effects

Detector effects arise from the material of sensitive detector components and their support structures traversed by a particle. The interactions with the material lead to changes of the trajectory. Even if they are incorporated correctly in the track model, they are reflected by non-Gaussian behaviour of the normalised residuals. The main effects which need to be regarded are the multiple scattering changing step-wise the direction while crossing material, and the energy loss. The description of the material budget in the software is important. A simplification is that everything is separated in thin layers using the corresponding approximations for thin scatterers. In addition, the space between modules is treated as empty, and the corresponding material budget is assigned to the modules. Also deviations between the real tracker material budget and the assumed one, which is also used in simulation, would lead to wrong errors. Studies about the tracker material are presented in [180].

Another effect is given by the strong magnetic field used for bending the tracks in order to measure their curvature. The field in the tracker volume is almost homogeneous at 3.8 T. Especially in the outer endcap regions however, there is a transverse component of the magnetic field, which needs to be taken into account given the good resolution of the tracker. In the track reconstruction a magnetic field map is used, describing the local field strength. Discrepancies between the model and the real magnetic field can lead to deviations in the track parameterisation.

Further detector effects stem from the digital readout and the electronics. The cluster digitisation, which depends on calibration constants, leads to non-Gaussian staircase distributions, especially degenerated for signals coming from one channel. The hit parametrisation is influenced by problematic channels. If a strip is dead or noisy, it is not clear whether it belongs to the cluster or not. Furthermore crosstalk due to capacitive couplings between neighbouring strips washes out the cluster width and the shape of the induced charge distribution. The APVs as used for the readout of 128 channels each, show a significant increase of the noise when going to their edges. This of course can also influence the cluster shapes and sizes and the appearance of fake or missed hits.

A.5.5 Biases from Track Reconstruction

The track prediction is of course biased if a measurement is used which does not belong the real track. Either is comes from another track or is a fake measurement. This is a non-Gaussian but small effect in the residual distributions. However it would increase if the alignment precision is overestimated.

Due to the hit and track models in use, there can occur wrong position and uncertainty estimates. Wrong positions would mainly lead to non-Gaussian behaviour. But wrong uncertainties are very dangerous, since they can broaden and narrow the residual distribution. The uncertainties of the track depend on the track model and on the effects described so far. The uncertainty of the hit itself is estimated together with the track parameters by a cluster parameter estimator (CPE).

In very few cases, the squared errors of a track are negative. This can happen, if the matrix inversion for the track prediction fails. Negative squared errors can also occur for the hit errors in TID and TEC. The representation in unbiased $(x|y)$ coordinates requires a back-transformation from the Cartesian in the angular measurement frame. Due to computational precision, the values get falsified. This is true especially for small error values of hits close to the edges of the modules, where the Cartesian correlations get big. Those residuals containing negative squared error contributions are simply rejected. Incorrect but positive values though cannot be excluded. They are expected to be of similar size and thus insignificant. In principle explicit requirements can be set up to select hits with wrong errors only above a certain precision, as can be estimated from the transformation equations.

A.5.6 Implementation of Local Method

The estimation of the alignment precision is separated in intervals of the residual resolution, to analyse the normalised residual distributions for about constant values of the residual resolution. But in fact Gaussian behaviour is only given for constant values of the residual resolution. This is approximately valid for intervals, which are small compared to the mean value. Thus, especially intervals at low values of the residual resolution, like the interval 5–10 μm, do not fulfil this criterion. But smaller intervals are not possible due to the resulting lack of statistics in this region.

Another aspect of the chosen binning of the residual resolution is, that it is identical for all detector regions, although there are very different hit and track resolutions, depending on the topology of a module and its global position. This could be optimised for different regions individually, but it does not seem to be necessary, since the binning is chosen such, that for all regions more than one interval have significant statistical power. Depending on the detector region, these can be intervals at very low values or at high values or sometimes even spanning the whole analysed region containing enough hits in each interval.

The local method is based on iterations. As explained, the alignment precision values which are used in the track refit cannot be separated from the track errors. The intrinsic hit resolution itself stays independent of the alignment precision. The residual resolution gets a dependence on the alignment precision used for the neighbouring layers of the hit under study. During the iterations the residuals can migrate between the intervals of the residual resolution and are then analysed in different distributions of different intervals. Again, mainly low values of the residual resolution are influenced. This effect should not be a problem, since the track parameters and their errors get more correct, and thus also the track prediction as used for the residual calculation. However, since the estimation of the nominal residual width Δ_0 is based on simulation without misalignment, the modelling of the data could become worse, and thus the results also. But this effect is expected to be small.

The assumption of a Gaussian fit model is also not completely valid because of the mentioned non-Gaussian effects. The goodness of the fit varies with different intervals of the residual resolution and throughout the detector regions. The effect is also expected to be small, since the broadening of the normalised residual distribution also leads to a broadening of the fitted Gaussian in general, although the shape is not correctly described.

Finally the convergence of the iterative method can have an impact. It is steered by only one smoothing parameter (see Equation 4.16) which is the same for all detector regions; and it is tuned for good and fast convergence for all detector regions in common, although some specific regions might need other tunes.

A.5.7 Incorrect Modelling of Data

Due to discrepancies amongst normalised residual distributions in different detector regions and for different hit and track topologies arising from the biases in the track reconstruction, the behaviour cannot be described assuming a constant nominal residual width Δ_0 throughout the different intervals of the residual resolution and all detector regions. The described solution is the determination of an effective Δ_0 for each regarded detector region, which is determined from simulation based on design geometry. The basic idea is to have the same non-ideal descriptions in data and simulation, and to use the same problematic input from hits and tracks with the same statistical power in both cases. This requires an accurate modelling of the data, which means similar hit and track topologies—the track and hit selection needs to be optimised. In addition, possible systematic deviations between real and simulated hits could bias the results.

A.6 Modelling of Data and Event Selection

The modelling of data with simulated events is necessary to estimate the nominal residual width Δ_0 for perfect alignment from simulation using the design geometry. The selection of useful events is partly connected to the data modelling since corresponding samples need to be available, spanning sufficient events for comparisons on a similar statistical level. The modelling aims for similar hit and track topologies.

The decision is made to rely on tracks from isolated muons, which have to fulfil the identification and selection criteria as described in Chapter 3.5.3, for several reasons. The defined muons are well identified with high efficiency and low fake rate. Muon triggers are efficient and well simulated, and single isolated muon triggers could still be kept unprescaled in 2011 for medium p_T-thresholds. The lowest unprescaled trigger for the 2011 data has $p_\mathrm{T} > 17\,\mathrm{GeV}$ and is used in this analysis (see Chapter 3.2.2). The main component of the triggered muons originates from electroweak processes of $\mathrm{W}^{\pm}$ and Z^{0} decays, and have high p_T-values of the order of half the gauge boson mass. Since these default electroweak Standard Model processes are of importance for physics analyses, enough simulated samples and a sufficient trigger rate in data is guaranteed. The muons mainly originate from the well understood and well modelled hard interactions incorporating electroweak processes, and not from the underlying event, which relies on tuning of Monte-Carlo generators. In addition, all tracks belong to muons which all have the same and well known mass. The mass is important to treat the detector effects correctly in the track parameterisation. The assumed mass in the used refit is by default the muon mass, but in principle it is configurable. The detector effects itself play an even more important role in the choice of muons. Due to the minimal-ionising particle signature of muons the multiple scattering and the energy loss is minimal, and also other effects like bremsstrahlung or strong interactions are suppressed. In this way, systematic detector effects are minimised, which gives better track predictions and improved comparability with simulation, since the modelling of the material budget is less important.

Summarising, tracks from isolated muons are chosen since they allow a fair comparison between data and simulation. They enable analyses with minimal detector effects, to keep additional interactions than ionisation of the sensitive material as low as possible. Last but not least, muons are measured very precise, thus having high sensitivity and are very useful for the method.

The data in use stems from the prompt reconstruction of the 2011 data. The run range spans the run numbers 165071–172619, which are taken between mid of May and mid of July. As can be seen from Table A.1 the data corresponds to different IOVs, namely E–P2.

The modelling is based on retrieving similar distributions in the track parameters p_T, η, ϕ, d_0 and d_z, and consequently also similar distributions in the most important hit parameter, the incident angles on the modules. This leads to residuals containing similar fractions of track and hit errors coming from identical topologies, and having similar values. The full detailed decomposition of the data itself is not important as long as these parameters are described well. It is sufficient to assemble simulated samples with isolated muons and notable cross sections. Four samples are used. One describes the enormous multijet event rate (QCD) and is enriched with muons of $p_{\mathrm{T}} > 15\,\mathrm{GeV}$ to compose the contribution to the isolated muon selection with samples of reasonable size. Another one describes leptonic decays of the $\mathrm{W}^{\pm}$ in all flavours ($\mathrm{W} \rightarrow \mathrm{l}\nu$). Direct muonic $\mathrm{W}^{\pm}$ decays or indirect ones via taus are the main contribution to the selected dataset. The third important component are Drell–Yan processes with decays $\mathrm{Z}^0/\gamma^* \rightarrow \mu^+\mu^-$. Due to divergencies, the cross section is only defined for gauge bosons above a certain threshold on the invariant mass. Two different samples are used, one ($\mathrm{Z}^0 \rightarrow \mu\mu$ 20) has a threshold $M_{\mathrm{Z}^0} \geq 20\,\mathrm{GeV}$, and the second ($\mathrm{Z}^0 \rightarrow \mu\mu$ 10) complements the region below this value and above $M_{\mathrm{Z}^0} \geq 10\,\mathrm{GeV}$. The QCD sample is simulated with PYTHIA6; $\mathrm{W} \rightarrow \mathrm{l}\nu$ with MadGraph and interfaced with the PYTHIA parton shower and the decay of the τ is done with TAUOLA; $\mathrm{Z}^0 \rightarrow \mu\mu$ 20 and $\mathrm{Z}^0 \rightarrow \mu\mu$ 10 are both simulated with POWHEG and interfaced with the PYTHIA parton shower. The corresponding cross sections are taken from [181].

The full event selection is as follows. Data events have to be certified as of good quality (see Chapter 3.2.3). In data, the presence of at least one good primary vertex as defined in Chapter 3.5.1 is required to ensure a real collision. The vertex selection is also applied on simulated samples. Both data and simulation events have to be triggered by the single muon trigger with threshold $p_{\mathrm{T}} > 17\,\mathrm{GeV}$. Only tracks coming from good identified and isolated muons are used. Additional preselections on the tracks are already applied, since the data and the simulated samples are produced in a specific alignment data stream. However these selections are all less restrictive as the ones which will be introduced in the following section. The only exception is the isolation, where a second different requirement is in use.

For fast turnaround, analysing the events in the samples needs to be parallelised. In addition, preselected samples reduced to the necessary event content for the given analysis are stored, called skimmed events. This preselection is stricter than the preselection of the original data stream, but not as strict as the final preselection. They have to fulfil the event selection criteria above, and at least one track in the event needs to fulfil the preselection. These skimmed events are stored in several files of similar size, allowing parallel processing of them. Table A.2 gives an overview over the sizes of data and simulated samples.

Table A.2: Content of data and simulated samples. Given are the used theory cross sections σ, the number of all events of the simulated sample, the number of events after skimming, the number of files containing the skimmed events, and the corresponding integrated luminosity $\mathcal{L}$.

Sample	σ [pb]	All events	Skimmed events	Files	$\mathcal{L}$ [pb^{-1}]
QCD	84679	25064715	588022	1	296
$W \rightarrow l\nu$	31314	81352581	14280339	15	2598
$Z^0 \rightarrow \mu\mu$ 10	3457	9780633	114536	1	2829
$Z^0 \rightarrow \mu\mu$ 20	1666	29743564	14231674	21	17853
Data			9391335	10	≈ 924

A.7 Track and Hit Selection

The dependence of the nominal residual width Δ_0 over different intervals of the residual resolution and over detector regions shows, that the result of the method depends on the track and hit selection. It is necessary to exclude or to correct for big systematic biases. The behaviour of the normalised residual distributions is studied for different track and hit parameters to see where discrepancies occur. A track and hit selection is applied in order to remove sources of systematic effects, without rejecting too many events.

Changes of the alignment precision during iterations change the track parameters, especially their errors. Thus the selection of tracks and hits to study can fluctuate slightly. This is also valid for the outlier rejection in the refit. And also when applying different detector geometries to compare their behaviour the track parameters change slightly leading to small deviations in the selection of tracks.

The figures which are shown in this section contain the following information. The tracks are based on the refit. In data, the conditions as used for the prompt reconstruction are used, except of the alignment precision, which is set to 0. In simulation, the ideal conditions are used; the alignment precision is set to 0, but this is anyway the setup of ideal conditions. The tracks which are used for the figures need to fulfil the track selection criteria as explained in the following, furthermore they need to contain at least one hit which fulfils the following hit selection criteria, and thus are used in the alignment precision estimate. Only these hits are used in the figures which contain distributions of hit parameters.

A.7.1 Track Selection

The track selection as follows is applied, and is outlined together with the event selection in Table A.3. As already stated, the tracks need to originate from a good identified and isolated muon. However, not the global muon fit is used, but only the fit of the tracker track, since the behaviour of the tracker should be studied. The tracks are required to be flagged as of high purity by the track reconstruction algorithm in order to minimise incorrect cluster assignments. A selection on the minimal number of hits in the pixel and in the strip detector separately is applied. This is to ensure well measured track parameters, the momentum measurement mainly depends on the strip detector, the impact parameter mainly on the pixel detector. The lower thresholds are optimised to 2 hits (11 hits) in the pixel (strip) detector, based on the behaviour of the normalised residuals. In addition, upper thresholds of 7 hits (35 hits) in the pixel (strip) detector are applied, since tracks coming from a collision should not exceed a certain number of hits, depending on the detector region. Few tracks are excluded, which might occur from cosmic tracks. The hit distributions are visualised in Figure A.3. Data shows in general smaller numbers, but the differences are small.

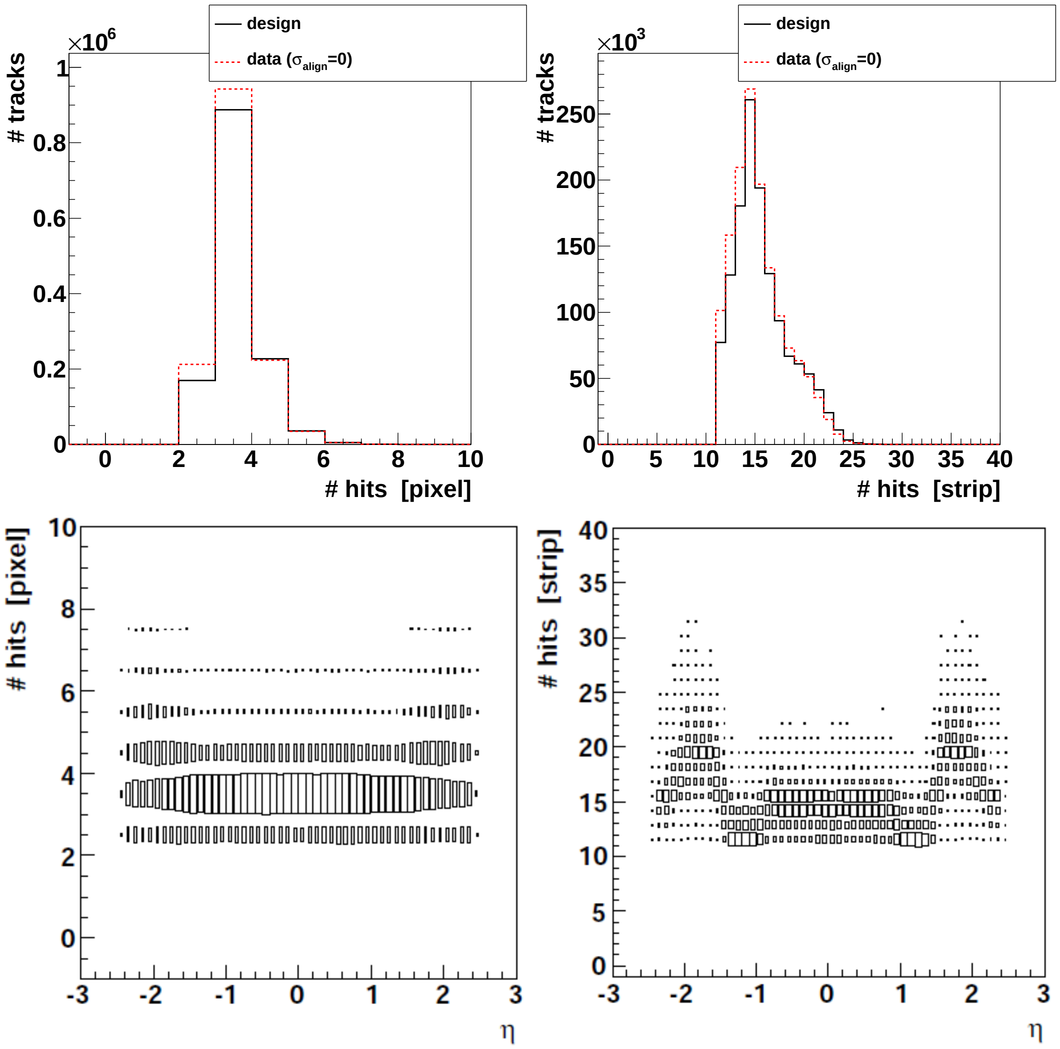

Figure A.3: Number of hits per track in pixel and strip detector. The bottom plots, showing the numbers versus the pseudorapidity of the tracks, are taken from simulation, but are almost identical for data.

Table A.3: Event and track selection. The selection is applied to all events and is the basis for the final modelling of the data.

Event selection	Track selection
Specific alignment data stream Data certified as ‘good quality’ Single isolated muon trigger ($p_T > 17\,\text{GeV}$) ≥ 1 good primary vertex	Good identified and isolated muons Flagged as ‘high purity’ # hits (pixel) $\in [2, 7]$ # hits (strip) $\in [11, 35]$ $p_T \in [25\,\text{GeV}, 150\,\text{GeV}]$ $\lvert\eta\rvert < 2.5$ $\lvert d_0\rvert < 200\,\mu\text{m}$ $\lvert d_z\rvert < 15\,\text{cm}$ $\chi^2/f \leq 5$

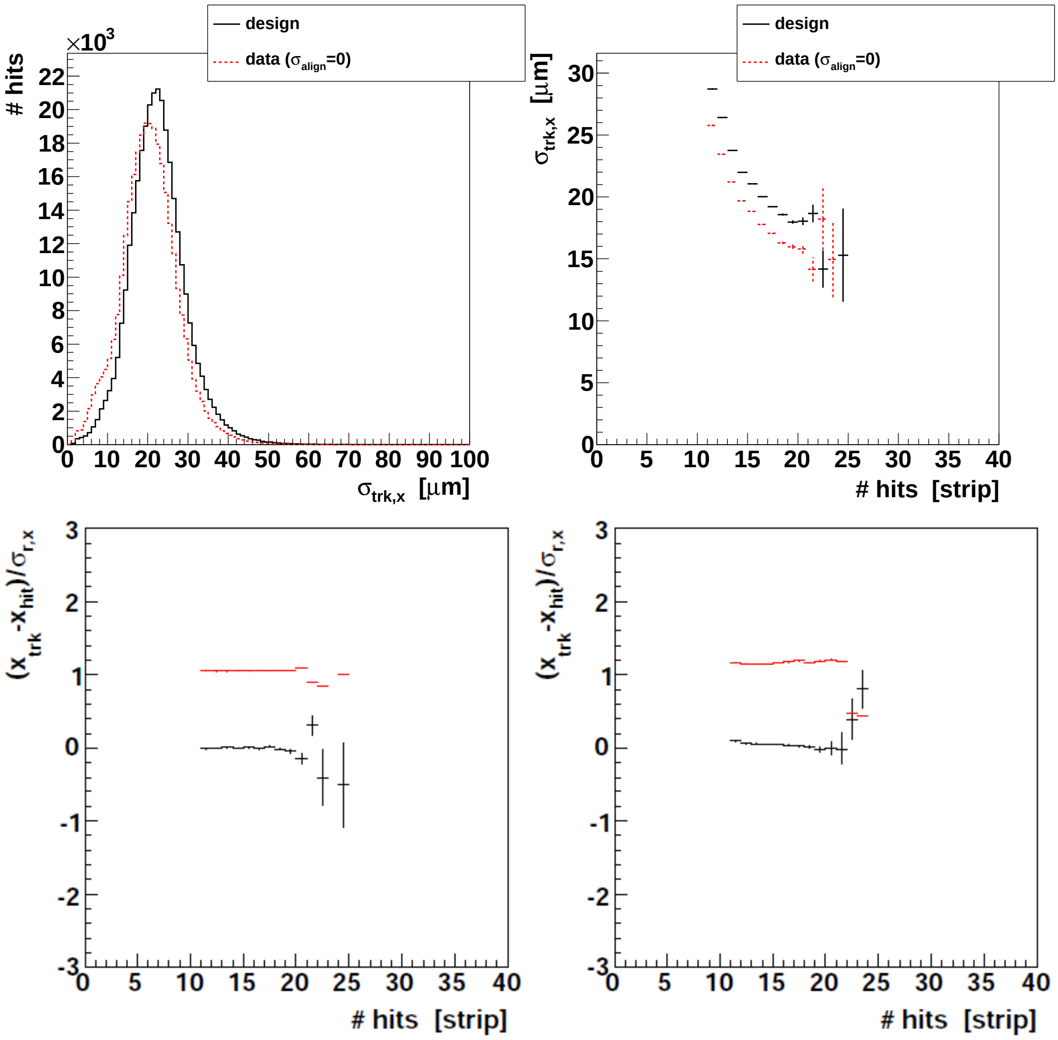

Figure A.4: Track error distribution (top right – comparison data/simulation), and dependency of track error (top right – comparison data/simulation) and normalised residuals in simulation (bottom left) and in data (bottom right) on number of hits in strip detector in sector "TOB L1So".

The normalised residual plots show the following: The black diagram around 0 shows the central value with its statistical uncertainty in each interval, the red diagram around 1 shows the corresponding r.m.s. value.

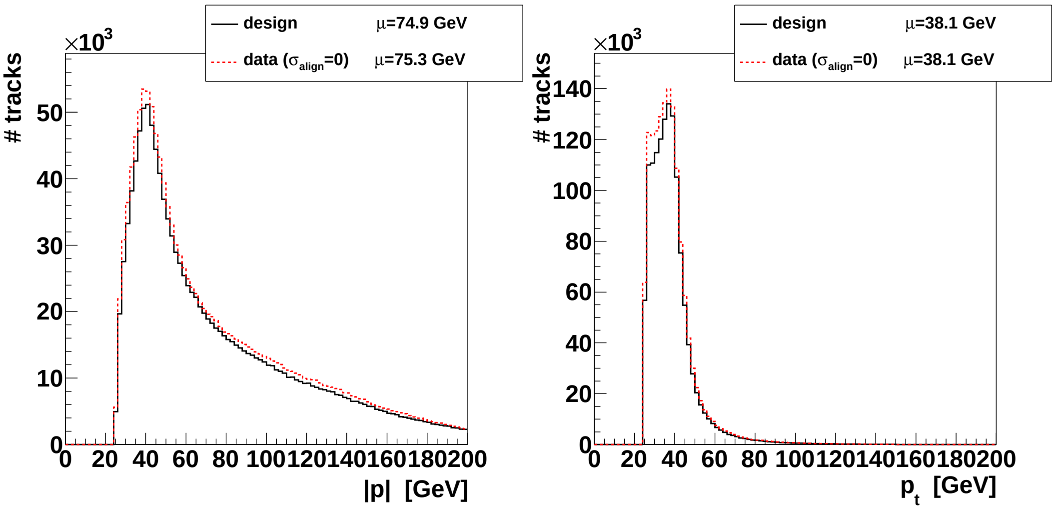

Figure A.5: Absolute and transverse momentum distribution.

The basis of the optimisation of the selection criteria are distributions as shown in Figure A.4 for the number of hits in the strip detector for one exemplary sector. The uncertainty of the track prediction on the module's surface shows often deviations between data and simulation, but the general behaviour is similar. For each track parameter, and analogical the hit parameters in the next section, the dependency of the normalised residual distribution is monitored for the different sectors. In simulation, the mean value should be close to 0 for the selected parameter space, i.e. the central values should not be biased systematically, and the width of the distribution should be close to 1. The latter shall guarantee, that the hit and track error description is well under control. Such a behaviour can be achieved for all track parameters in almost all sectors; some sectors show slight deviations, but the impact on the results is small. The analogue diagram for the data shows influences from misalignment, the mean values are less constant, and the width is also less constant and bigger than 1. The selection is global, the optimisation is done in order to achieve acceptable behaviour while guaranteeing enough statistical power for all sectors in common.

The transverse momentum is required to be $p_\mathrm{T} \in [25\,\mathrm{GeV}, 150\,\mathrm{GeV}]$, distributions can be seen in Figure A.5. The upper threshold is applied since the uncertainty of the tracks, which are fit without the information from the muon system, increases drastically due to the small curvature (see Figure 3.7). The lower threshold reflects a reduction of several systematic influences for data and simulation separated, but also for discrepancies between both. Effects of the trigger efficiency for the trigger threshold $p_\mathrm{T} > 17\,\mathrm{GeV}$ are minimised, since the values are well above the turn-on curve. The QCD sample is enriched with muons only above $p_\mathrm{T} > 15\,\mathrm{GeV}$. The Drell–Yan samples do not cover the invariant mass region of $M_{\mathrm{Z}^0/\gamma*} < 10\,\mathrm{GeV}$. Muons originating from their decays are in general with low momenta. Requiring tracks with high momentum further reduces the influence from detector material. These muons give the most sensitive track topologies for the measurement of the alignment precision.

In order to select collision tracks only, the pseudorapidity is restricted to $|\eta| < 2.5$, which is the geometrical range of the tracker. The impact parameter is required to be close to the beamspot with maximum transversal distance $|d_0| < 200\,\mu\mathrm{m}$ and longitudinal range of $|d_z| < 15\,\mathrm{cm}$. In this way, non-collision events like cosmics are rejected, and it is most likely that these muons really originate from the hard scattering process, thus mainly from the electroweak decays. The final selection criterion is based on the goodness of the track fit. The χ^2-value, normalised to the number of degrees of freedom in the fit f, has to fulfil $\chi^2/f \leq 5$. This ensures that bad track fits, e.g. due to misassigned hits, are not regarded. The track parameter distributions are given in Figure A.6.

Another example of the typical optimisation diagrams can be found in Figure A.7 for the longitudinal impact parameter d_z. This sector shows significant differences in the track error, and the error increases slightly for bigger values of d_z. But the residual behaviour shows that there is no dependency on this parameter visible, the error assignments seem to be correct. This example visualises a perfect case in simulation.

The used refit of the tracks is done assuming the muon mass for the particle. An outlier rejection is applied in order to deselect wrongly assigned hits and thus to guarantee well reconstructed tracks. A hit is not used in the refit, if its contribution to the χ^2-value of the track fit exceeds 25, which means that the normalised residual in this coordinate fulfils $r_{\mathrm{norm}} \leq \sqrt{25} = 5$. The parameters of pixel hits are estimated on templates, which are matched to the measured signal. Hits are rejected if the geometrical probability P_{xy} of this template matching is very low, and kept if they fulfil $\lg P_{xy} > -14$; only very few hits are rejected. Depending on this hit rejection, tracks can be shortened or completely rejected in the refit, compared to the reconstructed ones. This comes from the fact, that only a maximum number of subsequent layers without hits are allowed, and that a minimum number of hits per track is required in the refit.

The final composition of events from the simulated samples in use is based on the correct description of these track parameters. Since the QCD sample corresponds to an integrated luminosity of less than $300\,\mathrm{pb}^{-1}$, the analysed amount of data is selected to be $\mathcal{L} \approx 250\,\mathrm{pb}^{-1}$. The simulated samples are not weighted—instead only a fraction of the skimmed events is used to reach similar statistical power as in data. As a first step to find the right composition of events, the number or events for each sample is chosen such, that they correspond to the same luminosity as the data. For the electroweak processes with well defined cross sections the description is adequate, as can be seen from the shoulder in the p_{T}-spectrum around half the boson mass, and in the charge asymmetry, and in the number of selected tracks in the event (see Figure A.8). The charge asymmetry is due to the favoured positive charge of the $\mathrm{W}^{\pm}$ in proton-proton collisions, the events with two well selected tracks stem mainly from the Z^0 decays. The other components however seem to be

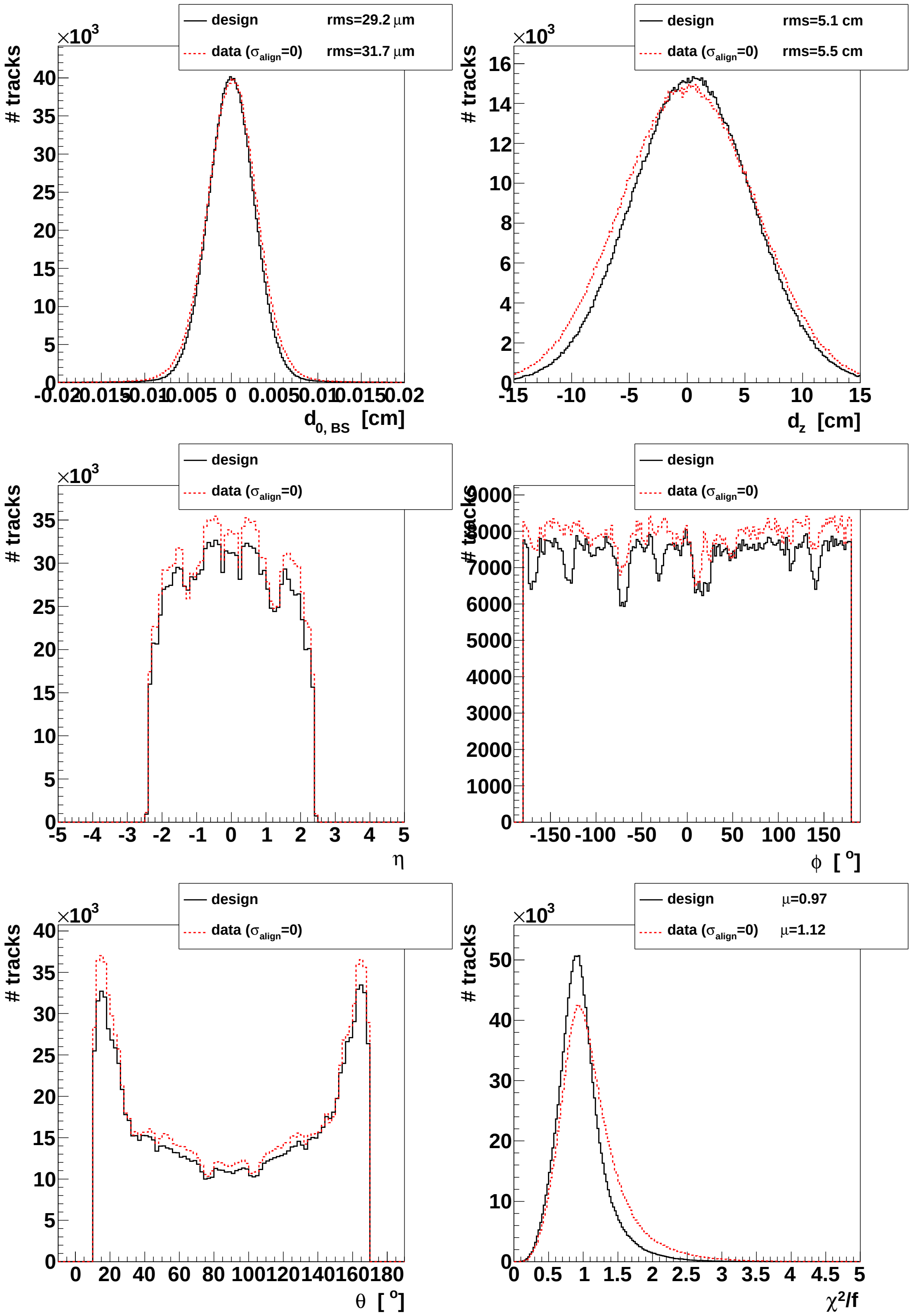

Figure A.6: Geometrical track parameters and χ^2-value.

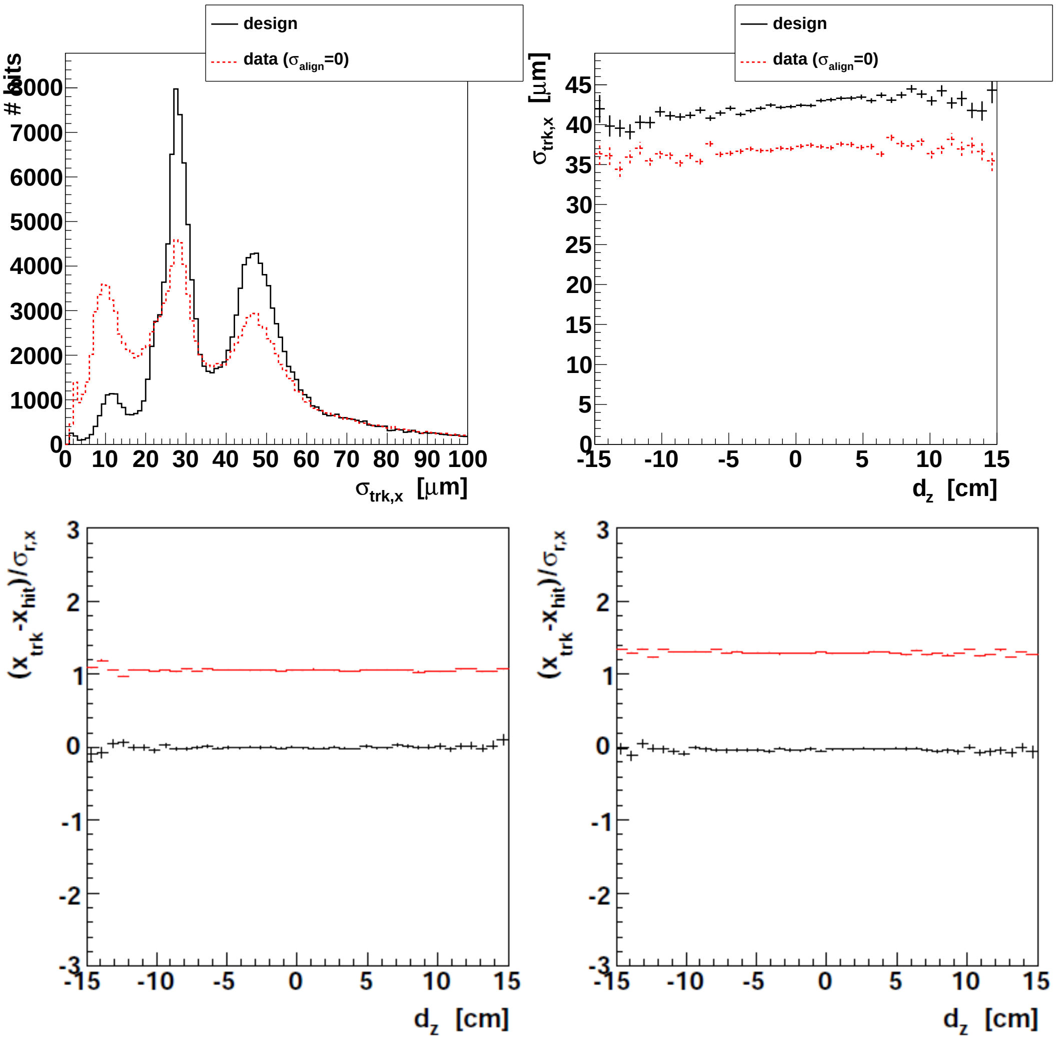

Figure A.7: Track error distribution (top right – comparison data/simulation), and dependency of track error (top right – comparison data/simulation) and normalised residuals in simulation (bottom left) and in data (bottom right) on longitudinal impact parameter in sector “TECp R7”.

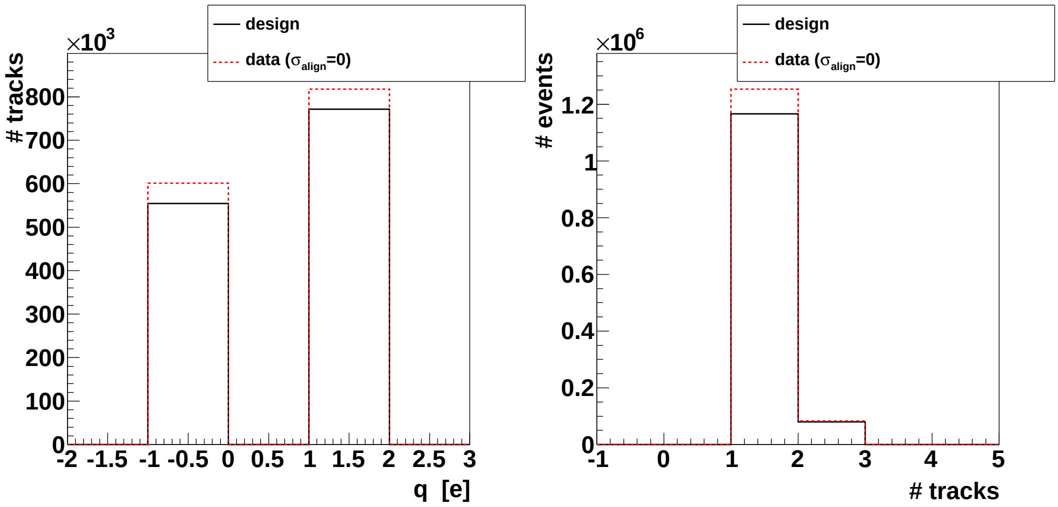

Figure A.8: Track charges and number of selected tracks per event.

Table A.4: Number of events in use. Given is the of skimmed number events which are used in the analysis, taken from the full amount as given in Table A.3. They are read in parallel from all skimmed files with identical amounts of events. The number of files is also shown. Furthermore the corresponding integrated luminosity $\mathcal{L}$ of the samples is listed.

Sample	Skimmed events in use	Files	$\mathcal{L}$ [pb^{-1}]
QCD	550000	1	277
W → lν	1374187	15	250
$Z^0 \to \mu\mu$ 10	10121	1	250
$Z^0 \to \mu\mu$ 20	199287	21	250
Data	2540946	10	250

underestimated, especially in the lower p_T-regions. As solution, the number of events from the QCD sample, which has anyway only a coarse theoretical cross-section estimate, is scaled up by about 10.7%. The final numbers of skimmed events which are used in the analysis are listed in Table A.4, together with the number of files from which they are analysed in parallel. Identical numbers of events are read from the beginning of each stored file of a sample. With this configuration, the wall-clock time used for one iteration is below half an hour. Since the data is read from these different input files, they do not stem from a single run period; they are mixed from different run periods, thus stemming from several IOVs.

The track parameters are not perfectly, but well described, which should be sufficient for the analysis goals. The impact parameters show slight deviations due to the difference of the beamspot in position and size between data and simulation. The χ^2-distribution shows in data a significant increase, which reflects the present misalignment. The track selection fulfils the most

Table A.5: Hit selection in pixel and strip detector. For the strip clusters which are required to have a width $w_{\mathrm{cl}} = 3$ strips, the cluster charge c_{cl} is split in the charge on the middle strip c_{M}, and on the left c_{L} and the right strip c_{R}.

Hit selection (pixel)	Hit selection (strip)
$w_{\mathrm{cl}} \geq 2\,$pixels Clusters not flagged 'unphysical' Clusters not flagged 'low charge' $c_{\mathrm{cl}} \geq 10000\,$e Deselect clusters on module edges $\lg(P_{xy}) > -5$	$w_{\mathrm{cl}} = 3\,$strips $c_{\mathrm{M}} > c_{\mathrm{L}}$, $c_{\mathrm{M}} > c_{\mathrm{R}}$ $c_{\mathrm{L}} + c_{\mathrm{R}} \leq c_{\mathrm{M}}$ $20 \leq s/N \leq 50$

important criterion—the dependence of the normalised residual distribution is mainly eliminated in all sectors.

A.7.2 Hit Selection

As can be seen, a good agreement between data and simulation is achieved on global track parameters. However local hit and cluster parameters do not show such a good agreement. But on average, the parameters are good enough described to deliver track parameters which are obviously in agreement with data. The hit selection is mainly driven by the idea first to use clusters with charge profiles allowing an accurate position measurement, and second to minimise systematic influences without reducing the statistical power too much. The selection is distinguished between pixel and strip detector as summarised in Table A.5 and described in the following.

The hit selection is optimised for all detector regions in common. Since the distributions of the hit parameters are different for different detector regions, a regional selection could help to further reduce the systematic biases.

Pixel Cluster Selection

Pixel clusters are required to be flagged from the reconstruction neither as unphysical, nor as built from low charge. In addition, clusters lying on the edge of the modules are removed—they do not need to be complete measurements, since the active material ends. An additional requirement on the cluster charge is applied, $c_{\mathrm{cl}} \geq 10000\,$e, to remove hits with bad described residuals. The same argument is valid for the restriction on the geometric probability P_{xy} from the template matching of the cluster to $\lg(P_{xy}) > -5$. The latter two selections remove only a very small fraction of the hits. The width of the cluster needs to be $w_{\mathrm{cl}} \geq 2\,$pixels for each measurement direction to allow sensitive estimates weighted from the charge induced on several pixels. Clusters of width $w_{\mathrm{cl}} = 1\,$pixel only have the digital single-channel resolution. The two

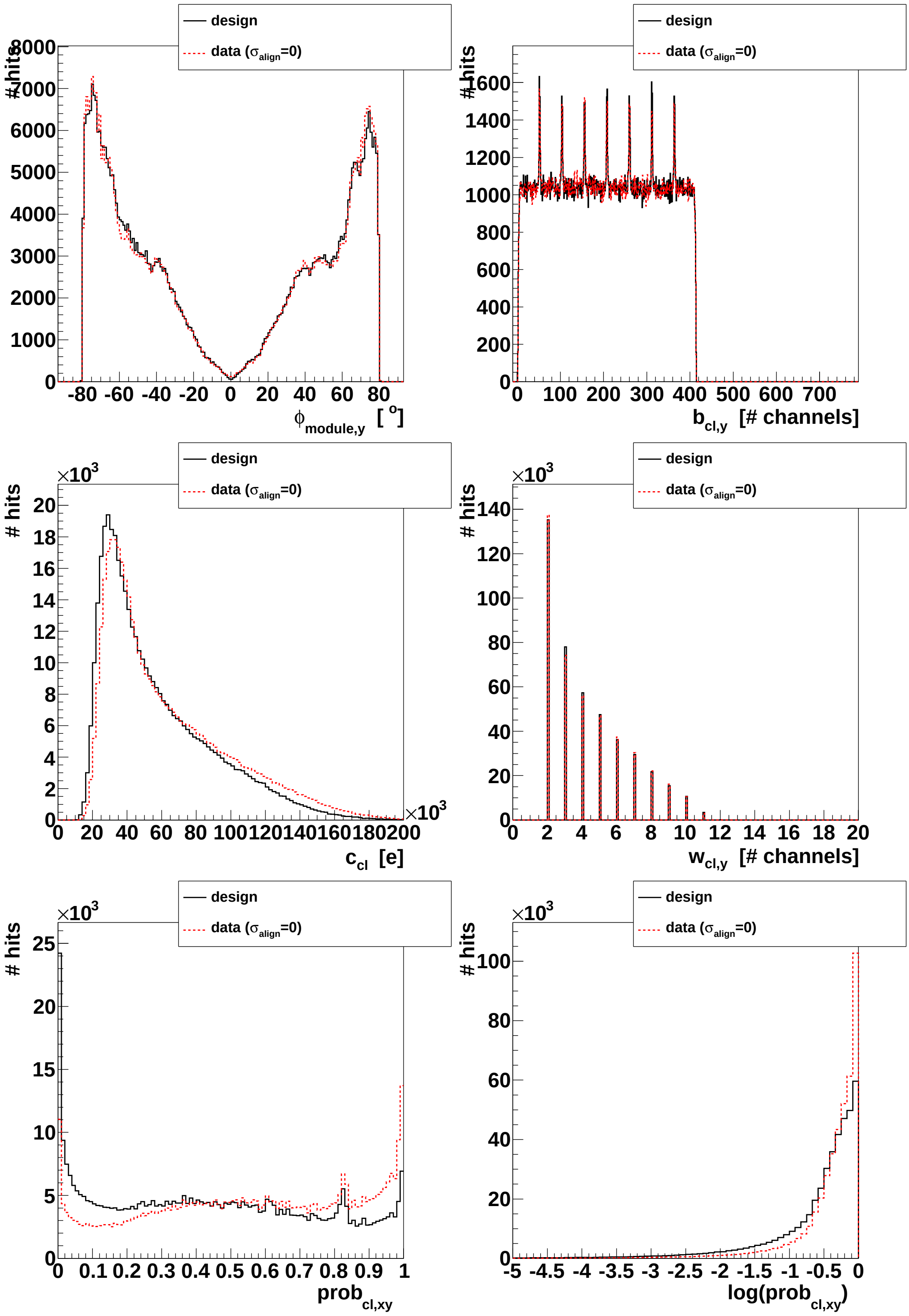

Figure A.9: Pixel cluster parameters for y-coordinate in sector “BPIX L1o”.

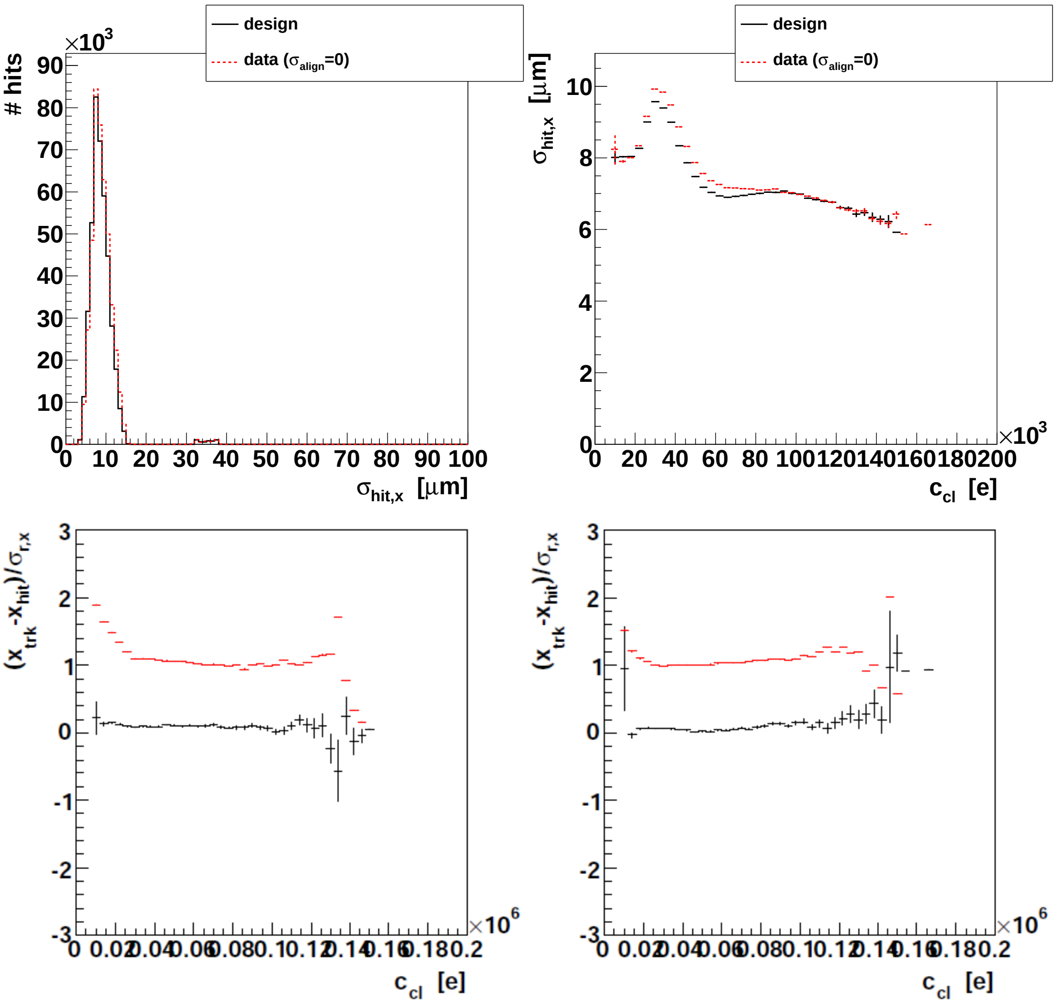

Figure A.10: Hit error distribution (top right – data vs. simulation), and dependency of hit error (top right – data vs. simulation) and normalised residuals in simulation (bottom left) and in data (bottom right) on pixel cluster charge in x-coordinate of sector “BPIX L3i”.

measurement coordinates are treated independent, i.e. that hits can be used for both directions, but also for only one of them, depending on the width in each direction. Important cluster parameters are shown in Figure A.9 for one sector. The pixel charge barycentre b_{cl} shows spikes, which reflect the borders between two ROCs—they might originate from noise, which is bigger at the edges of the ROCs, and should probably be excluded. The charge distribution shows deviations, and for some other sectors this is even more pronounced. The same holds for the cluster template probability $\mathrm{prob}_{\mathrm{cl},xy} = P_{xy}$.

Exemplary diagrams for the selection optimisation can be found for the x-direction in Figure A.10 and for the y-direction in Figure A.11. The hit error distributions are similar for data and simulation. The examples show problematic hit quantities with respect to the normalised residual behaviour. Even in simulation there is a dependence on the cluster charge in some sectors,

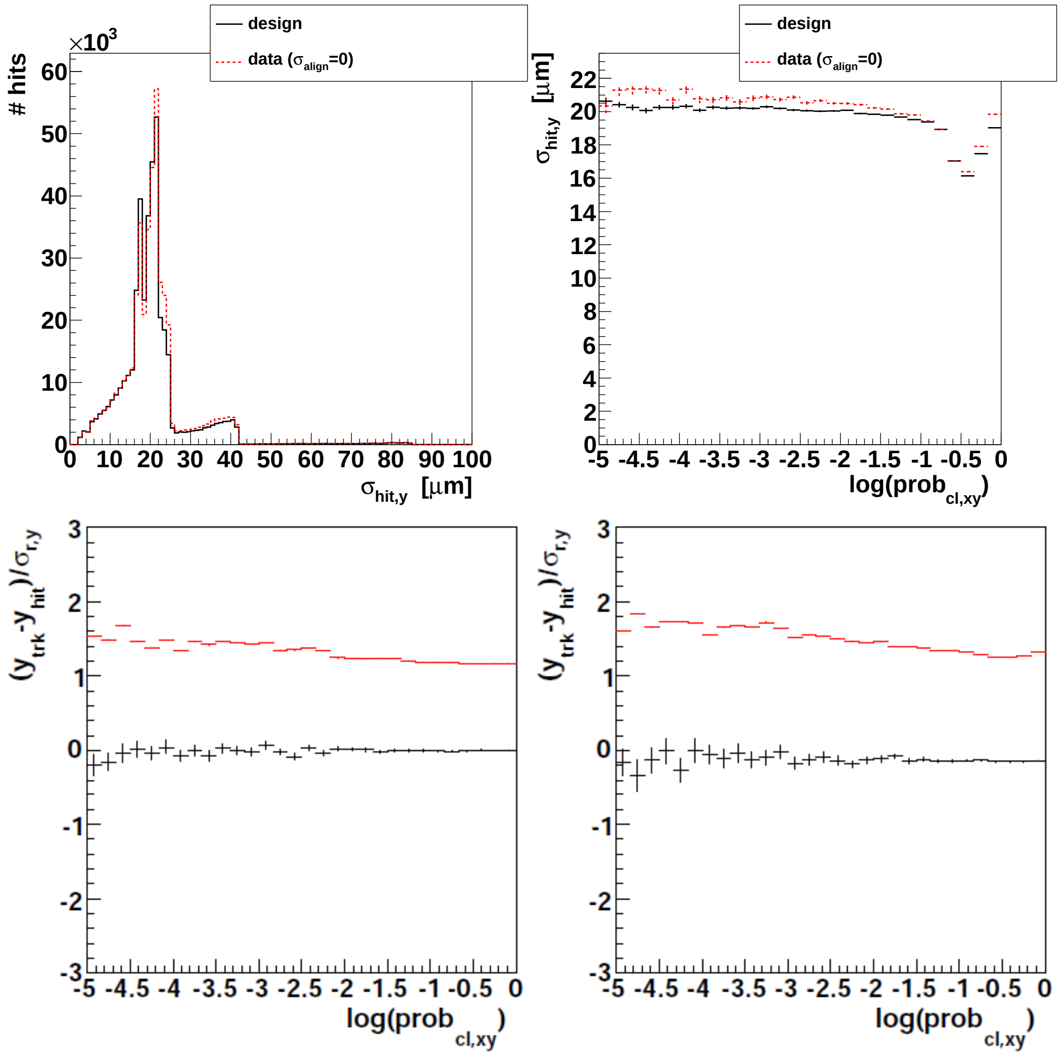

Figure A.11: Hit error distribution (top right – data vs. simulation), and dependency of hit error (top right – data vs. simulation) and normalised residuals in simulation (bottom left) and in data (bottom right) on pixel template probability in y-coordinate of sector “BPIX L3i”.

but a bigger threshold would exclude many hits in some sectors, especially in FPIX. And also the cluster template probability shows deviations from a constant width in several sectors. But systematic shifts of the central values are mainly excluded with the final selection.

Strip Cluster Selection

An important criterion of a good measurement from a strip cluster is, whether its width w_{cl} matches to the projected track length p. As explained in Chapter A.4.2, the track projection is assigned as matched for $w_{\mathrm{cl}} - p \leq 3.5$. With the selection of tracks of high transverse momentum, the angles are mainly small and so is the cluster width. In all detector regions clusters with width $w_{\mathrm{cl}} = 3\,\mathrm{strips}$ are the most common. Due to the crosstalk, they are everywhere compatible with the track projection. Strip clusters of two or three strips are the most precise hit measurements, 1-strip clusters give only digital position information. To reduce systematic effects, it is decided to choose only one kind of clusters, those with $w_{\mathrm{cl}} = 3$. Some important cluster parameters are shown in Figure A.12. Since the chosen sector is in TIB – where the modules are slightly rotated around the y-axis to optimise the readout for the Lorentz angle – the track incident angle ϕ_{module} is shifted to negative values.

The charge profile of the 3-strip clusters is given by the charge on the middle strip c_{M} and the charge on the left c_{L} and the right strip c_{R}. Their residual description is best for clusters with the maximum charge deposit on the middle cluster. This is expected, since these hits are less probable incomplete truncated clusters. Only those clusters are selected, $c_{\mathrm{M}} > c_{\mathrm{L}}$ and $c_{\mathrm{M}} > c_{\mathrm{R}}$. A positive side effect is, that this removes most of the clusters at the module edges and also at the APV edges, stemming from the increase of the noise. Another important selection criterion is $c_{\mathrm{L}} + c_{\mathrm{R}} \leq c_{\mathrm{M}}$, i.e. the charge distribution is not allowed to be almost flat over the cluster, a significant charge profile needs to be visible. The value is optimised on the dependence of the normalised residuals. The same is valid for the final criterion, the signal-to-noise ratio s/N has to be within $20 \leq s/N \leq 50$. Figure A.13 contains the typical optimisation diagrams. There is no dependence of the residuals on the position on the cluster on the module, given by the charge barycentre b_{cl}, the hit uncertainty is dominated by the geometrical situation. The distribution of the charge on the two edge strips however shows a dependency on the cluster shape, the normalised residual width depends on the detailed cluster selection. For both distributions, the data shows influences from misalignment. Not all systematic influences for each sector on the residual width are eliminated with the given selection, but the biases on the central values are.

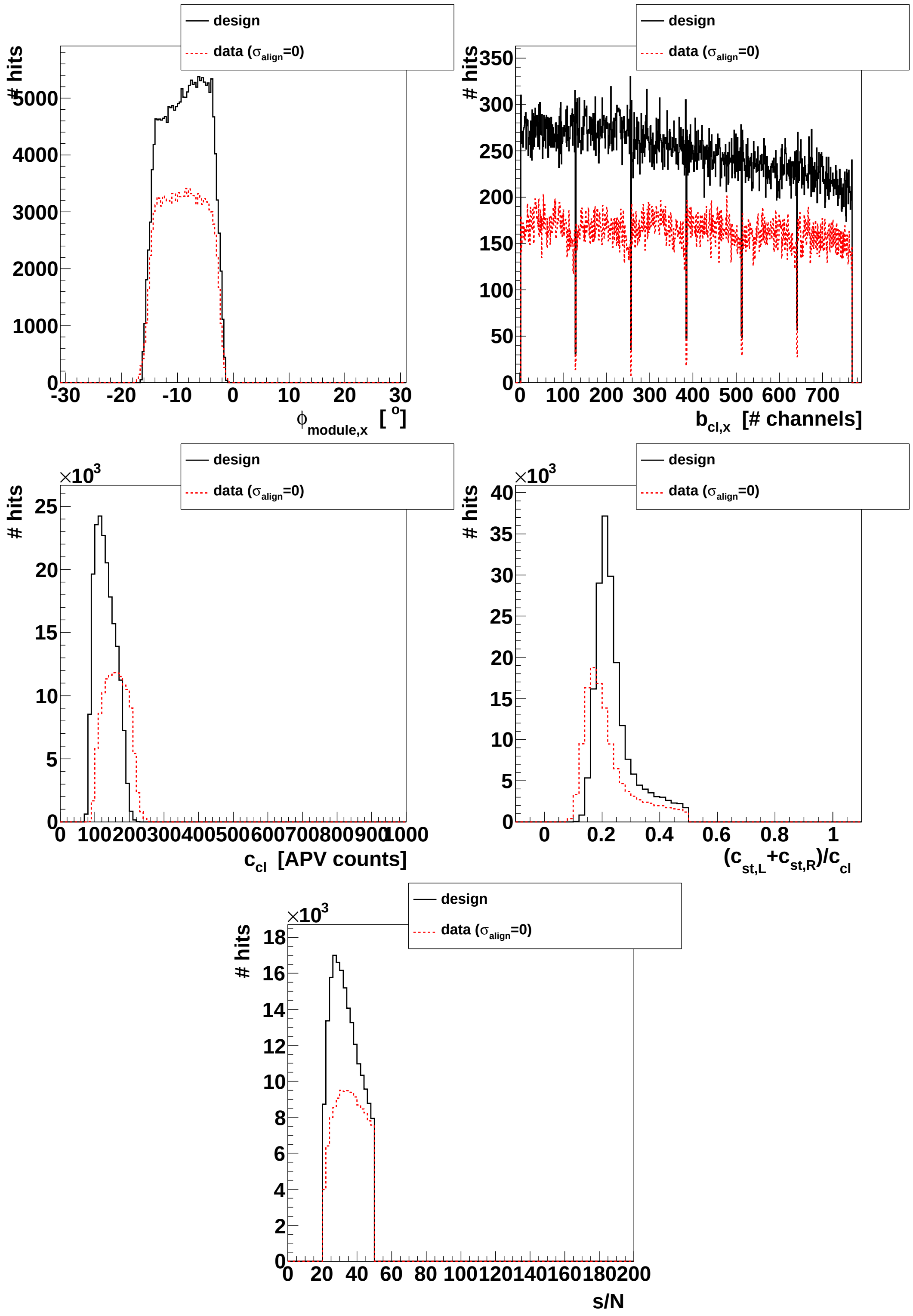

Figure A.12: Strip cluster parameters for sector “TIB L1Ro”.

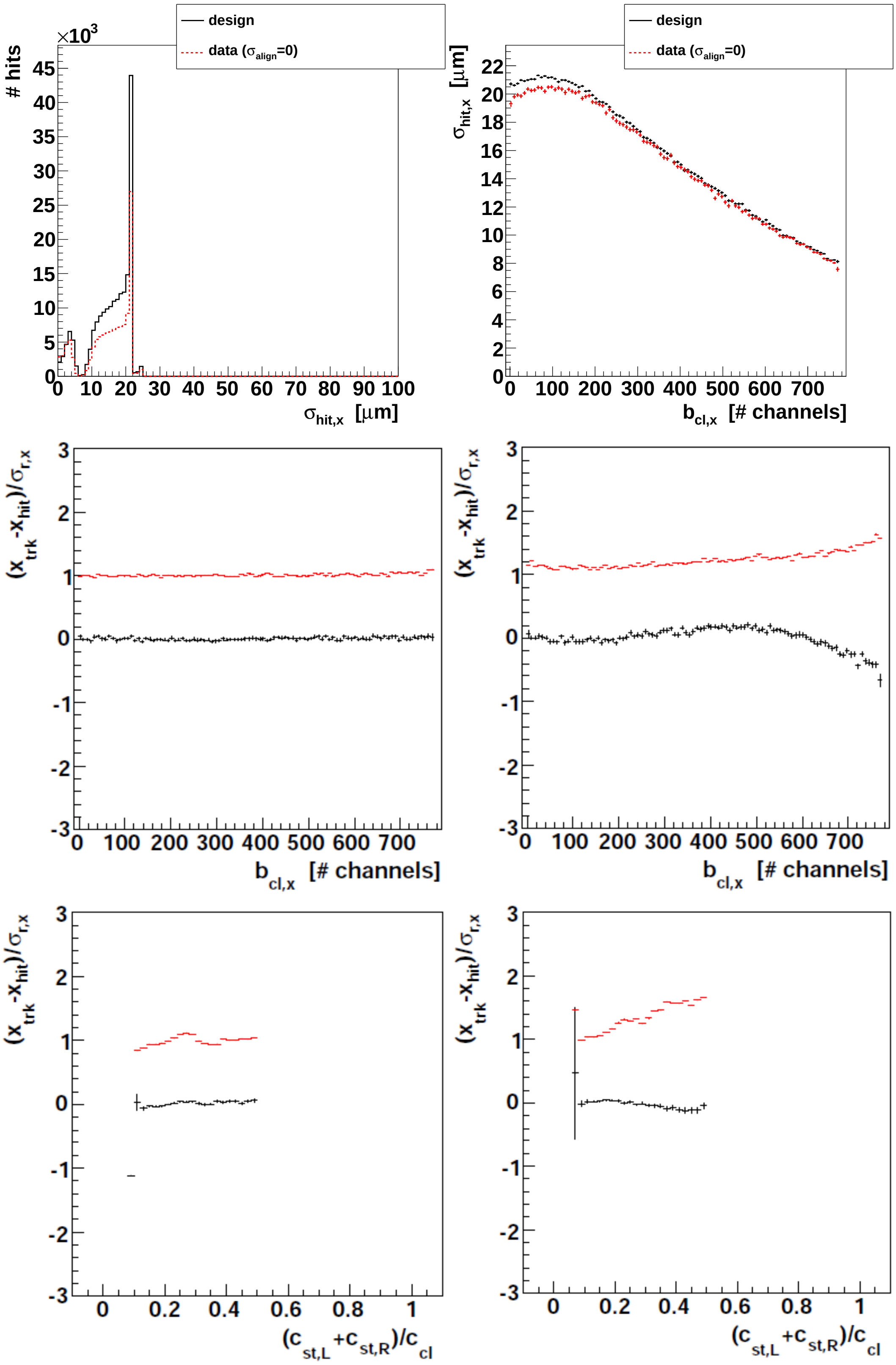

Figure A.13: Hit error distribution (top right – data vs. simulation), and dependency of hit error (top right – data vs. simulation) and normalised residuals in simulation (middle left) and in data (middle right) on cluster charge barycentre, and dependency of normalised residuals in simulation (bottom left) and in data (bottom right) on cluster charge on edges in sector “TIB L1Ro”.

A.8 Results

A.8.1 Additional Figures for Prompt Geometry

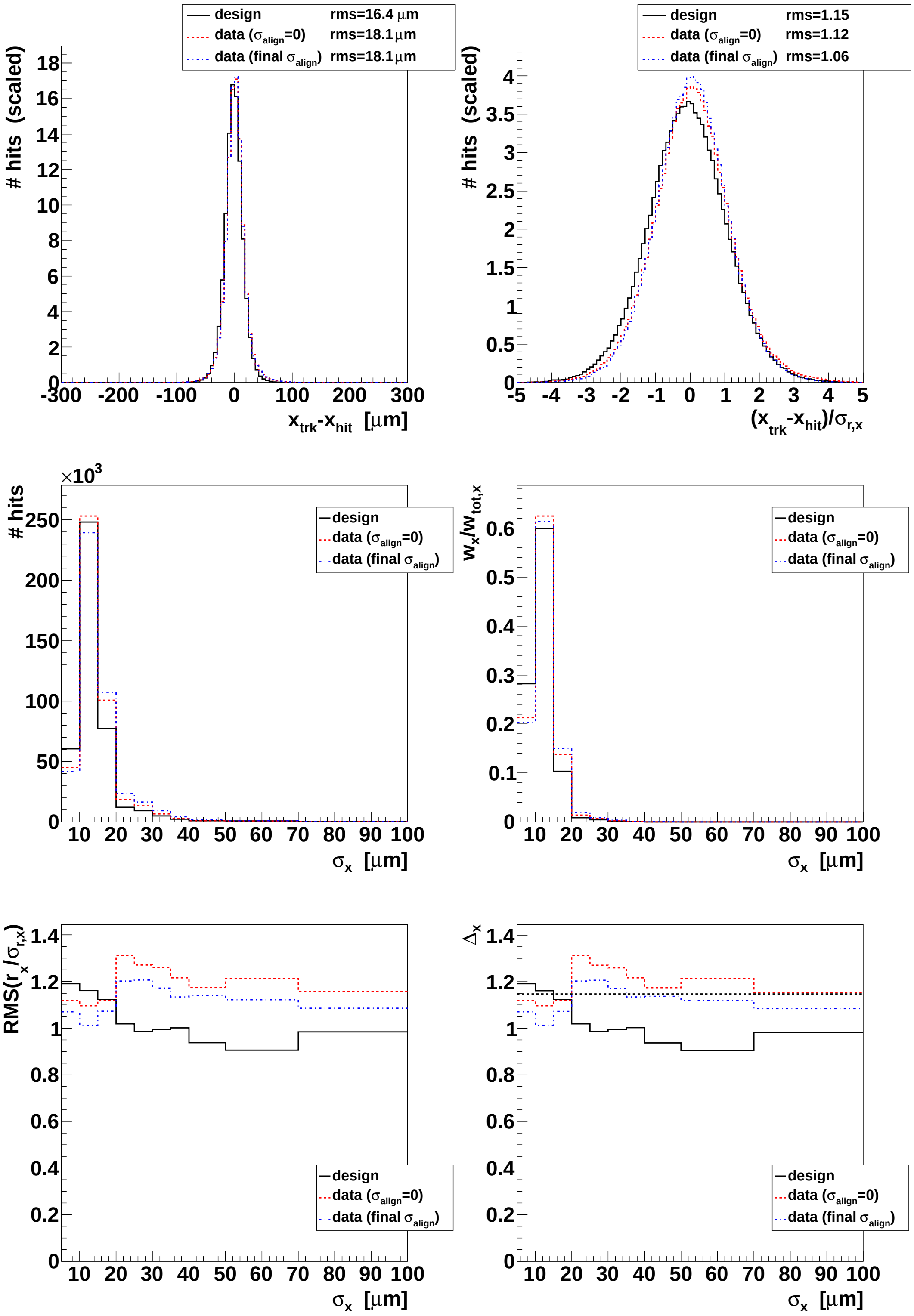

Figure A.14: Figures for alignment precision in sector "BPIX L1o".

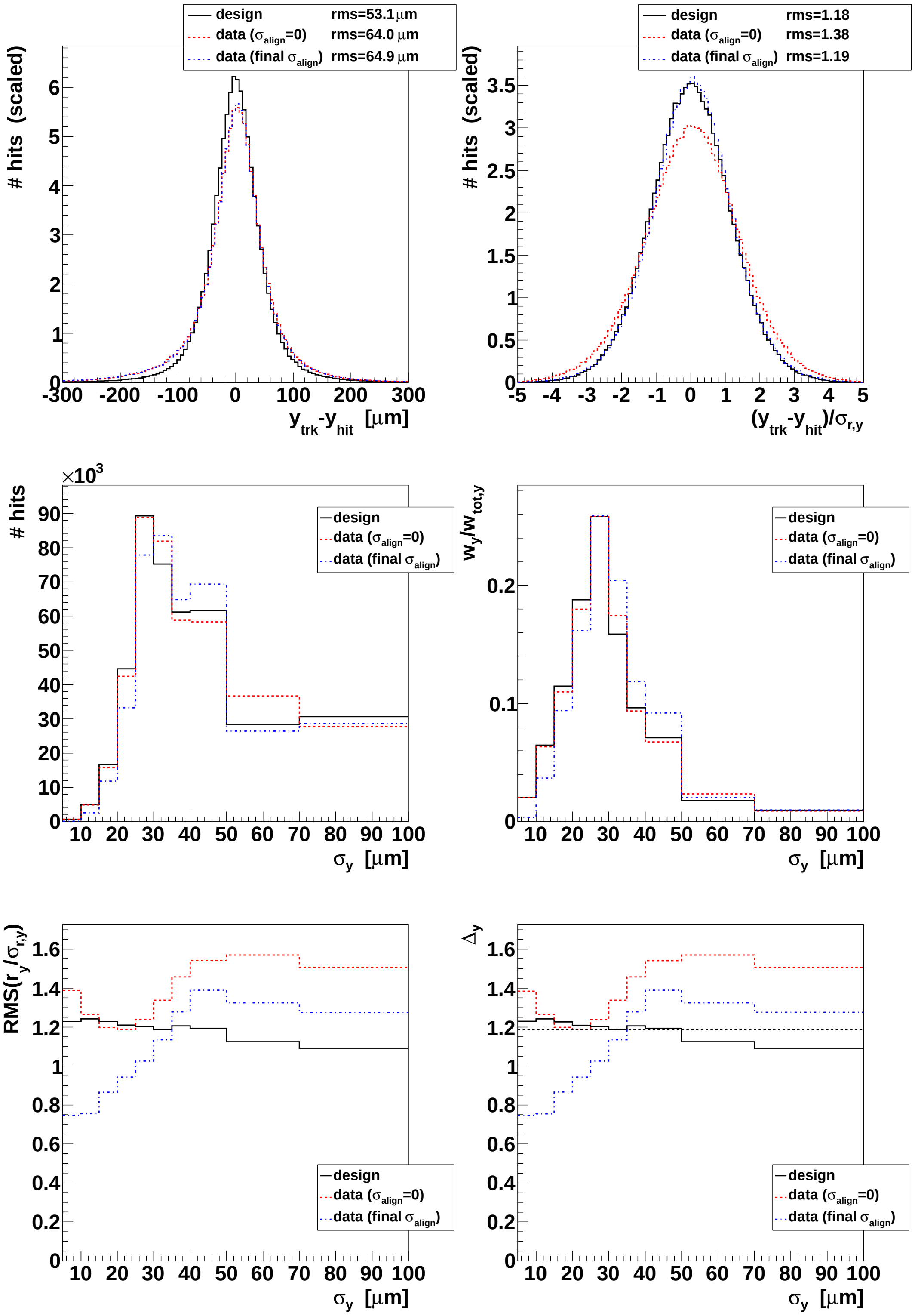

Figure A.15: Figures for alignment precision in sector “BPIX L1o”.

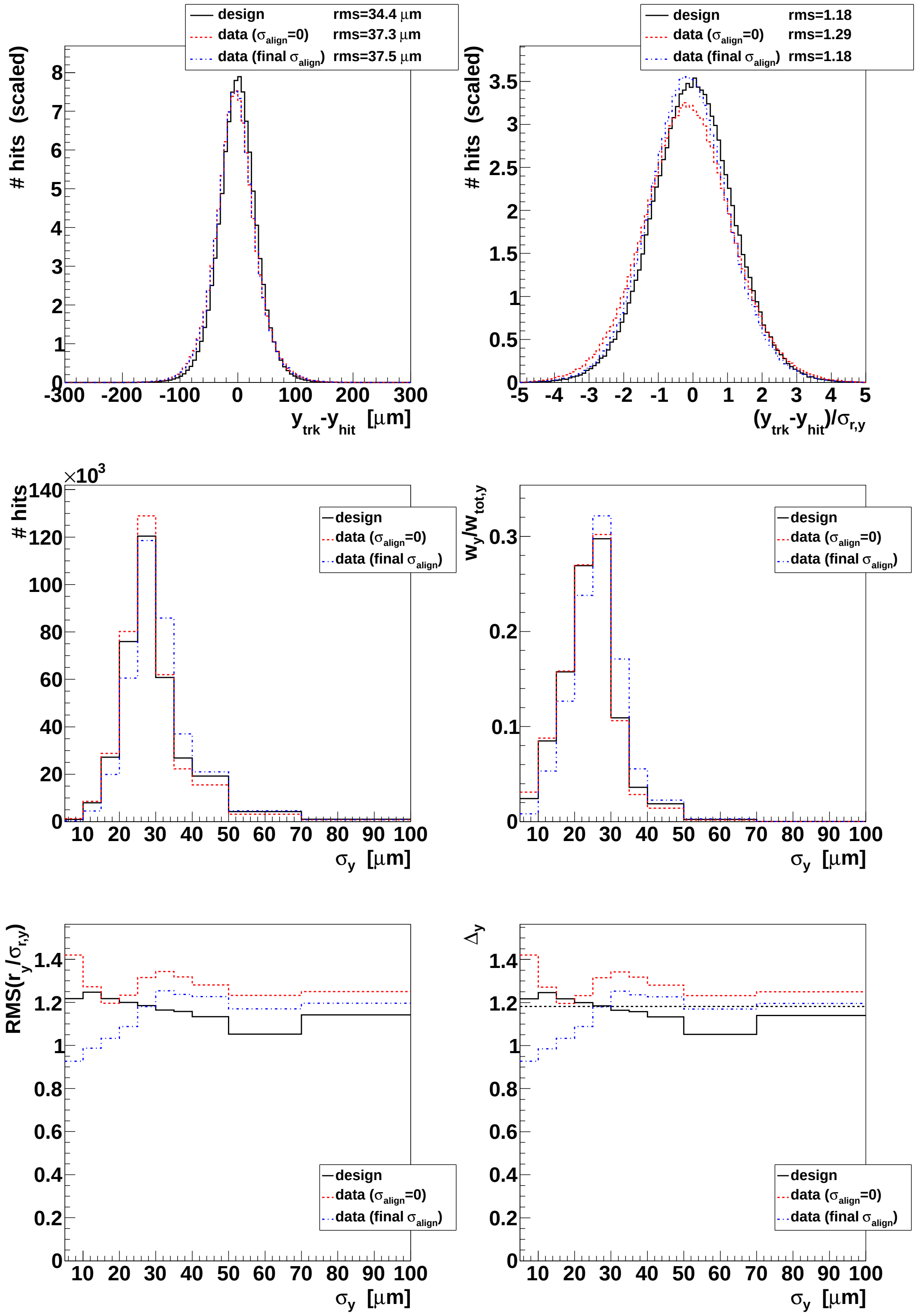

Figure A.16: Figures for alignment precision in sector “BPIX L3i”.

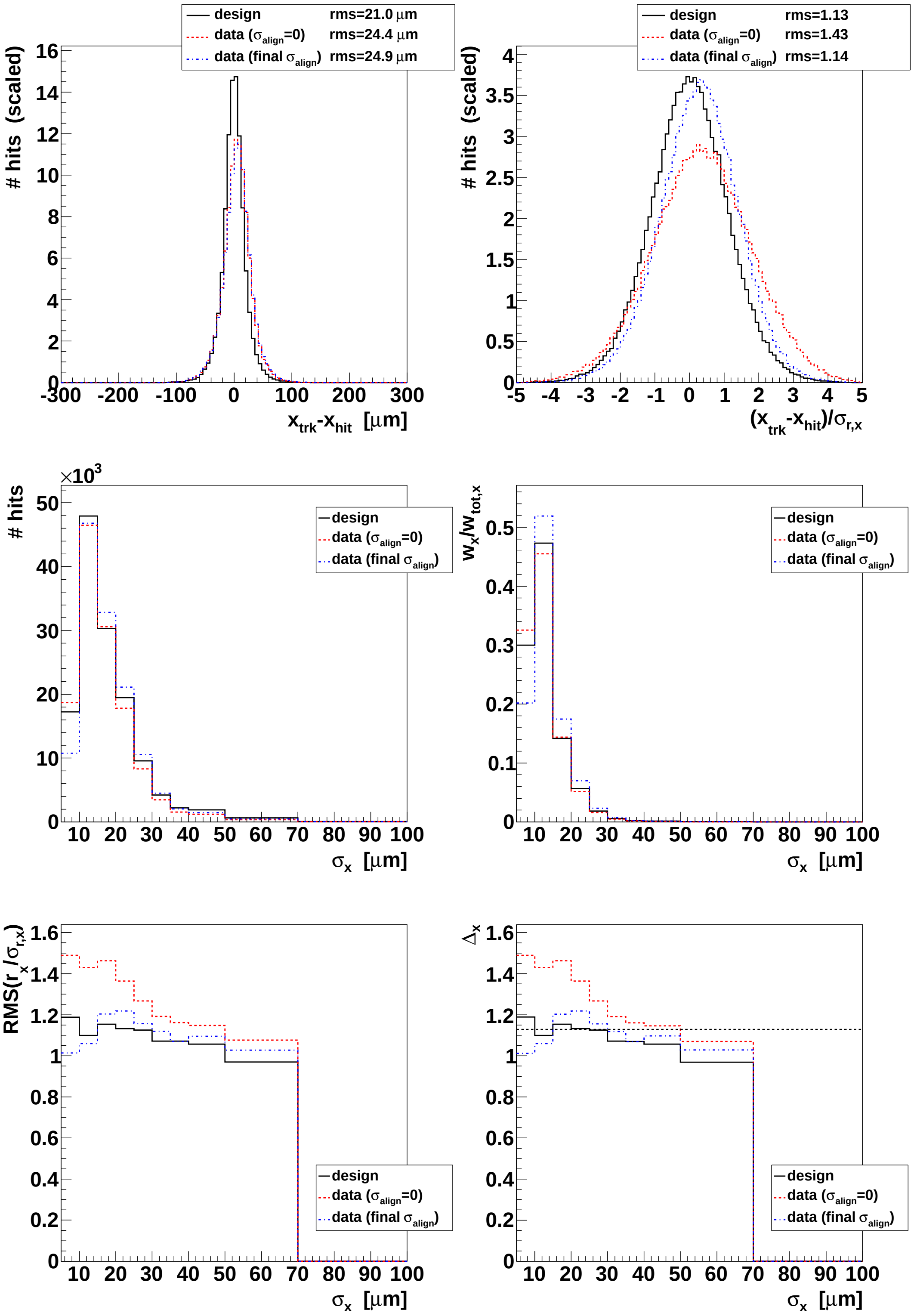

Figure A.17: Figures for alignment precision in sector “FPIXm L1”.

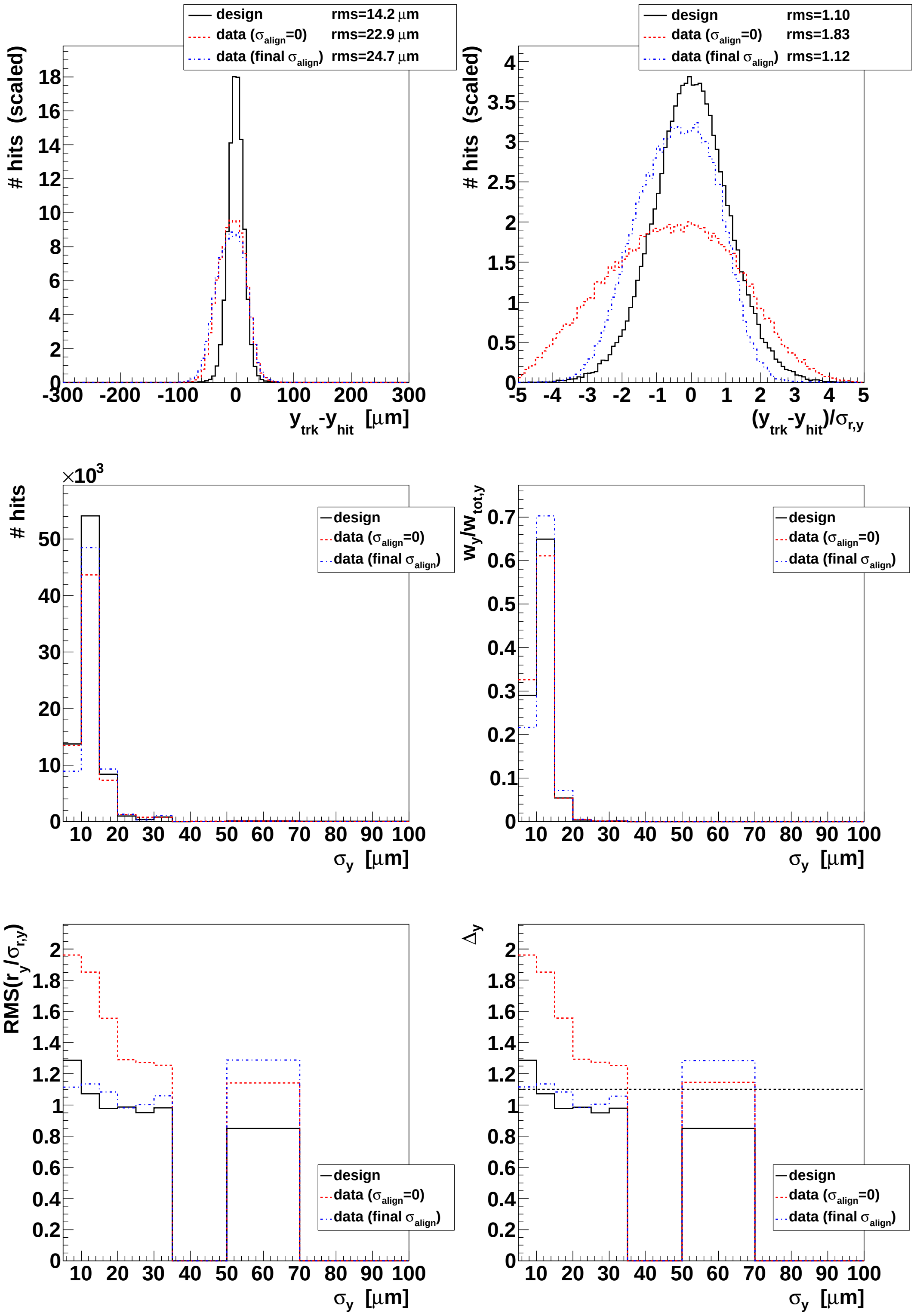

Figure A.18: Figures for alignment precision in sector "FPIXm L1".

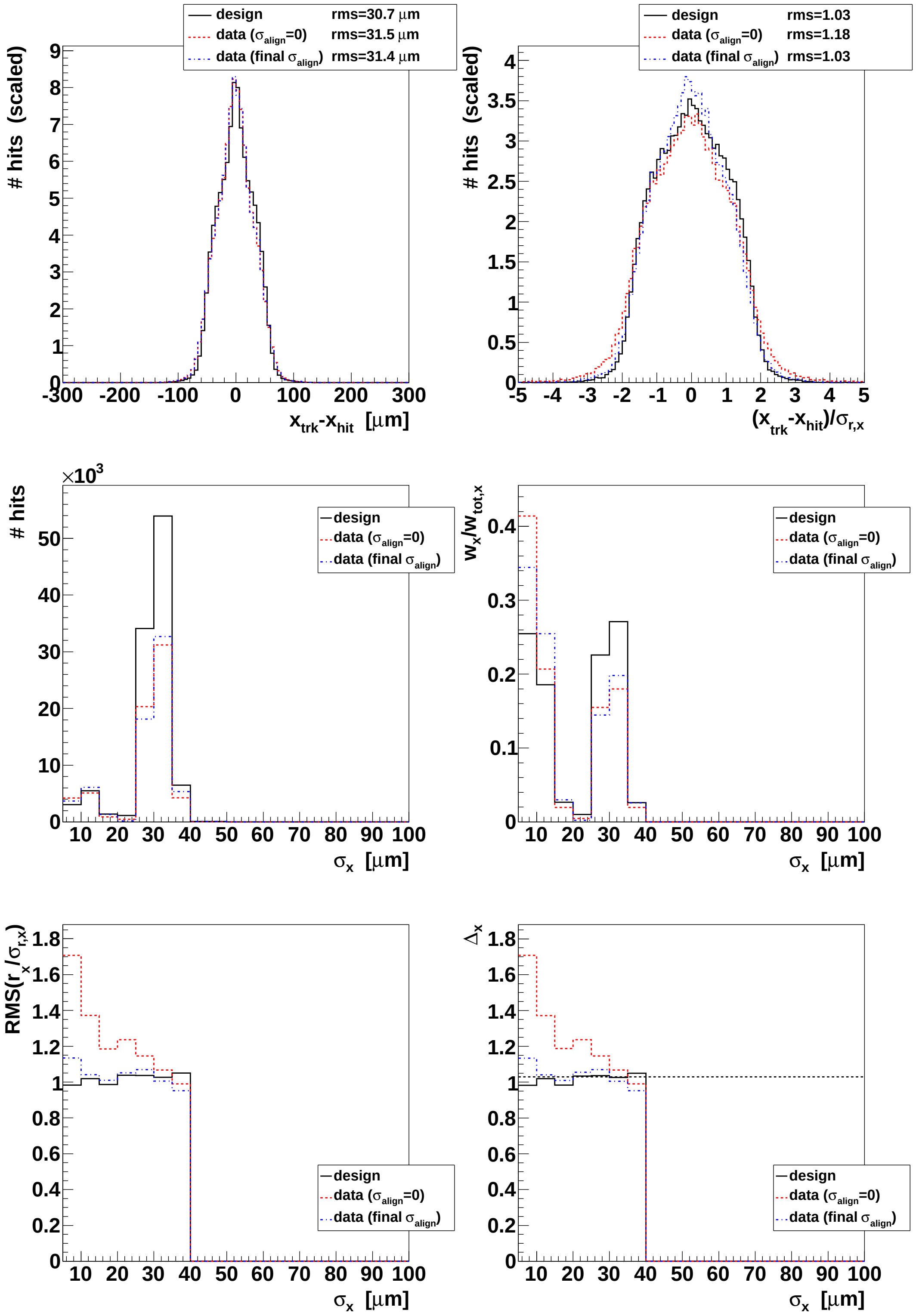

Figure A.19: Figures for alignment precision in sector “TIB L4i”.

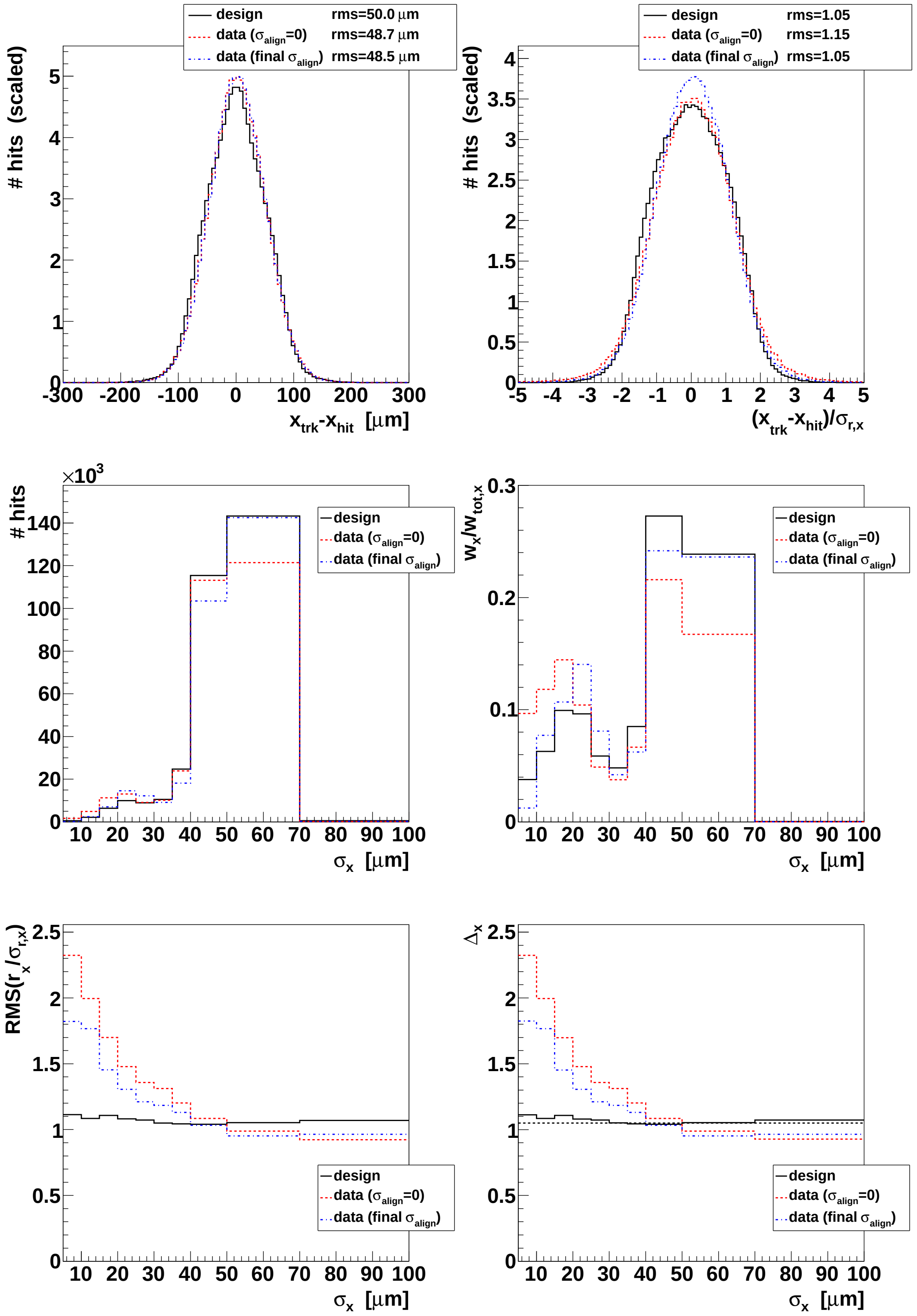

Figure A.20: Figures for alignment precision in sector "TOB L1So".

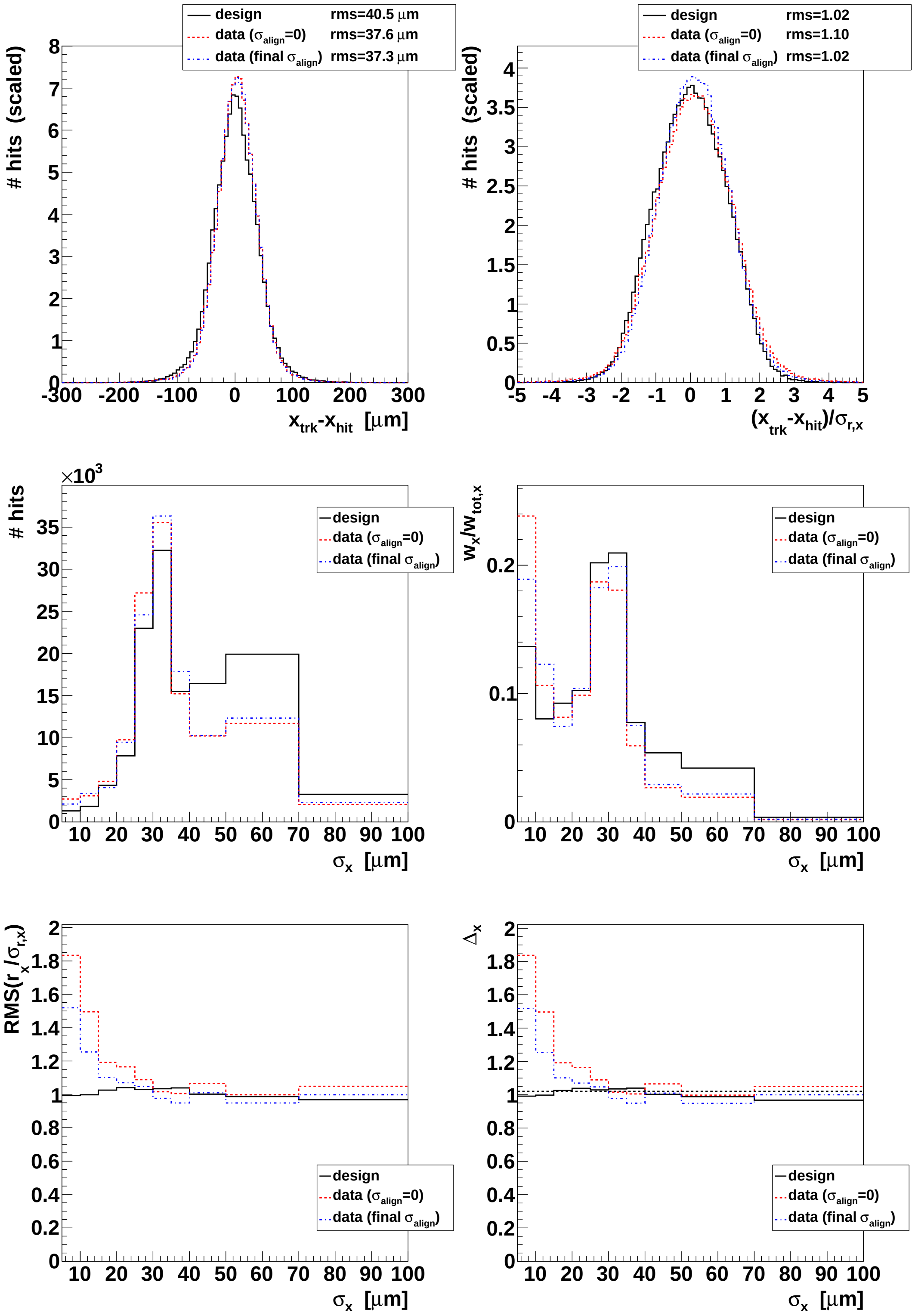

Figure A.21: Figures for alignment precision in sector "TOB L5o".

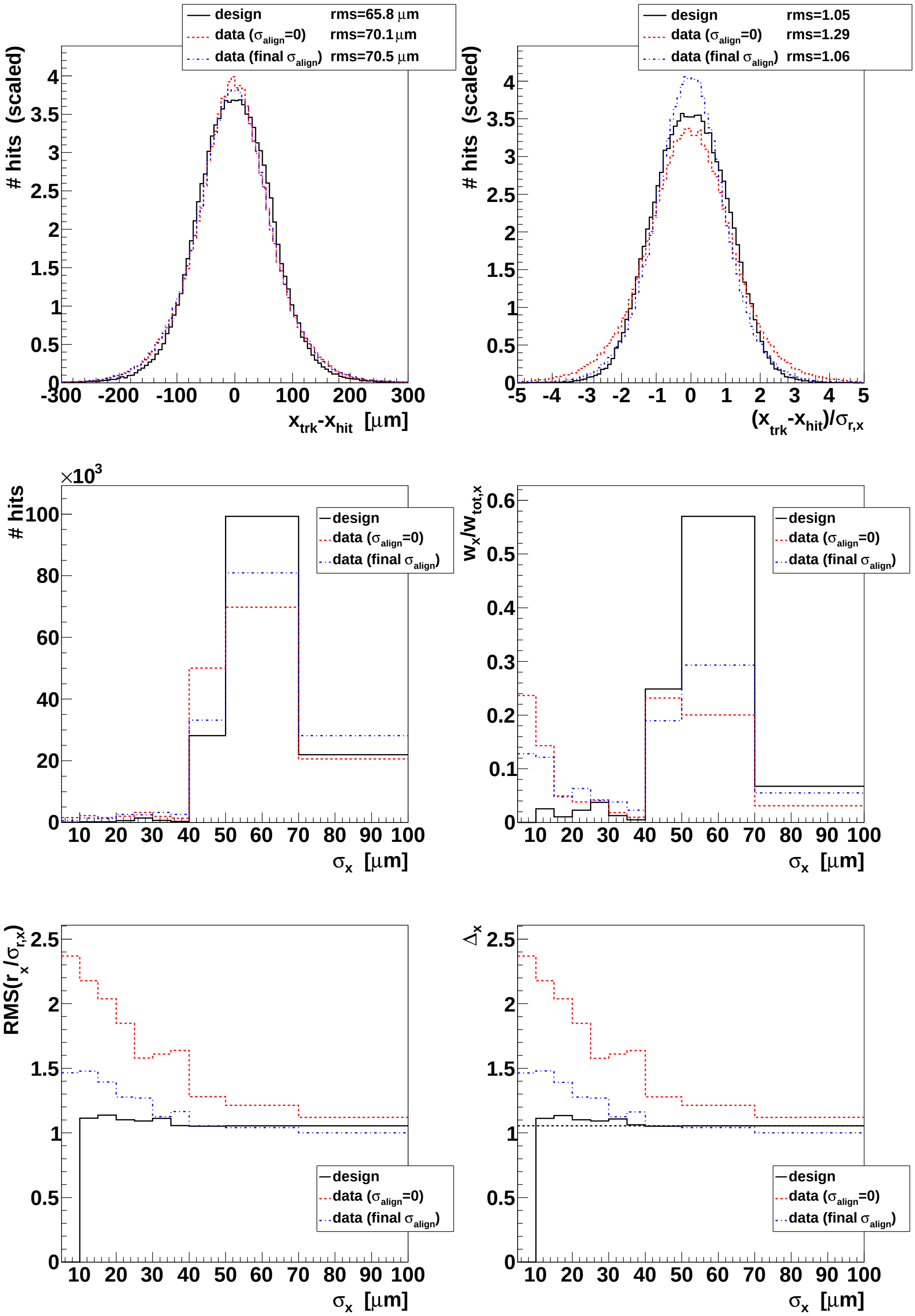

Figure A.22: Figures for alignment precision in sector "TECp R7".

Appendix B

Appendix for Chapter 6

B.1 Updated Result of Correction Factor $\boldsymbol{\rho_{R_{\mathrm{t\bar{t}}}}}$

This appendix shows an update of the correction factor $\rho_{R_{\mathrm{t\bar{t}}}}$ of the ratio of $\mathrm{t\bar{t}}$ events inside and outside the signal region as described in Chapter 6.5.2. The result here uses the final analysis as of [148], whereas the result used in the thesis is a preliminary result with bigger systematic errors. However the central values change only marginal. The updated ratio is shown in Table B.1. The updated correction factor, estimated from the quotient of the ratios, yields

$$\rho_{R_{\mathrm{t\bar{t}}}} = \frac{R_{\mathrm{t\bar{t}}}^{\text{top, data}}}{R_{\mathrm{t\bar{t}}}^{\text{top, simu}}} = 1.047 \pm 0.059\,(\text{stat.}) \pm 0.071\,(\text{syst.})\,. \tag{B.1}$$

Table B.1: Normalised cross sections $\frac{1}{\sigma}\frac{d\sigma}{dM^{l^+l^-}}$ in $\left[\left(\frac{\mathrm{GeV}}{c^2}\right)^{-1}\right]$ from the top analysis, differential in dilepton mass $M^{l^+l^-}$ [165]. Results are shown for the eμ channel, and for the MadGraph prediction. The last row gives the in/out ratio $R_{\mathrm{t\bar{t}}}^{\text{top}}$ for the two cases. Statistical and systematic errors are given separate. The values are scaled by a factor 1000.

$M^{l^+l^-}$	$\frac{1}{\sigma}\frac{d\sigma}{dM^{l^+l^-}}$ ($e\mu$)	$\frac{1}{\sigma}\frac{d\sigma}{dM^{l^+l^-}}$ (MadGraph)
[60 GeV, 120 GeV]	$7.56 \pm 0.27 \pm 0.30$	7.55
[120 GeV, 400 GeV]	$1.09 \pm 0.05 \pm 0.06$	1.14
$R_{\mathrm{t\bar{t}}}^{\text{top}}$	$1.486 \pm 0.083 \pm 0.101$	1.419

Table B.2: Number of observed events in data inside and outside the signal region. Results are given for the dataset corresponding to 2.1 fb^{-1}.

Selection	$N_{\mathrm{obs}}^{\mathrm{in}}$	$N_{\mathrm{obs}}^{\mathrm{out}}$
1 b (HE)	4026	486
1 b (HP)	1991	347

B.2 $\mathrm{t\bar{t}}$ Background in bZ^0, Z^0 → ee

This appendix shows results of the $\mathrm{t\bar{t}}$ background estimate for the bZ^0 analysis in the $\mathrm{Z^0 \to e^+e^-}$ decay channel – produced with the same method as described in Chapter 6.5 for the $\mathrm{Z^0} \to \mu^+\mu^-$ decay channel – and correlations between both decay modes.

$\mathrm{t\bar{t}}$ Contamination Estimate in the Electron Decay Channel

The bZ^0 analysis in the electron channel measures a slightly different phase space, since the electrons are selected with $p_{\mathrm{T}} > 25\,\mathrm{GeV}$ (compared to $p_{\mathrm{T}} > 20\,\mathrm{GeV}$ for muons) and $|\eta| < 2.5$, but excluding also the ECAL barrel-to-endcap transition region $1.444 < |\eta_{\mathrm{TR}}| < 1.566$ (compared to $|\eta| < 2.1$ for muons).

Results in the decay channel $\mathrm{Z^0}/\gamma^* \to \mathrm{e^+e^-}$ are produced in the same way as it is described for the muonic decay mode, using the $\mathrm{t\bar{t}}$ dominated upper sideband in the dielectron mass and extrapolate to the signal region. However, the method is directly adapted without studies of systematic effects, contrary to the muonic analysis. Results are produced for the two different b-tagging selections (steps "1 b (HE)" and "1 b (HP)"). Needed are the number of observed events in the signal region $N_{\mathrm{obs}}^{\mathrm{in}}$ and the sideband region $N_{\mathrm{obs}}^{\mathrm{out}}$, as listed in Table B.2. Furthermore, the ratios $R_{\mathrm{t\bar{t}}}$ and $R_{\mathrm{Z^0}}$ for the extrapolation between both regions are required, and taken from simulation. Table B.3 shows the necessary input values, Table B.4 shows the resulting ratios. The simulated samples are fully reweighted for pileup, lepton and b-tagging efficiencies, but they are not scaled to data luminosity. The statistical errors of $R_{\mathrm{t\bar{t}}}$ and $R_{\mathrm{Z^0}}$ are slightly too big, since the weights of the reweightings are not fully correct taken into account. But the values are conservative since the weights are lower than 1, and the influence on the $\mathrm{t\bar{t}}$ estimate is negligible.

The yields are in general lower as for the muonic decay, both in data and in simulation. Differences occur from the different kinematic acceptance regions. There are more events selected due to the wider pseudorapidity range, faced by a reduction of selected events due to the higher threshold on p_{T}. But the main difference is due to the selection efficiencies, which are lower in the electron case; e.g. the isolation criterion is different and isolation but also the energy measurement are more affected by pileup. In addition, the ratios get smaller,

Table B.3: Relevant input values from simulation for estimation of $\mathrm{t\bar{t}}$ contribution. Shown are the event yields in the signal region and in the sideband. Z^0 and $\mathrm{t\bar{t}}$ yields are not scaled to luminosity, because only their ratio is needed.

Selection	$n^{\mathrm{in}}_{\mathrm{t\bar{t}}}$	$n^{\mathrm{out}}_{\mathrm{t\bar{t}}}$	$n^{\mathrm{in}}_{\mathrm{Z}^0}$	$n^{\mathrm{out}}_{\mathrm{Z}^0}$
1 b (HE)	4663.0	4219.3	21301.0	362.0
1 b (HP)	3525.0	3204.9	9776.0	143.9

Table B.4: Ratios $R^{\mathrm{in/out}}$ and corresponding statistical errors as taken from simulation.

Selection	$R^{\mathrm{in/out}}_{\mathrm{t\bar{t}}}$	$R^{\mathrm{in/out}}_{\mathrm{Z}^0}$
1 b (HE)	1.105 ± 0.023	58.84 ± 3.12
1 b (HP)	1.100 ± 0.027	67.94 ± 5.71

but in agreement between data and simulation. The selection efficiency is smaller in the signal region than in the sideband region.

Corrections and uncertainties arising from systematic effects are taken as for the muonic analysis. The estimated $\mathrm{t\bar{t}}$ contamination in the signal region is stated in Table B.5. The results are similar to the muon case, but slightly higher. As already stated, there are reasons for slight differences in the two final states. The measured phase space differs slightly, and detector effects are very different for muons and electrons and lead to different dependencies of the selection efficiencies. The $\mathrm{t\bar{t}}$ contamination is also in the sideband bigger than for the muon case, but again the differences are small.

The uncertainty is smaller than in the muon case, because the full data sample corresponding to $2.1\,\mathrm{fb}^{-1}$ is used. The relative contributions of the uncertainties of the input parameters to the uncertainty of the $\mathrm{t\bar{t}}$ estimate are listed in Table B.6. The dominant uncertainty is the systematic error of $R_{\mathrm{t\bar{t}}}$, as for the muonic analysis.

Cross Checks

The $\mathrm{t\bar{t}}$ estimate can be cross checked identical to the muonic analysis (see Chapter 6.5.3). The results can be compared to estimates taken purely from simulation, scaling the samples to the integrated luminosity and theoretical cross sections—the yields used are taken from [150]. Furthermore, it can

Table B.5: Absolute estimated (N) and relative fractions (f) of $\mathrm{t\bar{t}}$ events inside and outside the signal region. Also resulting fractions of Z^0 events are shown.

Selection	$N^{\mathrm{in}}_{\mathrm{t\bar{t}}}$	$N^{\mathrm{out}}_{\mathrm{t\bar{t}}}$	$f^{\mathrm{in}}_{\mathrm{t\bar{t}}}$ (%)	$f^{\mathrm{out}}_{\mathrm{t\bar{t}}}$ (%)	$f^{\mathrm{in}}_{\mathrm{Z}^0}$ (%)	$f^{\mathrm{out}}_{\mathrm{Z}^0}$ (%)
1 b (HE)	492.3 ± 55.8	425.9	12.23 ± 1.39	87.6	87.8	12.4
1 b (HP)	371.7 ± 43.1	323.2	18.67 ± 2.16	93.1	81.3	6.9

Table B.6: Influence of the different uncertainties of the ingredients on the relative uncertainty $\sigma_f = \frac{\Delta f^{\text{in}}_{\mathrm{t\bar{t}}}}{f^{\text{in}}_{\mathrm{t\bar{t}}}}$ of the estimated $\mathrm{t\bar{t}}$ fraction $f^{\text{in}}_{\mathrm{t\bar{t}}}$. Shown are the influences from the statistical errors of $N^{\text{in}}_{\text{obs}}$ and $N^{\text{out}}_{\text{obs}}$, the influences from the statistical errors of the simulated samples for $R_{\mathrm{t\bar{t}}}$ and $R_{\mathrm{Z^0}}$, and all other uncertainties for $R_{\mathrm{t\bar{t}}}$ and $R_{\mathrm{Z^0}}$ gathered in the systematic error. All values are relative uncertainties of the estimated $\mathrm{t\bar{t}}$ fraction and are given in %.

Selection	σ_f $[N^{\text{in}}_{\text{obs}}]$	σ_f $[N^{\text{out}}_{\text{obs}}]$	σ_f $[R_{\mathrm{t\bar{t}}}\,(\text{stat.})]$	σ_f $[R_{\mathrm{Z^0}}\,(\text{stat.})]$	σ_f $[R_{\mathrm{t\bar{t}}}\,(\text{syst.})]$	σ_f $[R_{\mathrm{Z^0}}\,(\text{syst.})]$
1 b (HE)	0.3	5.3	2.2	0.8	9.7	1.4
1 b (HP)	0.2	5.9	2.5	0.6	9.6	0.8

Table B.7: Comparison of estimated $\mathrm{t\bar{t}}$ fraction $f^{\text{in}}_{\mathrm{t\bar{t}}}$ amongst the result of sideband extrapolation (based on $2.1\,\text{fb}^{-1}$) and as taken from simulation (based on $2.1\,\text{fb}^{-1}$) and the result from the template fit (based on $1.1\,\text{fb}^{-1}$). The sideband results include also systematic uncertainties. The values of simulation are gained dividing the $\mathrm{t\bar{t}}$ expectation by the expectation of all regarded samples summed up. The error of the template fit is statistical only. All values are in %.

Selection	$f^{\text{in}}_{\mathrm{t\bar{t}}}$ (sideband)	$f^{\text{in}}_{\mathrm{t\bar{t}}}$ (simulation)	$f^{\text{in}}_{\mathrm{t\bar{t}}}$ (template)
1 b (HE)	12.23 ± 1.39	10.13	11.5 ± 1.1
1 b (HP)	18.67 ± 2.16	15.64	17.6 ± 1.7

be compared to the values of the template fit to the dielectron mass distribution [150]. The comparison is summarised in Table B.7. The estimation purely on simulation is significantly below the sideband estimate, data-driven estimates are definitely necessary. The templated fit is in better agreement, the statistical errors are highly correlated.

Results and Correlations in Electron and Muon Decay Channel

For electron and muon channel, some of the uncertainties are fully correlated, others mainly uncorrelated. Although the dimuon and dielectron selections are not complementary, they lead to almost uncorrelated samples, since the probability to find two good muons and two electrons and a b-jet inside the acceptance region is very low. Thus, the statistical errors in data $\sigma_f[N^{\text{in}}_{\text{obs}}]$ and $\sigma_f[N^{\text{out}}_{\text{obs}}]$ are treated as uncorrelated. The same is valid for the statistical errors of the simulated samples $\sigma_f[R_{\mathrm{t\bar{t}}}\,(\text{stat.})]$ and $\sigma_f[R_{\mathrm{Z^0}}\,(\text{stat.})]$, which are used to estimate the uncorrected ratios $R_{\mathrm{t\bar{t}}}$ and $R_{\mathrm{Z^0}}$.

The systematic uncertainties $\sigma_f[R_{\mathrm{t\bar{t}}}\,(\text{syst.})]$ and $\sigma_f[R_{\mathrm{Z^0}}\,(\text{syst.})]$, arising from the fact that the ratios are taken from simulation, are treated as fully correlated. For $R_{\mathrm{t\bar{t}}}$ the same correction factor is applied for both channels, as taken

Table B.8: Uncorrelated, correlated and total relative uncertainties $\sigma_f = \frac{\Delta f^{\mathrm{in}}_{\mathrm{t\bar{t}}}}{f^{\mathrm{in}}_{\mathrm{t\bar{t}}}}$ of the estimated $\mathrm{t\bar{t}}$ fraction $f^{\mathrm{in}}_{\mathrm{t\bar{t}}}$ for the two different Z^0 decay channels. Shown are the results for the selection step "1 b (HP)". All values are relative uncertainties of the estimated $\mathrm{t\bar{t}}$ fraction and are given in %.

Decay channel	σ_f[uncorr.]	σ_f[corr.]	σ_f
$\mathrm{Z}^0/\gamma^* \to \mu^+\mu^-$	7.60	9.71	12.33
$\mathrm{Z}^0/\gamma^* \to \mathrm{e}^+\mathrm{e}^-$	6.40	9.65	11.58

Table B.9: Estimated $\mathrm{t\bar{t}}$ fraction $f^{\mathrm{in}}_{\mathrm{t\bar{t}}}$ for the two different Z^0 decay channels, shown for two different selections. All values are given in %.

Selection	$f^{\mathrm{in}}_{\mathrm{t\bar{t}}}[\mathrm{Z}^0/\gamma^* \to \mu^+\mu^-]$	$f^{\mathrm{in}}_{\mathrm{t\bar{t}}}[\mathrm{Z}^0/\gamma^* \to \mathrm{e}^+\mathrm{e}^-]$
1 b (HE)	11.31 ± 1.36	12.23 ± 1.39
1 b (HP)	18.40 ± 2.27	18.67 ± 2.16

from the eμ analysis, together with the corresponding uncertainty. The assumed uncertainty of R_{Z^0} is also taken identical. It is possible, that they are not fully correlated, since the efficiencies in the signal region and in the side-band region do not need to be described equally good for both channels, but these are small effects. Uncertainties arising from other backgrounds would also be mainly correlated, but they are small and anyway neglected in this analysis. The correlated and uncorrelated components of the estimated $\mathrm{t\bar{t}}$ fraction can be seen in Table B.8, while the results for the important selection steps are gathered in Table B.9.

List of Tables

2.1 Branching ratios of $t\bar{t}$ decays 21

2.2 Branching ratios of Z^0 decays 23

3.1 Design parameters of CMS 33

3.2 Characteristics of silicon modules 42

3.3 Iterative tracking steps 47

4.1 Change of variables by assignment of finite value of the alignment precision 79

4.2 Granularity for alignment precision estimate in BPIX, FPIX, TIB and TOB 86

4.3 Granularity for alignment precision estimate in TID and TEC . 87

5.1 Summary of simulated data samples 107

5.2 Single muon triggers used to select data events 108

5.3 Number of expected signal and background events in the $t\bar{t}$ analysis 110

5.4 Number of expected signal and background events in the Z^0 analysis 113

5.5 Scale factors and systematic uncertainties of the Z^0 analysis . . 120

5.6 Scale factors and systematic uncertainties of the top analysis . . 122

5.7 Cross section of the Drell–Yan process with muonic decay 124

6.1 Summary of simulated data samples 131

6.2 Number of expected signal and background events 134

6.3 Number of observed events in data inside and outside the signal region 147

6.4 Relevant input values from simulation for estimation of $t\bar{t}$ contribution 147

6.5 Ratios $R^{\mathrm{in/out}}$ and corresponding statistical errors as taken from simulation 148

6.6 Normalised cross sections from the top analysis, differential in dilepton mass . . . 151

6.7 Normalised cross sections from the top analysis, differential in dilepton mass . . . 152

6.8 Absolute estimated and relative fractions of $\mathrm{t\bar{t}}$ events . . . 153

6.9 Influence of the different uncertainties of the ingredients on the relative uncertainty of the estimated $\mathrm{t\bar{t}}$ fraction . . . 155

6.10 Comparison of estimated $\mathrm{t\bar{t}}$ fraction between result of sideband extrapolation and as taken from simulation . . . 156

6.11 Dependence of $R_{\mathrm{t\bar{t}}}$ on pileup . . . 157

6.12 Dependence of $R_{\mathrm{Z^0}}$ on pileup . . . 157

6.13 Dependence of estimates of the relative fraction of $\mathrm{t\bar{t}}$ events on pileup . . . 160

6.14 Comparison of event yields for all relevant simulation samples separately . . . 162

6.15 Comparison of event yields for simulation and data corresponding to 191 pb^{-1} . . . 162

6.16 Ingredients of the cross-section calculation and corresponding uncertainties . . . 168

6.17 Influence of all systematic effects considered on the measured cross section . . . 169

A.1 Tracker alignment periods in 2011 defined by their interval of validity (IOV) . . . 181

A.2 Content of data and simulated samples . . . 200

A.3 Event and track selection . . . 202

A.4 Number of events in use . . . 208

A.5 Hit selection in pixel and strip detector . . . 209

B.1 Normalised cross sections from the top analysis, differential in dilepton mass . . . 227

B.2 Number of observed events in data inside and outside the signal region . . . 228

B.3 Relevant input values from simulation for estimation of $\mathrm{t\bar{t}}$ contribution . . . 229

B.4 Ratios $R^{\mathrm{in/out}}$ and corresponding statistical errors as taken from simulation . . . 229

B.5 Absolute estimated and relative fractions of $\mathrm{t\bar{t}}$ events . . . 229

B.6 Influence of the different uncertainties of the ingredients on the relative uncertainty of the estimated $\mathrm{t\bar{t}}$ fraction . . . 230

B.7 Comparison of estimated $t\bar{t}$ fraction between result of sideband extrapolation and as taken from simulation 230
B.8 Uncorrelated, correlated and total relative uncertainties of estimated $t\bar{t}$ fraction 231
B.9 Estimated $t\bar{t}$ fraction for the two different Z^0 decay channels . . 231

List of Figures

1.1 CERN accelerators 4

2.1 Elementary particles of the Standard Model 6
2.2 Exemplary Feynman diagrams for Bhabha scattering 8
2.3 Components of a proton-proton collision 14
2.4 MSTW NLO PDFs at $Q^2 = 10\,\mathrm{GeV}^2$ and $Q^2 = 10^4\,\mathrm{GeV}^2$ 16
2.5 MSTW Standard Model production cross sections at TeVatron and LHC in NLO 19
2.6 LO Feynman graphs of $\mathrm{t\bar{t}}$ production 20
2.7 LO Feynman graphs of Z^0/γ^* exchange 22
2.8 Hadronic cross section of Z^0/γ^* as a function of centre-of-mass energy 23
2.9 Initial state flavour decomposition of inclusive Z^0 cross sections in LO 25
2.10 LO Feynman graphs for bZ^0 production in 4-flavour scheme . . 26
2.11 LO Feynman graphs for bZ^0 production in 5-flavour scheme . . 26
2.12 Stopping power for positive muons in copper 28

3.1 Luminosity 32
3.2 CMS 34
3.3 CMS coordinate system 34
3.4 CMS electromagnetic calorimeters 36
3.5 CMS hadronic calorimeters 37
3.6 CMS muon system 38
3.7 Muon system momentum resolution 38
3.8 Level-1 trigger architecture 40
3.9 CMS tracker 41
3.10 Silicon strip modules 44
3.11 Drift of charge carriers in silicon sensors 45

3.12 Track pattern recognition 48
3.13 Track fitting 49
3.14 Basic steps common to most event generators 51
3.15 Muon reconstruction algorithms 55
3.16 Jet energy correction scheme 59
3.17 Topology of b jets 61

4.1 Silicon module coordinate system 67
4.2 Wedge-shaped strip module 69
4.3 Displaced silicon module 70
4.4 Alignment hierarchy of tracker 72
4.5 Effect of kinks and bows on χ^2-probability 75
4.6 Influence of misalignment on normalised residual distribution . . 78
4.7 Dependence of the measurability of misalignment on the residual resolution 80
4.8 Alignment precision during iterations in pixel detector 89
4.9 Alignment precision during iterations in strip detector 90
4.10 Figures for alignment-precision measurement in sector “BPIX L3i” 92
4.11 Figures for alignment-precision measurement in sector “TIB L1Ro” 93
4.12 Influence of alignment precision on track parameter errors . . . 95
4.13 Track quantities sensitive to alignment precision 96
4.14 Alignment-precision results 97
4.15 Alignment-precision results 98
4.16 Track quantities sensitive to alignment precision 99
4.17 Alignment-precision results in systematic studies 100
4.18 Alignment-precision results in systematic studies 102
4.19 Influence of alignment precision on track quantities for the biggest misalignment scenario 103

5.1 Muon isolation and dimuon mass distributions 109
5.2 Muon pseudorapidity and transverse momentum distributions . 112
5.3 Generated $Z^0(\gamma^*)$ boson mass of Drell–Yan process 117
5.4 Properties of muons from $Z^0(\gamma^*)$ decay 117

6.1 Dependence of muon isolation on pileup 133

6.2 Dimuon mass distribution and p_{T}-distribution of muon with bigger p_{T} . . . 135
6.3 Data-to-simulation comparison for selection step “1 jet” . . . 136
6.4 Modelling of pileup and $\not{E}_{\mathrm{T}}$ . . . 138
6.5 Data-to-simulation comparison for selection “1 b (HP)” . . . 139
6.6 Template fit of secondary vertex mass distribution . . . 143
6.7 Top analysis measurement in the decay channel with eμ final states . . . 150
6.8 Invariant dimuon mass spectrum from data and fitted contributions . . . 154
6.9 Average relative isolation of muons as function of muon p_{T} . . . 159
6.10 Transverse momentum of selected muons in events with at least 2 muons . . . 160
6.11 Comparison of $\not{E}_{\mathrm{T}}$-distribution between all relevant simulation samples and data . . . 163

A.1 Alignment precision as used for data reconstruction . . . 183
A.2 Default strip CPE . . . 191
A.3 Number of hits per track in pixel and strip detector . . . 202
A.4 Dependencies on number of hits in strip detector . . . 203
A.5 Absolute and transverse momentum distribution . . . 204
A.6 Geometrical track parameters and χ^2-value . . . 206
A.7 Dependencies on longitudinal impact parameter . . . 207
A.8 Track charges and number of selected tracks per event . . . 208
A.9 Pixel cluster parameters . . . 210
A.10 Dependencies on pixel cluster charge . . . 211
A.11 Dependencies on pixel template probability . . . 212
A.12 Strip cluster parameters . . . 214
A.13 Dependencies on cluster charge barycentre and charge on edges 215
A.14 Figures for alignment precision . . . 217
A.15 Figures for alignment precision . . . 218
A.16 Figures for alignment precision . . . 219
A.17 Figures for alignment precision . . . 220
A.18 Figures for alignment precision . . . 221
A.19 Figures for alignment precision . . . 222
A.20 Figures for alignment precision . . . 223
A.21 Figures for alignment precision . . . 224
A.22 Figures for alignment precision . . . 225

Bibliography

[1] L. Evans and P. Bryant. LHC Machine. *JINST*, 3(S08001), 2008. `http://www.iop.org/EJ/journal/-page=extra.lhc/jinst`.

[2] CMS Collaboration. The CMS experiment at the CERN LHC. *JINST*, 3(S08004), 2008. `http://www.iop.org/EJ/journal/-page=extra.lhc/jinst`.

[3] CERN Accelerator Complex. `http://user.web.cern.ch/public/en/research/AccelComplex-en.html`.

[4] D. Perkins. *Introduction to High Energy Physics*. Cambridge University Press, 4th edition, 2000. ISBN 0 521 62196 8.

[5] Dirk Dammann. Production Cross Section Measurement of Top-Antitop Pairs in the Dimuon Decay Channel at $\sqrt{s} = 7\,\mathrm{TeV}$ with the CMS Experiment. *PhD Thesis*, 2011. `http://www.physnet.uni-hamburg.de/services/fachinfo/disslist2011.php`.

[6] K. Nakamura et al. PDG Particle Listings. *J.Phys.*, G37:075021, 2010. `http://pdg.lbl.gov/2010/listings/contents_listings.html`.

[7] H. J. Bhabha. The Scattering of Positrons by Electrons with Exchange on Dirac's Theory of the Positron. *Proc.R.Soc.*, A154:195–206, 1936. `http://rspa.royalsocietypublishing.org/content/154/881/195`.

[8] M. Weitz, A. Huber, F. Schmidt-Kaler, D. Leibfried, and T. W. Hänsch. Precision measurement of the hydrogen and deuterium 1 S ground state Lamb shift. *Phys.Rev.Lett.*, 72(3):328–331, 1994. `http://prl.aps.org/abstract/PRL/v72/i3/p328_1`.

[9] D. Berkeland, E. Hinds, and M. Boshier. Precise Optical Measurement of Lamb Shifts in Atomic Hydrogen. *Phys.Rev.Lett.*, 75(13):2470–2473, 1995. `http://prl.aps.org/abstract/PRL/v75/i13/p2470_1`.

[10] H1 Collaboration and ZEUS Collaboration. Resonance searches at HERA. 2009. `http://arxiv.org/abs/0907.4574`.

[11] Gargamelle Collaboration: F. J. Hasert et al. Observation of neutrino-like interactions without muon or electron in the gargamelle neutrino experiment. *Phys.Lett.*, B46(1):138–140, 1973. `http://cdsweb.cern.ch/record/203096`.

[12] UA1 Collaboration: G. Arnison et al. Experimental observation of isolated large transverse energy electrons with associated missing energy at $\sqrt{s} = 540\,\mathrm{GeV}$. *Phys.Lett.*, B122:103–116, 1983. `http://cdsweb.cern.ch/record/142059/`.

[13] UA1 Collaboration: G. Arnison et al. Experimental observation of lepton pairs of invariant mass around $95\,\mathrm{GeV}/c^2$ at the CERN SPS collider. *Phys.Lett.*, B126:398–410, 1983. `http://ccdb4fs.kek.jp/cgi-bin/img_index?8306331`.

[14] UA2 Collaboration: M. Banner et al. Observation of single isolated electrons of high transverse momentum in events with missing transverse energy at the CERN anti-p p collider. *Phys.Lett.*, B122:476–485, 1983. `http://cdsweb.cern.ch/record/142759`.

[15] ALEPH, DELPHI, L3, OPAL, SLD Collaborations, the LEP Electroweak Working Group, the SLD Electroweak and Heavy Flavour Groups. Precision Electroweak Measurements on the Z Resonance. *Phys.Rept.*, 427:257, 2006. `http://arxiv.org/abs/hep-ex/0509008`.

[16] ALEPH Collaboration, CDF Collaboration, D0 Collaboration, DELPHI Collaboration, L3 Collaboration, OPAL Collaboration, SLD Collaboration, LEP Electroweak Working Group, Tevatron Electroweak Working Group, and SLD electroweak heavy flavour groups. Precision Electroweak Measurements and Constraints on the Standard Model, 2009. `http://arxiv.org/abs/0911.2604`.

[17] M. Kobayashi and T. Maskawa. CP Violation in the Renormalizable Theory of Weak Interaction. *Prog.Theor.Phys.*, 49:652–657, 1973. `http://ptp.ipap.jp/link?PTP/49/652/`.

[18] C. S. Wu, E. Ambler, R. W. Hayward, D. D. Hoppes, and R. P. Hudson. Experimental Test of Parity Conservation in Beta Decay. *Phys.Rev.*, 105(4):1413–1415, 1957. `http://prola.aps.org/abstract/PR/v105/i4/p1413_1`.

[19] James Cronin. CP Symmetry Violation – The Search for Its Origin. *Nobel Lectures*, 1980. `http://www.nobelprize.org/nobel_prizes/physics/laureates/1980/cronin-lecture.html`.

[20] Val Fitch. The Discovery of Charge – Conjugation Parity Asymmetry. *Nobel Lectures*, 1980. `http://www.nobelprize.org/nobel_prizes/physics/laureates/1980/fitch-lecture.html`.

[21] J. W. F. Valle. Neutrino physics overview. 2006. `http://arxiv.org/abs/hep-ph/0608101v1`.

[22] M. Nakagawa Z. Maki and S. Sakata. Remarks on the Unified Model of Elementary Particles. *Prog.Theor.Phys.*, 28(5):870–880, 1962. `http://ptp.ipap.jp/link?PTP/28/870/`.

[23] NuTeV Collaboration: G. P. Zeller et al. A Measurement of the Weak Mixing Angle in Neutrino-Nucleon Scattering at NuTeV. 1999. `http://arxiv.org/abs/hep-ex/9906024`.

[24] SLAC E158: P. L.Anthony et al. Precision measurement of the weak mixing angle in Moeller scattering. *Phys.Rev.Lett.*, 95:081601, 2005. `http://arxiv.org/pdf/hep-ex/0504049`.

[25] S. L. Glashow. Partial-symmetries of weak interactions. *Nucl.Phys.*, 22(4):579–588, 1961. `www.slac.stanford.edu/spires/find/hep/www?j=NUPHA,22,579`.

[26] P. Higgs. Spontaneous Symmetry Breakdown without Massless Bosons. *Phys.Rev.*, 145(4):1156–1163, 1966. `http://prola.aps.org/abstract/PR/v145/i4/p1156_1`.

[27] B. W. Lee, C. Quigg, and H. B. Thacker. Weak interactions at very high energies: The role of the Higgs-boson mass. *Phys.Rev.*, D16(5): 1519–1531, 1977. `http://prd.aps.org/abstract/PRD/v16/i5/p1519_1`.

[28] J. Einasto. Dark Matter, 2009. `http://arxiv.org/abs/0901.0632`.

[29] R. S. Chivukula. Electroweak symmetry breaking. *J.Phys.: Conf.Ser.*, 37:28–33, 2006. `http://www.iop.org/EJ/abstract/1742-6596/37/1/007`.

[30] N. Arkani-Hamed, S. Dimopoulos, and G. Dvali. The hierarchy problem and new dimensions at a millimeter. *Phys.Lett.*, B429(3–4):263–272, 1998. `http://arxiv.org/abs/hep-ph/9803315`.

[31] D. Kapner, T. Cook, E. Adelberger, J. Gundlach, B. Heckel, C. Hoyle, and H. Swanson. Tests of the Gravitational Inverse-Square Law below the Dark-Energy Length Scale. *Phys.Rev.Lett.*, 98:021101, 2007. `http://arxiv.org/abs/hep-ph/0611184`.

[32] Paul Wesson. *Space-Time-Matter: Modern Kaluza-Klein Theory*. 1999. ISBN 9810235887.

[33] Ian J R Aitchison. Supersymmetry and the MSSM: An Elementary Introduction, 2005. `http://arxiv.org/abs/hep-ph/0505105`.

[34] J. W. Hustonand W. J. Stirling J. M. Campbell. Hard Interactions of Quarks and Gluons: A Primer for LHC Physics. *Rept.Prog.Phys.*, 70:89, 2007. `http://arxiv.org/abs/hep-ph/0611148v1`.

[35] Niladri Sen. Measurement of the Energy Flow at Large Pseudorapidities for $\sqrt{s} = 0.9\,\text{TeV}$ and $\sqrt{s} = 7\,\text{TeV}$ at the Large Hadron Collider Using the Compact Muon Solenoid. *PhD Thesis*, 2011. `http://www.physnet.uni-hamburg.de/services/fachinfo/disslist2011.php`.

[36] CDF Collaboration. Studying the Underlying Event in Drell-Yan and High Transverse Momentum Jet Production at the Tevatron. *Phys.Rev.*, D82:034001, 2010. doi: 10.1103/PhysRevD.82.034001. `http://arxiv.org/abs/1003.3146`.

[37] S. D. Drell and T. Yan. Massive Lepton-Pair Production in Hadron-Hadron Collisions at High Energies. *Phys.Rev.Lett.*, 25(5):316–320, 1970. `http://prl.aps.org/abstract/PRL/v25/i5/p316_1`.

[38] MSTW. MSTW homepage. `http://mstwpdf.hepforge.org/`.

[39] V. N. Gribov and L. N. Lipatov. Deep inelastic e p scattering in perturbation theory. *Sov.J.Nucl.Phys.*, 15:438–450, 1972.

[40] L. N. Lipatov. The parton model and perturbation theory. *Sov.J.Nucl.-Phys.*, 20:94–102, 1975.

[41] Y. L. Dokshitzer. Calculation of the Structure Functions for Deep Inelastic Scattering and e+ e- Annihilation by Perturbation Theory in Quantum Chromodynamics. *Sov.Phys.JETP*, 46:641–653, 1977.

[42] G. Altarelli and G. Parisi. Asymptotic freedom in parton language. *Nucl.Phys.*, B(2):298–318, 1977. `http://adsabs.harvard.edu/abs/1977NuPhB.126..298A`.

[43] H1 and ZEUS Collaboration. Combined measurement and QCD analysis of the inclusive $e^{\pm}p$ scattering cross sections at HERA. *Journal of High Energy Physics*, 2010:1–63, 2010. ISSN 1029-8479. `http://dx.doi.org/10.1007/JHEP01(2010)109`. 10.1007/JHEP01(2010)109.

[44] New Muon Collaboration: M. Arneodo et al. Measurement of the proton and deuteron structure functions, F2(p) and F2(d), and of the ratio sigma(L)/sigma(T). *Nucl.Phys.*, B483:3–43, 1997. `http://arxiv.org/abs/hep-ph/9610231`.

[45] NuTeV Experiment: M. Tzanov et al. Precise Measurement of Neutrino and Anti-neutrino Differential Cross Sections. *Phys.Rev.*, D74:012008, 2005. `http://arxiv.org/abs/hep-ex/0509010`.

[46] Daniel Stump, Joey Huston, Jon Pumplin, Wu-Ki Tung, Hung-Liang Lai, Steve Kuhlmann, and Joseph Francis Owens. Inclusive jet production, parton distributions, and the search for new physics. *Journal of High Energy Physics*, 2003(10):046, 2003. `http://stacks.iop.org/1126-6708/2003/i=10/a=046`.

[47] A. D. Martin, W. J. Stirling, R. S. Thorne, and G. Watt. Parton distributions for the LHC. *EPJ*, C63:189, 2009. `http://arxiv.org/abs/0901.0002`.

[48] P. Bartalini. The underlying event at the LHC. *CMS Note*, 2006/067, 2006. `http://cdsweb.cern.ch/record/973110/`.

[49] CDF Collaboration: F. Abe et al. Observation of Top Quark Production in $p\bar{p}$ Collisions with the Collider Detector at Fermilab. *Phys.Rev.Lett.*, 74(14):2626–2631, 1995. `http://arxiv.org/abs/hep-ex/9503002`.

[50] D0 Collaboration: S. Abachi et al. Observation of the Top Quark. *Phys.Rev.Lett.*, 74(14):2632–2637, 1995. `http://arxiv.org/abs/hep-ex/9503003`.

[51] N. Kidonakis. Higher-order corrections to top-antitop pair and single top quark production. 2009. `http://arxiv.org/abs/0909.0037v1`.

[52] B. R. Webber R. K. Ellis, W. J. Stirling. *QCD and Collider Physics*. Cambridge Monographs on Particle Physics, Nuclear Physics and Cosmology, 1st edition, 1996. ISBN 0 521 54589 7.

[53] Jan Kieseler. Measurement of the Top-Antitop and Z^0-Boson Production Cross Sections and Their Ratio in the Dileptonic Decay Channels at $\sqrt{s} = 7$ TeV with the CMS Experiment. 2012.

[54] James Stirling. James Stirling homepage. `http://www.hep.phy.cam.ac.uk/~wjs/`.

[55] CMS Collaboration. Measurement of the rapidity and transverse momentum distributions of Z bosons in pp collisions at $\sqrt{(s)}$=7 TeV. *Phys. Rev. D*, 85:032002, Feb 2012. doi: 10.1103/PhysRevD.85.032002. `http://link.aps.org/doi/10.1103/PhysRevD.85.032002`.

[56] CMS Collaboration. Observation of Z+b. *CMS PAS*, EWK-10-015, 2011. `http://cdsweb.cern.ch/record/1337739`.

[57] Rikkert Frederix, Stefano Frixione, Valentin Hirschi, Fabio Maltoni, Roberto Pittau, and Paolo Torrielli. W and Z/γ^* boson production in association with a bottom-antibottom pair. *Journal of High Energy Physics*, 2011:1–19, 2011. ISSN 1029-8479. `http://dx.doi.org/10.1007/JHEP09(2011)061`. 10.1007/JHEP09(2011)061.

[58] J. Campbell, R. K. Ellis, F. Maltoni, and S. Willenbrock. Associated production of a Z boson and a single heavy-quark jet. *Phys. Rev. D*, 69: 074021, Apr 2004. doi: 10.1103/PhysRevD.69.074021. `http://link.aps.org/doi/10.1103/PhysRevD.69.074021`.

[59] Fabio Maltoni, Thomas McElmurry, and Scott Willenbrock. Inclusive production of a Higgs or Z boson in association with heavy quarks. *Phys. Rev. D*, 72:074024, Oct 2005. doi: 10.1103/PhysRevD.72.074024. `http://link.aps.org/doi/10.1103/PhysRevD.72.074024`.

[60] J. Campbell, R. K. Ellis, F. Maltoni, and S. Willenbrock. Production of a Z boson and two jets with one heavy-quark tag. *Phys. Rev. D*, 73: 054007, Mar 2006. doi: 10.1103/PhysRevD.73.054007. `http://link.aps.org/doi/10.1103/PhysRevD.73.054007`.

[61] J. Campbell, R. K. Ellis, F. Maltoni, and S. Willenbrock. Production of a Z boson and two jets with one heavy-quark tag. *Phys. Rev. D*, page 054007, Mar 2006. doi: 10.1103/PhysRevD.73.054007. `http://link.aps.org/doi/10.1103/PhysRevD.73.054007`.

[62] CDF Collaboration. Measurement of the b jet cross section in events with a Z boson in $p\overline{p}$ collisions at $\sqrt{s} = 1.96$ TeV. *Phys. Rev. D*, 74: 032008, Aug 2006. doi: 10.1103/PhysRevD.74.032008. `http://link.aps.org/doi/10.1103/PhysRevD.74.032008`.

[63] D0 Collaboration. Measurement of the Ratio of Inclusive Cross Sections $\sigma(p\overline{p} \to Z + b\,\text{jet})/\sigma(p\overline{p} \to Z + \text{jet})$ at $\sqrt{s} = 1.96$ TeV. *Phys. Rev. Lett.*, 94:161801, Apr 2005. doi: 10.1103/PhysRevLett.94.161801. `http://link.aps.org/doi/10.1103/PhysRevLett.94.161801`.

[64] C. Amsler et al. Passage of particles through matter. *Phys. Lett.*, B667(1), 2008. `http://pdg.lbl.gov/2008/reviews/passagerpp.pdf`, update: `http://pdg.lbl.gov/2011/reviews/rpp2011-rev-passage-particles-matter.pdf`.

[65] ATLAS Collaboration. The ATLAS Experiment at the CERN Large Hadron Collider. *JINST*, 3(S08003), 2008. `http://www.iop.org/EJ/journal/-page=extra.lhc/jinst`.

[66] ALICE Collaboration. The ALICE experiment at the CERN LHC. *JINST*, 3(S08002), 2008. `http://www.iop.org/EJ/journal/-page=extra.lhc/jinst`.

[67] LHCb Collaboration. The LHCb Detector at the LHC. *JINST*, 3(S08005), 2008. `http://www.iop.org/EJ/journal/-page=extra.lhc/jinst`.

[68] LHCf Collaboration. The LHCf detector at the CERN Large Hadron Collider. *JINST*, 3(S08006), 2008. `http://www.iop.org/EJ/journal/-page=extra.lhc/jinst`.

[69] TOTEM Collaboration. The TOTEM Experiment at the CERN Large Hadron Collider. *JINST*, 3(S08007), 2008. `http://www.iop.org/EJ/journal/-page=extra.lhc/jinst`.

[70] Luminosity 2010, . `https://twiki.cern.ch/twiki/bin/view/CMSPublic/LumiPublicResults2010`.

[71] Luminosity 2011, . `https://twiki.cern.ch/twiki/bin/view/CMSPublic/LumiPublicResults`.

[72] CMS Collaboration. Measurement of Tracking Efficiency. *PAS*, TRK-10-002, 2010. `http://cdsweb.cern.ch/record/1279139/`.

[73] CMS Collaboration. Tracking and Primary Vertex Results in First 7 TeV Collisions. *PAS*, TRK-10-005, 2010. `http://cdsweb.cern.ch/record/1279383/`.

[74] CMS Collaboration. Measurement of Momentum Scale and Resolution of the CMS Detector using Low-mass Resonances and Cosmic Ray Muons. *PAS*, TRK-10-004, 2010. `http://cdsweb.cern.ch/record/1279137/`.

[75] CMS Collaboration. *CMS Physics Technical Design Report, Volume I: Detector Performance and Software.* Technical Design Report CMS. CERN, Geneva, 2006.

[76] CMS Collaboration. CMS Physics Technical Design Report, Volume II: Physics Performance. *Journal of Physics G: Nuclear and Particle Physics*, 34(6):995, 2007.
`http://stacks.iop.org/0954-3899/34/i=6/a=S01`.

[77] Markus Stoye. Calibration and Alignment of the CMS Silicon Tracking Detector. *PhD Thesis*, 2007. `http://www.physnet.uni-hamburg.de/services/fachinfo/dissfb12_2007.html`.

[78] CMS Collaboration. Commissioning and performance of the CMS silicon strip tracker with cosmic ray muons. *Journal of Instrumentation*, 5(03): T03008, 2010.
`http://stacks.iop.org/1748-0221/5/i=03/a=T03008`.

[79] P. Lenzi, C. Genta, and B. Mangano. Track reconstruction of real cosmic muon events with CMS tracker detector. *Journal of Physics: Conference Series*, 119(3):032030, 2008.
`http://stacks.iop.org/1742-6596/119/i=3/a=032030`.

[80] R. Frühwirt. *Data Analysis Techniques for High-Energy Physics*. 2000.

[81] Iterative Tracking Steps. `https://twiki.cern.ch/twiki/bin/view/CMSPublic/SWGuideIterativeTracking`.

[82] Fabio Cossutti and the CMS Offline project. Tuning and optimization of the CMS simulation software. *Journal of Physics: Conference Series*, 219(3):032005, 2010.
`http://stacks.iop.org/1742-6596/219/i=3/a=032005`.

[83] Rick Field. Early LHC Underlying Event Data - Findings and Surprises. (arXiv:1010.3558), Oct 2010.
`http://arxiv.org/abs/1010.3558`. Comments: Invited talk at HCP2010, Toronto, August 23, 2010.

[84] CMS Collaboration. Measurement of the underlying event activity at the LHC with $\sqrt{s} = 7\,\text{TeV}$ and comparison witn $\sqrt{s} = 0.9\,\text{TeV}$. *Journal of High Energy Physics*, 2011:1–31, 2011. ISSN 1029-8479. http://dx.doi.org/10.1007/JHEP09(2011)109. 10.1007/JHEP09(2011)109.

[85] T. Sjöstrand, S. Mrenna, and P. Skands. Pythia 6.4 Physics and Manual. *JHEP*, 05:026, 2006. http://arxiv.org/abs/hep-ph/0603175.

[86] F. Maltoni and T. Stelzer. MadEvent: Automatic Event Generation with MadGraph. *JHEP*, 0302:027, 2003. http://arxiv.org/abs/hep-ph/0208156.

[87] MCFM – Monte Carlo for FeMtobarn processes. http://mcfm.fnal.gov/.

[88] John M. Campbell and R.K. Ellis. MCFM for the Tevatron and the LHC. *Nuclear Physics B - Proceedings Supplements*, 205-206(0):10–15, 2010. ISSN 0920-5632. doi: 10.1016/j.nuclphysbps.2010.08.011. http://www.sciencedirect.com/science/article/pii/S0920563210001945. Loops and Legs in Quantum Field Theory. Proceedings of the 10th DESY Workshop on Elementary Particle Theory.

[89] Stephen Mrenna and Peter Richardson. Matching matrix elements and parton showers with HERWIG and PYTHIA. *Journal of High Energy Physics*, 2004(05):040, 2004. http://stacks.iop.org/1126-6708/2004/i=05/a=040.

[90] Zbigniew Was. TAUOLA for simulation of tau decay and production: perspectives for precision low energy and LHC applications. *IFJPAN*, IV-2011-1, 2011. http://arxiv.org/abs/1101.1652.

[91] Paolo Nason. A new method for combining NLO QCD with shower Monte Carlo algorithms. *Journal of High Energy Physics*, 2004(11):040, 2004. http://stacks.iop.org/1126-6708/2004/i=11/a=040.

[92] Stefano Frixione, Paolo Nason, and Carlo Oleari. Matching NLO QCD computations with Parton Shower simulations: the POWHEG method. *JHEP*, 11:070, 2007. doi: 10.1088/1126-6708/2007/11/070.

[93] Simone Alioli, Paolo Nason, Carlo Oleari, and Emanuele Re. NLO vector-boson production matched with shower in POWHEG. *JHEP*, 07:060, 2008. doi: 10.1088/1126-6708/2008/07/060.

[94] S. Agostinelli et al. Geant4—a simulation toolkit. *Nucl.Inst.Meth.*, A506 (3):250 – 303, 2003. http://www.sciencedirect.com/science/article/B6TJM-48TJFY8-5/2/23ea98096ce11c1be446850c04cfa498.

[95] J. Allison et al. Geant4 developments and applications. *IEEE Trans. Nucl. Sci.*, 53:270, 2006. `http://ieeexplore.ieee.org/xpl/freeabs_all.jsp?arnumber=1610988`.

[96] H. Bethe. Zur Theorie des Durchgangs schneller Korpuskularstrahlen durch Materie. *Annalen der Physik*, 397:325–400, 1930. `http://onlinelibrary.wiley.com/doi/10.1002/andp.19303970303/abstract`.

[97] CMS Collaboration. Performance of muon identification in pp collisions at $\sqrt{s} = 7$ TeV. *PAS*, MUO-10-002, 2010. `http://cdsweb.cern.ch/record/1279140/`.

[98] Muon Reconstruction, . `https://twiki.cern.ch/twiki/bin/view/CMSPublic/WorkBookMuonAnalysis`.

[99] Muon Identification, . unpublished, restricted access at `https://twiki.cern.ch/twiki/bin/view/CMS/VbtfWmunuBaselineSelection`.

[100] J E Huth, N Wainer, K Meier, N J Hadley, F Aversa, Mario Greco, P Chiappetta, J P Guillet, S Ellis, Z Kunszt, and D E Soper. Toward a standardization of jet definitions. (FERMILAB-CONF-90-249-E):7 p, Dec 1990. `http://lss.fnal.gov/archive/1990/conf/Conf-90-249-E.pdf`.

[101] Gavin P. Salam and Grégory Soyez. A practical seedless infrared-safe cone jet algorithm. *Journal of High Energy Physics*, 2007(05):086, 2007. `http://stacks.iop.org/1126-6708/2007/i=05/a=086`.

[102] CMS Collaboration. Performance of Jet Algorithms in CMS. *PAS*, JME-07-003, 2007. `http://cdsweb.cern.ch/record/1198227/`.

[103] Stephen D. Ellis and Davison E. Soper. Successive combination jet algorithm for hadron collisions. *Phys. Rev. D*, 48:3160–3166, Oct 1993. doi: 10.1103/PhysRevD.48.3160.
`http://link.aps.org/doi/10.1103/PhysRevD.48.3160`.

[104] S. Catani, Yu.L. Dokshitzer, M.H. Seymour, and B.R. Webber. Longitudinally-invariant K_t-clustering algorithms for hadron-hadron collisions. *Nuclear Physics B*, 406(1-2):187 – 224, 1993. ISSN 0550-3213. doi: 10.1016/0550-3213(93)90166-M.
`http://www.sciencedirect.com/science/article/pii/055032139390166M`.

[105] M. Cacciari and G. Salam. The anti k_t jet clustering algorithm. *JHEP*, 04:063, 2008. `http://arxiv.org/abs/0802.1189`.

[106] CMS Collaboration. Jet Performance in pp Collisions at $\sqrt{s} = 7$ TeV. *PAS*, JME-10-003, 2010. `http://cdsweb.cern.ch/record/1279362/`.

[107] CMS Collaboration. Particle-Flow Event Reconstruction in CMS and Performance for Jets, Taus, and E_T^{miss}. *PAS*, PFT-09-001, 2009. http://cdsweb.cern.ch/record/1194487/.

[108] CMS Collaboration. Determination of the Jet Energy Scale in CMS with pp Collisions at $\sqrt{s} = 7$ TeV. *PAS*, JME-10-010, 2010. http://cdsweb.cern.ch/record/1308178/.

[109] CMS Collaboration. Determination of jet energy calibration and transverse momentum resolution in CMS. *Journal of Instrumentation*, 6(11): P11002, 2011.
http://stacks.iop.org/1748-0221/6/i=11/a=P11002.

[110] K. Kousouris. Relative Response from Dijet Balance with 7 TeV data. JEC Meeting, August 2010. unpublished, restricted access at http://indico.cern.ch/getFile.py/access?contribId=2&resId=0&materialId=slides&confId=105277.

[111] Jet Identification. unpublished, restricted access at https://twiki.cern.ch/twiki/bin/viewauth/CMS/JetID.

[112] Andrea Rizzi, Fabrizio Palla, and Gabriele Segneri. Track impact parameter based b-tagging with CMS. Technical Report CMS-NOTE-2006-019. CERN-CMS-NOTE-2006-019, CERN, Geneva, Jan 2006. http://cdsweb.cern.ch/record/927385.

[113] CMS Collaboration. Algorithms for b Jet identification in CMS. *PAS*, BTV-09-001, Jul 2009. http://cdsweb.cern.ch/record/1194494.

[114] CMS Collaboration. Commissioning of b-jet identification with pp collisions at $\sqrt{s} = 7$ TeV. *PAS*, BTV-10-001, 2010. http://cdsweb.cern.ch/record/1279144/.

[115] S. van der Meer. Calibration of the effective beam height in the ISR. oai:cds.cern.ch:296752. (CERN-ISR-PO-68-31. ISR-PO-68-31), 1968. http://cdsweb.cern.ch/record/296752/.

[116] CMS Collaboration. Measurement of CMS Luminosity. *PAS*, EWK-10-004, 2010. http://cdsweb.cern.ch/record/1279145.

[117] CMS Collaboration. Absolute luminosity normalization. *Detector Performance Summary*, DP-2011-002, Mar 2011. http://cdsweb.cern.ch/record/1335668/.

[118] CMS Collaboration. Absolute Calibration of Luminosity Measurement at CMS: Summer 2011 Update. *PAS*, EWK-11-001, 2011. http://cdsweb.cern.ch/record/1376102.

[119] CMS Collaboration. Absolute Calibration of the Luminosity Measurement at CMS: Winter 2012 Update. *PAS*, SMP-12-008, 2012. http://cdsweb.cern.ch/record/1434360/.

[120] F. P. Schilling. Track Reconstruction and Alignment with the CMS Silicon Tracker. oai:cds.cern.ch:986350. (CMS-CR-2006-061. CERN-CMS-CR-2006-061), Sep 2006. Manuscript not submitted to the proceedings ICHEP06. `http://cdsweb.cern.ch/record/986350/`.

[121] Johannes Hauk. Estimation of the Tracker Alignment Precision. *CMS Analysis Note*, 12/235, 2012. unpublished, restricted access at `http://cms.cern.ch/iCMS/jsp/db_notes/noteInfo.jsp?cmsnoteid=CMS%20AN-2012/235`.

[122] CMS Collaboration. CMS Tracker Alignment Paper. *Paper in preparation*, TRK-11-002, expected 2012. unpublished, restricted access at `http://cms.cern.ch/iCMS/analysisadmin/cadi?ancode=TRK-11-002`.

[123] CMS Collaboration. Alignment of the CMS silicon strip tracker during stand-alone commissioning. *Journal of Instrumentation*, 4(07):T07001, 2009. `http://stacks.iop.org/1748-0221/4/i=07/a=T07001`.

[124] Johannes Hauk. Validation of Alignment Constants of the CMS Track Detector with Cosmic Muons. (In German). *Diploma Thesis*, CMS TS-2009/001, 2008. `http://pubdb.desy.de/anonymous/index.php?index=520&cmd=search&lid=7199`.

[125] V. Karimäki. Hit covariances in strip detector simulation and reconstruction. (CMS TN-1995/170), 1995. `http://cms.cern.ch/iCMS/jsp/db_notes/noteInfo.jsp?cmsnoteid=CMS%20TN-1995/170`.

[126] Jula Draeger. Track Based Alignment of the CMS Silicon Tracker and its Implication on Physics Performance. *PhD Thesis*, 2011. `http://www.physnet.uni-hamburg.de/services/fachinfo/disslist2011.php`.

[127] Nhan Tran. Spin Correlations at the LHC. *PhD Thesis*, 2011. `http://www.pha.jhu.edu/~gritsan/research/cms.html`.

[128] Marco Musich. The Alignment of the CMS Tracker and its Impact on the early Quarkonium Physics. *PhD Thesis*, 2011. `http://dottorato.ph.unito.it/Studenti/Tesi/XXIII/`.

[129] CMS Collaboration. Impact of Tracker Misalignment on the CMS b-Tagging Performance. *PAS*, BTV-07-003, Aug 2009. `http://cdsweb.cern.ch/record/1198691/`.

[130] Armin Scheurer. Algorithms for the Identification of b-Quark Jets with First Data at CMS. *PhD Thesis*, 2008. `http://cdsweb.cern.ch/record/1311175/`.

[131] Veikko Karimäki, Tapio Lampen, and Frank-Peter Schilling. The HIP Algorithm for Track Based Alignment and its Application to the CMS Pixel Detector. (CMS-NOTE-2006-018. CERN-CMS-NOTE-2006-018), Jan 2006. `http://cdsweb.cern.ch/record/926537/`.

[132] V. Blobel. Software alignment for tracking detectors. *Nuclear Instruments and Methods in Physics Research Section A: Accelerators, Spectrometers, Detectors and Associated Equipment*, 566(1):5 – 13, 2006. ISSN 0168-9002. doi: 10.1016/j.nima.2006.05.157. `http://www.sciencedirect.com/science/article/pii/S0168900206007984`. Proceedings of the 1st Workshop on Tracking in High Multiplicity Environments.

[133] Claus Kleinwort and Frank Meier. Alignment of the CMS silicon tracker – and how to improve detectors in the future. *Nuclear Instruments and Methods in Physics Research Section A: Accelerators, Spectrometers, Detectors and Associated Equipment*, 650(1):240 – 244, 2011. ISSN 0168-9002. doi: 10.1016/j.nima.2010.11.187. `http://www.sciencedirect.com/science/article/pii/S0168900210027373`. International Workshop on Semiconductor Pixel Detectors for Particles and Imaging 2010.

[134] Johannes Hauk. Interplay of normalized hit residuals and corresponding errors. *Presentation in CMS Tracker Local Reconstruction Meeting*, 2009. unpublished, restricted access at `https://indico.cern.ch/conferenceDisplay.py?confId=56297`.

[135] T. Aaltonen et al. First Measurement of the Ratio $\sigma_{\mathrm{t\bar{t}}}/\sigma_{\mathrm{Z}^0/\gamma^*\to ll}$ and Precise Extraction of the $\mathrm{t\bar{t}}$ Cross Section. *Phys. Rev. Lett.*, 105:012001, 2010. doi: 10.1103/PhysRevLett.105.012001.

[136] J. Hauk et al. Measurement of the Cross-Section Ratio of Top-Pair Production and Z^0 Production in pp Collisions at $\sqrt{s} = 7\,\mathrm{TeV}$ using the CMS Detector. *CMS Analysis Note*, 10/429, 2011. unpublished, restricted access at `http://cms.cern.ch/iCMS/jsp/db_notes/noteInfo.jsp?cmsnoteid=CMS%20AN-2010/429`.

[137] CMS Collaboration. Measurement of the $\mathrm{t\bar{t}}$ production cross section and the top quark mass in the dilepton channel in pp collisions at $\sqrt{s} = 7\,\mathrm{TeV}$. *Journal of High Energy Physics*, 2011:1–49, 2011. ISSN 1029-8479. doi: 10.1007/JHEP07(2011)049. `http://dx.doi.org/10.1007/JHEP07(2011)049`.

[138] D. Dammann et al. Measurement of the Top Quark Pair Production Cross Section in the Dimuon Decay Channel at $\sqrt{s} = 7\,\mathrm{TeV}$. *CMS Analysis Note*, 10/428, 2011. unpublished, restricted access at `http://cms.cern.ch/iCMS/jsp/db_notes/noteInfo.jsp?cmsnoteid=CMS%20AN-2010/428`.

[139] Vardan Khachatryan et al. Measurements of Inclusive W and Z Cross Sections in pp Collisions at $\sqrt{s} = 7\,\mathrm{TeV}$. *JHEP*, 01:080, 2011. doi: 10.1007/JHEP01(2011)080.

[140] CMS Collaboration. Measurements of Inclusive W and Z Cross Sections in pp Collisions at $\sqrt{s} = 7\,\mathrm{TeV}$. *CMS PAS*, EWK-10-005, 2011. http://cdsweb.cern.ch/record/1337017/.

[141] CMS Collaboration. Measurement of the inclusive W and Z production cross sections in pp collisions at $\sqrt{s} = 7\,\mathrm{TeV}$ with the CMS experiment. *Journal of High Energy Physics*, 2011:1–76, 2011. ISSN 1029-8479. http://dx.doi.org/10.1007/JHEP10(2011)132. 10.1007/JHEP10(2011)132.

[142] Reference Page for Top Dilepton Analysis. unpublished, restricted access at https://twiki.cern.ch/twiki/bin/view/CMS/TopDileptonRefAnalysis2010Pass6.

[143] Common Systematics for 2010 Top Analyses. unpublished, restricted access at https://twiki.cern.ch/twiki/bin/view/CMS/TopLeptonPlusJets2010Systematics.

[144] V. Krutelyov et al. A measurement of top quark pair production cross section in dilepton final states in pp collisions at 7 TeV. *CMS Analysis Note*, 10/410, 2011. unpublished, restricted access at http://cms.cern.ch/iCMS/jsp/db_notes/noteInfo.jsp?cmsnoteid=CMS%20AN-2010/410.

[145] CMS Collaboration. First Measurement of the Cross Section for Top-Quark Pair Production in Proton-Proton Collisions at sqrt(s)=7 TeV. *Phys. Lett.*, B695:424–443, 2011. doi: 10.1016/j.physletb.2010.11.058.

[146] Pavel M. Nadolsky et al. Implications of CTEQ global analysis for collider observables. *Phys. Rev.*, D78:013004, 2008. doi: 10.1103/PhysRevD.78.013004.

[147] Cross Sections of several Standard Model Processes for CMS. unpublished, restricted access at https://twiki.cern.ch/twiki/pub/CMS/GeneratorMain/ShortXsec.pdf.

[148] CMS Collaboration. Measurement of Top Quark Pair Differential Cross Sections at $\sqrt{s} = 7\,\mathrm{TeV}$. *PAS*, TOP-11-013, 2012. http://cdsweb.cern.ch/record/1422425/.

[149] M. Aldaya et al. Measurement of Top Quark Pair Differential Cross Sections in the Dilepton Final State at $\sqrt{s} = 7\,\mathrm{TeV}$. *CMS Analysis Note*, 11/186, 2012. unpublished, restricted access at http://cms.cern.ch/iCMS/jsp/db_notes/noteInfo.jsp?cmsnoteid=CMS%20AN-2011/186.

[150] R. Castello, L. Ceard, C. Deleare, T.A. du Pree, A. Gilbert, J. Hauk, N. Heracleous, A.-M. Magnan, E. Migliore, and M. Musich. Aspects of the Z+b cross-section measurement related to b-jet reconstruction. *CMS Analysis Note*, 11/263, 2012. unpublished, restricted access at http://cms.cern.ch/iCMS/jsp/db_notes/noteInfo.jsp?cmsnoteid=CMS%20AN-2011/263.

[151] CMS Collaboration. Measurement of the Z^0/γ^*+b-jet cross section in pp collisions at $\sqrt{s} = 7\,\mathrm{TeV}$. *submitted to Journal of High Energy Physics*, 2012. `http://arxiv.org/abs/1204.1643`.

[152] Sami Lehti. Observability of bbZ Events at CMS as a Benchmark for MSSM bbH Search. *CMS Note*, 2006/099, Jun 2006. `http://cdsweb.cern.ch/record/962052`.

[153] CMS Collaboration. Measurement of the Z b b-bar, Z to lepton lepton cross section with 100 inverse picobarns of early CMS data at the LHC. *CMS PAS*, EWK-08-001, Jan 2009. `http://cdsweb.cern.ch/record/1152574`.

[154] Alexander Nikitenko Anne-Marie Magnan. Measurement of $b\bar{b}Z$, Z→ ll cross section with CMS. *CMS Analysis Note*, 10/027, 2010. unpublished, restricted access at `http://cms.cern.ch/iCMS/jsp/db_notes/noteInfo.jsp?cmsnoteid=CMS%20AN-2010/027`.

[155] ATLAS Collaboration. Measurement of the cross-section for b-jets produced in association with a Z boson at $\sqrt{s} = 7\,\mathrm{TeV}$ with the ATLAS detector. *Physics Letters B*, 706(4–5):295 – 313, 2012. ISSN 0370-2693. doi: 10.1016/j.physletb.2011.11.059.
`http://www.sciencedirect.com/science/article/pii/S0370269311014389`.

[156] CMS internal page. Study of Z/W + heavy flavour. unpublished, restricted access at `https://twiki.cern.ch/twiki/bin/viewauth/CMS/VectorBosonPlusHeavyFlavor`.

[157] Matteo Cacciari and Gavin P. Salam. Pileup subtraction using jet areas. *Physics Letters B*, 659(1–2):119 – 126, 2008. ISSN 0370-2693. doi: 10.1016/j.physletb.2007.09.077.
`http://www.sciencedirect.com/science/article/pii/S0370269307011094`.

[158] S. de Visscher, A. Gilbert, A.-M. Magnan, A. Nikitenko, E. Migliore, and M. Musich. Study of the theoretical aspects for Z+b-jet(s) production. *CMS Analysis Note*, 11/305, 2011. unpublished, restricted access at `http://cms.cern.ch/iCMS/jsp/db_notes/noteInfo.jsp?cmsnoteid=CMS%20AN-2011/305`.

[159] R. Castello, L. Ceard, C. Deleare, T.A. du Pree, A. Gilbert, N. Heracleous, and A.-M. Magnan. Leptons efficiency and jets selection for the measurement of Z+b-jet (Z→ l^+l^-) cross section. *CMS Analysis Note*, 11/264, 2011. unpublished, restricted access at `http://cms.cern.ch/iCMS/jsp/db_notes/noteInfo.jsp?cmsnoteid=CMS%20AN-2011/264`.

[160] N. Adam et al. Generic Tag and Probe Tool for Measuring Efficiency at CMS with Early Data. *CMS Analysis Note*, 09/111, 2009. unpublished,

restricted access at http://cms.cern.ch/iCMS/jsp/db_notes/noteInfo.jsp?cmsnoteid=CMS%20AN-2009/111.

[161] CMS Collaboration. Performance of the b-jet identification in CMS. *CMS PAS*, BTV-11-001, 2011. http://cdsweb.cern.ch/record/1366061/.

[162] J. Alwall, S. Höche, F. Krauss, N. Lavesson, L. Lönnblad, F. Maltoni, M.L. Mangano, M. Moretti, C.G. Papadopoulos, F. Piccinini, S. Schumann, M. Treccani, J. Winter, and M. Worek. Comparative study of various algorithms for the merging of parton showers and matrix elements in hadronic collisions. *The European Physical Journal C - Particles and Fields*, 53:473–500, 2008. ISSN 1434-6044. http://dx.doi.org/10.1140/epjc/s10052-007-0490-5. 10.1140/epjc/s10052-007-0490-5.

[163] Johan Alwall, Simon de Visscher, and Fabio Maltoni. QCD radiation in the production of heavy colored particles at the LHC. *Journal of High Energy Physics*, 2009(02):017, 2009. http://stacks.iop.org/1126-6708/2009/i=02/a=017.

[164] CMS Collaboration. Status of b-tagging and vertexing tools for 2011 data analysis. *CMS PAS*, BTV-11-002, 2011. http://cdsweb.cern.ch/record/1395489/.

[165] Wolf Behrenhoff. Private Communication.

[166] T. Gleisberg, S. Höche, F. Krauss, M. Schönherr, S. Schumann, F. Siegert, and J. Winter. Event generation with sherpa 1.1. *Journal of High Energy Physics*, 2009(02):007, 2009. http://stacks.iop.org/1126-6708/2009/i=02/a=007.

[167] aMC@NLO Web Page. http://amcatnlo.web.cern.ch/amcatnlo/.

[168] G. Corcella et al. HERWIG 6.5 Release Note. *arXiv*, hep-ph/0210213v2, 2005. http://arxiv.org/abs/hep-ph/0210213.

[169] CMS Collaboration. Estimating Systematic Errors Due to Pileup Modeling. unpublished, restricted access at https://twiki.cern.ch/twiki/bin/viewauth/CMS/PileupSystematicErrors.

[170] Jonathan Pumplin, Daniel Robert Stump, Joey Huston, Hung-Liang Lai, Pavel Nadolsky, and Wu-Ki Tung. New Generation of Parton Distributions with Uncertainties from Global QCD Analysis. *Journal of High Energy Physics*, 2002(07):012, 2002. http://stacks.iop.org/1126-6708/2002/i=07/a=012.

[171] PDF4LHC Working Group. The PDF4LHC Working Group Interim Recommendations. *arXiv*, hep-ph/1101.0538v1, 2011. http://arxiv.org/abs/1101.0538.

[172] CMS Collaboration. Commissioning of the CMS experiment and the cosmic run at four tesla. *Journal of Instrumentation*, 5(03):T03001, 2010. `http://stacks.iop.org/1748-0221/5/i=03/a=T03001`.

[173] CMS Collaboration. Alignment of the CMS silicon tracker during commissioning with cosmic rays. *Journal of Instrumentation*, 5(03):T03009, 2010.
`http://stacks.iop.org/1748-0221/5/i=03/a=T03009`.

[174] Johannes Hauk. First Alignment of the CMS Tracker and Implications for the First Collision Data. *Poster Proceedings*, CMS CR-2010/026. doi: 10.3204/DESY-PROC-2010-04/P31.
`http://www-library.desy.de/preparch/desy/proc/proc10-04.html`. Prepared for 24th International Symposium on Lepton-Photon Interactions at High Energy (LP09), Hamburg, Germany, 17-22 Aug 2009.

[175] Gero Flucke. Alignment of the CMS Silicon Tracker. Technical Report CMS-CR-2011-323, CERN, Geneva, Nov 2011. Prepared for the 14th International Workshop on Advanced Computing and Analysis Techniques in Physics Research (ACAT 2011) `http://cdsweb.cern.ch/record/1406822`.

[176] CMS Tracker Alignment 2011. unpublished, restricted access at `https://twiki.cern.ch/twiki/bin/viewauth/CMS/TrackerAlignment2011`.

[177] Alignment Precision in Data Reconstruction. unpublished, restricted access at `https://hypernews.cern.ch/HyperNews/CMS/get/tk-alignment/960.html`.

[178] Johannes Hauk. Coordinate System in Alignment Validation. *Presentation in CMS Tracker Alignment Meeting*, 2009. unpublished, restricted access at `https://indico.cern.ch/getFile.py/access?contribId=15&sessionId=1&resId=0&materialId=slides&confId=55033`.

[179] Burton Betchart. A simple geometric model for rechits. 2009. unpublished, restricted access at `https://indico.cern.ch/conferenceDisplay.py?confId=56297`.

[180] CMS Collaboration. Studies of Tracker Material. *PAS*, TRK-10-003, 2010. `http://cdsweb.cern.ch/record/1279138/`.

[181] Top Dilepton Reference Analysis 2010. unpublished, restricted access at `https://twiki.cern.ch/twiki/bin/viewauth/CMS/TopDileptonRefAnalysis2010Pass6`.

Danksagung

Meinem Betreuer und Gutachter Achim Geiser danke ich sehr für die lehrreichen Jahre der Zusammenarbeit um diese Doktorarbeit erfolgreich zu erarbeiten. Mein Dank umfasst hierbei die wissenschaftliche Weitsicht, welche dazu führte, dass ich mich einerseits inhaltlich und methodisch ideal positionieren und signifikante Beiträge leisten konnte und andererseits tiefen Einblick bezüglich des Wirkens und der Abläufe innerhalb einer Kollaboration sowie innerhalb meines Institutes gewinnen konnte, gerade auch in Hinblick auf die menschliche Komponente in der Wissenschaft. Darüber hinaus möchte ich mich explizit für alle nicht-physikalischen Gespräche, die ebenfalls Teile einiger Abende ausfüllten und sehr interessant waren, und das große Verständnis für private Problematiken, bedanken. Den Professoren Joachim Mnich und Peter Schleper danke ich für die Übernahme der weiteren Gutachten.

Ich danke allen meinen Arbeitskollegen die mich in diesen Jahren begleiteten, mit denen ich zusammenarbeitete oder auch interessante Gespräche führen konnte. Meinen Doktorandenkollegen Dirk Dammann und Wolf Behrenhoff möchte ich speziell für die fruchtbare Zusammenarbeit bei meinen Physikanalysen danken. Rainer Mankel hat mir inhaltlich, aber besonders auch mit organisatorischer Unterstützung in sämtlichen Belangen, vieles erleichtert oder gar ermöglicht. Gero Flucke war wie bereits während der Diplomarbeit ein wichtiger Ansprechpartner, mit dem ich auch jede freie Minute bei Dienstreisen oder anderen Möglichkeiten sehr genossen habe. Bezüglich meiner dokumentierten technischen Analyse im Bereich Alignment gilt mein besonderer Dank Claus Kleinwort, dem möglicherweise weltbesten Aligner. Die Diskussionen mit ihm für die Entwicklung und Verwendung der Methode, aber auch generell über Alignment und Zugehöriges, waren enorm hilfreich. Weitere wichtige Unterstützung für meine Physikanalysen und meine wissenschaftliche Wahrnehmung fand ich in Andreas Meyer. Selbiges gilt auch für Maria Aldaya, mit der eine unkomplizierte und effektive Zusammenarbeit jederzeit möglich war.

Der Zufall wollte, dass ich die Turiner Arbeitsgruppe um Ernesto Migliore während Diplom- und Doktorarbeit in fast allen Analysen wiederfand und gerne mit ihnen gearbeitet habe, vor allem auch mit Roberto Castello. Im Bereich Alignment gilt mein Dank noch Alessio Bonato. Bei der ersten Physikanalyse (Wirkungsquerschnittsverhältnis) war die angenehme Zusammenarbeit mit Slava Krutelyov eine Bereicherung. Betreffend der zweiten Physikanalyse möchte ich dem gesamten Z+b-Team für die erfolgreiche Zusammenarbeit danken, im Speziellen Anne-Marie Magnan und Tristan du Pree. Für ein angenehmes Umfeld danke ich den zeitweiligen Bürokollegen Jan, Alexander, Niladri und Agni, den Bekannten während meiner Genf-Aufenthalte Jan, Stefan und Klemens, und weiteren beeindruckenden Personen die ich auf Konferenzen oder sonstigen Veranstaltungen näher kennenlernen durfte, vor allem Ludivine.

Jenseits meiner wissenschaftlichen Unterstützung danke ich all denen Personen auf die ich mich auch in schwierigen Situationen verlassen und stützen konnte, und die somit diese Arbeit erst ermöglicht haben. Hierbei danke ich meiner ganzen Familie für die stetige Förderung, speziell meinen geliebten Eltern für alle Sicherheit und Perspektive die sie mir bieten konnten, und natürlich auch für das wundervolle Buffet zu meiner Disputation. Meiner Schwester Susanne danke ich für jede gemeinsame Minute und das umfassende Verständnis. Für den Rückhalt den ich bei Freunden und Familie finden konnte als ich ihn am Dringendsten brauchte kann ich euch allen mit Worten gar nicht sagen wie viel mir das bedeutet hat. Dies betrifft Manuel in besonderem Maße der viel Zeit für mich geopfert hat, aber natürlich auch alle anderen Hamburger: Eva, Michael, Daniel, Daniel, Clarissa, Katharina, Martin, Jannes, Philipp, Johanna, Erik, Irene. Und ebenso alle vom Rest der Welt, die ich zwar nicht oft zu Gesicht bekommen habe während meiner Doktorarbeit, mir aber jedesmal enorm gut getan haben: Tobi, Toby, Helge, Annette, Vincent, Miriam, Urs, Elena. Vielen Dank für alle Rücksicht, für den mentalen Ausgleich, für jedes Stück geteilte Freud, geteiltes Leid; ohne euch hätte ich das nicht geschafft. Danke für eure Existenz!